Technical Physics Letters, Vol. 26, No. 9, 2000, pp. 751–753. Translated from Pis'ma v Zhurnal Tekhnicheskoĭ Fiziki, Vol. 26, No. 17, 2000, pp. 1–5.
Original Russian Text Copyright © 2000 by Didyk, Latyshev, Semina, Stepanov, Suvorov, Fedotov, Cheblukov.

Effect of 305-MeV Krypton Ions on the Surface of Highly Oriented Pyrolytic Graphite

A. Yu. Didyk, S. V. Latyshev, V. K. Semina, A. É. Stepanov, A. L. Suvorov, A. S. Fedotov, and Yu. N. Cheblukov

Institute of Theoretical and Experimental Physics, State Scientific Center of the Russian Federation, Moscow, 117259 Russia

Received April 20, 2000

Abstract—The surface of highly oriented pyrolytic graphite (HOPG) irradiated by 305-MeV krypton ions was studied in a scanning tunneling microscope. It was found that inelastic energy losses of the krypton ions do not significantly affect the sputtering of carbon from the surface of crystalline HOPG grains. Similarly to the case of metals, preferential sputtering takes place in the grain boundaries. The inhomogeneous sputtering of polycrystalline conductors has to be taken into account in interpreting experimental data on the sputtering of such targets by high-energy heavy ions in the range of inelastic energy losses. The results can be also implemented in the technology of ion implantation into deep layers of solids. *© 2000 MAIK "Nauka/Interperiodica".*

In the past decade, several experimental works [1–3] were reported on the sputtering of coarse-grained polycrystalline metals by high-energy heavy ions in the range of inelastic energy losses. The results of these experiments showed that the inelastic losses do not significantly affect the sputtering yield. Our study of the surface of sputtered metals by scanning electron microscopy (SEM) revealed for the first time the phenomenon of inhomogeneous sputtering of the polycrystalline targets by high-energy heavy ions in the range of inelastic energy losses [4]. It was found that the boundaries of crystalline grain were sputtered at a markedly higher rate as compared to that of the grain surface, a characteristic sputtering yield for the grain boundaries being $\geq 10^3$ atom/ion [4]. As the radiation defects in the target were accumulated in the course of irradiation by 305-MeV heavy (krypton) ions with the fluence increasing up to 3×10^{15} ion/cm^2, the sputtering yield from the grain surface also increased to a level comparable with that from the grain boundaries. This effect is explained by the fact that the accumulation of defects in the crystal leads to a decrease in the time of energy transfer from the electron subsystem (excited by the high-energy heavy projectiles) to atoms in the crystal lattice. As a result, a hot track is formed along the ion trajectory and the evaporation sputtering mechanism is switched on.

Below, we report on the results of investigation of the surface of highly oriented pyrolytic graphite (HOPG) irradiated by 305-MeV krypton ions. The target surface before and after irradiation was studied in air by scanning tunneling microscopy (STM). Using STM (instead of SEM as in [4]) allowed us to study the samples irradiated to low fluences.

In the first experiment, a HOPG sample was irradiated by 305-MeV krypton ions to a fluence of 6×10^{11} ion/cm^2. Subsequent investigation of numerous regions on the irradiated HOPG surface by STM at a resolution of ~10 Å showed no evidence of the sample surface modification as a result of the ion–target interaction. One of the scanned regions exhibited a superperiodic structure (Fig. 1). Structures of this type were frequently observed on the surface of unirradiated HOPG samples (see, e.g., [15] and references therein). Apparently, this superperiodic structure is not related to the action of krypton ions upon the HOPG surface. At the same time, there are publications [6, 7] where the formation of "islands" featuring a superperiodic structure was attributed to ion irradiation of the sample surface.

In the second experiment, the HOPG samples were irradiated by 305-MeV krypton ions to a fluence of 5×10^{12} ion/cm^2. During the exposure, half of the sample surface was shielded by a mask. After irradiation, the sample surface was examined by STM so as to reveal the regions containing HOPG grain boundaries. Figure 2 shows the STM images of such regions on both unirradiated and irradiated HOPG surface. The unirradiated surface (Fig. 2a) shows a typical grain boundary region with a height difference of ≤5 Å. The STM image of the irradiated surface (Fig. 2b) clearly reveals preferential sputtering of the grain boundary.

The above results agree with the data reported previously [1–4], according to which the inelastic (bremsstrahlung) losses weakly affect the sputtering yield from the surface of single-crystalline grains of conductors while markedly changing the sputtering from the regions containing a large amount of defects (the characteristic sputtering yield increases to $\geq 10^3$ atom/ion), in

1063-7850/00/2609-0751$20.00 © 2000 MAIK "Nauka/Interperiodica"

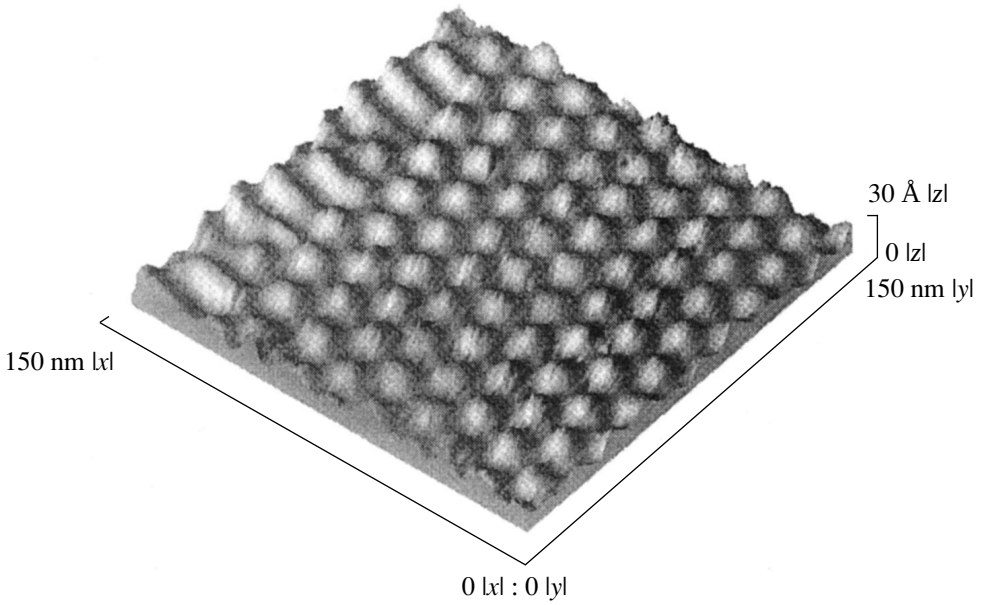

Fig. 1. The STM image of an "island" featuring a superperiodic structure on the HOPG sample surface.

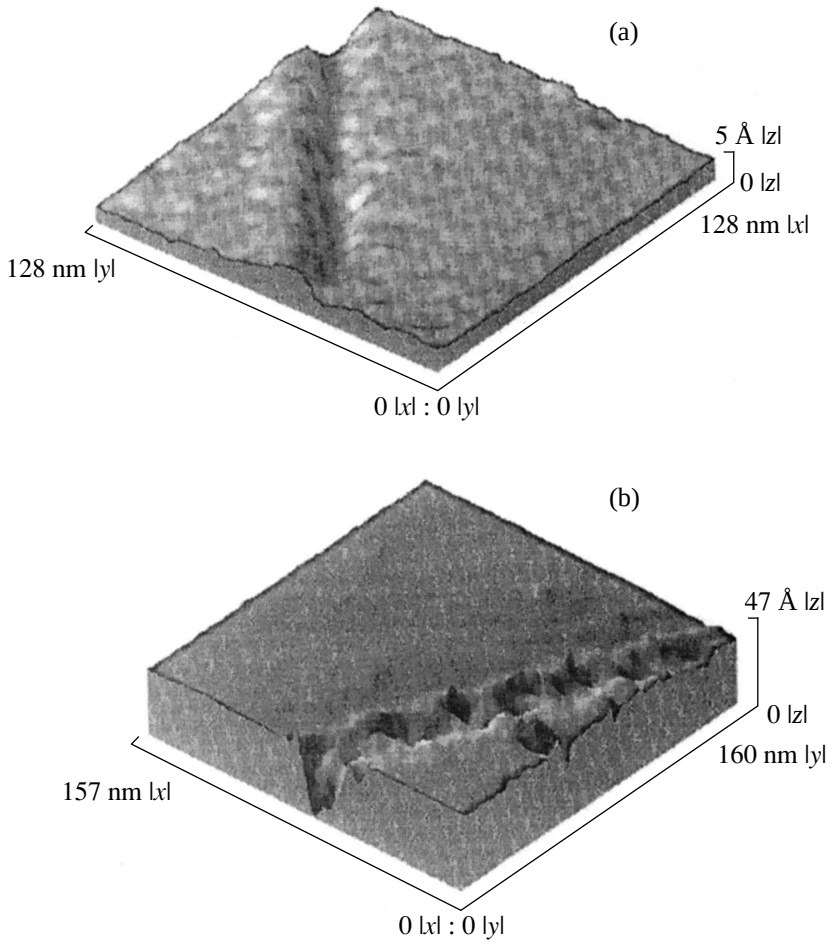

Fig. 2. The STM images of (a) unirradiated and (b) irradiated HOPG surface bombarded with 305-MeV krypton ions to a fluence of 5×10^{12} ion/cm^2.

particular, from the boundaries of crystalline grains. The phenomenon of preferential sputtering has to be taken into account in interpreting experimental data on the sputtering of polycrystalline targets by high-energy heavy ions in the range of inelastic energy losses. The results must also be taken into account in the technology of ion implantation into deep layers of solids.

REFERENCES

1. Yu. N. Cheblukov, D. G. Koshkarev, A. R. Peuto, *et al.*, Part. Accel. **37**–**38**, 351 (1992).
2. G. I. Akap'ev, A. N. Balabaev, N. A. Vasil'ev, *et al.*, Zh. Tekh. Fiz. **68** (1), 134 (1998) [Tech. Phys. **43**, 120 (1998)].
3. H. D. Mieskes, W. Assmann, M. Brodale, *et al.*, Nucl. Instrum. Methods Phys. Res. B **146**, 162 (1998).
4. A. Yu. Didyk, V. K. Semina, A. Khalil, *et al.*, Pis'ma Zh. Tekh. Fiz. **26** (2), 1 (2000) [Tech. Phys. Lett. **26**, 46 (2000)].
5. P. I. Oden, T. Thundat, L. A. Nagahara, *et al.*, Surf. Sci. Lett. **254**, 454 (1991).
6. D. V. Kulikov, A. L. Suvorov, R. A. Suris, *et al.*, Pis'ma Zh. Tekh. Fiz. **23** (14), 89 (1997) [Tech. Phys. Lett. **23**, 573 (1997)].
7. L. P. Biro, J. Gyulai, and K. Havancsak, Phys. Rev. B **52** (3), 2047 (1995).

Translated by P. Pozdeev

Technical Physics Letters, Vol. 26, No. 9, 2000, pp. 754–756. Translated from Pis'ma v Zhurnal Tekhnicheskoĭ Fiziki, Vol. 26, No. 17, 2000, pp. 6–10.
Original Russian Text Copyright © 2000 by Katerinchuk, Kovalyuk, Netyaga, Betsa.

Photoelectric Properties of the *n*-SnSSe–*p*-InSe Heterojunctions

V. N. Katerinchuk, Z. D. Kovalyuk, V. V. Netyaga, and T. V. Betsa

Institute of Materials Science Problems, National Academy of Sciences of Ukraine, Chernovtsy, 274001 Ukraine

Received February 15, 2000

Abstract—Photoelectric properties of the *n*-SnSSe–*p*-InSe heterojunctions were investigated. A special feature of these structures is the use of an $SnS_{2-x}Se_x$ alloy ($x = 0.5$) as a wide-bandgap window material, which makes it possible to shift a short-wavelength threshold (lying in the 0.8–1.0 μm range) of the heterojunction photosensitivity band. It is demonstrated that high-quality *p–n* heterojunctions can be fabricated from layered crystals joined to make an optical contact. *© 2000 MAIK "Nauka/Interperiodica".*

The spectral characteristic of a heterojunction photosensitivity depends on its composition and can be varied, in particular, by replacing the binary compounds forming the junction with their alloys. In the case of layered heterojunctions fabricated by applying one compound onto another so as to make the optical contact [1], there are no stringent limitations on the choice of materials and the task of changing the spectral characteristics can be easily solved. In this study, we examine the properties of a new SnSSe–InSe heterojunction, where the wide-bandgap window is formed by the SnSSe compound belonging to the SnS_2–$SnSe_2$ alloy system.

The SnSSe crystals were grown by the chemical transport reaction technique. High-quality small-size crystal samples were obtained in the form of plates chaotically arranged in a growth ampule. The crystals possess the electron conductivity with a majority charge carrier concentration of 10^{18} cm^{-3}. The InSe samples were prepared by splitting ingots, grown by the Bridgman method, into separate plates. To provide for the hole conductivity, the samples were doped by cadmium. The hole concentration in *p*-InSe was $(6–8) \times 10^{13}$ cm^{-3}. The values of the majority carrier concentration were used to determine the Fermi levels in the semiconductor samples. The heterojunctions were fabricated by the technique described in [1]. Pure indium was used to form the ohmic contacts.

It was found that the heterojunction samples are photosensitive, and their photoelectric characteristics were recorded to check for their high quality. Figure 1 shows the capacitance–voltage (*C–U*) characteristics from which the type of the *p–n* junction and the energy barrier height were determined. The curves are linear in the C^{-2} versus *U* coordinates, which corresponds to the abrupt junction model. A bending point occurs in the curves at a high reverse bias, since the heterojunction depletion region begins to penetrate into both materials. Variation of the *C–U* characteristics with the measurement frequency is due to the influence of the series resistance [2]. With the heterojunction oriented parallel to the crystal layers, the current flows in the direction perpendicular to the layer planes. Due to a large anisotropy of the conductivity along the in-plane and normal directions, the series resistance in the heterojunctions under study is significant and should be accounted for in the analysis of the *C–U* and other characteristics. The cutoff voltage determined by extrapolating the linear *C–U* plots to the horizontal axis varies considerably for the measurements performed at different frequencies. This is related to the fact that the magnitudes of the real and imaginary parts of the heterojunction impedance are comparable, and the test voltage is redistributed in favor of the imaginary component at low measurement frequencies. The lower the frequency, the better the contact voltage U_0 is determined. The actual value of $U_0 = 0.4$ V was determined by extrapolating the $U_0(\omega)$ dependence to zero frequency [3] (see the inset to Fig. 1).

The heterojunction energy band diagram under equilibrium conditions is shown in the inset to Fig. 2. Due to a difference in the majority carrier concentrations in InSe and SnSSe, the band bending occurs entirely on the InSe side of the junction. It follows from the diagram obtained that the conduction and valence band offsets amount to $\Delta E_c = 0.32$ and $\Delta E_v = 0.72$ eV, respectively. Therefore, the electrons are in more favorable conditions than the holes to surmount the total heterojunction energy barrier ($\Delta E_{c(v)} + U_0$).

A mechanism of the current flow through the heterojunction was determined by studying the temperature dependence of the forward branch of the current–voltage (*I–U*) characteristics (see Fig. 3). Instead of recording the forward-bias *I–U* curves in the dark, we measured their photoelectric analog—the relation between

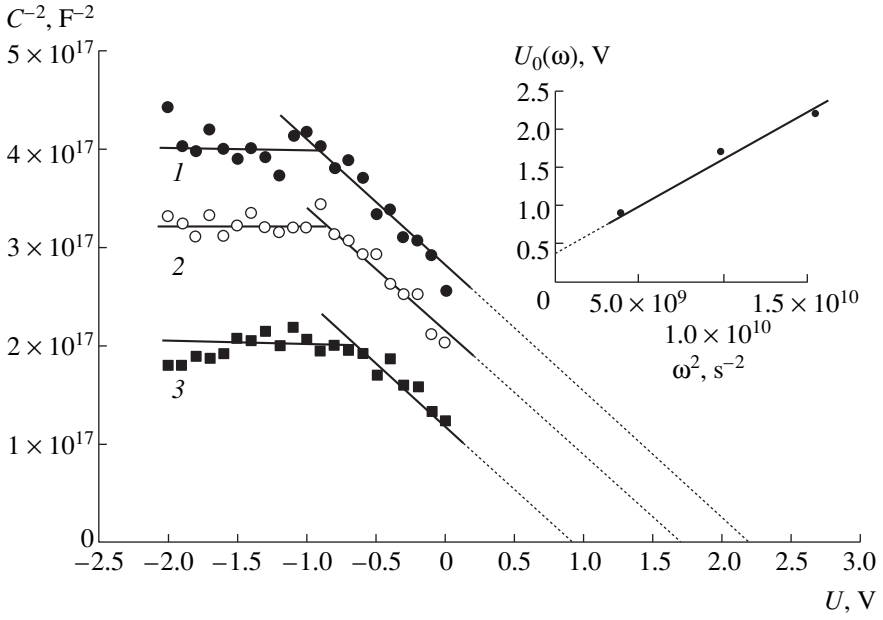

Fig. 1. Capacitance–voltage characteristics of a SnSSe–InSe heterojunction recorded at a frequency of (*1*) 19.8, (*2*) 15.8, and (*3*) 9.95 kHz. Inset: frequency dependence of the capacitance cutoff voltage. T = 295 K.

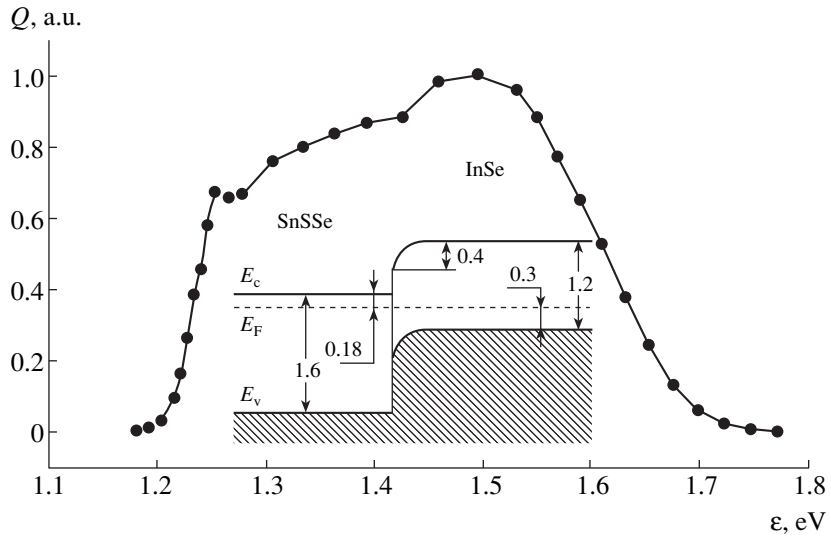

Fig. 2. Photosensitivity spectrum of a SnSSe–InSe heterojunction at room temperature (Q is the quantum yield). The inset shows a heterojunction energy band diagram under equilibrium conditions (all values are given in electronvolts).

the photocurrent and photo emf under variable illumination conditions [4]. This allowed us to obviate the difficulties in interpretation of the heterojunction current–voltage characteristics, which are especially substantial at low temperatures, where the effect of the series resistance on the *I–U* curves is more significant. On the other hand, with this photoelectric technique of the forward-bias current–voltage measurement, the region of higher voltages exceeding the open-circuit voltage cannot be accessed. It can be seen from Fig. 3 that two linear segments exist in the $I(U)$ dependences plotted in the semilogarithmic scale. The first, longer segment is characterized by the diode coefficient n substantially greater than 1. It is common to relate this region of the heterojunction *I–U* characteristics to the leakage currents [5]: the current values are low and the characteristic slope depends on the sample preparation. Experimental points in the second, shorter segment of the *I–U* curve are compared in Fig. 3 to the calculated ideal-diode characteristics, for which n = 1. A qualitative agreement between the two curves suggests that, starting from a certain voltage, the forward diffusion

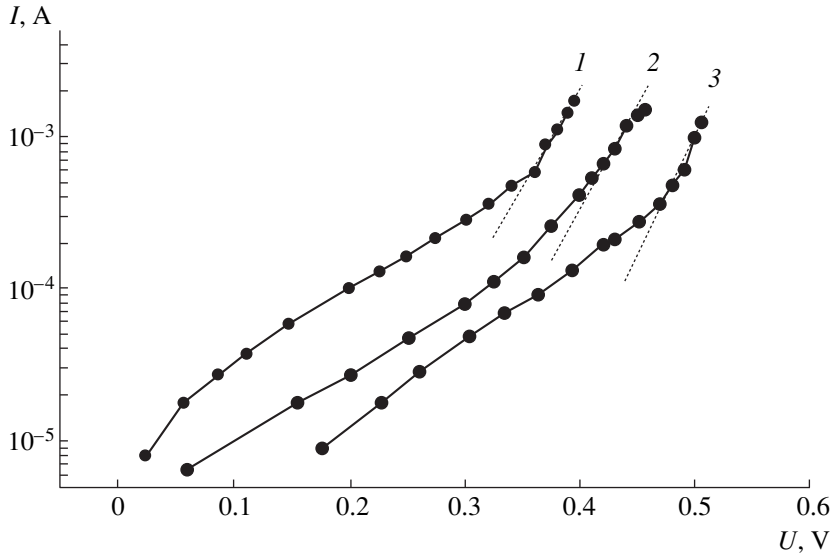

Fig. 3. The current–voltage characteristics of a SnSSe–InSe heterojunction at (*1*) 300, (*2*) 270, and (*3*) 240 K. Dotted lines represent the curves calculated for an ideal diode.

current through the heterojunction exceeds the leakage current, since they follow different exponential laws. Therefore, the diffusion mechanism should be regarded as the main one that determines the current flow through SnSSe–InSe heterojunctions.

Figure 2 shows a spectral characteristic of the heterojunction photosensitivity having the shape of a band with the edges determined by the fundamental light absorption in InSe (E_g = 1.2 eV) and SnSSe (E_g = 1.6 eV) [6]. Since an $SnS_{2-x}Se_x$ alloy of any other composition x can be used, it is possible to obtain different photosensitivity spectral bands using heterojunctions formed by layered semiconductors, whose high quality is corroborated by the study of the SnSSe–InSe heterojunctions.

REFERENCES

1. V. L. Bakumenko and V. F. Chishko, Fiz. Tekh. Poluprovodn. (Leningrad) **11**, 2000 (1977) [Sov. Phys. Semicond. **11**, 1171 (1977)].
2. A. M. Goodman, J. Appl. Phys. **34**, 329 (1963).
3. Yu. A. Gol'dberg, O. V. Ivanova, T. V. L'vova, and B. V. Tsarenkov, Fiz. Tekh. Poluprovodn. (Leningrad) **18**, 1472 (1984) [Sov. Phys. Semicond. **18**, 919 (1984)].
4. V. A. Manasson and A. I. Malik, Prib. Tekh. Éksp., No. 5, 190 (1981).
5. V. N. Katerinchuk and M. Z. Kovalyuk, Fiz. Tekh. Poluprovodn. (Leningrad) **25**, 954 (1991) [Sov. Phys. Semicond. **25**, 577 (1991)].
6. G. Perluzzo, S. Jandl, M. Aubin, and P. E. Girard, Solid State Commun. **27**, 1437 (1978).

Translated by M. Skorikov

Technical Physics Letters, Vol. 26, No. 9, 2000, pp. 757–759. Translated from Pis'ma v Zhurnal Tekhnicheskoĭ Fiziki, Vol. 26, No. 17, 2000, pp. 11–16.
Original Russian Text Copyright © 2000 by Matveeva, Vasin, Kozeratskaya, Totskiĭ.

Radiation-Resistant Free Germanium and Silicon Films for Nuclear Physics Experiments

L. A. Matveeva, A. V. Vasin, G. N. Kozeratskaya, and Yu. I. Totskiĭ

Institute of Semiconductor Physics, National Academy of Sciences of Ukraine, Kiev, Ukraine

Received December 23, 1999

Abstract—The structure, composition, and radiation resistance of free target films of germanium and silicon prepared under various conditions were studied. Under the experimental conditions encountered in nuclear physics, the targets prepared by pulsed thermal deposition in vacuum are stable for a longer period of time as compared to the samples prepared in a continuous deposition regime. © *2000 MAIK "Nauka/Interperiodica".*

As is known [1], the experimental investigations of nuclear reactions involving accelerated particles and ions require the preparation of thin free (unsupported) targets. For nuclear research centers, the preparation of sufficiently strong free film targets of large area and uniform thickness is still a difficult task. High-precision measurements of the differential cross sections for a reaction involving the transfer of a few nucleons to a low-Z target at low and medium particle energies require using the target films with a minimum possible content of foreign impurities [2]. The purpose of this work was to develop a method for the preparation of thin free films of germanium and silicon with large area and high purity, strength, and radiation resistance for experiments in nuclear physics.

The samples were prepared on a VUP-2M system by thermal evaporation of Ge and Si in vacuum from ohmically heated tantalum and tungsten boats, respectively. The films were deposited onto glass substrates (uviol cover glass plates) with preliminarily deposited sodium chloride underlayers. The Ge and Si films were separated from substrates, so as to retain continuity of the deposit, by immersion (similar to that used to separate the carbon recharge foils [3]) into distilled water. The films separated from substrates were mounted in a copper holder with a diameter of 25–30 mm. The layer thickness in the course of deposition was monitored by a quartz crystal thickness meter of the KIT-1 type. After termination of the deposition cycle, the film thickness was also determined gravimetrically. Finally, the thickness and its uniformity over the film area were checked by measuring the energy losses of α-particles emitted from a standard ^{226}Ra source and passing through the target [4]. Perfectness of the crystalline structure of the samples was assessed by the electron diffraction patterns obtained with an EMR-100 electronograph. The sample surface morphology was studied on a JSM-100CX (JEOL, Japan) electron microscope operating in the scanning and transmission modes. Elemental composition of the film targets was determined by the Rutherford backscattering (RBS) of protons and α-particles with an energy of E = 1.5–1.85 MeV at an angle of $\Theta = 160°$ [5]. The films of NaCl, Ge, and Si were prepared by heating evaporators in different regimes: continuous (first series) and pulsed (second series). The vapors were deposited onto unheated substrates in order to provide for an amorphous structure of the deposit that was expected to increase the radiation resistance of the target films [3, 6, 7].

An analysis of the proton RBS spectra showed that the main impurities in targets of the first series were oxygen and carbon. A combination of data for the scattering of protons and heavier projectiles (α-particles) provided increased resolution with respect to the analyzed element mass. Some impurities not revealed by the proton scattering were observed in the RBS spectra of α-particles. Targets of the first series were found to contain additional impurities of the evaporator material, as well as Na and Cl atoms resulting from diffusion at the film–substrate interface.

Films obtained in a continuous evaporation regime possessed a polycrystalline structure that reduced radiation resistance of the targets as a result of the radiation-induced swelling [7]. These films could withstand a single exposure to charged particle beam because of rapid mechanical damage (cracks, discontinuities).

The free films prepared using a continuous evaporation regime exhibited twisting caused by residual mechanical stresses arising in the course of continuous heating of the substrate by radiation from the evaporation source. This circumstance complicated mounting of the free films in the copper holder.

Films of the second series, prepared by pulsed thermal evaporation with deposition onto unheated substrates, possessed an amorphous structure homogeneous both in depth and over the entire film area. The structure remained unchanged upon interaction with charged particles. These films exhibited a higher strength (as compared to samples of the first series), did not twist upon separation from substrates, and could be

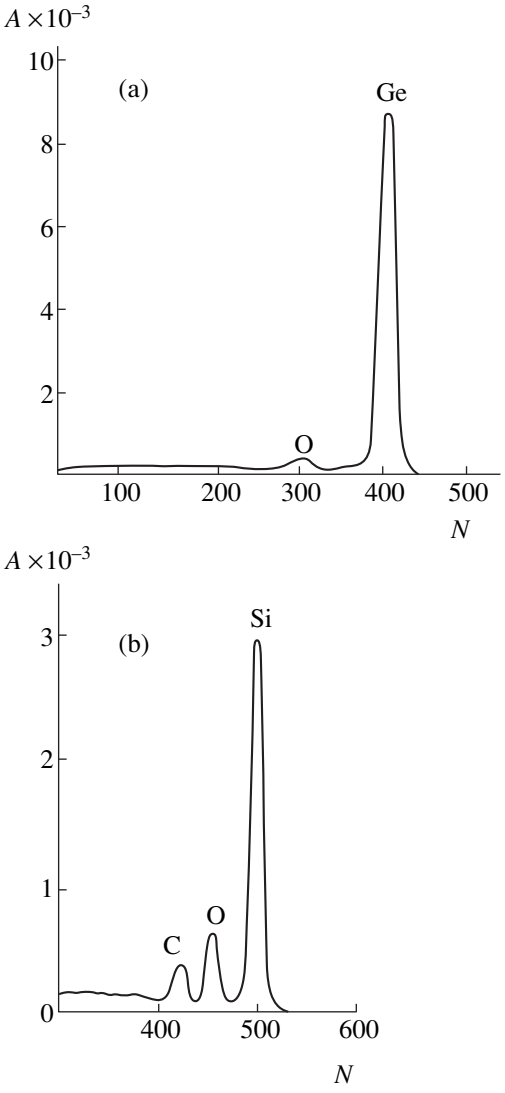

Fig. 1. Rutherford backscattering spectra of protons in (a) germanium and (b) silicon target films prepared by pulsed thermal deposition in vacuum (*A* is the number of counts, *N* is the energy channel number).

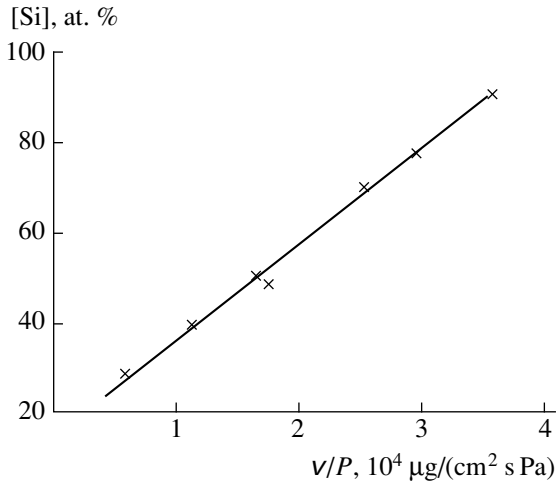

Fig. 2. The plot of silicon content versus v/P ratio.

repeatedly employed in the nuclear physics experiments. In order to obtain the films with uniform thickness, the substrates were excentrically rotated at a rate of 20 rpm under the three evaporators in the course of film deposition. Parameters of the pulsed deposition regimes used to obtain samples of the second series are listed in Table 1. Targets of the second series exhibited a homogeneous surface morphology both before and after irradiation and contained a lower amount of impurities. Figures 1a and 1b show the proton RBS spectra of germanium and silicon targets from the second series. These films, in contrast to samples of the first series, contained no heavy metal impurities from the evaporator boats. Oxygen and carbon impurities were uniformly distributed over the film volume, as evidenced by the symmetry of bands in the proton RBS spectra (Fig. 1).

Samples of the second series were used to study a relationship between the deposition rate v, residual pressure P (vacuum level), and elemental composition of the targets. Figure 2 shows a plot of the main element concentration versus the v/P ratio for a silicon target. As seen, an increase in the deposition rate v (at a constant pressure P) or in the vacuum level (at a constant deposition rate) leads to better purity of the film target. Data on the composition of film targets of the second series are summarized in Table 2.

The target films from both the first and second series were used in the nuclear physics experiments. Targets of the second series, studied by the Coulomb backscattering technique and analyzed for the elemental composition and homogeneity by the RBS method using hydrogen and helium ions with energies in the 1.5–1.85 MeV range, could be repeatedly used in subsequent experiments. These samples remained intact upon multiply repeated cycles of evacuation and transfer, whereas targets of the first series could be used in a single experiment.

In experiments devoted to the study of displacement reactions, performed using an MSP-144 magnetic spectrometer, no radiation damage was observed in the ^{72}Ge targets with an effective thickness of 250 μg/cm^2 continuously irradiated with 60-MeV $^{12}C^{2+}$ ions for 27 h to accumulate a total fluence of 10^{14} cm^{-2} at a current of 700 nA. These targets were also employed in several multihour cycles of measurements using 60-MeV beams of $^{14}N^{3+}$ ions with a current of 300–400 mA (dose rate, 4×10^{15} cm^{-2} s^{-1}) and $^{12}C^{2+}$ ions with a current of 150–500 mA, in which a total fluence reached up to 10^{19} cm^{-2}. No signs of the sample degradation or fracture were observed upon the exposure.

Thus, the method of pulsed thermal deposition in vacuum was successfully used to obtain free (unsupported) silicon and germanium films for 30-mm-diam targets. The samples contained a minimum amount of impurities and exhibited uniform thickness and homogeneous composition both in depth and over the film area. Possessing an amorphous structure and high

Table 1. Parameters of the pulsed regime of film deposition (the second series of samples)

Element	v, μg/(cm^2 s)	τ, s	T, s	δ, μg/cm^2
Ge	14–30	8–10	2–5	150–1000
Si	2–4	5–6	20–25	70–550

Note: τ is the pulse duration, T is the interval between pulses, δ is the film thickness.

Table 2. Compositions of the films deposited under various conditions (the second series of samples)

v, μg/(cm^2 s)	P, 10^{-4} Pa	Element	[Si, Ge], at. %	Impurities (content, at. %)
20	2.7	Ge	73	^{16}O (27)
2		Si	70	^{16}O (13.6); ^{12}C (16.4)
30	1.1	Ge	98–99	^{16}O (1–2)
4		Si	95–96	^{16}O (1–2); ^{12}C (2–3)

purity and homogeneity, these targets exhibited excellent radiation resistance to provide for a markedly increased efficacy of the nuclear physics experiments.

REFERENCES

1. R. Rengo, Nucl. Instrum. Methods Phys. Res. B **56**/**57**, 933 (1991).
2. A. P. Klyucharev, L. I. Kovalenko, L. G. Lishenko, *et al*., *Thin Foils of Metal Isotopes* (Énergoizdat, Moscow, 1981).
3. A. V. Vasin, V. G. Vysotskiĭ, and L. A. Matveeva, Pis'ma Zh. Tekh. Fiz. **24** (15), 79 (1998) [Tech. Phys. Lett. **24**, 616 (1998)].
4. F. F. Komarov, M. A. Kumakhov, and I. S. Tashlykov, *Nondestructive Analysis of Solid Surfaces by Ion Beams* (Minsk. Gos. Univ., Minsk, 1987).
5. Yu. G. Mashkarov, V. N. Sarana, and G. N. Kozeratskaya, in *Proceedings of the 3rd All-Union Conference on Microanalysis Using Accelerated Particle Beams, Kharkov, 1992*, p. 275.
6. N. G. Kozeratskaya, N. F. Onoshko, and V. A. Stepanenko, Preprint No. KIYaI-87-50 (Institute for Nuclear Research, Kiev, 1987).
7. G. V. Kiselev, É. V. Strakhov, and V. K. Sharov, Preprint No.168, ITÉF (Institute of Theoretical and Experimental Physics, Moscow, 1988).

Translated by P. Pozdeev

Technical Physics Letters, Vol. 26, No. 9, 2000, pp. 760–763. Translated from Pis'ma v Zhurnal Tekhnicheskoĭ Fiziki, Vol. 26, No. 17, 2000, pp. 17–24.
Original Russian Text Copyright © 2000 by Krutikov, Lopatnev.

A Possible Method for Finding the Value of Indeterminate Near Wave Field of an Expanding Cylinder

V. S. Krutikov* and A. G. Lopatnev**

** Institute of Pulsed Processes and Technologies, National Academy of Sciences of Ukraine, Kiev, Ukraine*

*** State Marine Technical University, Nikolaev, Ukraine*

Received April 3, 2000

Abstract—A strict analytical solution of the wave equation with cylindrical symmetry in a region with mobile boundaries was obtained by the method of inverse problems with an allowance for the interaction of nonlinear arguments. The method is universal and applicable to solving both inverse and direct problems for arbitrary values of the initial radius and displacements. The solution describes a near wave field of an expanding plasma piston, including that formed in the initial moments of a pulsed process. *© 2000 MAIK "Nauka/Interperiodica".*

A characteristic feature of the pulsed processes (electric discharge, laser pulses, explosions in solid and gaseous explosive mixtures, etc.) developing in a compressible medium is the presence of a mobile interphase (plasma–liquid, gas–liquid) boundary. Taking into account the influence of this boundary and the initial radius r_0 is necessary, for example, in describing plasmas (generated by an electric discharge column, laser pulse, etc.) in liquids, studying wave processes (including a near region of the expanding plasma cavity), solving problems of controlled pulsed processes, and modeling the breakdown in an interelectrode gap (which is a very special separate problem).

As a rule, the modeling and numerical realization of an expanding plasma piston are performed assuming that the plasma channel with a radius r_0 and a temperature T_0 already exists at the initial time instant. The initial r_0 and T_0 values are selected within certain intervals, based on the experimental data available for the processes in air [1–3] and in water [4, 5]. Variation of the initial conditions within the range of their values determined in experiment produces no significant effect on the results of calculations. The corresponding solutions rapidly attain close regimes.

It should be noted that this approach rules out the possibility of considering changes in the functions of pressure, particle velocity, etc., within the very first moments of the process. However, with this stage missing, it is hardly possible to understand and model the breakdown development in an interelectrode gap, as well as many other physical processes involved in the pre- and postbreakdown stages.

In this work, we have attempted at quantitatively estimating the kinematic and dynamic parameters of an expanding cylindrical plasma piston development in a compressible medium, including the very first moments of the pulsed process.

Assuming small density perturbations, the motion of a plasma piston expanding in an infinite compressible liquid medium can be described by the wave equation. Solving this problem in the case of cylindrical symmetry encounters extremely large difficulties. To the present, no one strict analytical solution of the wave equation in the regions with cylindrical boundaries was reported; this class of the mathematical physics problems remains virtually unstudied.

Let the law of the pressure variation $P = f(r_1, t)$ at a definite point r_1 of the wave field be known (i.e., the inverse problem is solved). It is necessary to determine the functions of interest at the other points, including those on the mobile boundaries; the law of the boundary motion is unknown and also has to be determined. A solution to the wave equation (with zero initial conditions) obtained by the method of inverse problems with an allowance for the interaction of nonlinear arguments [6–9] has the following form:

$$\bar{\varphi} = -\frac{\bar{f}(r_1, s)K_0(\mu r)}{s\rho K_0(\mu r_1)}, \qquad (1)$$

where $\mu = s/a$, s is the Laplace transformation parameter, a is the velocity of the perturbation propagation in the resting medium, ρ is the density of the medium, K_0 and K_1 are the modified Bessel's (MacDonald's) functions, and φ is the velocity potential.

The inverse transform in Eq. (1) for each particular case can be performed in a rational way, depending on the shape of the function f. For $P(r_1, t)$ represented in the class of Bessel's functions, the corresponding solutions are as follows:

$$P(r_1, t) = A\left[t^2 - \frac{(r_1 - r_0)^2}{a^2}\right]^{-1/2},$$

1063-7850/00/2609-0760$20.00 © 2000 MAIK "Nauka/Interperiodica"

$$t > (r - r_0)/a,$$

$$v(r, t) = \frac{At}{(r - r_0)\rho}\left[t^2 - \frac{(r - r_0)^2}{a^2}\right]^{-1/2}, \quad (2)$$

$$P(R(t), t) = A\left[t^2 - \frac{(R(t) - r_0)^2}{a^2}\right]^{-1/2},$$

$$v(R(t), t) =$$

$$= \frac{At}{(R(t) - r_0)\rho}\left[t^2 - \frac{(R(t) - r_0)^2}{a^2}\right]^{-1/2} = \frac{dR(t)}{dt}, \quad (3)$$

$$(R(t) - r_0)^2 = \frac{2A}{\rho}\sqrt{t^2 - \frac{(R(t) - r_0)^2}{a^2}} + \frac{2A^2}{\rho^2 a^2}\ln\left|\sqrt{t^2 - \frac{(R(t) - r_0)^2}{a^2}} - \frac{A}{\rho a^2}\right|. \quad (4)$$

For $a \longrightarrow \infty$,

$$R(t) - r_0 = \left[\frac{2At}{\rho}\right]^{1/2}$$

and for $r_0 = 0$, formula (4) transforms into an expression obtained previously [6, 9].

Equation (4) clearly demonstrates an essentially nonlinear character of the relationship between the law of variation of the mobile boundary radius and the functions of interest. For an arbitrary form of the function $P = f(r_1, t)$, the solutions were presented in [6, 9]. Note that the obtained relationships represent strict solutions: substituted into the left-hand part of the wave equation, these functions make it identical zero. We have compared these functions with the results of numerical solution obtained by the method of characteristics of a complete system of equations [11, Eqs. (1)] and determined for the first time the domain of applicability of the wave equation and its strict solutions to the problems of pulsed hydrodynamics and acoustics. This domain is limited by the condition $M = v/a \le 0.2$ [11], where v is the piston expansion velocity. The shock wave instantaneously goes out of the expanding cavity at a velocity of $a_0 = \text{const}$. In some cases, an energy supplied to the channel may give rise to intensive "evaporation" of the medium, which converts into a vapor or plasma at the inner mobile boundary of the plasma cavity. This phenomenon markedly changes a hydrodynamic pattern of the plasma channel expansion both at the initial instant and in the following stage. These phenomena can be described using a mathematical model with mobile permeable boundary [8].

As is seen from Eq. (4) with $t \longrightarrow 0$ and $R(t) = r_0$, the functions $P(R(t), t)$ and $v(R(t), t)$ tend to infinity. In order to find the values of these indeterminate functions, we will use MacDonald's function in the following representation:

$$K_0(x) \approx \sqrt{\frac{\pi}{2x}}e^{-x}\left(1 - \frac{1}{8x} + \ldots\right),$$

$$K_1(x) \approx \sqrt{\frac{\pi}{2x}}e^{-x}\left(1 + \frac{1}{8x} + \ldots\right), \quad x \longrightarrow \infty.$$

Using Eq. (1) with $f(r_1, t) = \sum_{m=0}^{\infty} A_m\left(t - \frac{r_1 - r_0}{a}\right)^m$, we readily obtain

$$\varphi(r, t) = -\frac{1}{\rho}\sqrt{\frac{r_1}{r}}\int_0^t f(t - \tau)\sigma_0\left(\tau - \frac{r - r_0}{a}\right)d\tau,$$

$$P(r, t) = \sqrt{\frac{r_1}{r}}\sum_{m=0}^{\infty} A_m\xi^m = F_1, \quad \xi = t - \frac{r - r_0}{a}, \quad (5)$$

$$v(r, t) = \frac{1}{\rho}\sqrt{\frac{r_1}{r}} \times \left[\frac{1}{2r}\sum_{m=0}^{\infty}\frac{A_m}{m+1}\xi^{m+1} + \frac{1}{a}\sum_{m=0}^{\infty}A_m\xi^m\right] = F_2,$$

where A_m are the coefficients of the Lagrange polynomial of the mth power and σ_0 is the zero-order unit discontinuous function. For a mobile boundary $r = R(t)$, we obtain

$$P(R(t), t) = F_1(R(t), t),$$

$$v(R(t), t) = F_2(R(t), t),$$

$$\frac{2}{5}\frac{[R^{5/2}(t) - r_0^{5/2}]\rho}{\sqrt{r_1}} \quad (6)$$

$$= \frac{1}{2}\sum_{m=0}^{\infty}\frac{A_m}{(m+1)(m+2)}\xi^{m+2} + \frac{R(t)}{a}\sum_{m=0}^{\infty}\frac{A_m}{m+1}\xi^{m+1}.$$

For $r = R(t)$ and $t \longrightarrow 0$, Eq. (5) yields $R(t) = r_0$ and

$$P(R(t), t) = \sqrt{\frac{r_1}{r_0}}A_0, \quad v(R(t), t) = \frac{1}{\rho a}\sqrt{\frac{r_1}{r_0}}A_0. \quad (7)$$

An analysis of Eqs. (5) and (7) in comparison with the exact numerical solution obtained by the method of characteristics of a complete system [11, Eqs. (1)] for

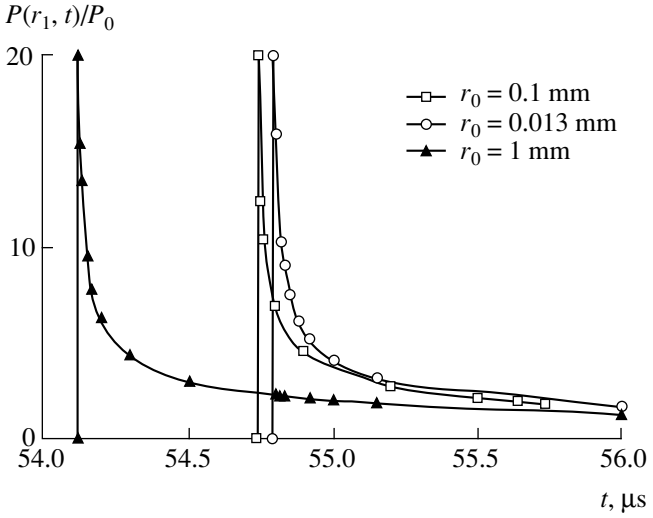

Fig. 1. Initial data used for restoring the pressure kinetics at a given point in the wave zone for three values of the initial radius.

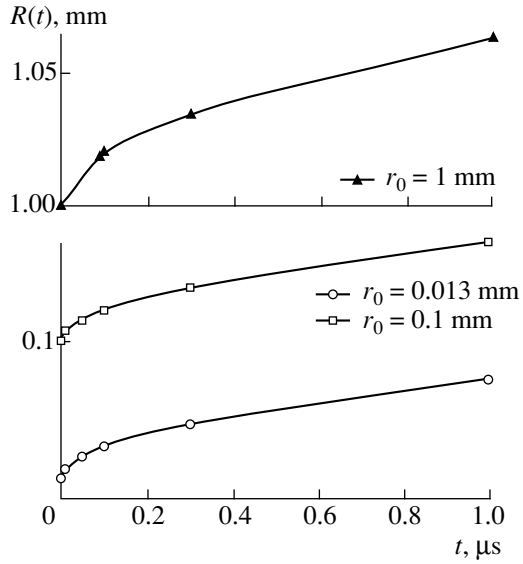

Fig. 2. Time variation of the radius of the expanding plasma piston boundary for various values of the initial radius.

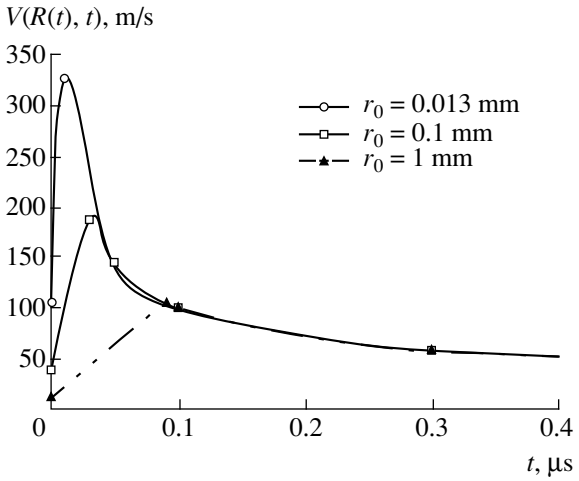

Fig. 3. Time variation of the velocity of the expanding plasma piston boundary for various values of the initial radius.

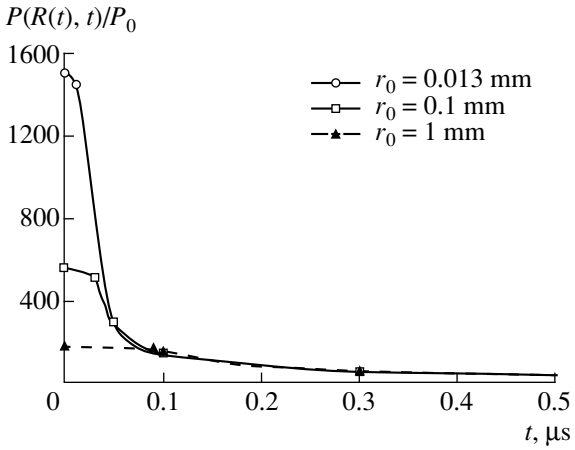

Fig. 4. Kinetics of the pressure variation on the expanding plasma piston boundary calculated taking into account a nonlinear term in the Cauchy–Lagrange integral [12] for a preset pressure at a point of the wave zone (Fig. 1) and various values of the initial radius.

the equations of motion, continuity, and state in the Tate form showed that acceptable solutions can be obtained by solving the inverse problem for pressures at an arbitrary point in the wave zone (at a mobile piston boundary, only at the initial time instant). As for the direct problem (with the known piston expansion velocity), neither pressures nor particle velocities in the wave zone can be determined by formulas (5) and (6) [10].

Figures 1–4 show the results of calculations performed by Eq. (4) for $A = 20 \times 10^{-6}$ kgf s/cm^2; ρ = 102 (kgf s)/m^4; a = 1460 m/s; three values of the initial radius: r_0 = 0.013, 0.1, and 1 mm; r_1 = 0.08 m; and A_0 = 20 kgf/cm^2; the values of pressures and velocities on the mobile plasma cavity boundary at $t \longrightarrow 0$ were determined by formula (7).

As seen in Figs. 3 and 4, the pressures and velocities on the mobile plasma piston boundary in the initial stage (t = 0–0.1 μs) differ significantly (sometimes, by one order of magnitude) from the values for $t > 0.1$ μs. In addition, the functions $P(R(t), t)$ and $V(R(t), t)$ markedly depend on the initial radius r_0: the pressures and velocities reached in the initial stage may differ several times for various r_0 values indicated above.

For $t > 0.1$ μs, the pressures and velocities at the mobile boundary are virtually independent of the initial radius r_0 for the problem parameters selected: all three curves in Figs. 3 and 4 coincide. These results can be

used for investigating the near wave field in the expanding plasma cavity, solving the problems of controlled pulsed processes, modeling the breakdown in an electrode gap, and studying plasma channels.

REFERENCES

1. N. G. Basov, B. P. Borovich, V. S. Stoĭlov, *et al.*, Zh. Tekh. Fiz. **40** (3), 516 (1970) [Sov. Phys. Tech. Phys. **15**, 399 (1970)].
2. A. F. Aleksandrov, V. V. Zosimov, S. P. Kurdyumov, *et al.*, Zh. Éksp. Teor. Fiz. **61** (5), 1841 (1971) [Sov. Phys. JETP **34**, 979 (1971)].
3. V. K. Dubovenko, Élektron. Obrab. Mater., No. 2, 62 (1990).
4. K. A. Naugol'nykh and N. A. Roĭ, *Electric Discharges in Water* (Nauka, Moscow, 1971).
5. L. M. Lyamshev, Usp. Fiz. Nauk **151** (3), 479 (1987) [Sov. Phys. Usp. **30**, 252 (1987)].
6. V. S. Krutikov, Pis'ma Zh. Tekh. Fiz. **14** (6), 510 (1988) [Sov. Tech. Phys. Lett. **14**, 226 (1988)].
7. V. S. Krutikov, Prikl. Mat. Mekh. **55** (6), 1058 (1991).
8. V. S. Krutikov, Dokl. Akad. Nauk **333** (4), 512 (1993).
9. V. S. Krutikov, Dokl. Akad. Nauk **364** (1), 17 (1999) [Dokl. Phys. **44**, 674 (1999)].
10. V. S. Krutikov, *One-Dimensional Problems in the Mechanics of Continuous Media with Mobile Boundaries* (Naukova Dumka, Kiev, 1985).
11. V. S. Krutikov, Akust. Zh. **42** (4), 534 (1996) [Acoust. Phys. **42**, 471 (1996)].
12. L. I. Slepyan, Dokl. Akad. Nauk SSSR **282** (4), 809 (1985) [Sov. Phys. Dokl. **30**, 448 (1985)].

Translated by P. Pozdeev

Technical Physics Letters, Vol. 26, No. 9, 2000, pp. 764–766. Translated from Pis'ma v Zhurnal Tekhnicheskoĭ Fiziki, Vol. 26, No. 17, 2000, pp. 25–30.
Original Russian Text Copyright © 2000 by Klyuev, Toporov, Zagorskiĭ, Dem'yanets, Munchaev.

Effect of the Crystal Face Orientation on the Thermostimulated Exoelectron Emission from Leucosapphire and Zinc Oxide Crystals

V. A. Klyuev, Yu. P. Toporov, D. L. Zagorskiĭ, L. N. Dem'yanets, and A. I. Munchaev

Institute of Physical Chemistry, Russian Academy of Sciences, Moscow, 117071 Russia
Shubnikov Institute of Crystallography, Russian Academy of Sciences, Moscow, 117333 Russia

Received March 14, 2000

Abstract—It is established that the character of thermostimulated exoelectron emission from the surface of leucosapphire and zinc oxide single crystals depends on the crystal face orientation. The temperature of the electron emission peak increases with the surface energy and reticular density of the face studied. © *2000 MAIK "Nauka/Interperiodica".*

Introduction. The method of thermostimulated exoelectron emission (TSEE) is based on the measurement of the temperature variation of intensity of a nonstationary emission of low-energy (0.2–0.6 eV) electrons from the surface of a solid preliminarily excited into a nonequilibrium state. The excitation (activation) is achieved by exposure of the sample surface to a flux of γ-quanta or to a gas-discharge plasma. The subsequent measurements are performed in a vacuum, whereby the TSEE process is stimulated by the thermal energy supplied through heating the sample to a temperature below a threshold corresponding to the appearance of stationary thermionic emission phenomena. Useful information about the TSEE effect is carried by electrons emitted from an excited surface layer of the sample.

Recording of the TSEE response during a linear increase in the sample temperature (heating at a constant rate) yields a characteristic curve (glow curve) with peaks, the temperature positions of which depend on the types of structural defects formed in the near-surface layer of the sample, while the peak intensity is proportional to the concentration of emitting centers [1].

Being highly sensitive to features of the defect structure in the activated surface layer, the TSEE method can be used as a tool for studying solid surfaces. Application of the TSEE technique to investigations of the surface of crystalline materials requires taking into account possible effects of the crystal face orientation upon the exoelectron emission from a sample studied. Obviously, anisotropy—a fundamental property of the crystalline solids—must be manifested by features in the exoelectron emission characteristics of various faces. However, although the exoelectron emission from various crystal faces was studied, for example, in alkali halide crystals [2], the general problem concerning the influence of crystallographic orientation of the emitting surface on the TSEE spectrum has not yet been formulated.

The purpose of this work was to study the effect of the crystal face orientation on the TSEE parameters of leucosapphire and zinc oxide crystals.

Experimental. The experiments were performed with the crystals of leucosapphire (below, sapphire) α-Al_2O_3 and zinc oxide ZnO representing dielectric and semiconductor materials, respectively. The selection was based on the fact that both crystalline substances are oxides with a hexagonal lattice and the hcp package of oxygen atoms [3–7]. The metal atoms occupy either tetrahedral (Zn in ZnO) or octahedral voids (Al in Al_2O_3). The crystalline oxides were obtained by different methods: ZnO was grown from a high-temperature aqueous solution, while Al_2O_3, from a pure melt. This circumstance allowed us to exclude influence of the growth medium and the sample preparation on the phenomenon studied and to concentrate on the surface orientation effects in analysis of the TSEE spectra.

The sapphire single crystals were grown from melt by the method of directed (horizontal) crystallization [4] at a rate of 8 mm/h. Orientations of the upper ingot surface and the crystallization front were (0001) and $(11\bar{2}0)$, respectively. The as-grown ingots were annealed at 1600°C in a vacuum of 0.1 Pa to release the internal stresses. The synthesized crystals had the unit cell parameters $a = 4.748$ Å, $c = 12.965$ Å and belonged to the space group $R3c$. The measurements were performed on plane-parallel plates with an area of 15×15 mm and a thickness of 0.3–0.5 mm cut from the ingot parallel to the (0001) pinacoidal, $(10\bar{1}0)$ and $(11\bar{2}0)$ prismatic, and

1063-7850/00/2609-0764$20.00 © 2000 MAIK "Nauka/Interperiodica"

$(10\bar{1}1)$ rhombohedral faces with an accuracy of ~40′. The surface of the samples was prepared to the measurements by conventional methods.

The zinc oxide single crystals were obtained by the method of hydrothermal crystallization from alkaline solutions. A ZnO charge was dissolved in a 4–8 M KOH solution containing 0.2–1.5 M LiOH. The temperature regime was as follows: growth zone, 230–280°C; dissolution zone, 250–350°C; temperature difference, 5–25°C. The samples crystals were grown using ZnO seeding plates cut perpendicularly to the polar *c*-axis. The as-grown crystals had the unit cell parameters $a = 3.251$ Å, $c = 5.209$ Å and belonged to the space group $P6_3mc$. The measurements were performed on plane-parallel plates with an area of $10 \times 10 \times 1$ mm and a thickness of 1 mm cut parallel to the (0001) monohedral and $(10\bar{1}0)$ prismatic faces; in the former case, the plates were cut from a growth pyramid of the positive rhombohedron with an accuracy of ~10′. Preliminary investigations were performed on the ZnO samples without any special surface preparation.

Prior to the TSEE measurements, the samples were activated by exposure to a negative corona discharge plasma in air. The TSEE effect was studied using a standard instrumentation [8] in a vacuum of no worse that 10^{-3} Pa. The samples were heated according to a linear law at a constant rate of 10 K/min. The emitted electrons were detected using a KEU-6 secondary-electron multiplier of the open type. The TSEE intensity measurements were performed in the pulse count mode.

Results and discussion. Figure 1 shows typical TSEE spectra representing the plots of emission current versus temperature (glow curves) for all four sapphire crystal face orientations studied. Figure 2 shows the glow curves for two orientations of a zinc oxide crystal surface. As seen, the shape of the TSEE spectrum depends on the crystallographic orientation of the samples: both amplitude of the TSEE current and the number and positions of the peaks exhibit changes. As is known, the number and positions of the exoelectron emission peaks are the most informative characteristics of TSEE. The number of peaks corresponds to the number of types of the structural defects capable of trapping electrons during the sample activation. The peak position (temperature) corresponds to the energy necessary for exoelectrons to escape from a given trap level to the vacuum, thus characterizing the trapping energy level.

An analysis of the data presented in Fig. 1 suggests that the surfaces of samples with different crystallographic orientations contain traps (structural defects) with different energies. The temperature position of the main TSEE peak observed for the α-Al_2O_3 crystal increases upon going from $(11\bar{2}0)$- to (0001)-oriented samples: $T\{11\bar{2}0\} < T\{10\bar{1}1\} < \{10\bar{1}0\} < T\{0001\}$). The similar trend is observed for ZnO: $T\{10\bar{1}0\} <$

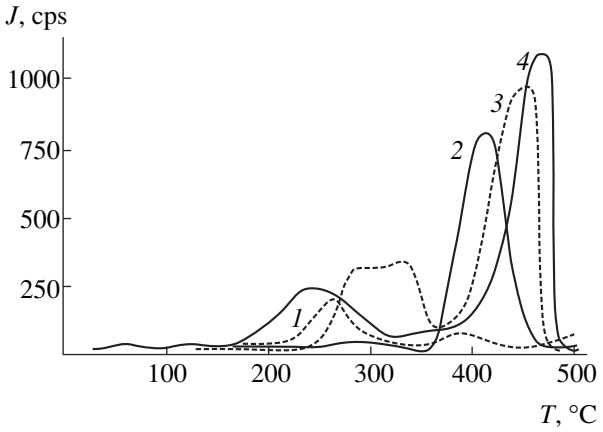

Fig. 1. TSEE glow curves for Al_2O_3 crystal surfaces with various orientations: (*1*) $(11\bar{2}0)$; (*2*) $(10\bar{1}1)$; (*3*) $(10\bar{1}0)$; (*4*) (0001).

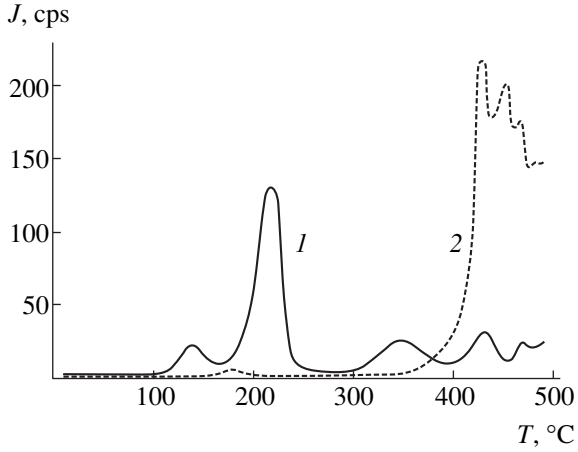

Fig. 2. TSEE glow curves for ZnO crystal surfaces with various orientations: (*1*) $(10\bar{1}0)$; (*2*) (0001).

$T\{0001\}$. As is known, Al atoms in the Al_2O_3 structure occupy two-thirds of the octahedral voids in the hcp package of oxygen atoms. Faces of the main simple forms $\{0001\}$, $\{10\bar{1}0\}$, and $\{11\bar{2}0\}$ differ by their reticular densities d_r. A still greater difference in d_r is observed for the ZnO crystal structure, where Zn atoms occupy tetrahedral voids in the hcp package of oxygen atoms. An analysis of the crystal structure of the samples studied showed that the reticular density in both cases increases in the order $d_r\{11\bar{2}0\} < d_r\{10\bar{1}0\} < d_r\{0001\}$ This series coincides with the above sequence of temperatures of the main TSEE peaks for the crystal samples with different orientations. Thus, our results demonstrate a relationship between the temperature position of the main peak on the TSEE glow curve and the reticular density of the emitting surface.

In this stage of investigations, we may conclude on the qualitative relationship between the temperature

position of the main TSEE glow curve peak and the reticular density: the greater the d_r value (and, hence, the surface energy) of a given face, the higher the temperature of the main peak in the TSEE spectrum of this surface.

Conclusion. The results of our work confirm that an anisotropy in the surface structure of crystals is manifested in their exoelectron emission properties. The general character and positions of the emission peaks are related to the reticular density and surface energy of the sample surface. As the surface energy increases, the exoelectron emission peaks shift toward higher temperatures.

We may suggest that the observed relationship between the TSEE character and the crystal face orientation must be also manifested in some other substances and may be used for determination of the crystal face orientation.

REFERENCES

1. V. S. Kortov, A. I. Slesarev, and V. V. Rogov, *Exoemission Control of the Surface of Articles after Cutting* (Naukova Dumka, Kiev, 1986).
2. A. V. Gerasimov, M. M. Merkin, and A. A. Tservadze, in *Proceedings of the 4th All-Union Symposium "Electron Emission and Its Application", Tbilisi, 1985*, p. 18.
3. *Ruby and Sapphire* (Nauka, Moscow, 1974).
4. Ch. S. Bagdasarov, E. R. Dubrovinskaya, and V. V. Pishchik, in *Modern Trends in Crystallography and Synthesis of Perfect Corundum Crystals*, Monokrist. Tekh. **6**, 3 (1972).
5. I. P. Kuz'mina, and V. A. Nikitenko, *Zinc Oxide. Preparation and Optical Properties* (Nauka, Moscow, 1984).
6. S. C. Abrahams and I. L. Bernstein, Acta Crystallogr. B **25**, 1233 (1969).
7. W. Hirschwald, P. Bonsewicz, L. Ernst, *et al.*, Curr. Top. Mater. Sci. **7**, 143 (1981).
8. *Techniques and Principles of the Measurement of Exoelectron and Acoustic Emission*, Tr. Ural. Politekh. Inst., No. 215 (1973).

Translated by P. Pozdeev

Technical Physics Letters, Vol. 26, No. 9, 2000, pp. 767–770. Translated from Pis'ma v Zhurnal Tekhnicheskoĭ Fiziki, Vol. 26, No. 17, 2000, pp. 31–36.
Original Russian Text Copyright © 2000 by Kuznetsova, Reznichenko, Razumovskaya, Shilkina, Klevtsov.

Shockwave Activation of High-Temperature Ferroelectric Powders

E. M. Kuznetsova, L. A. Reznichenko, O. N. Razumovskaya, L. A. Shilkina, and A. N. Klevtsov

Institute of Physics, Rostov State University, Rostov-on-Don, Russia

e-mail: esmit@krinc.ru

Received March 30, 2000

Abstract—Shockwave loading in various technological stages may significantly influence the defect state of synthesized $LiNbO_3$, $LiTaO_3$, $Sr_2Nb_2O_7$, and $Ca_2Nb_2O_7$ powders. This factor, in addition to comminution of the materials, leads to a sharp decrease in the temperature of synthesis and sintering, with a simultaneous increase in the relative density and degree of crystal structure perfection of the final ceramics. These effects can markedly simplify the technology of production of these ferroelectric materials. *© 2000 MAIK "Nauka/Interperiodica".*

Ferroelectric compounds with extremely high Curie temperatures (T_c) are of special interest for the high-temperature piezotechnology both as independent base materials and as components of more complicated mixtures. These compounds include lithium metaniobate $LiNbO_3$ (**1**) with $T_c \sim 1220$°C, strontium pyroniobate $Sr_2Nb_2O_7$ (**2**), and calcium pyroniobate $Ca_2Nb_2O_7$ (**3**). Compounds **2** and **3** possess the maximum Curie temperatures (T_c = 1340 and 1830°C, respectively) among the known readily available ferroelectrics.[1] However, the promising properties of these substances were mostly realized only in the compositions based on compound **1**. Compounds **2** and **3** are much less studied and, therefore, virtually not used in practice. The main reason for these compounds being unclaimed is the impossibility to provide for a sufficiently high density of the final materials under conditions of the conventional ceramic technologies. This is related to a low reactivity of mixtures and difficulties encountered in the process of press-powder compaction, which requires using extremely high temperatures in the stages of synthesis (T_1 > 1300°C) and sintering (T_2 > 1400°C).

We failed to facilitate the synthesis of compounds **2** and **3** using a number of technological methods, including dispersion of the main initial component Nb_2O_5. In this work, we attempted to exert a high-energy action upon substances by shockwave loading (SWL) of the powders in various technological stages in order to produce considerable activation of the reaction mixtures and the synthesized products, so as to obtain final ceramics of a higher density at markedly lower T_1 and T_2 values.

The shockwave (explosion) processing was applied either to the initial reaction mixture (R) or to the synthesized powder (S) or a product (P) upon the second intermediate firing stage. We have also tried the combined R–S and R–P regimes.[2] The synthesis of compound **1** and lithium metatantalate $LiTaO_3$ (**4**) was conducted for **4** h at 770°C, while compounds **2** and **3** were obtained by multiply repeated cycles of firing at increasing temperatures (800, 1000°C, …) with grinding of the intermediate products. The final sintering was effected at fixed temperatures in the intervals 1000–1180°C (for compound **1**), 1000–1400°C (**2**, **3**), and 1000–1300°C (**4**). The product quality was assessed based on the data of the X-ray diffraction analysis used to calculate the unit cell parameters and the characteristics of crystal structure perfection (defectness) including the total width of the diffraction lines (b_{hkl}); microdeformations ($\Delta d/d$); stacking fault probability (α); root-mean-square atomic displacements from regular positions ($\sqrt{\overline{U^2}}$); and the values of measured density (ρ_1), X-ray density (ρ_2), and relative density ($\rho_3(\rho_1/\rho_2)$) of the ceramics.

Figure 1a shows the values of T_1 (providing for the crystallization of impurity-free compounds **2** and **3**) and T_2 (ensuring sintering of these powders into ceramics with $\rho_3 = 0.95 \pm 0.02$) for various SWL regimes. A maximum decrease in T_1 (to 1000°C) was observed upon the SWL of intermediate powders (P regime). As for the sintering temperature, the maximum effect was observed upon the double shockwave processing of

[1] Comparable or somewhat higher T_c values were observed only for lanthanide-containing compounds $La_2Ti_2O_7$ (1530°C), $Pr_2Ti_2O_7$ (1755°C), and $Nd_2Ti_2O_7$ (1850°C).

[2] These experiments were performed by V.D. Rogozin (Volgograd) using a specially designed setup [1].

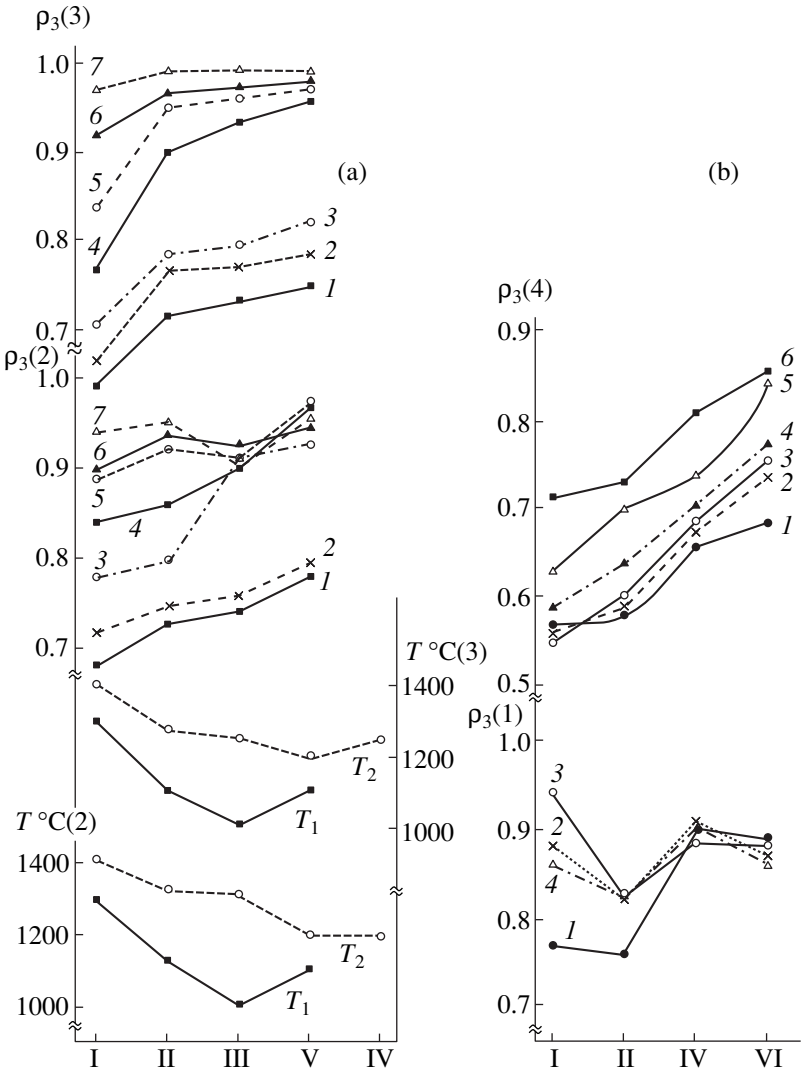

Fig. 1. Variation of the T_1, T_2 and ρ_3 values in various stages of SWL experiments: (I) no SWL; (II) explosion–shockwave treatment of the initial charge; (III) SWL upon intermediate firing; (IV) SWL of the as-synthesized powders; (V) combination of regimes II and III (R–P); (VI) combination of regimes II and IV (R–S). (a) Compounds $Sr_2Nb_2O_7$ (**2**) and $Ca_2Nb_2O_7$ (**3**): T_2 = 1000 (*1*); 1100 (*2*); 1150 (*3*); 1200 (*4*); 1250 (*5*); 1300 (*6*); 1400°C (*7*). (b) Compounds $LiNbO_3$ (**1**) and $LiTaO_3$ (**4**): T_2 = 1000 (*1*); 1050 (*2*); 1100 (*3*); 1180 and 1150 for **1** and **4**, respectively (*4*), 1200 (*5*); 1300°C (*6*).

powders (R–P regime). In both cases, the process temperature was decreased by 200°C. The maximum ρ_3 values were also reached in the samples treated in the combined regimes. Some decrease in ρ_3 at $T > 1150$°C observed for compound **2** processed in the P regime was explained by inhomogeneous composition of the mixture related to the coexistence of two orthorhombic phases with close values of the unit cell parameters.[3]

Compound **4** also exhibited a considerable decrease in T_1 and T_2 at a sufficiently high level of ρ_3 (Fig. 1b).[4] It was only in compound **1** that SWL did not lead to the expected decrease in T_1 and T_2 and an increase in ρ_3 (Fig. 1b).

The positive effect of SWL observed in compounds **2**–**4** was obviously related to the high level of local mechanical stresses and temperatures developed in the material particles which, despite short time of the activation process, sharply intensified interactions between the particles. These interactions led not only to comminution of the material (and, hence, to an increase

[3] The inhomogeneity was caused by violation of the stoichiometry with respect to Sr as a result of the partial sublimation of SrO from the reaction mixture at high temperatures ($T > 900$°C). SrO appears as a result of dissociation of the unreacted $SrCo_3$. This process was facilitated in mechanical mixtures and "undersynthesized" powders with unstable chemical bonds and was additionally stimulated by the external factors. This phenomenon was not observed in compound **3**, apparently, because of markedly lower volatility of CaO.

[4] We failed to obtain intact samples of compound **4** with $\rho_3 \geq 0.88$ because of strong cracking caused by a high rate of sample shrinkage in the course of sintering.

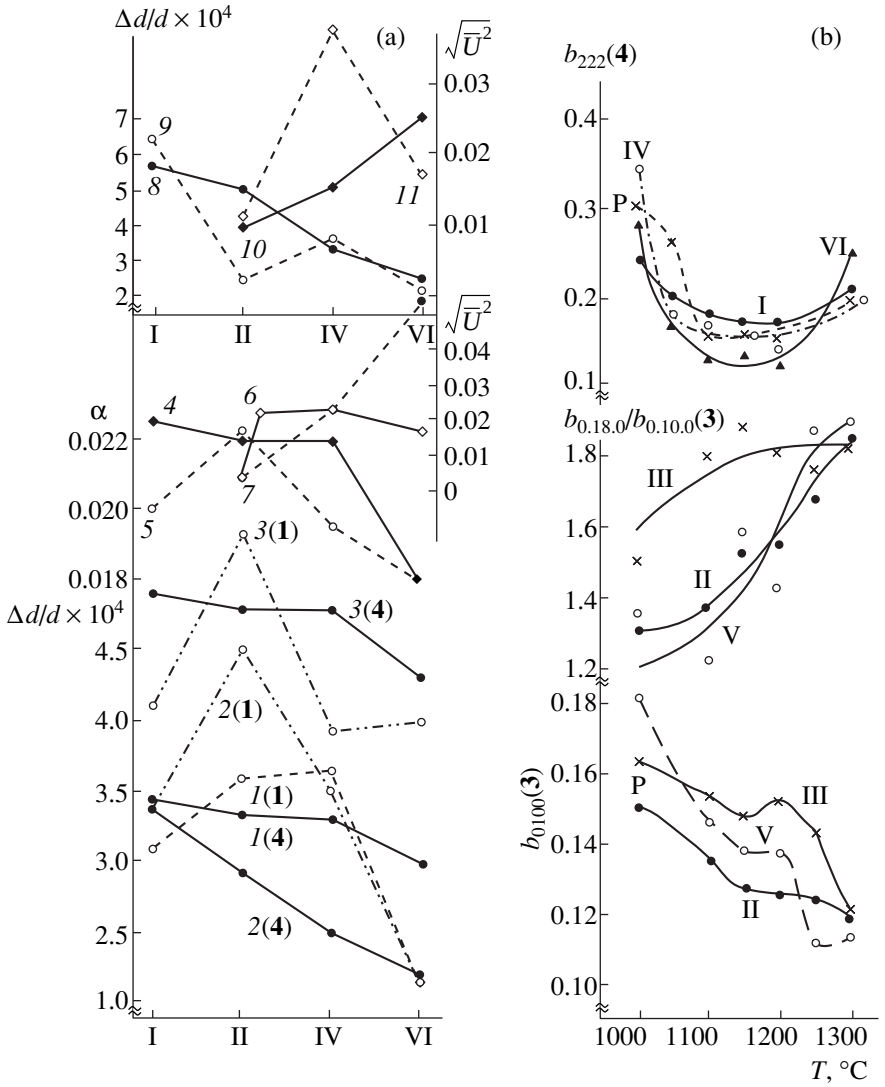

Fig. 2. (a) Variation of the $\Delta d/d$ values for compounds $LiNbO_3$ (**1**) and $LiTaO_3$ (**4**) [in the directions 104 (curve *1*), 110 (curve *2*), and 006 (curve *3*)] and for compounds $Ca_2Nb_2O_7$ (**3**) (curve *8*) and $Sr_2Nb_2O_7$ (**2**) (curve *9*, 041 direction). Variation of the α value for $LiTaO_3$ (curve *4*) and $LiNbO_3$ (curve *5*). Variation of $\sqrt{\overline{U}^2}$ for $LiTaO_3$ (curve *6*), $LiNbO_3$ (curve *7*), $Ca_2Nb_2O_7$ (curve *10*), and $Sr_2Nb_2O_7$ (curve *11*). (b) The plots of b_{hkl} (ang. deg) versus T_2 for $LiTaO_3$ (**4**) and $Ca_2Nb_2O_7$ (**3**) with and without SWL (see Fig. 1 for the explanation of regimes I–VI).

in the specific surface) but to the accumulation of various defects (as evidenced by the diffraction line broadening) increasing the free energy and the thermodynamic activity as well. The absence of the positive effect in compound **1** was related to the SWL-induced activation of the secondary stepwise recrystallization processes accompanied by rapid growth of ideomorphic grains (reaching very large size). This grain growth led to the development of microcracks and resulted in loosening and weakening of the ceramic samples

In all the ceramics studied, SWL favored the formation of more perfect structures upon sintering. This is illustrated in Fig. 2a showing variation of the parameters $\Delta d/d$, α, and $\sqrt{\overline{U}^2}$ in ceramics **1**–**4** processed in various SWL regimes and sintered at the optimum T_2 values. As seen, the SWL process always decreased these parameters, the minimum values being observed upon the treatment in combined regimes. Some increase in $\Delta d/d$ in sample **1** treated in the R–S regime was probably caused by the activation of recrystallization processes.

Figure 2b shows the plots of b_{hkl} versus T_2 for the samples of ceramics **3** and **4** obtained with and without SWL. As seen, a considerable defectness (large b_{220} values) in the samples of SWL-processed compound **4** (exceeding that in the untreated samples) was retained at $T_2 \le 1000$°C. In the 1000–1100°C interval, the struc-

ture became more perfect (b_{220} decreased). The effect was most pronounced for the R–S regime that provided for the formation of a most perfect structure (minimum b_{220}) at T_2 = 1100–1200°C (Fig. 2b). The same favorable effect was produced by the combined R–P regime in compound **3** (a sharp decrease in $b_{0.10.0}$) sintered at $T_2 > 1250$°C. Figure 2b also presents data on the effect of T_2 upon the ratio $b_{0.18.0}/b_{0.10.0}$ characterizing the dynamics of variation of the defect state in compound **3**. Upon SWL in the R and R–P regimes, this ratio increased from approximately unity to a value close to 2. This change is indicative of the transition from a state in which a maximum contribution to defectness is due to the block structure, to the state in which the role of residual elastic deformations increases with T_2. In the samples processed in the R regime, these residual deformations were dominating at all T_2.

Thus, we have demonstrated that the explosion–shockwave processing may in fact significantly change the defect state of ceramic powders which, along with comminution of the material, favored a decrease in T_1 and T_2 process temperatures, an increase in the ρ_3 value, and the formation of a more perfect ceramic structure. The decrease in T_1 and T_2 markedly reduces the energy consumption and increases reliability of the thermal equipment operation by admitting departure from the limiting technological conditions ($T \geq 1400$°C) toward "mild," more readily realizable regimes. This, in turn, allows using serial commercial equipment, rather than special refractory furnaces, thus markedly reducing the cost of production. The increase in ρ_3 facilitates the polarization of samples, thus ensuring fabrication of high-quality elements for piezotransducers. All these advantages allow us recommend implementing the shockwave activation into practical technology of high-temperature ferroelectric materials.

The work was supported by the Russian foundation for Basic Research, project no. 99-02-17575.

REFERENCES

1. L. A. Reznichenko, E. M. Kuznetsova, O. N. Razumovskaya, *et al.*, in *Proceedings of the International Conference "Piezotechnology-99," Rostov-on-Don, 1999*, Vol. 1, p. 262.
2. E. I. Bondarenko, V. D. Komarov, L. A. Reznichenko, and V. A. Chernyshkov, Zh. Tekh. Fiz. **58** (9), 1771 (1988) [Sov. Phys. Tech. Phys. **33**, 1071 (1988)].

Translated by P. Pozdeev

Technical Physics Letters, Vol. 26, No. 9, 2000, pp. 771–774. Translated from Pis'ma v Zhurnal Tekhnicheskoĭ Fiziki, Vol. 26, No. 17, 2000, pp. 37–45.
Original Russian Text Copyright © 2000 by Kamanina, Vasilenko.

Space-Time Light Modulators with Improved Dynamic Characteristics. Fullerenes Increase Sensitivity of the Light Modulators

N. V. Kamanina* and N. A. Vasilenko**

** Vavilov Optical Institute, State Scientific Center of the Russian Federation, St. Petersburg, 190164 Russia*

*** Karpov Institute of Physical Chemistry, State Scientific Center of the Russian Federation, Moscow, 103064 Russia*

Received October 21, 1999; in final form, March 23, 2000

Abstract—Ways to improve the dynamic characteristics of the space-time light modulators based on a polyimide–liquid crystal structure are considered. Application of a fullerene-containing polyimide increases sensitivity of the system. Characteristics of the polyimide-based light modulators with unmodified and dye-modified photosensitive layers are presented. © *2000 MAIK "Nauka/Interperiodica".*

Up to the present, a large number of various space-time light modulators (STLMs) have been developed [1]. Of special interest are the STLM structures with a liquid-crystalline (LC) mesophase used for the image readout. Important advantages of the LC structures are low control voltages, high sensitivity, large birefringence, and good technological properties. In addition, these devices possess good resolution and time characteristics. There is a large variety of the possible photosensitive media, including CdS, *a*-CdTe, ZnSe, ZnS, $As_{10}Se_{90}$, *a*-Si:H, *a*-SiC:H, polyimides, etc. [2–5], which provides for the obtaining of LC STLMs operating in a broad spectral range.

Among this variety, a special place with respect to the maximum possible resolution is occupied by the LC structures with a polyimide (PI) based photosensitive layer. These devices exhibit a maximum resolution of ~1500 mm^{-1} at an 0.1 level on the frequency–contrast characteristic (FCC) and provide for a maximum diffraction efficiency η approaching the theoretical limit (33.9%) in the case of thin phase holograms at sufficiently high spatial frequencies (100–150 mm^{-1}) [6]. These parameters are still unattainable for the photoconductor–liquid crystal structures with the photosensitive layers of other types. For example, high-speed LC STLMs with an *a*-Si:H layer exhibit a diffraction efficiency as small as 5% (at 25 mm^{-1}) and a resolution of 120 mm^{-1} (at 0.1η). Light modulators with a ZnSe layer have a still lower resolution of 35 mm^{-1} (at an 0.5 FCC level) [5].

Were have successfully used the PI–liquid crystal structures for correcting phase aberrations in systems using a single wavelength [7] and different wavelengths [8] for the data record and readout. The purpose of this work was to improve the dynamic characteristics of the PI–liquid crystal system without significant loss in resolution. The task was solved by optimizing the STLM operating conditions and using fullerenes to increase sensitivity of the photoconductor layer.

The STLM samples studied in this work represented structures of a sandwich type described previously [9], with the main functional role played by a photosensitive PI and a liquid crystal of the cyanobiphenyl group. Thin (0.7–1 μm thick) films of a water-soluble PI (6B grade) were obtained by the two-stage polycondensation of an aromatic heteroatomic diamine with dianhydrides of tetracarboxylic aromatic acids [10]. The synthesized PIs possessed intrinsic photosensitivity in the UV and blue visible range, with a maximum absorption at 350 nm and a longwave absorption edge at 600 nm. The sensitivity band was extended to 532 nm by doping the PI with synthetic organic dyes (representing compounds with intramolecular charge transfer possessing a maximum absorption at 530 nm) and fullerenes C_{60} and C_{70}, the absorption spectrum of which overlaps with the spectrum of PI in the region of 520–550 nm.

The electrooptical layers (5–10 μm thick) were made of the ZhK 1289 and E7 (BDH) LC compositions characterized by a positive optical and dielectric anisotropy. The light modulators operation is based on the *S*-effect in the transmission mode. A sinusoidal grating was recorded under the Raman–Nath diffraction conditions using a single-pulse second-harmonic radiation of a neodymium-doped YAG laser with a pulse duration of 20 ns and a beam spot diameter on the photosensitive layer of 3 mm. The conditions of convergence of the object-modulated and reference beams allowed the spatial frequency Λ of recording to be varied from 50 to 800 mm^{-1}. Readout of the recorded potential relief was performed with a continuous-wave He–Ne laser with a

1063-7850/00/2609-0771$20.00 © 2000 MAIK "Nauka/Interperiodica"

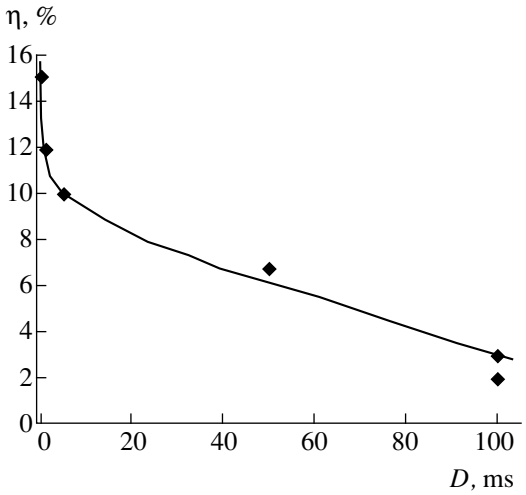

Fig. 1. The plot of diffraction efficiency η versus delay time D between a laser pulse and the modulator supply voltage pulse (Λ = 100 mm^{-1}; W_{wr} = 400 μJ/cm^2; A = 59.9 V; τ_{sup} = 50 ms; $1/T$ = 1 Hz).

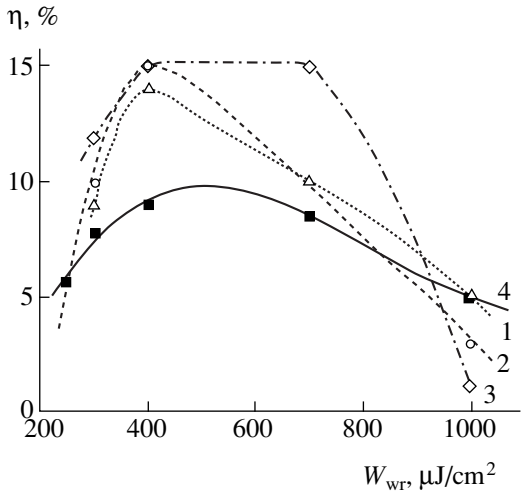

Fig. 2. The plots of diffraction efficiency η versus write energy density W_{wr} for various values of the supply voltage pulse duration τ_{sup} = 50, 80, and 200 ms (curves *1–3*, respectively) Curve *4* shows data for an STLM with a fullerene- containing PI (0.25 wt % C_{60}) measured at a dc voltage of 80 V. Λ = 100 mm^{-1}.

wavelength of 633 nm, a collimated beam diameter of 5 mm, and a power density of 10^{-4} W/cm^2. The optical response in the first order of diffraction was measured in the focal plane of a lens mounted behind the STLM. The sandwich structure was power supplied either by rectangular pulses with an amplitude of A = 30–60 V, a pulse duration of τ_{sup} = 30–300 ms, and a repetition rate of $1/T$ = 0.2–7 Hz, or by a dc voltage of V = 80–90 V.

Let us consider the experimental results. Figure 1 shows a plot of the diffraction efficiency η versus the delay time D between a laser pulse and the modulator supply voltage pulse. Since the inertia of the PI–liquid crystal system response varied from 400 μs to 0.1 s (depending on the particular STLM sample), we have studied the photoresponse in a range of delay times from 5 μs to 100 ms, completely covering the above interval. Note that an additional factor influencing selection of the delay time is the need in making an allowance for the characteristic time of image blurring. For STLMs of the type studied in this work, this time can be evaluated from a relationship $\tau = d^2/(\mu V)$, which yields a value of 2–20 ms (d is the photosensitive layer thickness, μ is the charge carrier mobility, and V is the supply voltage). The estimate refers to the charge carrier mobility in PIs (ranging from 10^{-7} to 10^{-5} cm^2/(V s) [6, 11]), the photosensitive layer thickness d = 1 μm, and V = 50 V (at the first instant, all the voltage supplied drops on this layer).

The high values of η = 15–20% observed for D from 3–5 μs up to 5 ms, followed by a decrease to η = 10% in the interval of D = 5–10 ms, correspond to a situation where the spreading of charge carriers is virtually not yet manifested. As the delay time increases from 10 to 80–100 ms, the resolution decreases as a result of the charge carrier spreading and the diffraction efficiency drops (Fig. 1). It should be noted that a shift in the photoresponse toward the trailing edge of the supply voltage pulse is probably related to an additional influence of interphase boundaries in the STLM sandwich structure. The presence of several interfaces (conducting film–photosensitive layer, photosensitive layer–orienting film, orienting film–liquid crystal, and orienting layer–conducting film) gives rise to the possibility of forming electric double layers screening the electric field and leading eventually to retardation of the charge transfer processes and a shift of the photoresponse toward greater delay times. Effects of the nature of orienting films on the time characteristics of LC cells and PI–liquid crystal STLMs were considered in detail in [12–14].

We have estimated the characteristic switching times for the system operated at D = 5 μs. The switch-on time was 5–7 ms, and the switch-off time was ~100–120 ms.

Figure 2 shows the plots of diffraction efficiency η versus write energy density W_{wr} for various values of the supply voltage pulse duration τ_{sup} = 50, 80, and 200 ms (curves *1–3*, respectively). Curve *4* shows the analogous plot for an STLM with a fullerene-containing PI (0.25 wt % C_{60} in the organic matrix) measured at a dc voltage of 80 V. As seen, the diffraction efficiency is retained on a level of 12–15% (curves *1–3*) at W_{wr} = 400–700 μJ/cm^2 for all τ_{sup}. However, when the W_{wr} value grows to 1000 μJ/cm^2 and/or τ_{sup} increases to 200 ms, the η values decreases in all curves. Thus, these conditions hinder the possibility of attaining the ideal case whereby virtually all charge carriers reach the second electrode (conducting film) of the structure. Here, the charge production–transfer–recombination processes are limited to a considerable extent by the

The main characteristics of LC STLMs with PI-based photosensitive layers

Photosensitive layer of STLM	Switch-on time, ms	Switch-off time, ms	Sensitivity, J/cm^2	Diffraction efficiency, % (for Λ = 90–100 mm^{-1})	Supply voltage, V	Write mode	Refs.
Unmodified PI	250	700	5×10^{-5}		dc	dc	[3]
Unmodified PI	50	500	–	18 (Λ = 40 mm^{-1})	dc	p	[16]
Dye-modified PI	5–10	120	5×10^{-6}	15–17	p	p	[12]
Dye-modified PI	25	150	–	10–12	dc	p	[17]
Fullerene-modified PI (85%C_{60} + 15%C_{70})	5	80	$(5–20) \times 10^{-7}$	7–8	dc, p	p	[18]
Fullerene-modified PI (C_{70})	5–10	80	5×10^{-7}	5–7	dc, p	p	This work
Modified PI (Fullerene + Malachite Green)	~5	80–100	$(2–5) \times 10^{-7}$	7–10	dc, p	p	This work

Note: Data refer to STLM with oxide orienting films at the PI–liquid crystal interface; supply voltage type: dc—direct-current, p—pulsed.

trapping centers. These centers are represented by increasing number of various defects related to rupture of the side-chain groups and breakage of the macromolecular conjugation chain at high intensity of the laser radiation and large τ_{sup} values. An additional source of the trapping centers is related to dissociation of the LC component. Charge carriers captured on the traps generate local electric fields producing (in the presence of an electrooptical effect in the liquid crystal) an uncontrolled random modulation of the refractive index. This results in violation of the optimum write–read conditions and leads to a decrease in the diffraction efficiency and, hence, in the spatial resolution of the system. This is clearly illustrated in Fig. 2 (curve *3*).

Using the data presented in Fig. 2, it is possible to estimate threshold levels of the write energy density for various τ_{sup} values and the maximum levels of illumination determining the structure sensitivity. It should be recalled that, according to the holographic technique, the sensitivity is determined as an exposure to the write light beam necessary to provide for a ~1% diffraction efficiency [1–6]. It was found that the threshold sensitivity level of the structure studied at τ_{sup} = 50 and 80 ms was 5–7 μJ/cm^2 and decreased (i.e., the sensitivity increased) to 1–2 μJ/cm^2 at τ_{sup} = 200 ms. As for the maximum illumination levels, the estimation yields ~1000 μJ/cm^2 at τ_{sup} = 200 ms, ~1500 μJ/cm^2 at 80 ms, and 1700–2000 μJ/cm^2 at 50 ms.

We have succeeded in providing a considerable (nearly tenfold) increase in sensitivity without significant loss in resolution by using a fullerene-containing polyimide in the photosensitive layer of the LC STLM structure. The threshold sensitivity level of this structure was 0.5 μJ/cm^2. The increase in sensitivity is related to the mechanism of complex formation between a triphenylamine donor fragment of the PI molecule and the fullerene molecule acting as the acceptor with an electron affinity twice that of the diamide acceptor fragment of PI. It was demonstrated [15] that the absorption cross section of the new complex is 300 times that for the intramolecular complex of PI. Some decrease in the η value for the fullerene-containing system is related to acceleration of the transient processes in the STLM, which is manifested by a decrease in the switch-off time to 80 ms. Comparative data on the parameters of LC STLMs with unmodified PI-based photosensitive layers and the layers of PI modified with dyes and fullerenes are presented in the table.

Thus, we have studied the effects of the operating conditions and fullerene modification on the diffraction efficiency, time characteristics, and sensitivity of liquid-crystalline STLMs. The results show that application of a fullerene-containing polyimide markedly increases sensitivity of the structure. A qualitative model explaining this effect is suggested.

The authors are grateful to Prof. O.D. Lavrentovich (Kent State University, USA) for kindly providing a sample of E7 (BHD), to Dr. Alex Leyderman (University of PR, USA) for providing C_{60} and C_{70} fullerenes, and to Prof. B.V. Kotov (Karpov Institute of Physical Chemistry, Moscow) for his help in work.

REFERENCES

1. A. A. Vasil'ev, D. Casasent, I. N. Kompanets, and A. V. Parfenov, *Space-Time Light Modulators* (Radio i Svyaz', Moscow, 1987).
2. F. L. Vladimirov, I. E. Morichev, N. I. Pletneva, and T. O. Reshetnikova, Opt.-Mekh. Prom-st., No. 6, 6 (1985).
3. V. S. Myl'nikov, E. A. Morozova, N. A. Vasilenko, *et al.*, Zh. Tekh. Fiz. **55**, 749 (1985) [Sov. Phys. Tech. Phys. **30**, 444 (1985)].
4. Yu. D. Dumarevskiĭ, T. V. Zakharova, N. F. Kovtonyuk, *et al.*, Opt.-Mekh. Prom-st., No. 12, 9 (1989).

5. N. L. Ivanova, V. V. Nikitin, and A. P. Onokhov, Opt. Zh. **60** (7), 45 (1993) [J. Opt. Technol. **60**, 475 (1993)].
6. V. S. Mylnnikov, Adv. Polym. Sci. **115**, 3 (1994).
7. N. V. Kamanina, L. N. Soms, and A. A. Tarasov, Opt. Spektrosk. **68** (3), 691 (1990) [Opt. Spectrosc. **68**, 403 (1990)].
8. V. A. Berenberg, N. V. Kamanina, and L. N. Soms, Izv. Akad. Nauk SSSR, Ser. Fiz. **55** (2), 236 (1991).
9. N. V. Kamanina and N. A. Vasilenko, Electron. Lett. **31** (5), 394 (1995).
10. P. I. Dubenskov, T. S. Zhuravleva, A. V. Vannikov, *et al.*, Vysokomol. Soedin., Ser. A **30** (6), 1211 (1988).
11. T. Hara, T. Tsutsui, and S. Saito, Jpn. J. Appl. Phys. **24** (8), 970 (1985).
12. N. V. Kamanina, Proc. SPIE **2731**, 220 (1996).
13. N. V. Kamanina and N. A. Vasilenko, Opt. Quantum Electron. **29**, 1 (1997).
14. N. V. Kamanina and V. I. Berendyaev, Proc. SPIE **3292**, 154 (1998).
15. Y. A. Cherkasov, N. V. Kamanina, E. L. Alexandrova, *et al.*, Proc. SPIE **3471**, 254 (1998).
16. M. A. Groznov, V. S. Myl'nikov, A. G. Sinikas, and L. N. Soms, Tr. Gos. Opt. Inst. **60**, 69 (1986).
17. N. V. Kamanina and N. A. Vasilenko, Zh. Tekh. Fiz. **67** (1), 95 (1997) [Tech. Phys. **42**, 82 (1997)].
18. N. V. Kamanina, N. M. Kozhevnikov, and N. A. Vasilenko, Proc. SPIE **3633**, 122 (1999).

Translated by P. Pozdeev

Technical Physics Letters, Vol. 26, No. 9, 2000, pp. 775–777. Translated from Pis'ma v Zhurnal Tekhnicheskoĭ Fiziki, Vol. 26, No. 17, 2000, pp. 46–52.
Original Russian Text Copyright © 2000 by A. Pozdnyakov, Ginzburg, O. Pozdnyakov, Redkov, Maricheva, Artem'eva, Kudryavtsev.

Thermodesorption States of Fullerene C_{60} in the Polyimide–Fullerene System

A. O. Pozdnyakov, B. M. Ginzburg, O. F. Pozdnyakov, B. P. Redkov, T. A. Maricheva, V. N. Artem'eva, and V. V. Kudryavtsev

Institute of Machine Science, Russian Academy of Sciences, St. Petersburg, Russia
Ioffe Physicotechnical Institute, Russian Academy of Sciences, St. Petersburg, 194021 Russia
Institute of Macromolecular Compounds, Russian Academy of Sciences, St. Petersburg, Russia
Received March 13, 2000

Abstract—The data of thermodesorption mass spectrometry indicate that fullerene C_{60} molecules are desorbed from a polyimide (PI) surface at temperatures below the PI decomposition onset temperature, while the desorption of C_{60} from the bulk begins in the temperature region of the polymer decomposition. It is suggested that strong chemical bonds between C_{60} and PI macromolecules are formed in the bulk in the stage of the polyamic acid preparation and are broken upon destruction of the polymer macromolecules. The character of C_{60} thermodesorption from the PI surface depends on thickness of the surface film of fullerene C_{60}. © *2000 MAIK "Nauka/Interperiodica".*

In the previous works [1–3], we demonstrated that the thermodesorption mass spectra of fullerene C_{60} observed on heating in various polymer–C_{60} systems are sensitive to both chemical and phase state of C_{60} molecules in the samples studied. The thermodesorption states of fullerene in the systems studied were observed in the region of temperatures corresponding to decomposition of the matrix polymers, including polystyrene (PS) [1], poly(methyl methacrylate) (PMMA) [3], and trifluorochloroethylene–vinylidene fluoride (TFCE–VDF) copolymer [2]. This observation does not exclude the possibility that fullerenes may interact in the stage of desorption with the free macroradicals formed upon thermal decomposition of the polymer matrix.

It was suggested that use of a polymer belonging to the class of polyimides (PIs), possessing comparatively high decomposition temperatures (the onset of decomposition in air is observed at 400°C and above [4, 5]), would allow us to eliminate the above uncertainty. Below, we present the first results of investigations of the thermodesorption states of fullerene molecules on the surface and in the bulk of a high-temperature-resistant rigid-chain PI.

The PI samples were synthesized in two stages. In the first stage, a polyamic acid (PAA) was synthesized from a mixture of 3,3',4,4'-diphenyloxytetracarboxylic acid dianhydride, *p*-phenylenediamine, and 2.5-bis-(4-aminophenyl)pyrimidine taken in the molar ratio 100 : 50 : 50. Prior to the synthesis, 3,3',4,4'-diphenyloxytetracarboxylic acid dianhydride (DPO) was recrystallized from *o*-xylene and treated at 100°C in vacuum (T_m = 226–227°C); *p*-phenylenediamine was distilled in vacuum (T_m = 139–141°C); 2.5-bis-(4-aminophenyl)pyrimidine was purified by sublimation (T_m = 226–227°C); *N*,*N*-dimethylacetamide (DMA) was dried over calcium hydride and distilled on a rectification column at a reduced pressure; *o*-dichlorobenzene was purified by distillation. Then, 0.6968 g (0.0065 mol) of *p*-phenylenediamine and 1.6903 g (0.0065 mol) of 2.5-bis-(4-aminophenyl)pyrimidine were dissolved with stirring in 47 ml of DMA. To this solution were added dropwise 5 ml of an *o*-dichlorobenzene solution containing 0.055 g (1% of the PAA weight) of a fullerene mixture (78 wt % C_{60} + 22 wt % C_{70}). The fullerene mixture was prepared by extraction from a fullerene soot.[1] Upon completely adding fullerenes, the mixture was stirred for 1 h.

To this fullerene-containing solution were added by portions with permanent stirring 3.5 g of DPO and then the stirring was continued for 5 h. The resulting PAA may probably contain a fraction of repeating units (about 1%) "modified" by fullerene. This circumstance must be borne in mind in interpreting the results of investigations, although which particular type of modification (complex formation or covalent binding resulting in the imide cycle distortion) takes place is yet unclear, being insignificant for the main conclusions of this work.

The fullerene-containing PAA solution (referred to below as PAA–fullerene) was applied onto a metal (stainless steel) plate to perform the second stage of PI formation—thermal imidization of the PAA–fullerene system. The process of imidization on substrate was effected in the following regime: air drying by heating to 80°C at a rate of 20 K/min was followed by additional

[1] The fullerene mixture was provided by the "Fullerenovye Tekhnologii" (Fullerene Technologies) company (St. Petersburg, Russia).

1063-7850/00/2609-0775$20.00 © 2000 MAIK "Nauka/Interperiodica"

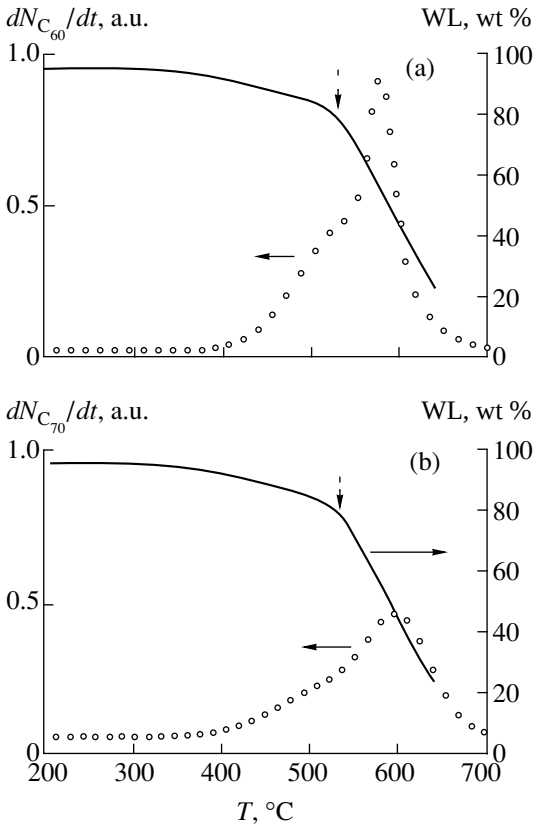

Fig. 1. Temperature variation of the relative weight loss (WL) and the rate of fullerene (a) C_{60} and (b) C_{70} evolution from thin PI–Fl films.

heating in a vacuum chamber of the mass spectrometer to 350°C at the same rate as above. Then, the samples were allowed to cool to the room temperature. The thickness of a thin PI film formed on the metal substrate (this product will be denoted as PI–Fl) was about 5 μm.

For a direct comparison between the kinetics of C_{60} evolution from the bulk and the kinetics of fullerene desorption from a PI– Fl sample surface, a solution of pure C_{60} (99.8%) in toluene was applied onto the PI–Fl sample and dried for a few minutes. Below we present the results on the fullerene desorption from ~100- and 10-nm-thick C_{60} layers formed on the surface of PI–Fl films. Layers of a greater thickness were obtained by applying 5 μl of a C_{60} solution with a concentration of 0.3 wt % onto a PI–Fl film surface, while thinner films were obtained by applying the same solution diluted to 0.03 wt %.

The thermodesorption experiments were performed on a magnetic mass spectrometer of the MX-1320 type specially adapted for heating thin-film samples in a temperature-programmed mode. The samples were heated at a constant rate of about 7 K/s. A residual pressure in the spectrometer chamber prior to the thermodesorption measurements was maintained on a level of 5×10^{-5} Pa. The *i*th peak height in a mass spectrum is proportional to the current partial pressure of the *i*th component in the system studied. Provided that the pumping rate is sufficiently high, this value is proportional to the rate of the *i*th volatile component formation dN_i/dt. Thus, measurements of the thermodesorption peak height provide quantitative information of the rate of formation (thermodesorption) of the compound studied. The rates of formation of various volatile products in the system studied were determined by calibrating the absolute sensitivity of the instrument with respect to a flow of methyl methacrylate from a weighed amount of PMMA heated in the same regime and using the tabulated values of relative sensitivities of the corresponding compounds.

In the course of thermodesorption experiments, we have also measured the total ion current $I(t)$. The $I(t)$ value is proportional to the total rate of evolution of all volatile products from the sample studied. The integral of $I(t)$ with respect to time from the heating start ($t = 0$) to a current time instant ($t = \tau$) is proportional to the total mass of volatile products evaporated from the sample, that is, to the sample weight loss Δm:

$$m_0 - m(\tau) = \Delta m(\tau) = \int_{t=0}^{t=\tau} kI(t)dt,$$

where k is the empirical coefficient and m_0 is the initial sample weight. This relationship was used to calculate the plots of the relative sample weight loss on heating.

The sample structures were studied by measuring the X-ray diffraction patterns on a DRON-2.0 diffractometer using Ni-filtered CuK_α radiation.

Figure 1 shows the temperature variation of the rate of fullerene (a) C_{60} and (b) C_{70} evolution from a PI–Fl film and the corresponding weight loss (WL) of the sample in the course of a thermodesorption experiment. The presence of bending points on the temperature dependence of the weight loss (indicated by vertical arrows) is evidence of different decomposition mechanisms operative in the PI–fullerene system in the temperature regions below and above 500°C. This result agrees with the data of mass-spectrometric investigation of the chemical processes accompanying heating of the PAA and PI samples [4]. Note that the low-temperature stage of the process is not observed during repeated heating of a sample preliminary heated to 500°C and cooled to room temperature (see, e.g., [5]). The release of C_{60} and C_{70} molecules is a two-stage process. The low-temperature stage coincides with the region of low-temperature degradation of the sample, while the high-temperature stage falls within the main (high-temperature) stage of the polymer decomposition. Taking into account that we studied thin (micron) films, these data can be considered as indirect evidence of the presence of strong chemical bonds between fullerene molecules and polymer chains, which are broken only upon development of the process of thermal decomposition of the latter macromolecules. Note also that the temperature interval corresponding to the evo-

lution of C_{60} molecules from a thin PI–Fl film is lying significantly (by approximately 200°C) above the analogous regions reported for some other polymer–fullerene systems such as PS–C_{60} [1], PTFCE–VDF copolymer–C_{60} [2], and PMMA–C_{60} [3].

The wide-angle X-ray diffractograms from pure PI and the PI–Fl film samples are virtually identical and display diffuse ring reflections characterized by 2θ values about 10.5, 18.9, and 25.2°C. The absence of qualitative distinctions between the diffractograms of pure PI and PI–fullerene systems suggests that fullerenes introduced in a small amount (below 1 wt %) into a PI film produce no significant effect upon the PI crystal structure and the fullerene molecules do not form a separate phase.

Figures 2a and 2b show a temperature dependence of the desorption of neutral C_{60} molecules from PI–Fl films with additional C_{60} overlayers. The data in Fig. 2a refer to the PI–Fl films with a calculated C_{60} layer thickness of 100 nm; Fig. 2b shows analogous data for a 10-nm-thick fullerene layer, The thermodesorption of fullerene from the film surface is observed at temperatures markedly lower (T_{max} ~ 570°C) as compared to the temperature corresponding to the maximum rate of fullerene evolution from the bulk of polymer. The process of desorption from the PI surface represents a superposition of at least two stages that are poorly resolved under our experimental conditions. In the case of a 10-nm-thick layer, T_{max} = 330 and 410°C, while the corresponding stages for the 100-nm-thick layer are observed at T_{max} = 380 and 430°C. By analogy with a mechanism proposed in [6], the two-stage desorption of C_{60} from the PI surface can be explained by superposition of the corresponding contributions related to the crystalline and molecular-dispersed C_{60} phases. In the latter phase, C_{60} molecules are bound directly to the surface macromolecules of the polymer. The calculated activation energy for the process of C_{60} desorption from the PI surface in this case amounts to 126 J/mol.

A comparison of the thermodesorption states of C_{60} on the surface and in the bulk of PI shows that the bonds between C_{60} and the surface macromolecules of a preformed PI film are weaker as compared to the bonds formed when C_{60} is introduced into the PI matrix. Obtaining more detailed information on the behavior of C_{60} molecules in the PI–fullerene composition and on the PI surface requires additional experiments. The results of this work unambiguously indicate that a high-temperature-resistant PI offers an adequate model polymer substrate for these investigations.

Thus, we have established that the escape of C_{60} molecules from a rigid-chain PI matrix takes place at markedly higher temperatures as compared to those observed in the polymer–fullerene systems studied previously [1–3]. The thermodesorption of C_{60} from the PI surface proceeds at temperatures substantially lower than the temperature of PI decomposition, while the desorption from the bulk of PI falls within the temperature range of the polymer matrix decomposition. The latter fact suggests that strong chemical bonds between C_{60} and PI macromolecules are formed in the bulk in the stage of the polyamic acid preparation.

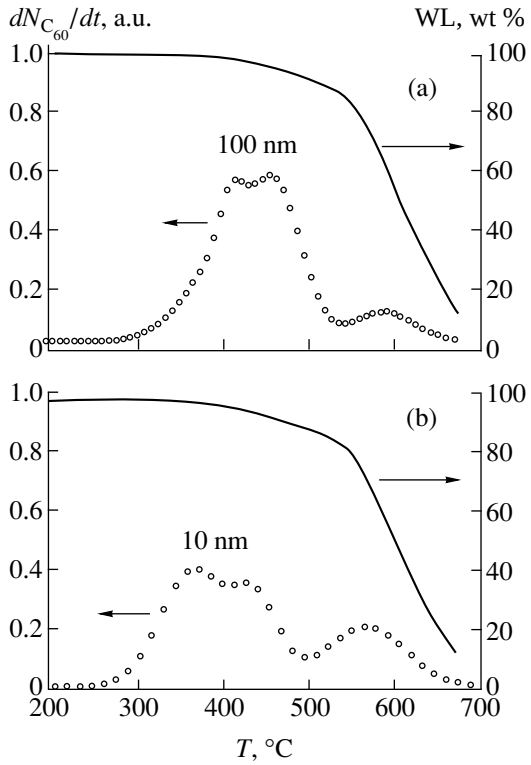

Fig. 2. Temperature variation of the relative weight loss (WL) and the rate of fullerene C_{60} desorption from (a) 100- and (b) 10-nm-thick layers on the surface of PI–Fl films.

The authors are grateful to L.P. Myasnikova for taking wide-angle X-ray diffraction measurements.

REFERENCES

1. A. O. Pozdnyakov, O. F. Pozdnyakov, B. P. Redkov, *et al.*, Pis'ma Zh. Tekh. Fiz. **22** (18), 57 (1996) [Tech. Phys. Lett. **22**, 759 (1996)].
2. A. O. Pozdnyakov, B. M. Ginzburg, O. F. Pozdnyakov, and B. P. Redkov, Zh. Prikl. Khim. (St. Petersburg) **37** (1), 135 (2000).
3. O. F. Pozdnyakov, B. P. Redkov, and A. O. Pozdnyakov, in *Proceedings of the International Workshop on New Approaches to Hi-Tech Materials NDTCS, St. Petersburg, 1997*, p. 33.
4. M.-J. Brekner and C. Feger, J. Polym. Sci., Part A: Polym. Chem. **25**, 2005 (1987).
5. M. I. Bessonov, M. M. Koton, V. V. Kudryavtsev, and L. A. Laĭus, *Polyimides—A Class of Thermostable Polymers* (Nauka, Leningrad, 1983).
6. Y. K. Bae, D. C. Lorents, and R. Malhotra, Mater. Res. Soc. Symp. Proc. **206**, 738 (1991).

Translated by P. Pozdeev

Technical Physics Letters, Vol. 26, No. 9, 2000, pp. 778–780. Translated from Pis'ma v Zhurnal Tekhnicheskoĭ Fiziki, Vol. 26, No. 17, 2000, pp. 53–58.
Original Russian Text Copyright © 2000 by Tutov, Andryukov, Ryabtsev.

Nonequilibrium Processes in Capacitive Sensors Based on Porous Silicon

E. A. Tutov, A. Yu. Andryukov, and S. V. Ryabtsev

Voronezh State University, Voronezh, Russia

E-mail: phssd28@main.vsu.ru

Received June 1, 2000

Abstract—The response of a capacitive sensor of the Al/por-Si/*n*-Si type to the presence of ammonia and water vapor in the gas phase was studied. It was found that illumination affects the process of capacitance relaxation.
© 2000 MAIK "Nauka/Interperiodica".

Porous silicon (por-Si) attracts the attention of researchers mostly due to its luminescent properties [1]. At the same time, extensive investigations of many other characteristics of por-Si showed good prospects for numerous alternative applications of this material in various fields such as solar cells, biotechnologies, and sensors [2].

Methods developed for the electrochemical etching of silicon provide a means of controlled modification of the parameters of a porous silicon layer in order to optimize its adsorption properties. The effect of adsorption of various gases, including ammonia and water vapor, on the electrical properties of por-Si and the possibility of using this phenomenon in sensors of the resistive, diode, and capacitive types were studied in [3–7].

Semiconductor adsorption gas sensors, albeit possessing a number of advantages, exhibit a principal drawback: low selectivity. One possible way to solve the problem consists in analysis of the response kinetics. This possibility can be markedly expanded by using optical stimulation of the surface processes, since this factor selectively affects various electron subsystems of the adsorbate. The influence of illumination upon the adsorption equilibrium and the chemisorption kinetics is called the photoadsorption effect [8].

The (100)-oriented single-crystal silicon plates of the KEF grade with an electron concentration of 1.3×10^{16} cm^{-3} was cleaned by rinsing in distilled water followed by etching in an HF + HNO_3 + CH_3COOH solution. Then the samples were electrochemically anodized in a HF/H_2O–C_3H_8O–H_2O_2 (2 : 2 : 1) electrolyte for 5 min at a current density of 15 mA/cm^2. Upon etching, the samples were washed in butyl alcohol and dried. The anodized silicon surface retained mirror appearance, which indicated the absence of micron-size inhomogeneities. A thickness of the porous layer produced by etching was about 10 μm, the porosity was 50–70%, and the oxide phase content in por-Si amounted to 3–4% [8]. Finally, contact squares with an area of 2 mm^2 were applied by thermal deposition of aluminum.

The high-frequency capacitance–voltage (*C–U*) characteristics were measured in a steady-state regime at a frequency of 1 MHz in a bias range of ±10 V using a test signal with an amplitude of 20 mV. The time required for taking a *C–U* curve was about 5 min. The leak current in the system did not exceed 1 mA. The spurious capacitance of connecting wires (~2 pF) was automatically subtracted from the results of *C–U* measurements.

The *C–U* measurements were performed on the por-Si samples mounted in a hermetically sealed experimental cell. A zero relative humidity (*RH* = 0) was obtained with the aid of a silica gel, over which a sample was heated for 30 min at *T* = 343 K. The source of NH_3 was a 10% aqueous ammonia solution. The kinetic characteristics were taken upon admitting a 5 cm^3 gas "pulse" (10% NH_3 or air wit *RH* = 100%) into the cell with a sample sensor. The sample surface was illuminated by the light of an incandescent lamp with a radiant power density of 0.01 W/cm^2.

Since the dielectric permittivity of silicon and silicon oxides is markedly lower than that of water (ε = 81), the adsorption of water vapor on the sample surface must lead to a considerable increase in the sensor capacitance. Figure 1 shows a typical *C–U* curve, the inset presenting a schematic diagram of the sample configuration with electrodes connected in a coplanar mode. This scheme is equivalent to the serial connection of two MOS capacitors shunted by a resistance of the por-Si layer. The capacitors have opposite polarities and the system capacitance for any applied bias voltage is determined (at *RH* = 0) by the capacitance of a space-charge region in one of the capacitors. As the relative humidity increases (Fig. 1, curve *b*), the effective dielectric permittivity of the por-Si layer and, hence, the system capacitance grow. At *RH* = 100%, the system exhibits an essentially nonequilibrium behavior and the *C–U* curve acquires an involved shape (Fig. 1,

curve *c*). This is explained by a reversible breakdown of the space-charge region in one of the capacitors (depending on the bias voltage polarity) at a large biases, whereas both capacitors operate in the vicinity of a zero bias. The increase in sensitivity observed for this sensor operation regime is explained by the fact that the entire por-Si surface between electrodes becomes active.

A similar behavior of the sensor was observed in response to the ammonia vapor; moreover, the effects are distinguished even on the background of *RH* = 100%.

Interesting features are characteristic of the process of sensor relaxation upon the "pulsed" action of ammonia or water vapors (Fig. 2). The physical adsorption (including the capillary condensation phenomenon) being a rapid process, the sensor response time is of the order of one second and the subsequent relaxation lasts over about one minute. However, illumination of the sample surface results in that the sensor recovery becomes incomplete. The compete restoration of the initial sensor capacitance is achieved only upon exposure of the sample in the dark for a few minutes. It should be noted that similar features were observed in the dc conductivity measurement mode [10].

The effect of illumination can be partly related to photochemical reactions such as the defect transformation stimulated by the surface recombination of minority charge carries, rather than entirely to the recharge of active centers. Similar reactions were observed in flat-band $A^{II}B^{VI}$ semiconductors [11]. Elucidation of the nature of these phenomena required additional detailed investigations.

The existence of metastable impurity–defect complexes in porous silicon and their reconstruction under the action of heat or illumination were studied in [12, 13]. Islam *et al.* [12] explained the observed effects by the presence of an amorphous hydrogenated silicon phase (*a*-Si:H) in the por-Si layer. It should be noted that the illumination-induced transformation of metastable defects in *a*-Si:H is known as the Staebler–Wronski effect [14].

The results of measurements of the electrical characteristics of por-Si may significantly depend both on the ambient conditions (in particular, on the *RH* value) and on the measuring system parameters determining the operation regimes (voltages) of heterojunctions and, hence, the mechanisms of charge transfer operative in the system (Fig. 1).

The known optical properties of por-Si allow us to believe that illumination of the samples in various spectral regions may be used for selective excitation of the corresponding electron subsystems in por-Si, thus providing for the controlled response and relaxation of the sensor. The resonance action of a monochromatic light with definite frequency upon the semiconductor surface may, in principle, perform selective recharge or excitation of the active surface centers or adsorbed molecules. This opens way to controlled selectivity in the adsorption–desorption phenomena.

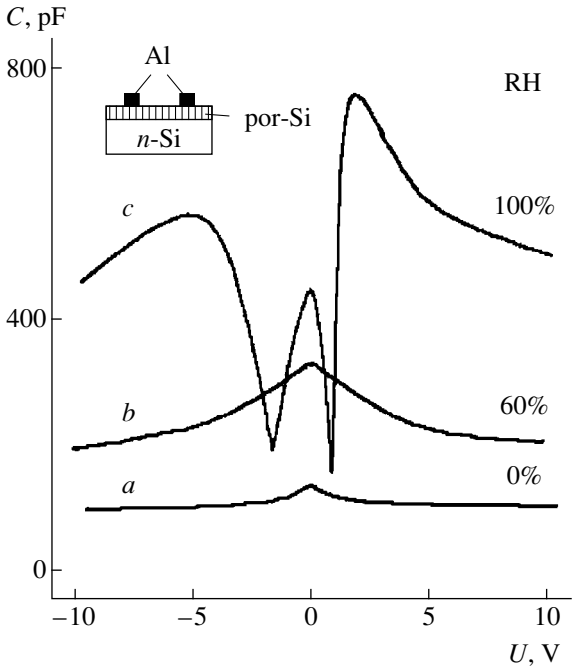

Fig. 1. High-frequency *C–U* curves of a Al/por-Si/*n*-Si type with electrodes connected in a coplanar mode, measured at various relative humidities *RH* = 0 (*a*); 60% (*b*); 100% (*c*).

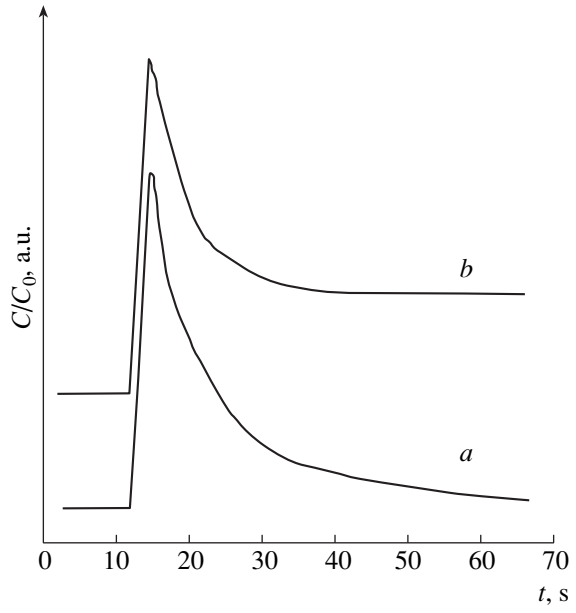

Fig. 2. The kinetics of a por-Si sensor response to ammonia (*a*) in the dark and (*b*) under illumination.

The illuminated (excited) por-Si surface may feature, besides the electric recharge processes, some photochemical ionic reactions leading to the appearance of new (or disappearance of the existing) defects in the semiconductor (recombination centers, traps, etc.).

This phenomenon can be used both for the control of characteristics of the por-Si-based sensors and for the study of structural and energetic characteristics of this material.

Finally, it should be noted that a microheterophase character of the porous silicon structure is manifested by the fact that the sign of response to the same adsorbate may change depending on the temperature [15]. All these features show por-Si to be a flexible functional material offering large possibilities in obtaining optimum properties for the creation of high-performance microelectronic sensors.

REFERENCES

1. K. H. Jung, S. Shih, and D. L. Kwong, J. Electrochem. Soc. **140** (10), 3046 (1993).
2. *Properties of Porous Silicon*, Ed. by L. Canham (INSPEC, London, 1997), EMIS Datareviews Series, No. 18.
3. V. M. Demidovich, G. B. Demidovich, E. I. Dobrenkova, and S. N. Kozlov, Pis'ma Zh. Tekh. Fiz. **18** (14), 57 (1992) [Sov. Tech. Phys. Lett. **18**, 459 (1992)].
4. V. M. Demidovich, G. B. Demidovich, S. N. Kozlov, *et al.*, Vestn. Mosk. Univ., Ser. 3: Fiz., Astron., No. 4, 99 (1996).
5. A. A. Kovalevskiĭ and I. L. Baranov, Mikroélektronika **25** (4), 298 (1996).
6. R. C. Anderson, R. S. Muller, and C. W. Tobias, Sens. Actuators A **23** (1–3), 835 (1990).
7. T. Taliercio, M. Dilhan, E. Massau, *et al.*, Sens. Actuators A **46** (1–3), 43 (1995).
8. Vol'kenshtein, *Electron Processes Accompanying Chemisorption on the Surface of Semiconductors* (Nauka, Moscow, 1987).
9. E. A. Tutov, A. Yu. Andryukov, and V. M. Kashkarov, Zh. Prikl. Khim. (St. Petersburg) **73** (6) (2000) (in press).
10. E. A. Tutov, S. V. Ryabtsev, and A. Yu. Andryukov, in *Proceedings of the 20th International Conference "Relaxation Phenomena in Solids" (Relax-XX), Voronezh, 1999*, p. 369.
11. *The Physics of II–VI Compounds*, Ed. by A. N. Georgobiani and M. K. Sheĭnkman (Nauka, Moscow, 1986).
12. Md. N. Islam, P. S. Dobal, H. D. Bist, and Kumar Satyendra, Solid State Commun. **107** (1), 43 (1998).
13. V. A. Perevoshchikov, V. D. Skuptsov, and V. G. Shengurov, Poverkhnost', No. 4, 44 (1998).
14. D. I. Staebler and C. R. Wronski, Appl. Phys. Lett. **31**, 292 (1977).
15. E. A. Tutov, S. V. Ryabtsev, V. M. Kashkarov, and E. P. Domashevskaya, in *Abstracts of the 7th European Conference on Applied Surface and Interface Analysis (ECASIA), Goteborg, 1997*, NM-19, p. 471.

Translated by P. Pozdeev

Technical Physics Letters, Vol. 26, No. 9, 2000, pp. 781–784. Translated from Pis'ma v Zhurnal Tekhnicheskoĭ Fiziki, Vol. 26, No. 17, 2000, pp. 59–66.
Original Russian Text Copyright © 2000 by Tsyrlin, Samsonenko, Petrov, Polyakov, Egorov, Masalov, Gorbenko, Golubok, Soshnikov, Ustinov.

Nanostructured InSiAs Solid Solution Grown by Molecular Beam Epitaxy on the Si(001) Surface

G. É. Tsyrlin, Yu. B. Samsonenko, V. N. Petrov, N. K. Polyakov, V. A. Egorov, S. A. Masalov, O. M. Gorbenko, A. O. Golubok, I. P. Soshnikov, and V. M. Ustinov

Institute for Analytical Instrumentation, Russian Academy of Sciences, St. Petersburg, 198103 Russia

Ioffe Physicotechnical Institute, Russian Academy of Sciences, St. Petersburg, 194021 Russia

e-mail: samsonenko@beam.ioffe.rssi.ru

Received April 21, 2000

Abstract—The possibility of obtaining a new nanostructured material, an InSiAs solid solution, by molecular beam epitaxy on the Si(001) surface is reported. It is demonstrated that, during simultaneous deposition of indium, silicon, and arsenic, nanometer-size islands with a rectangular base and the sides oriented along the {110} directions can form when the layer thickness exceeds 35 nm. After depositing a 100 nm thick layer of the solid solution, islands with the side ratio $d_{110}/d_{1\bar{1}0} = 1.35$ and a typical lateral size of $d_{1\bar{1}0} \sim 35 \pm 10$ nm are obtained. © *2000 MAIK "Nauka/Interperiodica".*

Considerable interest has been drawn in recent years to the process of direct nanostructure formation by the molecular beam epitaxy (MBE) on the surface of various semiconductor materials [1]. This is related both to the unique fundamental properties of the MBE-grown nanostructures and to their use in technological applications in solid-state physics, optoelectronics, biology, etc. Creation of the quantum-dot lasers and studies of the DNA molecules attached to the surface covered with an array of nanoobjects open new areas for the nanostructured material applications. Use of the molecular-beam epitaxy (MBE) technology in combination with the surface diagnostics methods such as the reflection high-energy electron diffraction (RHEED) and scanning tunneling microscopy (STM) not only makes it possible to predict the features of the surface morphology obtained, but enables one to synthesize new materials and to study their properties as well. In this paper, we report for the first time on the possibility of obtaining a new nanostructured material, an InSiAs solid solution, on the Si(001) surface. This material, owing to its structural properties, can find applications in different areas of modern nanotechnology (nanobiochips, multiple-tip cathodes, etc.).

The samples were grown in an EP 1203 MBE setup on (001)-oriented *p*-Si substrates of the KDB-7.5 grade. After the chemical treatment identical to that described in [2], the substrates were mechanically mounted on a molybdenum holder without using indium. The oxide layer was removed by increasing the substrate temperature T_s in the growth chamber to 870°C for 15 min, after which a (2×2) surface reconstruction typical of the Si(001) surface was observed. In addition to the regular temperature sensor assembly based on a VR5/VR20 thermocouple, an Ircon Modline Plus infrared pyrometer was used to monitor the substrate temperature. Monitoring of the oxide layer removal and *in situ* examination of the sample surface morphology during the growth process were carried out using an RHEED pattern registration and processing complex. The complex consists of a video camera, a video tape recorder for the subsequent detailed processing of the RHEED pattern dynamics, a computer for the real-time video information processing, and an interface connecting the video camera to the tape recorder and the computer [3]. Next, the sample temperature was reduced to 420°C to prevent InAs reevaporation from the surface, and the silicon, indium, and arsenic flux shutters were simultaneously opened to grow a 100-nm-thick layer. The indium flux, preliminarily calibrated using the specular RHEED reflection oscillations corresponded to 0.05 InAs monolayers per second

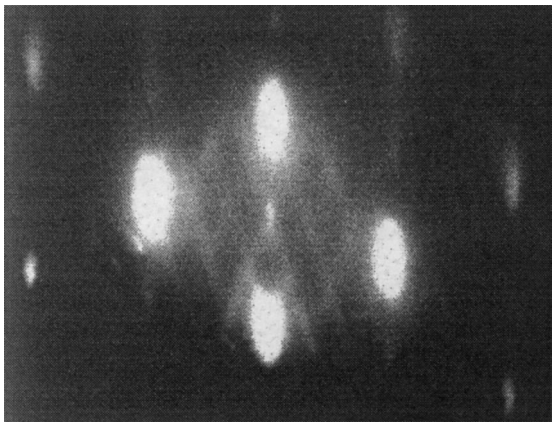

Fig. 1. RHEED pattern observed after deposition of a 35-nm-thick layer of InSiAs on the Si(001) surface.

1063-7850/00/2609-0781$20.00 © 2000 MAIK "Nauka/Interperiodica"

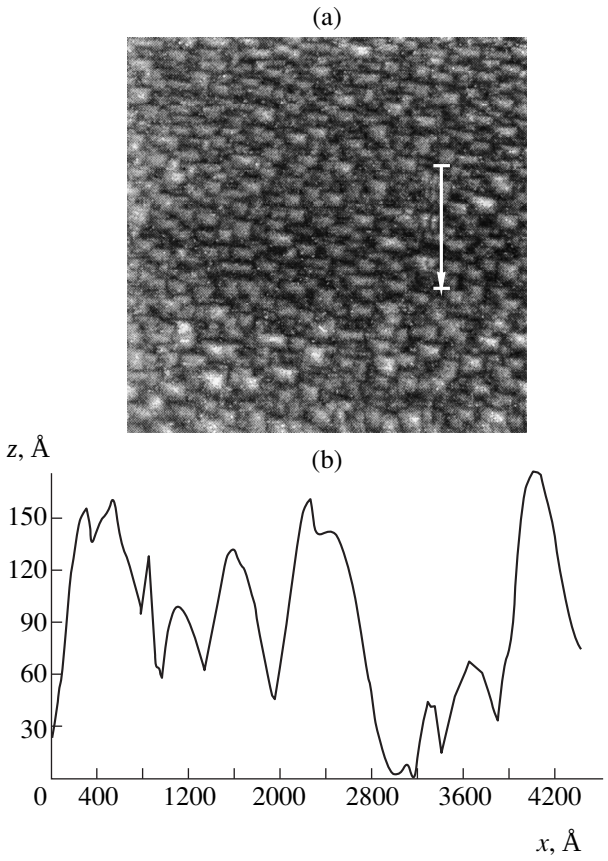

Fig. 2. (a) An STM image of a 1800×1800 nm region of the sample surface. The picture sides are parallel to the [110] and $[1\bar{1}0]$ directions. (b) A typical cross section of several surface nanoobjects. The cross-section direction is indicated by the arrow. The *x*-axis lies in the sample plane, and the *z*-axis is parallel to the growth direction.

for the growth of an InGaAs solid solution (with ~15% In content) on GaAs. The silicon flux also amounted to 0.05 monolayers per second. The group V to group III element flux ratio was equal to 10.

The sample surface morphology was studied *ex situ* by STM. The STM techniques and operation modes were similar to those employed earlier in the study of the InAs/GaAs system [4]. Repeatedly reproducible and stable STM images were obtained for different regions of the samples under study in a direct current mode under positive bias applied to the sample.

A diffraction pattern observed after growing of a 20-nm-thick silicon buffer layer is typical of the surfaces with the above-mentioned orientation, reflecting a (2×2) reconstruction along the [110] and $[\bar{1}10]$ directions. In the course of the InSiAs deposition, after the layer thickness reaching 35 nm, spot reflections appear in the diffraction pattern, which indicates the transition to the three-dimensional growth mode. Simultaneously, inclined linear reflections for the incident electron beam orientations of [110] and $[\bar{1}10]$ show up clearly (see Fig. 1) and remain in the diffraction pattern until the growth is terminated after reaching a layer thickness of 100 nm. The appearance of these linear reflections evidences the formation of atomically flat faces oriented at some angle to the (001) main growth direction. Comparing the spot and linear reflection patterns, we determined the face indexes as $(\bar{1}12)$ and $(1\bar{1}2)$ for the incident beam orientation of [110] and $[\bar{1}10]$, respectively. The calculated periodicity of linear reflections in the reciprocal space agrees with the period of bulk face-centered cubic lattice along

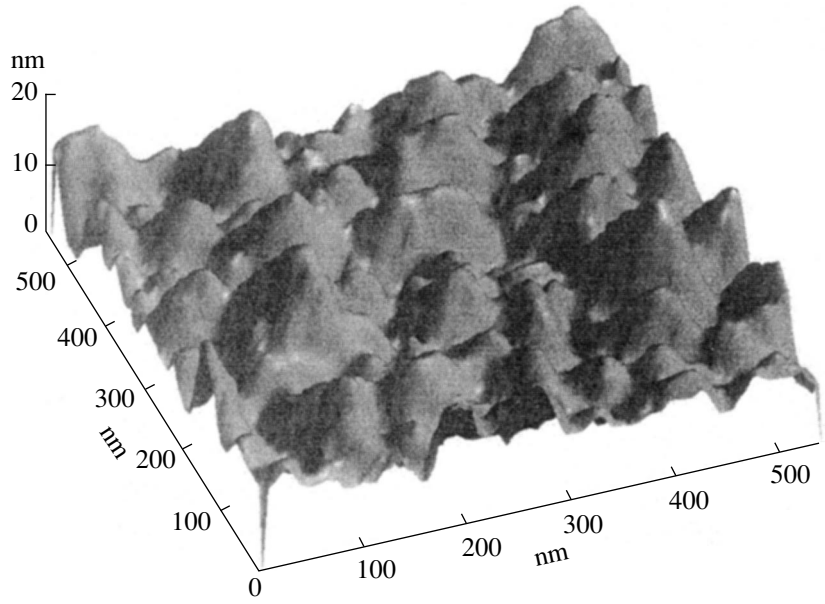

Fig. 3. Three-dimensional image of a surface region in axonometric projection.

the directions [$1\bar{1}1$] and [$\bar{1}11$], lying in the specified planes. This means that no high-order reconstruction occurs in these directions. Thus, our analysis the electron diffraction pattern suggested the existence of the pyramid-shaped formations on the initial (001) growth surface, which have rather clear faceting along the (112)-type planes, forming an angle of 35.3° with the surface.

This conclusion is corroborated by the STM data. A typical STM image of the sample surface is shown in Fig. 2a. It is seen that the surface formations possess rectangular bases oriented along the [110] and [$\bar{1}10$] directions. A cross section of several of these surface formations by a (110) plane drawn as close as possible to the centers of their horizontal projections is presented in Fig. 2b. This figure also shows evidence of the pyramidal shape of the surface formations, the angle formed by a lateral face with the pyramid base being about 30° for a smooth cross-section line. In other cases, clear steplike character of the lateral face cross section is observed, the step plane making the same angle with the base plane.

A three-dimensional image of the surface region displayed in Fig. 2a is represented in Fig. 3 by means of axonometric projection. This representation shows the size and shape of elements of the surface structure in the direction perpendicular to the STM scan plane. The STM data were also treated using an algorithm for the statistical analysis of the image element size. The algorithm is based on the calculation of the image spectral density and, upon single-pass processing of the STM-image file, yields the size distribution of the image elements. A distribution density of the nanoobject lateral size was obtained by calculations using the averaged cross section of the spectral density; the result is presented in Fig. 4. As seen, the mean lateral size of the islands is 35 ± 10 nm. The algorithm employed is described in detail in [5]. The STM images were also analyzed by means of the discrete Fourier transform. To give an example, in Fig. 5 we present such a Fourier transform of the STM image shown in Fig. 2a. Note that the algorithm used includes a routine for eliminating the central peak. The Fourier image has a rhomboidal shape, which evidences the formation of nanoislands mainly with a rectangular base shape. A typical ratio of the base dimensions can be estimated from the Fourier transform data as $d_{110}/d_{1\bar{1}0} = 1.35$. This value agrees well with the result obtained by the analysis of the STM image cross sections in the [110] and [$1\bar{1}0$] directions.

Preliminary measurements of the local current–voltage characteristics over these nanometer-size surface morphological features give evidence of the semiconductor nature of the three-dimensional islands. Numerically, the *I–V* curves recorded differ from those of the bulk silicon and of the InAs/GaAs and InAs/Si quantum dots, which confirms that the material obtained has different properties than these semiconductors. Analysis of the measured local electrical characteristics will be reported in a separate publication.

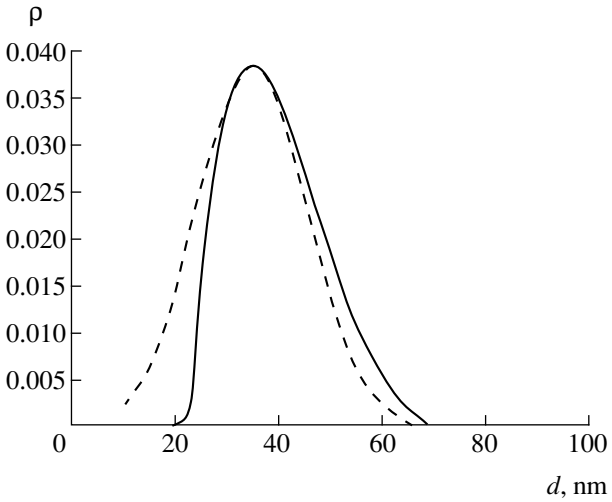

Fig. 4. Solid line: probability distribution ρ of the surface nanoobjects over their lateral size *d*; dashed line: approximation of the distribution by the Gauss function.

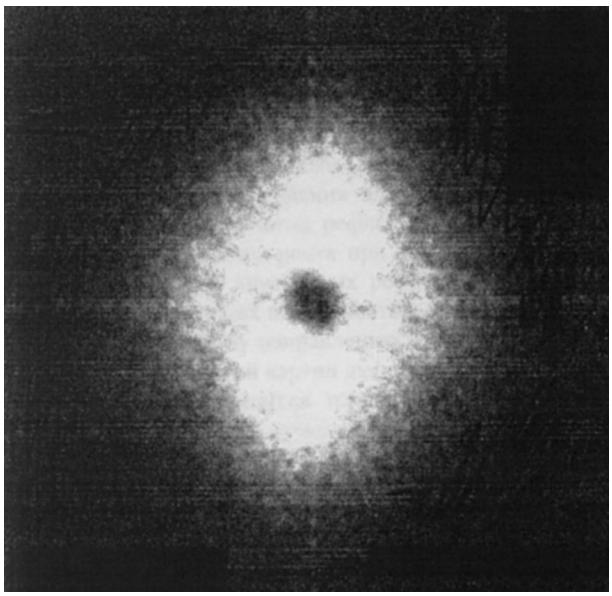

Fig. 5. A Fourier transform of the STM image displayed in Fig. 2a.

Thus, using the RHEED and STM methods, we experimentally demonstrated a principal possibility that a new nanostructured material, InSiAs solid solution, can be grown by the MBE technique on the Si(001) surface. For its structural properties, this material can find applications in different areas of modern nanotechnology, e.g., in microelectronics, biochips, etc. [6].

This work was supported in part by the INTAS Foundation (grant no. 96-0242), the Russian Foundation for Basic Research (project no. 99-02-16799), and the State Program "Promising Technologies and Devices of Micro- and Nanoelectronics" (project no. 02.04.5.1.40.E.46).

REFERENCES

1. N. N. Ledentsov, V. M. Ustinov, V. A. Shchukin, *et al.*, Fiz. Tekh. Poluprovodn. (St. Petersburg) **32**, 385 (1998) [Semiconductors **32**, 343 (1998)].
2. G. É. Tsyrlin, V. N. Petrov, N. K. Polyakov, *et al.*, Fiz. Tekh. Poluprovodn. (St. Petersburg) **33**, 1158 (1999) [Semiconductors **33**, 1054 (1999)].
3. V. N. Petrov, V. N. Demidov, N. P. Korneeva, *et al.*, Nauchn. Priborostr. **9** (1), 65 (1999).
4. A. O. Golubok, S. A. Masalov, N. B. Ponomareva, *et al.*, Poverkhnost', No. 2, 70 (1998).
5. O. M. Gorbenko, S. A. Masalov, P. A. Fridman, *et al.*, Nauchn. Priborostr. **10** (1) (2000) (in press).
6. Perspekt. Tekhnol. **7** (3) (2000) (in press).

Translated by M. Skorikov

Technical Physics Letters, Vol. 26, No. 9, 2000, pp. 785–786. Translated from Pis'ma v Zhurnal Tekhnicheskoĭ Fiziki, Vol. 26, No. 17, 2000, pp. 67–70.
Original Russian Text Copyright © 2000 by Vintizenko.

On the Possibility of Mechanical Tuning of a Periodic-Pulse Relativistic Magnetron

I. I. Vintizenko

Research Institute of Nuclear Physics, Tomsk Polytechnic University, Tomsk, Russia

e-mail: alex@atpha.npi.tpu.ru

Received February 8, 2000

Abstract—A method for the mechanical tuning of a periodic-pulse relativistic magnetron is described. The method, based on using an anode unit with the cavity edge lids having variable internal radius, allows the oscillation frequency to be varied within 8% without a significant loss in the output power. © *2000 MAIK "Nauka/Interperiodica".*

The relativistic magnetron is one of the most powerful and effective devices used in the relativistic microwave electronics [1, 2]. In recent years, devices of this type are frequently supplied from induction linac sections [3, 4]. A characteristic feature of the linac developed at the Research Institute of Nuclear Physics (Tomsk Polytechnic University) is the use of a magnetic system for the strip forming line commutation, which allows the magnetron to generate microwave pulses with a repetition rate of up to 400 Hz, highly reproducible pulse shape and amplitude (voltage, 300–400 kV; current, 3–4 kA), and a microwave power up to ~200 MW.

This paper describes a rather simple method for mechanical tuning of the oscillation frequency of a relativistic magnetron and presents the results of experimental implementation of this method. The experiments were performed with a 6-cavity anode unit for a 10-cm wavelength range (S-band) with the internal and external cavity radii of R_1 = 2.15 cm and R_2 = 4.3 cm, respectively, and a height of 7.2 cm. In relativistic magnetrons, the working frequencies cannot be separated between different oscillation modes with the aid of couplers. The task is usually solved by using the anode units with edge lids. For this reason, the classical method of mechanical frequency tuning by varying the edge cavity size is inapplicable. The magnetron frequency can only be changed through variation of the cathode radius [5]. For example, an increase in the cathode radius of the given magnetron from 0.9 to 1.1 cm changed the magnetron oscillation frequency from 2840 to 2790 MHz (i.e., by less than 2%). When the cathode radius decreased below 0.9 cm or increased above 1.1 cm, the output power dropped because of a mismatch between the impedances of magnetron and linac. Levine *et al.* [6] reported on the results of testing a system for the mechanical tuning of relativistic magnetrons but presented no description of the patented device.

We have used an anode unit with cavity edge lids, which differs from both open and half-open units (the latter provided with a single edge lid with the internal radius R_1 = 2.15 cm) by variation of the alternating electric field along the cavity length, with the antinode at the center and the nodes at the edges [7]. The microwave radiation is extracted from one of the cavities via a coupling slot with a smooth waveguide junction.

The presence of the electric field antinode created favorable conditions for the H_{10} wave excitation in the waveguide junction. The closed anode unit ensures, in addition to better mode frequency separation, the higher output parameters [8] because of a greater internal Q-value. As is known [7], the total efficiency of a magnetron is determined by the formula

$$\eta = \eta_1\eta_2 = \frac{Q_0}{Q_0 + Q_1}\eta_2, \qquad (1)$$

where η_2 is the electron efficiency; η_1 is the magnetron circuit efficiency; and Q_0 and Q_1 are the internal and external Q values, respectively.

The resonance mode frequencies of the close (f_1) and open (f_2)anode units obey the following relationship:

$$f_1 = f_2\sqrt{1 + (c/f_02h)^2}, \qquad (2)$$

where c is the speed of light.

In this work, the frequency of the relativistic magnetron was tuned by using the cavity edge lids with variable internal radius. The amplitude and frequency parameters of the output microwave pulses were measured using detector tubes and tunable filters with a bandwidth of ~17 MHz on a 3 dB level.

Plots of the relative microwave power, middle frequency, and internal Q value as functions of the edge lid radius are presented in the figure (the lid radius was varied either on both edges or on one edge with the other fixed at R_1 = 2.15 cm). As seen from these data, it is expedient to change the radius of both edge lids in

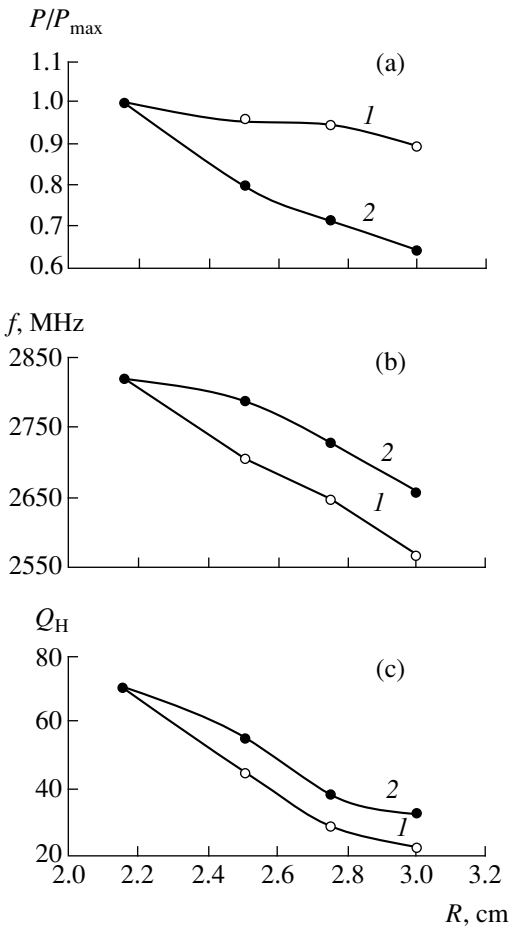

Fig. 1. The plots of (a) relative microwave power, (b) middle frequency, and (c) internal Q value as functions of the internal radius of the cavity edge lid for the lid radius varied (*1*) on one edge (with the other fixed at $R_1 = 2.15$ cm) and (*2*) simultaneously on both edges.

order to provide for the magnetron frequency tuning within 8%. In this case, a decrease in the output power, related to a change in the external Q value determined as $Q_2 = Q_1Q_0/(Q_1 + Q_0) = f/\Delta f$ (Δf is the generation bandwidth), would not exceed 10%. When the internal radius of only one lid is changed, the tuning range decreases and the power drop increases. This is explained by a displacement of the alternating electric field antinode away from the geometric center of the anode unit, a decrease in the energy transfer between electrons and the microwave field, and a violation of the conditions for the H_{10} wave excitation in the waveguide junction.

Thus, it is possible to control the frequency of microwave oscillations generated by a relativistic magnetron within 8% without a significant loss in the output power by changing the internal radius of the cavity edge lids.

The author is grateful to G.P. Fomenko for fruitful discussions and to A.I. Mashchenko for his help in conducting experiments.

REFERENCES

1. G. Bekefi and T. J. Orzechovski, Phys. Rev. Lett. **37** (6), 379 (1976).
2. V. E. Nechaev, A. S. Sulakshin, M. I. Fuks, and Yu. G. Shteĭn, in *Relativistic High-Frequency Electronics* (Inst. Prikl. Fiz. Akad. Nauk SSSR, Gorkiĭ, 1979), pp. 114–130.
3. V. V. Vasil'ev, I. I. Vintizenko, A. N. Didenko, *et al.*, Pis'ma Zh. Tekh. Fiz. **13** (12), 762 (1987) [Sov. Tech. Phys. Lett. **13**, 317 (1987)].
4. S. Ashly, R. Smith, N. Aiello, *et al.*, IEEE Trans. Plasma Sci. **20** (3), 344 (1992).
5. S. T. Spang, P. E. Anderson, K. O. Busly, *et al.*, IEEE Trans. Plasma Sci. **18**, 586 (1990).
6. J. S. Levine, B. D. Harteneck, and H. D. Price, in *Intense Microwave Pulsed. III. Proceedings SPIE, July, 10–12, San-Diego, 1995*, p. 74.
7. D. E. Samsonov, *The Principles of Calculation and Design of Multicavity Magnetrons* (Sov. Radio, Moscow, 1966).
8. I. I. Vintizenko, A. S. Sulakshin, and G. P. Fomenko, Pis'ma Zh. Tekh. Fiz. **13** (22), 1384 (1987) [Sov. Tech. Phys. Lett. **13**, 579 (1987)].

Translated by P. Pozdeev

Technical Physics Letters, Vol. 26, No. 9, 2000, pp. 787–788. Translated from Pis'ma v Zhurnal Tekhnicheskoĭ Fiziki, Vol. 26, No. 17, 2000, pp. 71–75.
Original Russian Text Copyright © 2000 by Makhniĭ, Sletov.

High-Temperature Edge Luminescence from Cubic Cadmium Selenide Layers

E. V. Makhniĭ and M. M. Sletov

Chernovitskiĭ State University, Chernovtsy, Ukraine

Received April 19, 2000

Abstract—High-temperature electrical and luminescent properties of β-CdSe layers synthesized by the solid-state substitution reaction were studied. In the temperature interval from 290 to 450 K, the edge emission band related to the annihilation of free excitons inelastically scattered from free charge carriers dominates in the photoluminescence spectrum. The binding energies of the excitons and optical phonons were measured. The bandgap width and the temperature coefficient of its variation were determined. *© 2000 MAIK "Nauka/Interperiodica".*

The single crystals and films of hexagonal cadmium selenide (α-CdSe) have been used for a long time as base materials for the photodetectors and light-emitting diodes operating in the visible spectral range [1–3]. The bandgap width of cadmium selenide with a cubic structure (β-CdSe) is 0.3 eV greater than that of α-CdSe, which makes it possible to shift the photosensitivity and emission peaks toward shorter wavelengths. Unfortunately, β-CdSe crystals are unstable [4], while synthesis of the epitaxial films of this single crystal type encounters considerable difficulties [3]. However, these difficulties can be obviated using the method of solid-state substitution reactions. In this case, the base substrate not only determines the structure of a converted crystal layer but produces stabilization of this layer as well [5]. It was established that the electrical and luminescent properties of the synthesized material remain unchanged upon multiply repeated thermal cycling in the 77–300 K range and upon a three-year room-temperature storage [6].

The most characteristic feature of these β-CdSe layers is the effective edge luminescence determined at 77 K by the annihilation of free excitons [6–8]. The purpose of this work was to study the features of emission from these samples at high temperatures.

The technology of the synthesis of cadmium selenide layers belonging to a cubic crystalline modification was described elsewhere [5, 6]. The electrical and luminescent properties of the β-CdSe samples were studied in the temperature interval from 290 to 450 K, with the upper limit determined by the melting temperature of indium contacts applied to the samples for measuring the β-CdSe layer resistance. The temperature dependence of the sample resistance was used to determine the activation energies of the electrically active donor centers. The activation energies were found to be 20 and 150 meV, in agreement with the depths of energy levels formed by the selenium vacancies and cadmium interstitials, respectively [2, 3]. The presence of these centers is quite natural for the β-CdSe layers obtained by annealing the ZnSe crystals in saturated cadmium vapors [5, 6]. In addition, the formation of these point defects is favored by the isovalent impurity representing residual zinc atoms from the base substrate [9]. Note also that both the absolute values of the sample resistances and their temperature profiles remained unchanged after several cycles of measurement in the 290–450 K range.

The photoluminescence (PL) spectra were measured using a conventional lock-in detection scheme and a wavelength modulation mode. The emission was excited by radiation of an N_2-laser, the excitation level L being controlled with the aid of a set of calibrated light filters. The PL spectra were plotted as the spectral density of photons N_ω versus the photon energy $\hbar\omega$. In the temperature interval studied, these curves have the shape of a single broad band possessing, like the spectrum measured at 77 K [6, 7], the following properties. First, the band maximum shifts toward lower photon energies when the excitation level L increases. Second, the emission intensity I depends on the excitation level L by the power law: $I \sim L^{1.5}$. Third, the low-energy wing of the band $N_\omega(\hbar\omega)$ has an exponential shape and the slope of the straight lines plotted in the $\mathrm{Ln}N_\omega$ versus $\hbar\omega$ coordinates at T = const decreases with increasing L. This behavior is characteristic of the annihilation of excitons inelastically scattered from free charge carriers [10]. Therefore, the main edge PL from β-CdSe at high temperatures (up to T = 450 K) is also of the exciton nature. This result is of interest from the standpoint of obtaining a laser effect in the samples studied. This possibility is suggested by data [10] on the electron-stimulated room-temperature (300 K) emission in the exciton band of β-CdSe crystals.

According to the proposed model, the intensity of the exciton–phonon interaction at L = const must

1063-7850/00/2609-0787$20.00 © 2000 MAIK "Nauka/Interperiodica"

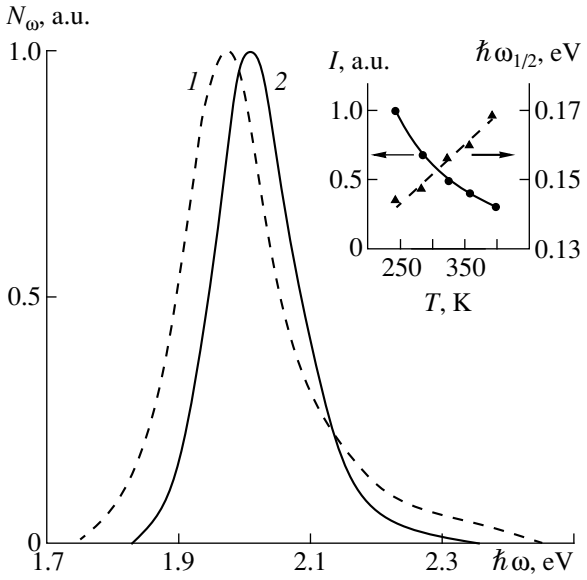

Fig. 1. The PL spectra of β-CdSe layers measured at (*1*) 290 and (*2*) 450 K. The inset shows temperature variation of the intensity I and halfwidth $\hbar\omega_{1/2}/E$ of the emission band.

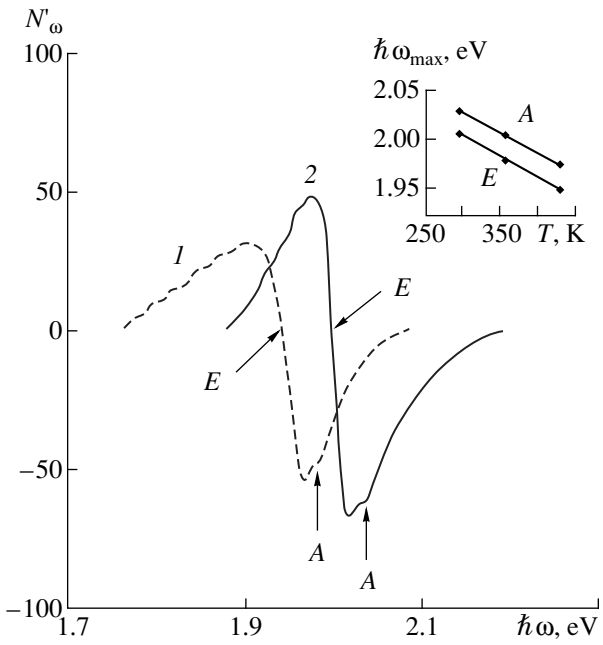

Fig. 2. Wavelength-modulated PL spectra of β-CdSe layers measured at (*1*) 290 and (*2*) 450 K; the inset shows the temperature dependence of the position of exciton (*E*) and interband (*A*) components.

increase with the temperature. This, in turn, has to be manifested by increasing band width in agreement with the inset in Fig. 1. Note a stronger temperature dependence in the high-energy wing of the band. This is explained by the fact that the band consists of two components, the exciton *E* and the interband *A* [6]. In the usual PL spectra, the latter component can be separately observed only at low temperatures; at high temperatures, this contribution can be determined by calculation. However, this problem can be readily solved by measuring the wavelength-modulated emission spectra. As seen from Fig. 2, a maximum of the exciton band corresponds to the point of intersection with the energy axis, while the interband component is manifested by a clearly pronounced shoulder on the high-energy wing of the spectrum. The bandgap width is 2.03 eV at 300 K and varies with temperature at a rate of 4.4×10^{-4} eV/K. As seen from the inset in Fig. 2, the plots of the energy positions of the exciton and interband components versus temperature are parallel, while the exciton energy is ~25 meV. The equidistant (spaced by ~20 meV) bending points observed on the low-temperature wing in the PL spectrum measured in the wavelength-modulated mode can be attributed to the energies of longitudinal optical phonons.

It should be noted that the above parameters of β-CdSe were determined for the first time. Note also a relatively weak temperature dependence of the *E*-band intensity in the 290–450 K range (see the inset in Fig. 1). This behavior indicates that the β-CdSe layers offer a promising source of radiation (including stimulated emission) with an energy of about 2 eV at high temperatures.

REFERENCES

1. S. V. Svechnikov, *The Elements of Optoelectronics* (Sov. Radio, Moscow, 1971).
2. A. V. Simashkevich, *Heterojunctions Based on II–VI Semiconductor Compounds* (Shtiintsa, Kishinev, 1980).
3. I. P. Kalinkin, V. B. Aleskovskiĭ, and A. V. Simashkevich, *Epitaxial Films of II–VI Compounds* (Leningr. Gos. Univ., Leningrad, 1978).
4. *Physics and Chemistry of II–VI Compounds*, Ed. by M. Aven and J. S. Prener (North-Holland, Amsterdam, 1967; Mir, Moscow, 1970).
5. M. M. Berezovskiĭ and E. V. Makhniĭ, Fiz. Tverd. Tela (St. Petersburg) **38** (2), 646 (1996) [Phys. Solid State **38**, 358 (1996)].
6. O. V. Makhniĭ and M. M. Sl'otov, Nauk. Visnik Chernivets. Univ., Fiz. **32**, 67 (1998).
7. O. V. Makhniy, M. M. Slyotov, and B. M. Sobischanskiy, in *Abstracts of Third International School-Conference "Physical Problems in Material Science of Semiconductors," Chernivtsi, Ukraine, 1999*, p. 142.
8. V. P. Makhniĭ, O. V. Makhniĭ, M. M. Sl'otov, and I. M. Fodchuk, Nauk. Visnik Chernivets. Univ., Fiz., Élektron. **66**, 20 (1999).
9. Koh Era and D. V. Langer, J. Lumin. **1**–**2**, 514 (1970).
10. V. S. Vavilov and É. L. Nolle, in *Exciton in Semiconductors* (Nauka, Moscow, 1968).

Translated by P. Pozdeev

Technical Physics Letters, Vol. 26, No. 9, 2000, pp. 789–790. Translated from Pis'ma v Zhurnal Tekhnicheskoĭ Fiziki, Vol. 26, No. 17, 2000, pp. 76–80.
Original Russian Text Copyright © 2000 by Dzhibuti, Dolidze.

On the Possible Spatial Orientation of a Radiation-Induced Defect Responsible for the 1.0-eV IR Absorption Band in Gallium Arsenide

Z. V. Dzhibuti and N. D. Dolidze

Tbilisi State University, Tbilisi, Georgia

Received March 13, 2000

Abstract—A possible spatial orientation of a radiation-induced defect responsible for the 1.0-eV IR absorption band in gallium arsenide was determined. The defect has a dipole moment oriented close to the ⟨110⟩ crystallographic axis and possesses a ⟨111⟩ atomic symmetry. Taking into account these results and assuming a divacancy character of this defect (suggested by some researchers), the defect is assigned a mixed divacancy structure of the $V_{Ga} + V_{As}$ type. *© 2000 MAIK "Nauka/Interperiodica".*

The properties of defects responsible for an absorption band observed at 1.0 eV in the IR spectrum of irradiated GaAs (referred to below as the 1.0-eV band) were studied in a number of works [1–7]. It was established that this defect has a relatively simple structure (not containing atoms of foreign impurity), and the 1.0-eV absorption band is due to intracenter transitions of the level–level type. Investigations on the GaAs samples oriented in the directions of three principal crystallographic axes showed that intensity of the 1.0-eV band in irradiated GaAs depends on the sample orientation [5], which is indicative of a certain spatial orientation of the corresponding defect. It was suggested [4–7] that the defect represents a divacancy, although it was still unclear which of the three types of divacancies possible in GaAs is realized. The purpose of this work was to study effects of the uniaxial sample compression and the light polarization on the 1.0-eV IR absorption band in order to determine the spatial orientation of the defect responsible for this band, which would allow us to judge on the defect structure.

The samples of *p*- and *n*-GaAs doped with Zn and Te to a concentration from 1×10^{16} to 1×10^{17} cm^{-3} were cut so as to be oriented strictly in the directions of three principal crystallographic axes ⟨111⟩, ⟨110⟩, and ⟨100⟩ (referred to below as the ⟨111⟩, ⟨110⟩, and ⟨100⟩ samples). The samples were bombarded at $T = 300$ K by electrons with the energy $E = 3$ MeV to a total fluence of $\Phi = 1 \times 10^{18}$ cm^{-2}. The IR absorption spectra were measured at 77 K, with a primary monochromatic beam incident on the samples perpendicularly to the principal crystallographic axes, along which the samples were uniaxially compressed. The primary monochromatic beam was either unpolarized (Π_0) or polarized perpendicularly ($\Pi_\perp$) or parallel ($\Pi_\parallel$) to the direction of compression. A change in the absorption coefficient was determined as $\Delta\alpha = \alpha_b - \alpha_c$, where α_b and α_c are the absorption coefficients of the bombarded and control samples, respectively.

The typical spectral dependences of $\Delta\alpha$ for uniaxially compressed ($\approx 1.5 \times 10^8$ Pa) *n*-GaAs samples of three various orientations, measured using the primary beams of various polarizations, are presented in the figure (a similar pattern was observed for the *p*-GaAs samples). As seen, the ⟨111⟩ samples exhibit the same intensity of absorption in the region of 1.0 eV (no dichroism), while the two other samples show a dichroic effect. In the ⟨110⟩ sample, the $\Delta\alpha_{1.0}$ values for $\Pi_\perp$ and $\Pi_\parallel$ coincide while differing from the $\Delta\alpha_{1.0}$ value for Π_0. In the ⟨100⟩ sample, the $\Delta\alpha_{1.0}$ value slightly decreases for the $\Pi_\parallel$ and somewhat increases for the $\Pi_\perp$ orientation as compared to the value for Π_0. Thus, a radiation-induced defect responsible for the absorption band at 1.0 eV exhibits the property of dichroism and, hence, is a complex defect of the dipole type. Qualitatively the same pattern is observed in the absence of the uniaxial compression. Application of pressure increases both $\Delta\alpha$ and the dichroism over the entire spectral range studied.

In the analysis of the obtained results, we proceed from the following commonly accepted concepts [8–11]: (a) the maximum absorption of a dipole is observed in the case when the electric vector of the incident light wave is parallel to the dipole axis, while a perpendicular polarization corresponds to the minimum absorption; (b) a change in the spectra measured for various polarizations of the incident light is related to a difference in the number of defects absorbing at the corresponding orientations. As seen from the figure, the ⟨111⟩ sample exhibit the same $\Delta\alpha_{1.0}$ value irrespective of the polarization. This implies that the dipole axis is parallel to the direction of light incidence (i.e., lies in the (111) plane. In the ⟨110⟩ sample, the $\Delta\alpha_{1.0}$ value exhibits the same change for both $\Pi_\perp$ and $\Pi_\parallel$, which

1063-7850/00/2609-0789$20.00 © 2000 MAIK "Nauka/Interperiodica"

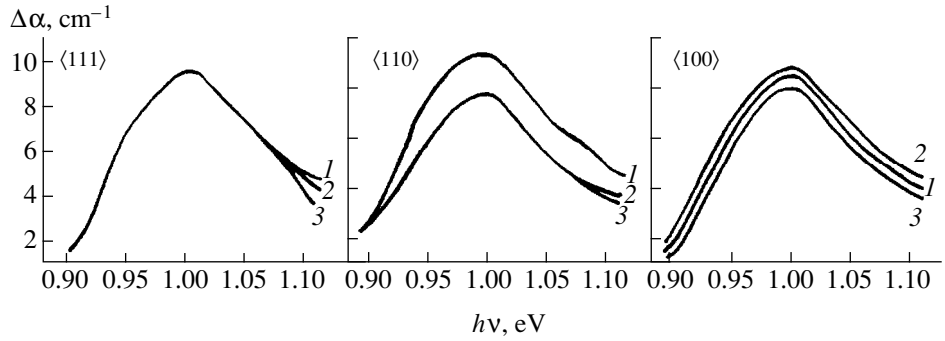

The plots of differential absorption coefficient $\Delta\alpha$ versus quantum energy for uniaxially compressed ($\approx 1.5 \times 10^8$ Pa) *n*-GaAs in three orientations measured with the incident light of various polarizations: (*1*) Π_0; (*2*) $\Pi_\perp$; (*3*) $\Pi_\parallel$.

indicates that the dipole axis makes an angle of ~45° with the (110) plane. Finally, in the ⟨100⟩ sample, the $\Delta\alpha_{1.0}$ value slightly decreases for the $\Pi_\parallel$, and somewhat increases for the $\Pi_\perp$ orientation as compared to the value for Π_0, which is possible only provided that the dipole axis makes a small angle with the direction of light incidence. From this, we infer that the dipole axis must be simultaneously lying in the (111) plane, making an angle of 45° with the (110) plane and making a small angle with the (100) plane. These requirements are satisfied for a direction close to the ⟨110⟩ crystallographic axis.

This orientation of a dipole-type complex was reported for divacancies in Si and Ge [8–11], where the defect was assigned a ⟨111⟩ atomic symmetry. The properties of divacancies in these materials are very much like those of the defect in GaAs studied in this work. If the defect in GaAs is a divacancy [4–7], then divacancies with similar properties would be characteristic of the crystals with a face-centered cubic lattice. Then, it would be reasonable to suggest that the defect responsible for the IR absorption band at 1.0 eV in GaAs possesses the same ⟨111⟩ atomic symmetry as that of its analogs in Si and Ge. In GaAs, this orientation is possible for divacancies of a single type, representing a mixed $V_{Ga} + V_{As}$ vacancy complex. Indeed, the dichroism in monoatomic semiconductors is revealed upon an electron reorientation of the defect, which requires a uniaxial compression at $T = 77$ K [8–11]. In contrast, a mixed divacancy in the $A^{III}B^{V}$ semiconductors must possess a dipolar moment (and, hence, exhibit dichroism) even in the absence of the uniaxial compression—in agreement with what is observed in experiment.

Thus, we have concluded that a defect responsible for the absorption band at 1.0 eV in the IR spectrum of irradiated GaAs is probably a mixed divacancy with a ⟨111⟩ atomic symmetry and a dipole moment oriented close to the ⟨110⟩ crystallographic direction.

REFERENCES

1. E. Yu. Brailovskiĭ, V. N. Brudnyĭ, M. A. Krivov, and V. B. Red'ko, Fiz. Tekh. Poluprovodn. (Leningrad) **6** (10), 2075 (1972) [Sov. Phys. Semicond. **6**, 1768 (1972)].
2. V. N. Brudnyĭ, E. Yu. Brailovskiĭ, M. A. Krivov, and V. B. Red'ko, Izv. Vyssh. Uchebn. Zaved., Fiz., No. 10, 118 (1974).
3. K. P. Aref'ev, V. N. Brudnyĭ, D. L. Budnitskiĭ, *et al.*, Fiz. Tekh. Poluprovodn. (Leningrad) **13** (6), 1142 (1979) [Sov. Phys. Semicond. **13**, 669 (1979)].
4. N. Kh. Pambukhchyan, Candidate's Dissertation in Mathematical Physics (Kiev, Yerevan, 1983).
5. Z. V. Dzhibuti, N. D. Dolidze, G. L. Ofengeĭm, *et al.*, Fiz. Tekh. Poluprovodn. (Leningrad) **21** (5), 930 (1987) [Sov. Phys. Semicond. **21**, 567 (1987)].
6. Z. V. Dzhibuti, Candidate's Dissertation in Mathematical Physics (Tbilisi, 1989).
7. Z. V. Dzhibuti and N. D. Dolidze, Pis'ma Zh. Tekh. Fiz. **17** (5), 41 (1992) [Sov. Tech. Phys. Lett. **17**, 172 (1991)].
8. L. J. Cheng, J. C. Corelli, J. W. Corbet, and G. D. Watkins, Phys. Rev. **152**, 761 (1966).
9. A. H. Kalma and J. C. Corelli, Phys. Rev. **173**, 734 (1968).
10. A. B. Gerasimov, N. D. Dolidze, R. M. Donina, *et al.*, Phys. Status Solidi A **70**, 23 (1982).
11. A. B. Gerasimov, N. D. Dolidze, G. L. Ofengeĭm, *et al.*, Vopr. At. Nauki Tekh., Ser.: Fiz. Radiats. Povrezhd. Radiats. Materialoved. **4** (5), 65 (1982).

Translated by P. Pozdeev

Technical Physics Letters, Vol. 26, No. 9, 2000, pp. 791–793. Translated from Pis'ma v Zhurnal Tekhnicheskoĭ Fiziki, Vol. 26, No. 17, 2000, pp. 81–87.
Original Russian Text Copyright © 2000 by Kuz'min.

The Pinning Enhancement upon the Magnetic Flux Trapping in the Clusters of a Normal Phase with Fractal Boundaries

Yu. I. Kuz'min

Ioffe Physicotechnical Institute, Russian Academy of Sciences, St. Petersburg, 194021 Russia

Received April 26, 2000

Abstract—The phenomenon of magnetic flux trapping in a hard superconductor with the normal phase clusters acting as the pinning centers is considered. The critical current distribution for the clusters of an arbitrary fractal dimension is determined. The fractal character favors the magnetic flux trapping, thus increasing the critical current. © *2000 MAIK "Nauka/Interperiodica".*

Isolated clusters of a normal phase in superconductors are capable of acting as the effective pinning centers [1–4]. The geometry and probabilistic behavior of these clusters may significantly affect the dynamics of a trapped magnetic flux and the values of critical currents, especially in the case when the normal phase clusters possess fractal boundaries [5–7].

Let us consider a superconducting film containing columnar inclusions of a normal phase oriented perpendicularly to the film surface. Cooled to a temperature below the critical level in a magnetic field directed along the axis of orientation of the normal phase inclusions, this superconducting structure will be characterized by a two-dimensional distribution of the trapped magnetic flux. If the relative film surface occupied by the normal phase is below the percolation threshold for the magnetic flow transfer, the fraction of the superconducting phase would exceed the percolation threshold. This implies that a superconducting percolation cluster carrying a transport current exists in the film surface.

When the current increases, the trapped flux remains unchanged until vortices begin to separate from the clusters in which the pinning force is smaller than the Lorentz force created by the transport current. As the magnetic flux separates from the pinning centers, each vortex has to cross the superconducting cluster. Initially, the vortices would pass along the weak junctions connecting clusters of the normal phase. In the high-temperature superconductors characterized by a small coherence length, these junctions readily form at various structural defects [8–11]. Moreover, the magnetic field decreases the coherence length further [12], thus favoring the formation of additional weak junctions. In traditional superconductors with large coherence lengths, weak junctions form due to the proximity effect at the sites characterized by a minimum distance between the neighboring normal phase clusters.

Depending on the configuration of weak junctions, each cluster of the normal phase is characterized by its own critical current contributing to the overall statistical distribution. A change in the trapped magnetic flux $\Delta\Phi$ as a result of the transport current action is proportional to the total number of the normal phase clusters having the critical currents below a preset level I. Then, a relative change in the magnetic flux can be expressed in terms of the accumulated probability function $F = F(I)$ describing distribution of the critical cluster currents

$$\frac{\Delta\Phi}{\Phi} = F(I), \quad F(I) = \mathbf{P}\{\forall I_j < I\}, \tag{1}$$

where $\mathbf{P}$ is the probability that the critical current I_j of an arbitrary jth cluster is below a preset upper limit I.

At the same time, the greater the size of a normal phase cluster, the greater the number of weak junctions occurring on the perimeter of the surrounding superconducting space and, hence, the smaller the critical current of this cluster. If the concentration of weak junctions per unit perimeter length is the same for all clusters, the critical current I is inversely proportional to the cluster perimeter length P: $I \propto 1/P$. Since the magnetic flux trapped in a cluster is proportional to the cluster area A, a change in the trapped flux can be expressed through the accumulated probability function $W = W(A)$ describing distribution of the normal phase cluster areas:

$$\frac{\Delta\Phi}{\Phi} = 1 - W(A), \quad W(A) = \mathbf{P}\{\forall A_j < A\}, \tag{2}$$

where $\mathbf{P}$ is the probability that the area A_j of an arbitrary jth cluster does not exceed a preset upper limit A. The function $W = W(A)$ of the cluster area distribution can be determined from the results of a geometric-probabilistic analysis of electron micrographs of the films [13]. For example, a practically important case of thick YBCO films with columnar defects [14] is characterized by an exponential distribution

$$W(A) = 1 - \exp\left(\frac{A}{\bar{A}}\right), \tag{3}$$

where $\bar{A}$ is the average cluster area.

1063-7850/00/2609-0791$20.00 © 2000 MAIK "Nauka/Interperiodica"

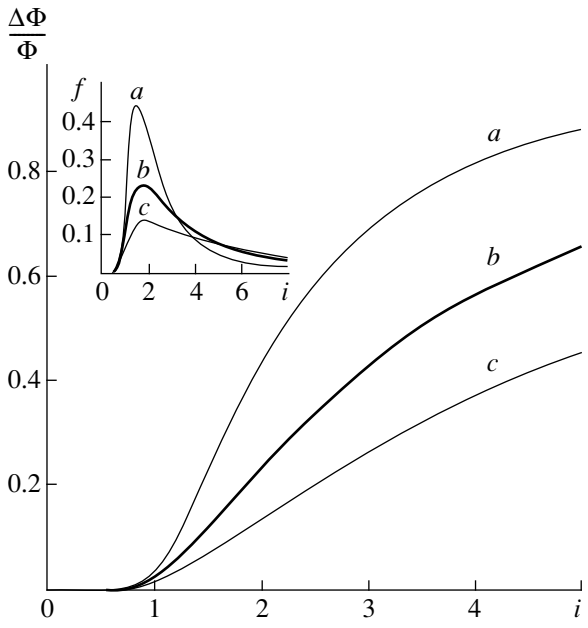

Fig. 1. The plots of a relative change in the magnetic flux versus critical current illustrating the effect of the fractal dimension of the cluster boundary on the magnetic flux trapping: $D = 1$ (*a*); 1.5 (*b*); 2 (*c*). The inset shows the corresponding probability density distributions of the critical current.

In order to establish how does the transport current affect the trapped magnetic flux, it is necessary to find a relationship between distributions of the critical currents (1) and areas (2) of the normal phase clusters. It was recently demonstrated [7] that the fractal properties of the normal cluster boundaries determine to a considerable extent the magnetic flux dynamics in superconductors. A relationship between the perimeter length and the area of a fractal cluster can be expressed as

$$P \propto A^{\frac{D}{2}}, \tag{4}$$

which leads the following expression for the critical current: $I = \alpha A^{-D/2}$, where α is the form factor and D is the fractal dimension of the cluster boundary.

Relationship (4) agrees with the generalized Euclid theorem [15], according to which the ratios of the corresponding measures reduced to the same dimension are equal. This yields a relationship $P^{1/D} \propto A^{1/2}$ that must be valid for both Euclidean ($D = 1$) and fractal ($D > 1$) geometric objects. Since the cluster boundary is a fractal, it is the statistical distribution of cluster areas, rather than of their perimeter lengths, that represents a fundamental property for determining the critical current distribution. The topological dimension of the perimeter (equal to unity) does not coincide with its Hausdorff–Bezikovich dimension (greater than unity). Therefore, the perimeter length of a fractal cluster is not a strictly determined value and depends on the accuracy of measurement. At the same time, the topological dimension of the cluster area coincides with the Hausdorff–Bezikovich dimension (both values equal to 2). This means that the area bounded by a fractal curve is a finite and well-determined quantity.

Speaking of the geometric characteristics of the normal phase clusters, we consider cross sections of the extended columnar defects by a plane carrying the transport current. Therefore, analysis of the geometric-probabilistic properties of a normal phase cluster can be restricted (despite this cluster representing a self-affine fractal [16]) to considering only such a cross section in which the cluster boundaries are statistically self- similar.

According to the initial relationships (1) and (2), a critical current distribution for the exponential cluster area distribution function (3) can be expressed as

$$F(i) = \exp\left(-\left(\frac{2+D}{2}\right)^{\frac{2}{D}+1}\frac{1}{i^{2/D}}\right), \tag{5}$$

where $i = I/I_c$, $I_c = \left(\frac{2}{2+D}\right)^{\frac{2+D}{2}}$, and $\frac{\alpha}{(\bar{A})^{D/2}}$ is the critical current for transition into a resistive state. Equation (5) fully describes effect of the transport current upon the trapped magnetic flux (Fig. 1). Once the accumulated probability function is known, we may determine the probability density $f(i) = dF/di$ for the critical current distribution

$$f(i) = \frac{2}{D}\left(\frac{2+D}{2}\right)^{\frac{2}{D}+1} i^{-\left(\frac{2}{D}+1\right)} \exp\left(-\left(\frac{2+D}{2}\right)^{\frac{2}{D}+1}\frac{1}{i^{2/D}}\right).$$

A relative change in the trapped flux $\Delta\Phi/\Phi$ determined by Eq. (5) is proportional to the density n of vortices separated from the pinning centers by the current i:

$$n(i) = \frac{B}{\Phi_0}\int_0^i f(i')di' = \frac{B}{\Phi_0}\frac{\Delta\Phi}{\Phi},$$

where B is the magnetic induction, $\Phi_0 \equiv hc/(2e)$ is the magnetic flux quantum, h is the Planck constant, c is the speed of light, and e is the electron charge. As seen from Fig. 1, the vortex separation becomes significant only for $i > 1$, that is, when the sample exhibits transition into a resistive state. Using Fig. 1, we may follow the effect of the cluster fractal dimension on the magnetic flux trapping. Curve *a* describes the Euclidean clusters ($D = 1$), while curve *c* corresponds to the maximum possible fractal dimension ($D = 2$) of the cluster boundary (this case is illustrated, for example, by the Peano curves). Independently of the cluster geometry and morphology, a curve representing the relationship between $\{\Delta\Phi/\Phi$ vs. $i\}$ and i will always fall within the region between the two limiting curves. An example is offered by curve *b* corresponding to $D = 1.5$.

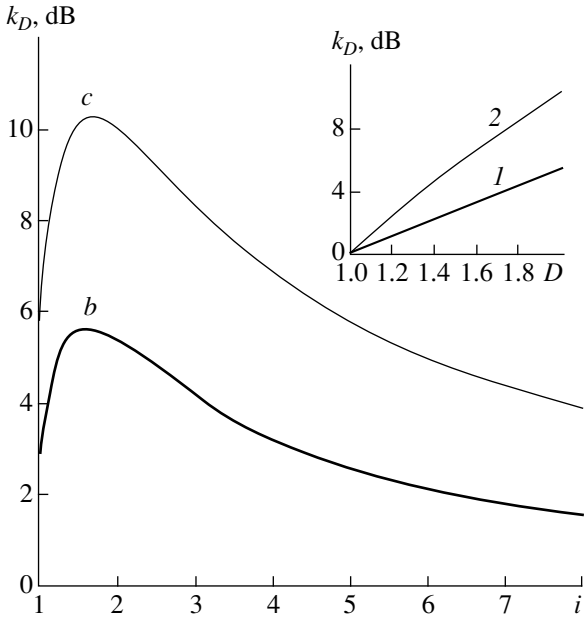

Fig. 2. Plots of the pinning enhancement coefficient k_D versus critical current I for various fractal dimensions of the cluster boundaries: D = 1.5 (*b*); 2 (*c*). Curve *c* exhibits a maximum at i = 1.6875. The inset shows the plots of k_D versus cluster fractal dimension D for a fixed transport current: i = 1 (*1*) and 1.6875 (*2*).

Figure 1 illustrates an important consequence of Eq. (5), according to which the fractal character favors the magnetic flux trapping, thus hindering its separation from the pinning centers and increasing the critical current (a maximum current that the sample can conduct remaining in the superconductive state). As seen in the inset to Fig. 1, an increase in the fractal dimension leads to smearing of the critical current distribution, whereby the curves expand toward greater i values. The pinning enhancement caused by the fractal character can be characterized by the enhancement coefficient $k_D \equiv \Delta\Phi(D = 1)/\Delta\Phi(D)$ representing a relative decrease in the fraction of a magnetic flux separated from fractal clusters with the dimension D compared to the case of Euclidean clusters (D = 1).

Figure 2 shows the plots of the pinning enhancement coefficient versus the transport current and the fractal dimension. As seen, the maximum pinning enhancement, attained at the fractal dimension D = 2, is $\max_D k_D = k_2 = \exp((4i - 3.375)/i^2)$. Note that the pinning enhancement coefficient characterizes the properties of a superconductor in the range of currents corresponding to a resistive state ($i > 1$). At lower currents, the trapped magnetic flux remains virtually unchanged (Fig. 1) because no pinning centers with sufficiently small critical currents are available and no vortex separation takes pace. As in any hard superconductor, the presence of dissipation in the resistive state is not yet indicative of the phase coherency breakage. Some dissipation related to the magnetic flux always takes place in any hard superconductor (at any transport current) even in the case of a very strong pinning. For this reason, the critical current in these materials cannot be determined as the maximum dissipation-free current. The superconductive state is broken only when the current reaches a level at which the dissipation increases in the avalanche manner because of the thermomagnetic instability development.

Thus, a fractal character of cluster boundaries increases the magnetic flux trapping. This phenomenon opens new possibilities for increasing the critical currents of composite superconductors by optimization their geometry and morphology characteristics.

REFERENCES

1. T. Higuchi, S. I. Yoo, and M. Murakami, Phys. Rev. B **59** (2), 1514 (1999).
2. E. Mezzetti, R. Gerbaldo, G. Ghigo, *et al.*, Phys. Rev. B **60** (10), 7623 (1999).
3. Ch. Jooss, R. Warthmann, H. Kronmüller, *et al.*, Phys. Rev. Lett. **82** (3), 632 (1999).
4. S. N. Dorogovtsev and Yu. I. Kuzmin, Phys. Lett. A **170** (3), 245 (1992).
5. R. B. Laibowitz, R. F. Voss, and E. I. Alessandrini, in *Percolation, Localization and Superconductivity*, Ed. by A. M. Goldman and S. A. Wolf (Plenum, New York, 1984), NATO ASI Ser., Ser. B **109**, 145 (1984).
6. C. J. Olson, C. Reichhardt, and F. Nori, Phys. Rev. Lett. **80** (10), 2197 (1998).
7. Yu. I. Kuzmin, Phys. Lett. A **267** (1), 66 (2000).
8. H. Küpfer, Th. Wolf, A. A. Zhukov, and R. Meier-Hirmer, Phys. Rev. B **60** (10), 7631 (1999).
9. H. R. Kerchner, D. R. Norton, A. Goyal, *et al.*, Phys. Rev. B **60** (9), 6878 (1999).
10. V. V. Bryksin, A. V. Goltsev, S. N. Dorogovtsev, *et al.*, J. Phys.: Condens. Matter **4** (7), 1791 (1992).
11. R. Haslinger and R. Joynt, Phys. Rev. B **61** (6), 4206 (2000).
12. J. E. Sonier, R. F. Kiefl, J. H. Brewer, *et al.*, Phys. Rev. B **59** (2), R729 (1999).
13. Yu. I. Kuz'min and I. V. Pleshakov, Pis'ma Zh. Tekh. Fiz. **25** (12), 30 (1999) [Tech. Phys. Lett. **25**, 475 (1999)].
14. Yu. I. Kuz'min, I. V. Pleshakov, and S. V. Razumov, Fiz. Tverd. Tela (St. Petersburg) **41** (10), 1739 (1999) [Phys. Solid State **41**, 1594 (1999)].
15. B. B. Mandelbrot, *The Fractal Geometry of Nature* (Freeman, San Francisco, 1982).
16. B. Mandelbrot, in *Fractals in Physics*, Ed. by L. Pietronero and E. Tosatti *et al.* (North-Holland, Amsterdam, 1986; Mir, Moscow, 1988).

Translated by P. Pozdeev

Technical Physics Letters, Vol. 26, No. 9, 2000, pp. 794–796. Translated from Pis'ma v Zhurnal Tekhnicheskoĭ Fiziki, Vol. 26, No. 17, 2000, pp. 88–93.
Original Russian Text Copyright © 2000 by Bespalov, Markov, Proskurovskiĭ, Ryzhov, Turchanovskiĭ.

The Effect of Reflected Beam Electrons on the Distribution of Energy Deposited in a Target

V. I. Bespalov, A. B. Markov, D. I. Proskurovskiĭ, V. V. Ryzhov, and I. Yu. Turchanovskiĭ

Institute of High-Current Electronics, Siberian Division, Russian Academy of Sciences, Tomsk, Russia
Tomsk Polytechnical University, Tomsk, Russia

Received March 9, 2000

Abstract—When a solid target is irradiated by an electron beam generated in a direct-action diode and transported to the target in a magnetic guide field, an important role belongs to electrons returned to the target as a result of multiple reflections from the target and the accelerating field region. The energy spectrum of electrons incident on the target and the deposited energy depth profile the target were studied by the Monte-Carlo method. An algorithm for calculating these characteristics was developed, based upon the method of separating the total electron flux into components with respect to the multiplicity of crossing of the target–vacuum interface. © *2000 MAIK "Nauka/Interperiodica".*

Thermal regimes established during the electron-beam processing of solid surfaces are usually calculated assuming that a target is bombarded by monoenergetic electrons. The electron energy E_0 is determined by the accelerating voltage U_0; the amount of incident electrons is determined by the accelerating diode current at a given time. However, experimental setups for the pulsed electron-beam surface processing frequently employ the beams generated in a direct-action diode and transported to a target in a strong magnetic guide field [1, 2]. Under these conditions, electrons reflected from the target move in the magnetic field, reverse their direction and, accelerated in the diode field, return to the target. As a result, the diode produces, in addition to the flux of primary electrons, a flux of *n*-fold-reflected electrons possessing broad angular and energy distributions. Since the fraction of energy reflected from materials with large atomic numbers *Z* amounts to 40%, the effect of the multiply reflected electrons is significant and must be taken into account in determining thermal parameters of the electron-beam surface processing.

In solving this problem, any functional of the radiation field in the target can be represented as expansion with respect to the multiplicity of the target–vacuum interface crossing by electrons [3]. In particular, the total deposited energy profile $D(z)$ in the target can be presented as

$$D(z) = \sum_{n=0}^{N} D_n(z), \tag{1}$$

where $D_n(z)$ is a partial deposited energy profile of electrons reflected and returned to the target *n* times and *N* is the maximum number of sequential reflections possible in the system. In a planar geometry,

$$D_n(z) = 2\pi \int_0^{E_0} dE' \int d\cos\theta' j_n^+(E', \cos\theta') \times D_0(E', \cos\theta'; z), \tag{2}$$

where $j_n^+(E, \cos\theta)$ is the differential current density with respect to the angle and energy for electrons upon the *n*-fold reflection (the surface source) and $D_0(E, \cos\theta; z)$ is the Green function describing the deposited energy distribution with depth *z* in the target due to electrons with the energy *E* incident at an angle θ (without reflections). The current densities of the incident (j_n^+) and reflected (j_n^-) electrons are related by the recurring relationships

$$j_n^+(E, \cos\theta) = j_n^-(E, \cos(\pi - \theta)),$$
$$j_n^-(E, \cos\theta) = 2\pi \int_E^{E_0} dE' \int d\cos\theta' \times (\eta((E', \cos\theta') \longrightarrow E, \cos\theta) j_{n-1}^+(E', \cos\theta')), \tag{3}$$

where η is the differential electron reflection coefficient with respect to angle and energy.

Effects of the multiply reflected electrons on the spatial distribution of energy deposited in the target were studied by the Monte-Carlo method [4]. The electron trajectories were simulated in a planar geometry of the accelerating gap–target system for an accelerating diode dc voltage of U_0 = 100–500 kV and the absorbing

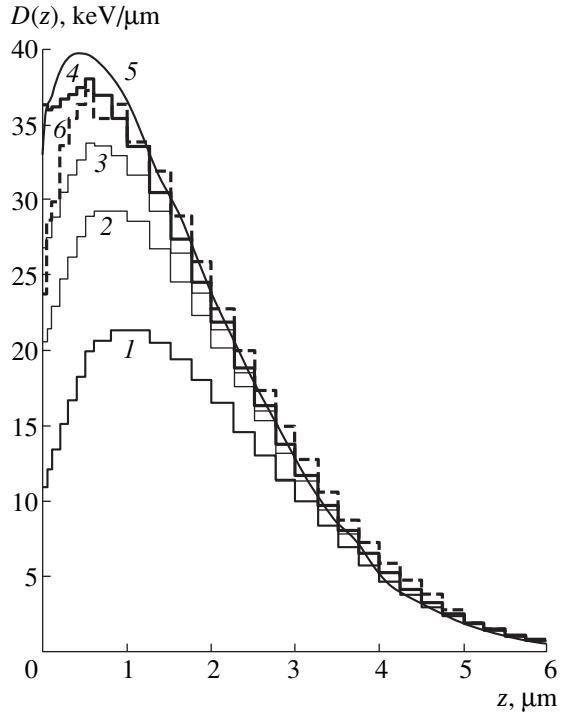

Fig. 1. The deposited energy profiles in a Pt target bombarded with an electron beam accelerated at U_0 = 100 kV, calculated by the Monte-Carlo method (*1*) ignoring reflections and (*2–4*) with an allowance for the contribution of reflected electrons: (*2*) n = 1; (*3*) 2; (*4*) all reflected electrons; (*6*) the approximation of normal incidence of all multiply reflected electrons (dashed). Curve *5* was calculated for n = 3 by the method described in [5].

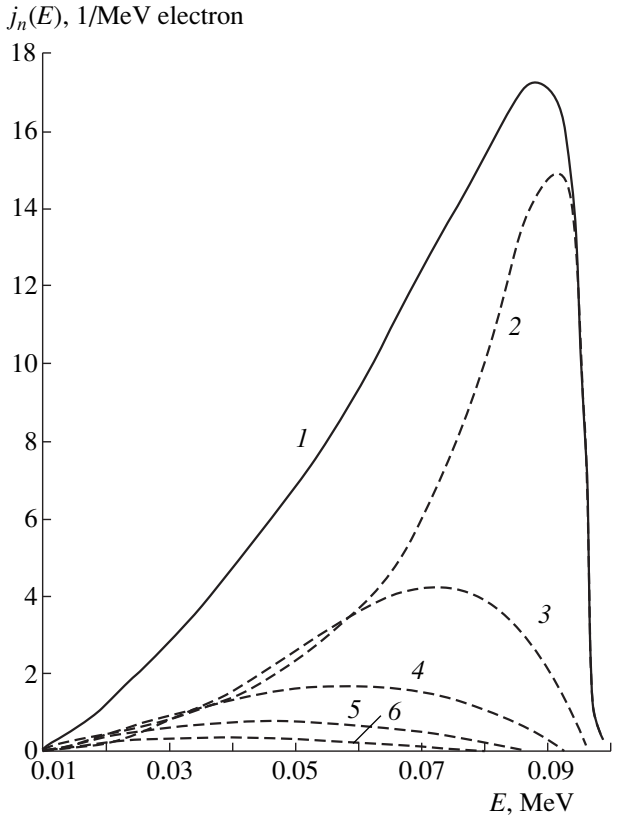

Fig. 2. Energy spectra of the current density of electrons upon reflected from a Pt target surface: (*1*) total spectrum of all reflected electrons; (*2–6*) partial spectra j_n for n = 1–5, respectively.

targets of Al, Fe, and Pt. Note that the Monte-Carlo simulation allows contributions from each group of the multiply reflected electrons with different n values to be separated and convergence of the series (1) to be analyzed.

As an example, Fig. 1 shows the deposited energy profiles in a Pt target calculated with an allowance for the contribution of multiply reflected electrons in a beam accelerated at U_0 = 100 kV. As seen, the return of reflected electrons not only increases the total energy deposited in the target but markedly changes the energy profile shape as well. Indeed, the energy deposited in a near-surface layer of platinum increases by a factor exceeding 3, while the energy deposited in deeper layers remains unchanged. Note that the contributions of electrons upon sequential reflections to the total deposited energy rapidly drop with increasing *n.* In Fig. 1, these contributions are 65, 18, 9, and 0.6 keV for n = 0, 1, 2, and 6, respectively. The results of our calculations showed that, for the diode energies in the range U_0 = 100–500 kV, making an allowance for the electrons reflected 3–4 times from target materials with large Z and 2–3 times from the materials with medium Z is sufficient to evaluate the total deposited energy with an accuracy not worse than 10–15%.

A change in shape of the deposited energy profile is related to modification of the energy spectrum of electrons incident on the target, whereby reflected low-energy electrons are added. Figure 2 shows the spectra of electrons for n = 1–5 crossings of the target–vacuum interface and the total spectrum of electrons reflected from a Pt target. The results of calculations showed that, provided reflected particles return to the target, the total spectrum of electrons incident on the target comprises a flux of the primary (nonreflected) electrons with the energy E_0 and the reflected electrons possessing lower energies.

Equations (1)–(3) can be used to obtain approximate analytical estimates of the contribution of reflected electrons on the deposited energy profile in the target [5]. These calculations can be performed, for example, with neglect of the angular distribution of incident electrons, assuming that the particles move perpendicularly to the target surface ("to and fro" approximation). In this calculation, the electron energies were measured in units of the incident energy, while the depths were expressed in units of the extrapolated range R_{ex}. It was suggested that the spectrum of reflected electrons $j_1(E/E_0)$ and the Green function $D_0(E/E_0, z/R_{ex})$ are universal cures independent of the incident electron energy [6–8]. In this

case, the spectra of reflected electrons $j_n(E/E_0)$ of any order n and their contributions to the total deposited energy can be calculated by the method described previously [5]. The results of our calculations for $n = 3$ are presented in Fig. 1 (curve *5*). Note that this curve is normalized to the primary electron energy E_0.

Figure 1 also shows a histogram (dash curve *6*) representing the results of calculations performed in the "to and fro" approximation, where the energies of electrons in all orders of reflection and the corresponding Green functions were determined by the Monte-Carlo method. As expected, calculations using this model and, accordingly, overstate the energy deposited in deeper layers.

Thus, when a solid target is irradiated by an electron beam generated in a direct-action diode and transported to the target in a magnetic guide field, electrons multiply reflected from and returned to the target significantly modify the profile of energy deposited in the target. For this reason, thermal regimes established during the electron-beam processing of solid surfaces must be calculated using distributions determined with an allowance for the effect of multiply reflected electrons, rather than the usual distributions of thermal sources. The results of calculations using refined distributions showed that data obtained by the Monte-Carlo method differ by no more than 10–15% from those calculated using the "to and fro" approximation for a finite number of reflections ($n \le 3$ for the target materials with large Z or $n \le 2$ for the materials with medium Z) with normalization to the total primary electron energy E_0. Once this accuracy is acceptable, the method described in [5] can be used to calculate the distribution of thermal sources in solving a problem of the solid target surface heating by a pulsed electron beam.

REFERENCES

1. D. S. Nazarov, G. E. Ozur, and D. I. Proskurovskiĭ, Prib. Tekh. Éksp., No. 4, 83 (1996).
2. G. Mueller, G. Schumacher, D. Strauss, *et al.*, in *Proceedings of the 11th International Conference on High-Power Particle Beams (BEAMS'96), Prague, 1996*, p. 267.
3. A. M. Kol'chuzhkin and V. V. Uchaĭkin, *Introduction to the Theory of Particles Penetrating Through Substances* (Atomizdat, Moscow, 1978).
4. V. I. Bespalov, V. V. Ryzhov, and I. Yu. Turchanovskiĭ, Pis'ma Zh. Tekh. Fiz. **24** (1), 45 (1998) [Tech. Phys. Lett. **24**, 20 (1998)].
5. A. B. Markov, Izv. Vyssh. Uchebn. Zaved., Fiz., No. 2, 65 (2000).
6. I. A. Abroyan, A. N. Andronov, and A. I. Titov, *Physical Principles of Electron and Ion Technology* (Vysshaya Shkola, Moscow, 1984).
7. S. Schiller, U. Heisig, and S. Panzer, *Elektronenstrahltechnologie* (Technik, Berlin, 1976; Énergiya, Moscow, 1980).
8. R. Shimizu, T. Ikuta, and K. Murata, J. Appl. Phys. **43** (10), 4233 (1972).

Translated by P. Pozdeev

Technical Physics Letters, Vol. 26, No. 9, 2000, pp. 797–798. Translated from Pis'ma v Zhurnal Tekhnicheskoĭ Fiziki, Vol. 26, No. 17, 2000, pp. 94–98.
Original Russian Text Copyright © 2000 by Trofimov.

Time-Dependent Parabolic Equations for Two-Dimensional Acoustic Waveguides

M. Yu. Trofimov

Pacific Institute of Oceanology, Far East Division, Russian Academy of Sciences, Vladivostok, 690000 Russia

e-mail: root%dan86@poi.marine.su

Received March 9, 2000

Abstract—Time-dependent parabolic equations for the amplitude of a packet of rapidly oscillating waves propagating in a two-dimensional nonstationary waveguide are derived using the multiscale method. The obtained formulas are compared to other known equations. © *2000 MAIK "Nauka/Interperiodica".*

Earlier [1, 2], time-dependent parabolic equations describing the propagation of sound in two- and three-dimensional waveguides were derived using the formal factorization of the Helmholtz operator and the multiscale method. Unlike stationary parabolic equations [3, 4], these relationships are not amplitude equations for envelopes of the wave packets but contain uninterpretable terms with integral operators. Methods used to solve such equations are inavoidably complicated.

In this paper, the generalized multiscale method [5] is used to derive time-dependent amplitude parabolic equations. In the derivation, we do not assume that the refractive index is almost constant and the density is independent of the horizontal variable, as it was adopted in [1–4]. Upon the passage to characteristic variables, the resulting equations can be solved using methods developed for the stationary equations.

We proceed from the wave equation for two-dimensional nonstationary media [6], which can be written in terms of slow variables $T = \epsilon t$, $X = \epsilon x$, and $Z = \epsilon^{1/2} z$ as

$$\epsilon^2\left(\frac{1}{\rho}p_X\right)_X + \epsilon\left(\frac{1}{\rho}p_Z\right)_Z - \epsilon^2\left(\frac{1}{\rho}n^2 p_T\right)_T = 0, \qquad (1)$$

where ϵ is the small parameter, p is the acoustic pressure, ρ is the density, $n = 1/c$ is the refractive index, and c is the speed of sound. The variables were reduced to the dimensionless form using the length ($\bar{l}$), time ($\bar{l}/\bar{c}$, where $\bar{c}$ is a typical value of the speed of sound), and density ($\bar{\rho}$, the typical value of density) scales.

Equation (1) is usually considered within a band $-H \le z \le 0$, and the particular form of boundary conditions is of no significance for our study.

Following the generalized multiscale method [5], we introduce a fast variable, $\eta = (1/\epsilon)\theta(X, Z, T)$, and postulate expansions

$$n = n_0(X, T) + \epsilon n_1(X, T, z) + \ldots,$$

$$p = p_0(X, T, Z, \eta) + \epsilon p_1(X, T, Z, \eta) + \ldots,$$

in which we explicitly show that the expansion terms are functions of the independent variables. As for the density ρ, we only assume that this quantity is independent of η, namely, $\rho = \rho(X, T)$.

Substitute these expansions into Eq. (1) and simultaneously transform partial derivatives according to

$$\frac{\partial}{\partial X} \longrightarrow \frac{\partial}{\partial X} + \frac{1}{\epsilon}\theta_X\frac{\partial}{\partial \eta}$$

using similar transformations for the derivatives with respect to Z and T. Separating coefficients at the different powers of ϵ, we obtain a set of boundary value problems indexed by the orders of parameter ϵ.

For the order $O(\epsilon^{-1})$, we obtain a relationship $(\theta_Z)^2 p_{0\eta\eta} = 0$ that can be satisfied assuming that θ is independent of Z.

For the order $O(\epsilon^0)$, we obtain the Hamilton–Jacobi equation

$$(\theta_X)^2 - \eta_0^2(\theta_T)^2 = (\theta_X + n_0\theta_T)(\theta_X - n_0\theta_T) = 0. \quad (2)$$

Further, studying waves propagating in the positive direction, we will assume that the Hamilton–Jacobi equation (2) contains only the first multiplier.

In view of formula (2), an equation obtained for the order $O(\epsilon^1)$ does not contain p_1. Substituting a solution of the form $p_0 = A(X, T, Z)\phi(\eta)$ into this equation, we obtain that, without loss in generality, we can adopt that

$\phi(\eta) = \exp(i\eta)$, $\mathrm{Im}\,\eta \geq 0$. As a result, we obtain the following equation for amplitude A:

$$2in_0\omega\frac{1}{\rho}[A_X + n_0A_T] + \left(\frac{1}{\rho}A_Z\right)_Z + \chi A = 0, \quad (3)$$

where $\omega = -\theta_T$ is the local frequency and

$$\chi = \left\{\left[\left(\frac{1}{\rho}n_0\right)_X + n_0\left(\frac{1}{\rho}n_0\right)_T\right]\omega i + 2\frac{1}{\rho}n_0n_1\omega^2\right\}. \quad (4)$$

Similar considerations applied to the order $O(\epsilon^2)$ result in the equation

$$2in_0\omega\frac{1}{\rho}[B_X + n_0B_T] + \left(\frac{1}{\rho}B_Z\right)_Z + \chi B + \mathcal{F} = 0, \quad (5)$$

where

$$\mathcal{F} = \left(\frac{1}{\rho}A_X\right)_X - \left(\frac{1}{\rho}n_0^2A_T\right)_T,$$

B is the amplitude of function p_1, and $p_1 = B(X, T)\exp(i\eta)$.

Let us compare the obtained equations to the wide-angle parabolic equation [4] in the stationary case of a harmonic time dependence $\omega = \text{const}$ and $A_T = B_T = 0$. The medium parameters are also assumed to be time-independent. In addition, we adopt that $n_0 = \text{const} = 1$ and $\rho = \text{const}$ (these assumptions were earlier used in [3, 4]). Equations (3) and (5) take the form

$$2\omega iA_X + A_{ZZ} + 2n_1\omega^2A = 0, \quad (6)$$

$$2\omega iB_X + B_{ZZ} + 2n_1\omega^2B + A_{XX} = 0. \quad (7)$$

Introducing amplitude $C = A + \epsilon B$, adding Eq. (6) to Eq. (7) multiplied by ϵ, and expressing the term A_{XX} using a derivative of Eq. (6) with respect to X, we obtain upon accomplishing transformations and neglecting terms of the order of $O(\epsilon^2)$ that

$$\left(1 + \frac{1}{4}\epsilon Q\right)C_X - i\omega\frac{1}{2}QC + \frac{1}{2}\epsilon n_{1X}C = 0, \quad (8)$$

where

$$Q = 2n_1 + \frac{1}{\omega^2}\frac{\partial^2}{\partial Z^2}.$$

The small parameter ϵ can be removed from Eq. (8) upon returning to the initial variables $z = (1/\sqrt{\epsilon})Z$ and $x = (1/\epsilon)X$ and introducing the quantity $n_1 = \epsilon n_1$. After these substitutions, the obtained equation differs only by the term $(1/2)n_{1x}C$ from a wide-angle parabolic equation with the homographic Pade approximation for the square root of Q [4]. Note that this term cannot be obtained via the formal factorization of the Helmholtz operator used in [4], because an assumption (standard for this method) of the commutativity of operator Q and differentiation with respect to x is not valid.

In underwater acoustics, Eqs. (2), (3), and (5) usually appear in a Cauchy problem with X treated as the evolutionary variable. It is convenient to solve this problem by passing to the characteristic variables s and τ specified by the conditions [7]

$$s = X, \quad \frac{dT}{ds} = n_0(s, T(s)), \quad \tau = T(0).$$

For these variables, the Cauchy problem with initial conditions specified at $X = 0$ reduces to the relationships

$$\theta(s, \tau) = \theta(0, \tau) = \theta_0(\tau),$$

$$\omega(s, \tau) = \omega(0, \tau)\exp\left(\int_0^s n_{0T}ds\right)$$

and to the sequential solution of a set of the Cauchy problems depending on the variable τ as a parameter:

$$2in_0\omega\frac{1}{\rho}A_s + \left(\frac{1}{\rho}A_Z\right)_Z + \chi A = 0, \quad A(0, \tau, Z) = A_0(\tau, Z), \quad (9)$$

$$2in_0\omega\frac{1}{\rho}B_s + \left(\frac{1}{\rho}B_Z\right)_Z + \chi B + \mathcal{F} = 0, \quad B(0, \tau, Z) = B_0(\tau, Z). \quad (10)$$

As can be easily shown, the following (with respect to the order ϵ) approximations take the same form; therefore, the scheme used to solve the problem with Eqs. (2), (3), (5) can be used for the subsequent refinement of the obtained solution. Problems (9) and (10) can be solved using the techniques developed for solution of the classical stationary narrow-angle parabolic equation [3].

This work was supported by the Russian Foundation for Basic Research, project no. 99-05-39140.

REFERENCES

1. M. D. Collins, J. Acoust. Soc. Am. **84**, 2114 (1988).
2. B. J. Orchard, W. L. Siegmann, and J. Jacobson, J. Acoust. Soc. Am. **91**, 788 (1992).
3. F. Tappert, *Wave Propagation and Underwater Acoustics*, Ed. by J. B. Keller and J. S. Papadakis (Springer-Verlag, Berlin, 1977), Lect. Notes Phys. **70** (1977).
4. R. R. Green, J. Acoust. Soc. Am. **76**, 1764 (1984).
5. A. H. Nayfeh, *Perturbation Methods* (Wiley, New York, 1973).
6. L. M. Brekhovskikh and O. A. Godin, *Acoustics of Layered Media* (Nauka, Moscow, 1989; Springer-Verlag, New York, 1990).
7. R. Courant, in *Methods of Mathematical Physics*, Vol. 2: *Partial Differential Equations* (Interscience, New York, 1962; Mir, Moscow, 1964).

Translated by A. Kondrat'ev

Technical Physics Letters, Vol. 26, No. 9, 2000, pp. 799–802. Translated from Pis'ma v Zhurnal Tekhnicheskoĭ Fiziki, Vol. 26, No. 17, 2000, pp. 99–104.
Original Russian Text Copyright © 2000 by Titov, Reznichenko, Razumovskaya, Shilkina, Dudkina.

Features of the Structure and Ferroelectric Properties of the Solid Solutions of Lead Titanate with Rare-Earth Metals

S. V. Titov, L. A. Reznichenko, O. N. Razumovskaya, L. A. Shilkina, and S. I. Dudkina

Institute of Physics, Rostov State University, Rostov-on-Don, Russia

Received April 6, 2000

Abstract—A secondary periodicity in variation of the properties of ferroelectric solid solutions of lead titanate with rare-earth metals is established. It is demonstrated that this behavior is related both to the modifying cations belonging to two natural subgroups and to the energetic features of their 4*f* levels. The extrema of the structural and ferroelectric characteristics correspond to the domains of electron instability. © *2000 MAIK "Nauka/Interperiodica".*

The group of ferroelectric (FE) materials based on lead titanate ($PbTiO_3$), including compositions with rare-earth metal (REM) atoms, have drawn considerable interest from the standpoint of both fundamental science and applications. This is explained by very special physical properties of these materials, offering a unique combination of highly anisotropic piezoelectric characteristics, low mechanical Q values, and high piezoelectric response. Possessing these properties, the lead titanate based ferroelectrics are indispensable in many applications such as the ultrasonic defectoscopy, thickness and flow rate measurements, and medical diagnostics [1]. In recent years, investigations of the $PbTiO_3$ based ferroelectric solid solutions revealed a number of new phenomena the nature of which still remains unclear. For example, solid solutions of the $Pb_{1-3/2x}(Ln)_xTi_{0.98}Mn_{0.02}O_3$ type (Ln = La, Ce, Pr, Nd, Sm, Gd) exhibit nonmonotonic variation of the piezoelectric characteristics and anisotropy of the piezoelectric response (reaching maximum in a composition with Sm [2]).

Recently [3], we have suggested for the first time that the properties of $PbTiO_3$ based ferroelectric solid solutions with REMs are affected by the electron structure of these elements. As is known, sequential filling of the 4*f* level in REMs—by half in the first subgroup including Ce, Pr, Nd, Pm, Sm, Eu, and Gd (I) and completely in the second subgroup containing Tb, Dy, Ho, Er, Tu, Yb, and Lu (II)—leads to periodicity in the variation of some properties (stability of the valence states, magnetic moments, ion color, solubility of certain solutions, stability of complex compounds, etc.). This behavior, in contrast to the general periodicity in properties underlying the entire system of elements, should be treated as a secondary phenomenon [4]. Taking this circumstance and the results reported in [2] into account, we may expect that the solid solutions with REMs of subgroup II would also exhibit a nonmonotonic variation of their characteristics, as was preliminarily reported in [3].

The purpose of this work was to study some features in the structure and ferroelectric properties of solid solutions of the $Pb_{1-x}(Ln)_xTiO_{3-x/2}$ (**1**) and $Pb_{1-3/2x}(Ln)_xTiO_3$ (**2**) types ($x = 0.04$). We aimed at finding the characteristics exhibiting periodicity of the secondary type mentioned above and establishing the role of defectness (nonstoichiometry) of the solid solutions and their preparation conditions in this periodicity.

The samples of polycrystalline solid solutions of types **1** and **2** were prepared using a conventional ceramic technology (solid-state synthesis at $T_1 = 850$°C and $T_2 = 1240$°C for $\tau_1 = 10$ h and $\tau_2 = 2$ h, respectively, followed by sintering at $T_{sint} = 1130$–1220°C for 2 h). The sample structures were studied by X-ray diffraction on a DRON-3.0 diffractometer using Mn-filtered FeK_α radiation. The lattice parameters (c, a), volumes (V_1), and deformations (c/a) of a unit cell of the solid solutions were determined with high precision by the techniques described in [5]. The degree of structure perfection was assessed by halfwidths of the X-ray diffraction lines (b_{002}) and the values of microdeformation ($\Delta d/d_{111}$).

The ferroelectric properties were studied using the samples having a disk shape (diameter, 10 mm; thickness, 1 mm) with silver electrodes deposited onto the flat surfaces. The samples were polarized by exposure for 40 min at 140°C to an applied electric field with a strength of 5 kV/cm in a liquid poly(ethylenesiloxane) medium. The polarized samples were characterized by the following parameters: relative permittivity before

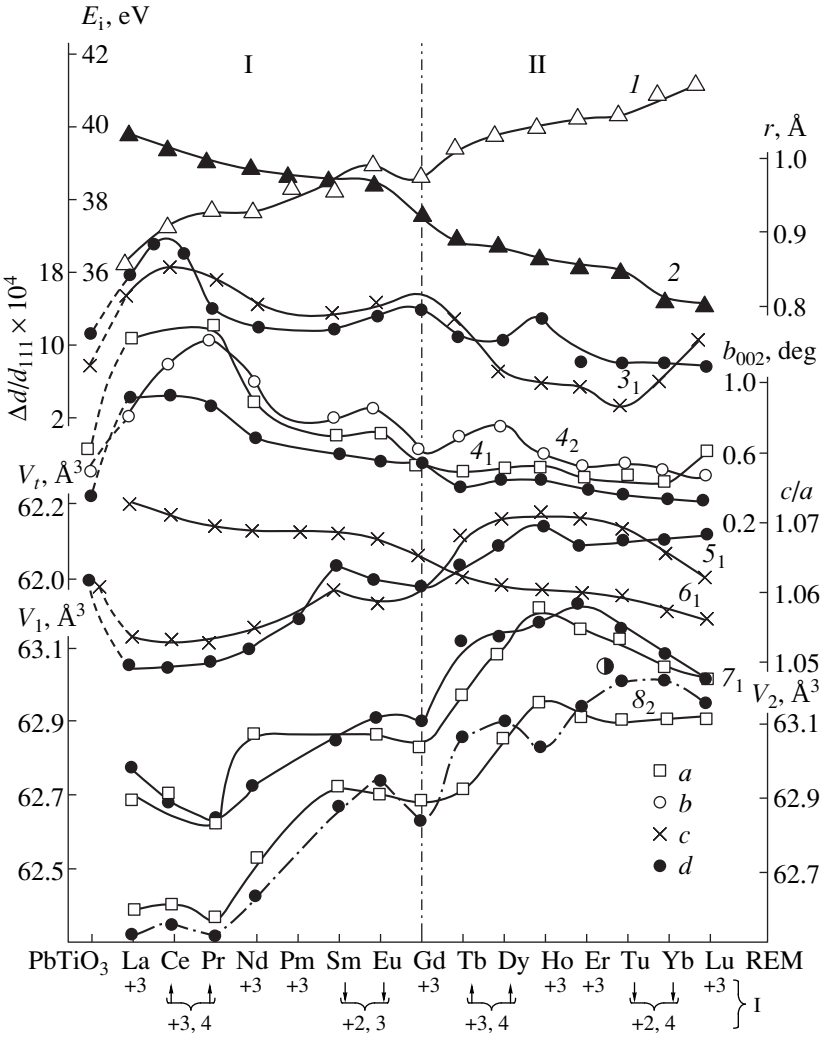

Fig. 1. Variation of the properties and structural parameters of lead titanate based solid solutions containing REMs (with the atomic number increasing from La to Lu): (*1*) E_i; (*2*) *r*; (3_1) $\Delta d/d_{111}$; (4_1, 4_2) b_{002}; (5_1) *c*/*a*; (6_1) V_t; (7_1) V_1; (8_2) V_2 (subscripts 1 and 2 indicate the solid solution type). The samples were sintered at T_{sint} = 1130 (a); 1160 (b); 1170 (c); 1220°C (d). I: realized valences.

($\varepsilon/\varepsilon_0$) and after ($\varepsilon_{33}^T/\varepsilon_0$) polarization; piezoelectric modulus (d_{33}); electromechanical coupling coefficient of the thickness oscillation mode (K_t).

The experimental results are summarized in Figs. 1 and 2. As the atomic number of the REM component increases in the series of elements from La to Lu, the structural parameters, the degree of surface perfection, and the dielectric and ferroelectric properties of the $PbTiO_3$ based solid solutions of both types vary in a nonmonotonic manner. Note that this behavior is most pronounced in the solid solutions of type 2 with vacancies in the *A*-sublattice, which were sintered at a maximum temperature. The oscillating character is superimposed onto increasing V_1 and decreasing b_{002} and $\Delta d/d_{111}$ values, showing alternating maxima and minima with gradually decreasing "amplitude" and "period" of these oscillations. In each of the subgroups I and II, the parameters exhibit either two maxima (V_1, $\Delta d/d_{111}$, d_{33}, K_t) or a single maximum (*c*/*a*), sometimes with an additional peak corresponding to Gd (b_{002}, $\varepsilon_{33}^T/\varepsilon_0$). The positions of these maxima coincide with the positions of anomalies observed in behavior of the characteristics of REMs with increasing atomic number, namely, the regions of a nonmonotonic decrease in the ion radius *r* (accompanying the "lanthanide contraction") and the periods of an increase in the ionization energy (E_i) $R^0 \longrightarrow R^{3+}$ or a change in stability of the valence states (Fig. 1).

These characteristics of REMs are determined, in turn, by special features of their electron structures: (i) nonmonotonic filling of the deep nonvalent 4*f* level; (ii) proximity of the 4*f* and 5*d* electron energies facilitating the *f*–*d* transitions (which explains the easy realization of valences different from +3); (iii) dependence of the binding energy of the 4*f* electrons on their number [this energy grows as the 4*f* level occupation

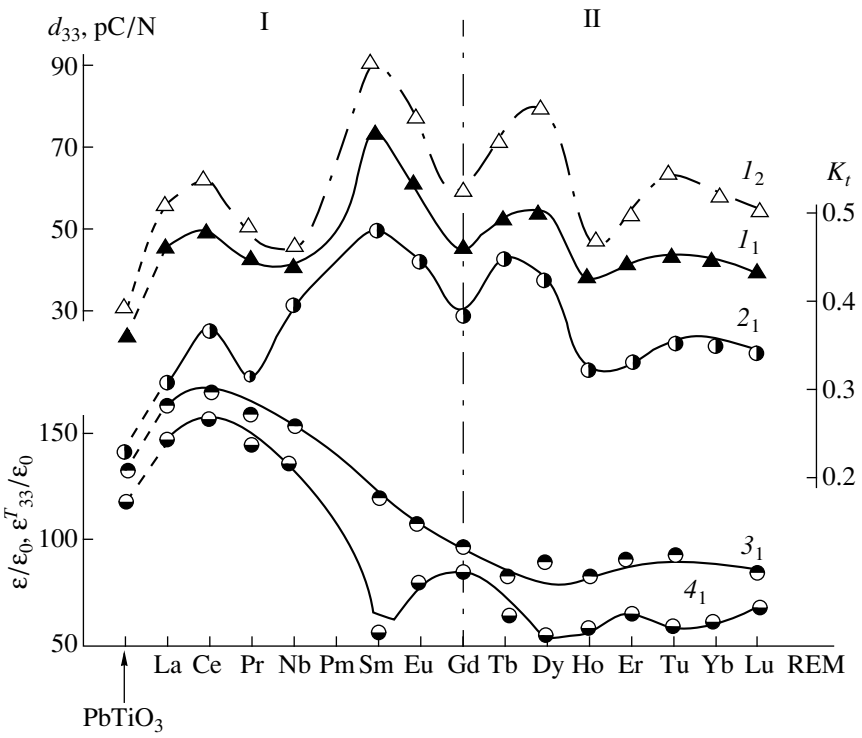

Fig. 2. Variation of the properties and structural parameters of lead titanate based solid solutions containing REMs (with the atomic number increasing from La to Lu): (1_1, 1_2) d_{33}; (2_1) K_t; (3_1) $\varepsilon/\varepsilon_0$; ($4_1$) $\varepsilon^T_{33}/\varepsilon_0$ (subscripts 1 and 2 indicate the solid solution type). The samples were sintered at T_{sint} = 1220°C.

increases to half (7 electrons) and then to complete (14 electrons), the most stable configurations being p (La), f^7 (Gd), and f^{14} (Lu)]; (iv) effective screening of the 4f electron orbitals from external fields by the $5s^2$–$4sp^6$ electron shells (this factor determines small influence of the coordination surrounding on the states arising from the $4f^n$ configuration). These and some other features account for the 4f electron configuration being a factor determining the properties not only of REMs proper, but of their compounds and complexes as well.

The above considerations indicate that behavior of the structural and physical parameters in the series of solid solutions containing REMs from subgroups I and II is also determined by special features of the electron structure of the corresponding REMs (even despite their small relative content). The observed periodicity in variation of the properties studied is related not only to the REMs being divided into two natural subgroups, but (judging from a nonmonotonic variation of the parameters inside each group) to the energetic features of their 4f levels as well. Exactly following these features, the periodicity is manifested by maxima in the characteristics falling within the domains of electron instability (Ce, Pr–Sm, Eu and Tb, Dy–Tm, and Yb).

An interesting general trend in the series of solid solutions studied is the tendency of V_1 to increase despite a decrease both in the ion radius of REM and in the theoretically calculated unit cell volumes V_t (Fig. 1). This is probably explained by the fact that only the first REMs (possessing small ion radii) in these series can build into the A-sublattice (V_1 slightly decreases), whereas the other REMs of subgroup I are redistributed between A- and B-sublattice sites. The REMs of subgroup II (possessing ion radii close to or smaller than 0.9 Å) mostly occupy the B-sublattice sites, which leads to an excess of the B-cations and their competition with Ti (resulting in separation of the impurity phases such as $LnPb_2O_7$). This arrangement of REMs is permitted by the conditions of existence of the perovskite type structure ($r_A \geq 0.90$ Å; $0.51 \leq r_B \leq 1.1$ Å; $r_A \geq r_B$ [5]) and is confirmed by the fact of increasing perfection of the solid solution structure (with decreasing b_{002} and $\Delta d/d_{111}$) on the passage from La to Lu, which can be related to the ion radius of REM approaching that of Ti (0.64 Å) and to the concentration of REMs of subgroup II in the lattice decreasing as a result of the impurity phase separation.

The general trends in variation of the solid solutions with REMs of subgroup II are the same as those observed for subgroup I, which implies that the effect of REMs on the properties of lead titanate based ferroelectric solid solutions is independent of the lattice sites occupied by these ions in oxides with a perovskite

structure. The laws established in this work can be used in the development of ferroelectric materials for piezoelectric transducers.

The work was supported by the Russian foundation for Basic Research, project no. 99-02-17575.

REFERENCES

1. A. Ya. Dantsiger, O. N. Razumovskaya, L. A. Reznichenko, *et al.*, in *High-Efficiency Piezoceramic Materials: A Reference Book* (Kniga, Rostov-on-Don, 1994).
2. T. Hiroshi *et al.*, J. Acoust. Soc. Am. **72** (4), 1114 (1982).
3. S. V. Titov, O. N. Razumovskaya, L. A. Reznichenko, *et al.*, in *Proceedings of the 15th All-Russia Conference on Physics of Ferroelectrics (VKS-XV), Rostov-on-Don, 1999*, p. 209.
4. V. I. Semishin, *Periodic System of Chemical Elements* (Khimiya, Moscow, 1972).
5. E. G. Fesenko, *Perovskite Family and Ferroelectricity* (Atomizdat, Moscow, 1972).

Translated by P. Pozdeev

Technical Physics Letters, Vol. 26, No. 9, 2000, pp. 803–805. Translated from Pis'ma v Zhurnal Tekhnicheskoĭ Fiziki, Vol. 26, No. 17, 2000, pp. 105–110.
Original Russian Text Copyright © 2000 by Grigor'ev, Makarov, Yakovlev.

The Avalanche Ionization Rate in Argon and Krypton Measured at the Shockwave Mach Numbers Close to the Flow Instability Development Threshold

P. V. Grigor'ev, Yu. P. Makarov, and V. I. Yakovlev

Institute of Theoretical and Applied Mechanics, Siberian Division, Russian Academy of Sciences, Novosibirsk, Russia

Received April 17, 2000

Abstract—The ionization rates of argon and krypton were measured in a relaxation zone behind the shockwave front for the Mach numbers corresponding to stable flow regimes close to the threshold for development of the flow instability of types I and II. The experimental rates of the avalanche ionization exceed theoretical predictions. It is suggested that the discrepancy is related to the existence of an additional channel for the energy transfer between particles. *© 2000 MAIK "Nauka/Interperiodica".*

As is known, the existing model describing the ionization kinetics behind the shockwave front in monoatomic gases [1, 2] cannot explain the anomalous effects or instabilities observed within certain intervals of the Mach number [3–12]. There were attempts at taking into account an increased number of the elementary processes involving metastable atoms and/or molecular ions [6] and a change in the relative contributions of collisional and radiative processes [7], which attribute the instability effects to the formation of additional channels for the energy transfer between particles. However, no direct experimental manifestations (except for the very fact of instability development) of the additional energy transfer mechanisms were observed, and only some indirect evidence was considered.

In particular, increased electron temperature (close to that behind the shockwave front) in the final stage of relaxation in argon was reported in [13, 14]. At the same time, the activation energy determined [15] from the ionization rate measured in the initial stage of the avalanche development was markedly lower than expected (excitation energy), which could not be explained within the framework of the commonly accepted model. Thus, there are significant discrepancies in the description of the ionization kinetics behind the shockwave front in monoatomic gases.

We propose a new approach to this problem, which reveals manifestations of the additional mechanisms of the energy transfer by directly comparing the experimental and theoretical values of the avalanche ionization rate. The latter value is calculated using an equation of the electron energy balance with an allowance for the known temperature variation of the avalanche ionization rate. We have studied the process under conditions closely approaching the threshold of the domain of instability development, assuming that the flow parameters still vary in a regular manner.

The experiments were conducted in a shockwave tube [8, 9] with an internal diameter of 76 mm and a low-pressure compartment with a length of 4.2 m using heated helium as a buffer gas. The electron density was measured by an interference technique with photoelectric signal registration. The measurements in argon were performed using radiation with a wavelength of 10.6 μm, while the measurements in krypton were effected simultaneously at 0.63 and 1.15 μm that allowed a change in the atomic density to be determined as well. The relative content of molecular impurities in argon and krypton was 2×10^{-4} and 10^{-5}, respectively.

The measured electron density profiles $n_e(t)$ were used to calculate the ionization rate (or the electron source S_e, in terms and notation of [2]) in an elementary volume of the medium behind the moving shockwave front. Taking into account that $S_e = dn_e u/dt$ and using conservation laws in the one-dimensional form, we obtain

$$S_e = \{1 - 2\alpha E_1/[5kT_1 + m_a V^2(1 - 4(\rho_1/\rho_2)^2)]\} \times (\rho_1/\rho_2)(dn_e/dt), \quad (1)$$

where E_1 is the ionization energy, α is the degree of ionization, ρ is the gas density, m_a is the atomic mass, and V is the shockwave velocity (subscript "1" refers to parameters in front of the shockwave). The derivative dn_e/dt is determined by directly differentiating the experimentally measured $n_e(t)$ profile.

1063-7850/00/2609-0803$20.00 © 2000 MAIK "Nauka/Interperiodica"

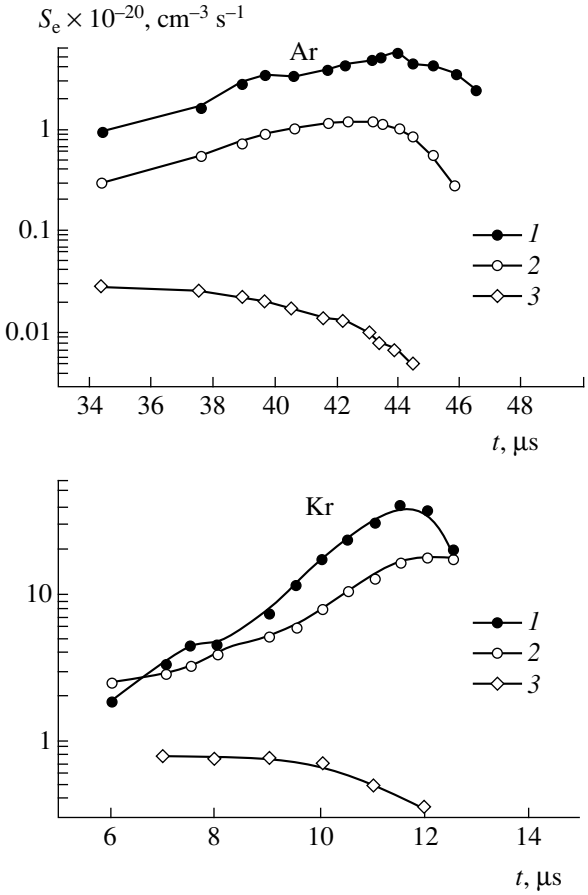

Time variation of the avalanche ionization rate behind the shockwave front in argon (M = 11.3; P_1 = 5 Torr) and krypton (M = 11.4; P_1 = 14 Torr): (*1*) experiment; (*2*) theory. Curves *3* show the rate of ionization by interatomic collisions calculated using the atomic temperatures determined from the energy integral.

Taking into account the quasi-stationary conditions, the electron temperature is determined by the local energy balance:

$$1.5kT_eS_e = Q_{el} - Q_{in}, \qquad (2)$$

where Q_{in} is the rate of the electron energy loss due to inelastic collisions (excitation and ionization events) and Q_{el} is the rate of heating due to elastic collisions with atoms (indicated below by subscript "a") and/or ions (subscript "i"). In the region of the avalanche ionization, where the role of interatomic collisions is negligibly small, the electron energy losses can be represented in the form of a sum $Q_{in} = E_1S_e + Q_R + Q_{st}$, with the three terms representing ionization, radiation, and excitation. According to [16], the heating rate is expressed as

$$Q_{el} = 1.5k(T_a - T_e)n_e2(m_e/m_a)(\nu_{ea} + \nu_{ei}),$$

where the ν_{ea} and ν_{ei} are the frequencies of elastic electron–atom and electron–ion collisions, respectively, determined by the corresponding cross sections σ:

$$\nu_{ea} = n_a(8\pi m_e/kT_e)^{1/2}\sigma_a(T_e),$$

$$\nu_{ei} = n_i(8\pi m_e/kT_e)^{1/2}\sigma_i(T_i).$$

The temperature dependence of σ_{ea} and σ_{ei} is known (see, e.g., [3, 4]).

Thus, using the energy balance equation (2) and the integral form of the energy conservation law

$$(T_a + \alpha T_e)/T_1 = 1 - 2\alpha E_1/5kT_1 + M^2[1 - (\rho_1/\rho_2)^2]/3 \equiv T_{a0} \qquad (3)$$

(M being the shockwave Mach's number), we obtain an equation for determining the electron temperature and the S_e value:

$$(1 + \alpha)T_e + [(1.5T_e + E_1)S_e + Q_R + Q_{st}] \times T_e^{3/2}/(An_e^2\ln\Lambda + Bn_en_a\sigma_a(T_e)T_e^2) = T_{a0}.$$

Here, $S_e = \beta n_e n_a[1 - n_e^2/n_aK(T_e)]$; $\beta(T_e)$ and $K(T_e)$ are the rate constants of the ionization rate and ionization equilibrium, respectively; A and B are constants depending on the gas type; and $\ln\Lambda$ is the Coulomb logarithm. The temperature dependence of the ionization rate constant $\beta(T_e)$ was calculated in the instantaneous ionization approximation [3, 4]. Taking into account a special structure of terms for the inert gases, we may put $Q_{st} = 0$ [2]. Under our experimental conditions, we may also use the approximation of $Q_R = 0$.

The results of our experiments are presented in the figure by curves *1* showing an S_e distribution behind the shockwave front in argon (M = 11.3; P_1 = 5 Torr) and krypton (M = 11.4; P_1 = 14 Torr) determined using Eq. (1). The values of $S_e = \beta n_e n_a[1 - n_e^2/n_aK(T_e)]$ calculated using T_e determined from Eq. (4) are depicted by curves *2*. For the comparison, curves *3* show the rates of ionization by interatomic collisions calculated using the atomic temperatures determined from the energy integral (3). With the latter (rather insignificant) correction, the measured S_e values correspond to the avalanche (electron–atom) ionization mechanism.

The comparative data indicate that the measured rate of the avalanche ionization exhibits a significant (severalfold for argon and more than twofold for krypton) excess over the calculated values determined within the framework of the commonly accepted model of the electron energy balance. This discrepancy cannot be related to the initial assumptions ($Q_{st} = 0$, $Q_R = 0$) since other radiation and excitation conditions would only increase the difference.

An analysis of a possible role of the boundary layer development in the shockwave tube channel indicates that an increase in the flow velocity may decrease the S_e value measured. Estimates obtained using a specially developed method for an argon flow (with a laminar

boundary layer) showed that this decrease in S_e cannot exceed 20% at almost unchanged calculated values. The measurements in krypton (possessing a shorter relaxation zone) showed that distribution of the gas density coincides with the calculated profile to within the experimental error. Therefore, the boundary layer effects can be also neglected. Estimates of the influence of uncertainty in the ionization coefficient (e.g., the values reported in [3] are 1.8 times those used in [2]) indicated that possible variations in β may increase the discrepancy by 25–36% (toward greater S_e values). A correction for the refined value of the Coulomb logarithm in the region of small Λ [16] also slightly (by 5–7%) increases the difference.

Thus, an excess in the avalanche ionization rate is observed in both gases studied. Since no ionization mechanisms were proposed as alternative to the avalanche development (consistent with a high density of electrons compared to the concentration of impurities, metastable particles, molecular ions, etc.), the discrepancy can be explained only by the presence of an additional channel for the energy transfer between particles leading to an increase in the electron temperature and, hence, in the avalanche ionization rate.

The work was supported by the Russian foundation for Basic Research, project nos. 97-01-00772 and 00-01-00829.

REFERENCES

1. P. E. Oettinger and D. Bershader, AIAA J. **5**, 1625 (1967).
2. L. M. Biberman, A. Kh. Mnatsakanyan, and I. T. Yakubov, Usp. Fiz. Nauk **102**, 431 (1970) [Sov. Phys. Usp. **13**, 728 (1970)].
3. I. I. Glass and W. S. Liu, J. Fluids Mech. **84** (1), 55 (1978).
4. I. I. Glass, W. S. Liu, and F. C. Tang, Can. J. Phys. **55**, 1269 (1977).
5. G. I. Mishin, A. P. Bedin, N. I. Yushchenkova, *et al.*, Zh. Tekh. Fiz. **51**, 2315 (1981) [Sov. Phys. Tech. Phys. **26**, 1363 (1981)].
6. N. I. Yushchenkova, G. I. Mishin, and O. R. Roshchin, Pis'ma Zh. Tekh. Fiz. **11**, 517 (1985) [Sov. Tech. Phys. Lett. **11**, 215 (1985)].
7. G. K. Tumakaev, in *High-Temperature Gas Dynamics, Shockwave Tubes, and Shockwaves* (ITMO, Minsk, 1983), pp. 154–160.
8. P. V. Grigor'ev, Yu. P. Makarov, and G. A. Pozdniakov, in *CD Rom Proceedings of the 8th International Symposium on Flow Visualization, 1994* (Levrotto and Bella, Torino, 1998), p. 53.1.
9. G. K. Tumakaev and Z. A. Stepanova, Zh. Tekh. Fiz. **52**, 2305 (1982) [Sov. Phys. Tech. Phys. **27**, 1420 (1982)].
10. P. V. Grigor'ev, in *Proceedings of the 2th International Conference on Experimental Fluid Mechanics* (Levrotto and Bella, Torino, 1994), p. 772.
11. G. K. Tumakaev, Z. A. Stepanova, and P. V. Grigor'ev, Zh. Tekh. Fiz. **64** (4), 46 (1994) [Tech. Phys. **39**, 373 (1994)].
12. G. K. Tumakaev, Z. A. Stepanova, and B. B. D'yakov, Zh. Tekh. Fiz. **62** (11), 25 (1992) [Sov. Phys. Tech. Phys. **37**, 1060 (1992)].
13. R. I. Soloukhin, Yu. A. Yacobi, and V. I. Yakovlev, Arch. Mech. **26**, 637 (1974).
14. C. O. Weiss and B. Kotzan, Appl. Phys. **7**, 203 (1975).
15. K.-P. Shneider and C. Park, Phys. Fluids **18**, 969 (1975).
16. M. Mitchner and C. Kruger, in *Partially Ionized Gases* (Wiley, New York, 1973).

Translated by P. Pozdeev

Technical Physics Letters, Vol. 26, No. 9, 2000, pp. 806–809. Translated from Pis'ma v Zhurnal Tekhnicheskoĭ Fiziki, Vol. 26, No. 18, 2000, pp. 1–8.
Original Russian Text Copyright © 2000 by Orlenko, Matisov.

Exchange-Induced Self-Polarization of an Electron Beam

E. V. Orlenko and B. G. Matisov

St. Petersburg State Technical University, St. Petersburg, Russia

e-mail: quark@citadel.stu.neva.ru

Received February 7, 2000

Abstract—A mechanism leading to self-polarization of a beam of free electrons injected from a light-emitting cathode is considered. It is shows that the exchange interaction may lead to self-polarization of an electron beam in vacuum and maintain the polarization of a beam in a substance. *© 2000 MAIK "Nauka/Interperiodica".*

1. The phenomenon of optical orientation of electron spins in semiconductors is widely used in various fields, including atomic and molecular physics, physics of continuum media [1], nuclear physics, and physics of elementary particles [2]. The appearance of charge carriers with oriented spins upon absorption of a circularly polarized light was originally studied by Garvin *et al.* [3] and by Lampel and Weibush [4]. Although the phenomenon of optical orientation of an electron beam has been studied in sufficient detail [5], the mechanisms responsible for a high degree of the beam polarization are still neither clearly understood nor uniquely interpreted [6, 7].

A principal mechanism of polarized electron production is photoemission in thin stressed epitaxial GaAs layers. A biaxial stress results in the splitting of the $p_{3/2}$ multiplet in the valence band, such that the state of one pair of sublevels is below the Fermi level (easy holes), while the state of another pair is above this level (heavy holes). This difference leads eventually to a change in population of these sublevels. A circularly polarized photon induces transition to the *s* state of the conduction band with a single definite value of the spin projection onto a special symmetry axis in the crystal. In this way, a high degree of electron polarization can be obtained under the symmetry conditions of a cubic GaAs crystal excited with a light of right- hand circular polarization. Using special activation of the crystal surface by depositing a Cs + O (or Cs + F) layer in combination with band bending, it is possible to increase the degree of electron polarization up to 83–90%.

A theoretical analysis of this phenomenon reduces to description and numerical modeling the process of electron diffusion from bulk to surface of the layer. The diffusion process can be considered as classical, with neglect of any manifestations of quantum transport features [6, 7] and collective quantum phenomena, but still with an allowance for spin relaxation mechanisms. Many of such mechanisms are worthy of special consideration with a view to their possible spin polarization effect. Apparently, the very high degree of electron beam polarization observed in the experiment could not exist if there were no mechanisms maintaining the mutual orientation of the spins. The spin coupling constant must significantly exceed the constants of interactions leading to breakage of the spin orientation.

In particular, a mechanism that is most competitive to any possible self-polarization factor is the Bir–Aronov–Pikus spin relaxation [8] with an interaction constant proportional to the exchange energy splitting of the exciton state (i.e., of the order of 50 μeV). The spin relaxation time in this case is about 1/100 of the time of spin destruction for the spin–orbit coupling [8, 9] according to the Elliott–Jassett mechanism. This is much shorter compared to the electron lifetime and, hence, the proposed mechanism of spin destruction is highly effective.

Another destruction mechanism, related to the spin splitting of the conduction band, was proposed by D'yakonov and Perel' [10]. This splitting is equivalent to an effective magnetic field acting upon spins, the direction of this field depending on the orientation of momentum. A characteristic band splitting energy for the spin–orbit coupling is $\hbar\Omega = (32/21)^{1/2}\alpha(T^3/E_g)^{1/2}$, where E_g is the bandgap width, α is a numerical coefficient proportional to the orbital quantum number, and T is the temperature against the energy scale. This mechanism becomes significant at high electron energies.

In this work, we will consider one possible mechanism maintaining the spin polarization in an electron beam, which is still operative when the electrons escape into vacuum. The interaction, capable of producing the spin ordering, is the Coulomb exchange interaction (the same as that between electrons in the conduction band). The effect of spin polarization observed for a beam of electrons in vacuum is analogous to the ferromagnetism of free electrons. In this case, the exchange interaction constant is markedly greater as compared to the constants of all relaxation mechanisms mentioned above.

2. The Heisenberg parameter can be calculated with an allowance for the interaction between an electron beam and the bound electrons of impurity atoms using

1063-7850/00/2609-0806$20.00 © 2000 MAIK "Nauka/Interperiodica"

the exchange perturbation theory (EPT) [11] specially developed for description of magnetic systems. The first-order EPT energy correction is given by the following expression [11]:

$$E^{(1)} = \langle \Phi(r_1, r_2)|\hat{V}|\Psi(r_1, r_2)\rangle, \quad (1)$$

where $\hat{V}$ is the operator describing the Coulomb interaction between electrons; Φ is the direct product of the coordinate-dependent parts of the single-electron wavefunctions; Ψ is the coordinate-dependent part of the wavefunction antisymmetric with respect to the electron permutations. For the beam electrons representing simple flat waves, the energy correction can be written in the form of $E^{(1)} = K \pm A$ or

$$E^{(1)} = K - \frac{A}{2} - 2A\hat{\mathbf{s}}_1 \cdot \hat{\mathbf{s}}_2, \quad (2)$$

where

$$K = \int \frac{e^2}{|\mathbf{r}_1 - \mathbf{r}_2|} d^3r_1 d^3r_2,$$

$$A = \int \frac{\exp(i(\mathbf{k}_1\mathbf{r}_1 + \mathbf{k}_2\mathbf{r}_2 - \mathbf{k}_1\mathbf{r}_2 - \mathbf{k}_2\mathbf{r}_1))}{|\mathbf{r}_1 - \mathbf{r}_2|} d^3r_1 d^3r_2 \frac{e^2}{\Omega^2},$$

($1/\Omega^2$ is the coefficient providing normalization to the total number of particles in the beam).

A contribution due to the exchange interaction under consideration, which accounts for the spin correlation in the beam, is $A(q) = \frac{e^2 n^{2/3}}{2\pi}\delta(q)$, where $q = |\mathbf{k}_1 - \mathbf{k}_2|$, δ is the Dirac delta function, and n is the electron concentration in the beam. Obviously, $q \geq 2\pi\hbar/L$, where L is the layer thickness. This is the only physical meaning of the δ-function.

Let us average the magnitude of the exchange interaction with respect to the energy scatter of electrons generated under the action of radiation with a spectral line of the Lorentz type. Since the frequency interval $\Delta\omega$ related to the radiation linewidth is proportional to the scatter of momenta $\hbar\Delta\omega \simeq \hbar^2 kq/m$, we may write

$$\langle A\rangle = \int A(q) \frac{\alpha}{1 + (\alpha q)^2} dq = \frac{e^2}{2\pi} n^{2/3} \alpha, \quad (3)$$

where $\alpha = \hbar k\tau/m$, τ^{-1} is the spectral linewidth. Note that the α value has the same order of magnitude as the diffusion mean free path of electrons. Therefore, $\langle A\rangle$ must depend on the intensity of the incident light exciting electrons from the valence band to the conduction band. Assuming for the estimate that $n \sim \alpha^{-3} \sim n_{\text{dop}} = 3 \times 10^{18}$ cm^{-3}, we obtain $\langle A\rangle = \frac{1}{2\pi}\frac{e^2}{\alpha_B}\left(\frac{a_B}{\alpha}\right) \sim \frac{1}{\pi}E_B \times 10^{-2} \sim 10^{-14}$ erg; the Heisenberg parameter is $j = 2A$, where A is taken with an allowance for the averaging. Thus, the constant of interaction leading to the spin orientation is sufficiently large and the spin correlation is retained even when the cathode is heated.

3. Let the unit vector $\mathbf{m}$ indicate the spontaneous moment direction. The energies of a particle, depending on the orientation of its spins relative to $\mathbf{m}$, can be expressed as [12]

$$\varepsilon(p, \mathbf{s}) = \varepsilon_0(p) - b(p)\hat{\mathbf{s}} \cdot \mathbf{m}. \quad (4)$$

According to this expression, the energy of an electron with a given spin projection onto the axis parallel to $\mathbf{m}$ is $\varepsilon_0 - b$; accordingly, the equilibrium distribution function is $n(\varepsilon_0 - b) = n_\uparrow$, while the opposite spin projection is characterized by $\varepsilon_0 + b$, $n(\varepsilon_0 - b) = n_\downarrow$. The quantities $n_\uparrow$ and $n_\downarrow$ represent (for the corresponding spin orientations) eigenvalues of the operator

$$\hat{n}_0(\mathbf{p}, \hat{\mathbf{s}}) = \frac{1}{2}(n_\uparrow + n_\downarrow) + (n_\uparrow - n_\downarrow)\hat{\mathbf{s}} \cdot \mathbf{m}, \quad (5)$$

representing the equilibrium density matrix.

The presence of a spontaneous orientation of spins to the extent of $\bar{\sigma} \sim b/\varepsilon_F$ or $\bar{\sigma} \sim b/T$ for a nondegenerate and nondegenerate gas, respectively, is ensured by the Boltzmann factor related to the shift of the states of easy and heavy holes relative to the Fermi level. In the three-dimensional case, the Fermi level is determined as

$$\varepsilon_{F\pm} = \varepsilon_F(1 \pm \bar{\sigma})^{2/3}. \quad (6)$$

Replacing ± 1 by the operator $\hat{p} = \frac{1}{2}(1 + 4\hat{\mathbf{s}} \cdot \hat{\mathbf{s}}')$ with the eigenvalues equal to ± 1 (for the corresponding spin orientation), we obtain

$$\varepsilon_{F\pm} = \varepsilon_F\left(1 + \frac{\bar{\sigma}}{2} + 2\bar{\sigma}\hat{\mathbf{s}} \cdot \hat{\mathbf{s}}'\right)^{2/3}. \quad (7)$$

The exchange interaction contributes to the effective energy per particle, the corresponding operator being

$$\hat{\varepsilon}_{\text{exc}} = -j\hat{\mathbf{s}} \cdot \hat{\mathbf{s}}'.$$

Thus, the Fermi distribution function can be written in the form of a density matrix with the spin variable:

$$\hat{n}_F = \frac{1}{\exp[(\varepsilon - j\hat{\mathbf{s}} \cdot \hat{\mathbf{s}}' - \varepsilon_{F\pm})/T] + 1}. \quad (8)$$

For $\sigma < 1$, expression (7) can be expanded into series to yield

$$\varepsilon_{F\pm} = \varepsilon_F\left(1 + \frac{\bar{\sigma}}{3} + \frac{4}{3}\bar{\sigma}\hat{\mathbf{s}} \cdot \hat{\mathbf{s}}'\right).$$

Using this expansion, operator (8) can be written in the

following form:

$$\hat{n}_F = n_F^0 - \hat{f}\frac{\partial n_F^0}{\partial \varepsilon}. \quad (9)$$

Here n_F^0 is the Fermi function without corrections to the kinetic energy and the Fermi energy, and $\hat{f}$ is an analog of the Landau function [9]:

$$\hat{f} = \frac{1}{\mathrm{Sp}\int \hat{n}_0(\mathbf{p}, \hat{\mathbf{s}})d^3p}\left[\frac{\Delta}{2} + (2\Delta + j)\hat{\mathbf{s}}\hat{\mathbf{s}}'\right]. \quad (10)$$

For electrons in the semiconductor studied (GaAs), the conduction band is above the Fermi energy level and, hence, the corresponding distribution is of the Boltzmann type:

$$n_\uparrow - n_\downarrow = n_0\exp(-b/T) - n_0\exp(b/T), \quad (11)$$

where $n_0 = e^{\frac{\mu - \varepsilon}{T}}$ and μ is the chemical potential of the classical ideal gas. In this case,

$$\mathrm{Sp}\int \hat{n}_0(\mathbf{p}, \hat{s})d^3p = n_0\exp(-b/T) + n_0\exp(b/T) = 2\cosh\frac{b}{T}. \quad (12)$$

There must be a specific relationship between Eqs. (4) and (10) caused by the exchange interaction. To determine this relationship, let us consider (by analogy with [9]) a change in the electron energy upon rotating vector $\mathbf{m}$ by $\delta\theta$ angle. Taking into account that $\delta\mathbf{m} = [\delta\boldsymbol{\theta} \times \mathbf{m}]$ and using Eq. (4), we obtain

$$\delta\varepsilon = -b[\mathbf{m} \times \hat{\mathbf{s}}]\delta\boldsymbol{\theta}. \quad (13)$$

At the same time, the change in $\mathbf{m}$ will modify the equilibrium distribution function (5)

$$\delta\hat{n}_0(\mathbf{p}, \hat{\mathbf{s}}) = \frac{1}{2}(n_\uparrow - n_\downarrow)[\mathbf{m} \times \hat{\mathbf{s}}]\delta\boldsymbol{\theta}, \quad (14)$$

and, hence, change the energy by

$$\delta\varepsilon = \mathrm{Sp}_{s'}\int \hat{f}\delta\hat{n}_0(\mathbf{p}', \hat{\mathbf{s}}')d^3p' = \mathrm{Sp}_{s'}\int\frac{1}{2}\hat{f}(n_\uparrow - n_\downarrow)[\mathbf{m} \times \hat{\mathbf{s}}']\delta\boldsymbol{\theta}d^3p'. \quad (15)$$

Equating expressions (13) and (15) for an arbitrary $\delta\theta$, we obtain a relationship for electrons in the conduction band:

$$-b[\mathbf{m} \times \hat{\mathbf{s}}] = \frac{\mathrm{Sp}_{s'}\int\frac{1}{2}\left(\frac{\Delta}{2} + (2\Delta + j)\hat{\mathbf{s}}\hat{\mathbf{s}}'\right)(n_\uparrow - n_\downarrow)[\mathbf{m} \times \hat{\mathbf{s}}']d^3p}{\mathrm{Sp}\int \hat{n}_0(\mathbf{p}, \hat{\mathbf{s}})d^3p}.$$

Substituting (11) and (12) and taking the trace, we arrive at

$$-b[\mathbf{m} \times \hat{\mathbf{s}}] = -\frac{\sinh(b/T)}{\cosh(b/T)}\frac{1}{2}(2\Delta + j), \quad (16)$$

or

$$b = \tanh(b/T)\frac{2\Delta + j}{2},$$
$$\frac{2b}{2\Delta + j} = \tanh\frac{b}{T},$$
$$\frac{b}{T}\frac{T}{\Delta + j/2} = \tanh\frac{b}{T},$$
$$\bar{\sigma}\frac{T}{\Delta + j/2} = \tanh\bar{\sigma}. \quad (17)$$

Thus, we obtained a transcendental equation (17) possessing a nonzero solution ($b \neq 0$) provided that the coefficient $T/(\Delta + j/2)$ is smaller than unity. As seen, both factors (deformation splitting Δ and exchange interaction j) favor the appearance of spontaneous spin orientation; for $(\Delta + j/2) > T$, the system features a second-order phase transition with the polarization $\sigma \longrightarrow 1$. The quantities Δ and j are of the same order of magnitude. For example, $\Delta_1 = 50$ meV $= 8 \times 10^{-13}$ erg (GaAs) and $\Delta_2 = 25$ meV $= 4 \times 10^{-13}$ erg (GaAsP) [13]; for the same materials, $j \sim (10–25) \times 10^{-14}$ erg.

Therefore, the exchange interaction is a competitive factor producing spontaneous polarization in an electron beam. This phenomenon can be treated as a kind of ferromagnetic amplification of spin polarization in the electron beam. Mechanisms considered above as capable of breaking the spin polarization cannot destruct this self-polarized system to any significant extent because their interaction constants are two orders of magnitude smaller than the constant of the exchange-induced spin structure ordering. This conclusion explains a great deal of experimental material reported on the spin-polarized beams.

The authors are grateful to B. Oskotskiĭ for kindly providing the experimental material. The work was supported by the Russian Foundation for Basic Research (project no. 99-02-17076).

REFERENCES

1. H. C. Siegmann, J. Phys.: Condens. Matter **4**, 8395 (1992).
2. C. Y. Prescott, W. B. Atwood, and R. L. A. Gottrell, Phys. Lett. B **77**, 347 (1978); **84**, 524 (1984).
3. E. Garvin, D. T. Pierce, and H. C. Siegmann, Helv. Phys. Acta **74**, 393 (1974).
4. G. Lampel and C. Weibush, Solid State Commun. **16**, 877 (1975).
5. B. P. Zakharchenya and F. Maĭer, *Optical Orientation* (Nauka, Moscow, 1989).
6. L. G. Gerchikov, B. D. Oskotskiĭ, and A. V. Subashiev, Phys. Rev. B **50**, 15416 (1994).

7. A. V. Subashiev, Y. A. Mamaev, Yu. P. Yashin, and J. E. Clenderein, Phys. Low-Dimens. Struct. **1**/**2**, 1 (1999).

8. G. L. Bir, A. G. Aronov, and G. E. Pikus, Zh. Éksp. Teor. Fiz. **69**, 1382 (1975) [Sov. Phys. JETP **42**, 705 (1975)].

9. R. J. Elliot, Phys. Rev. **96**, 266 (1954); Jassett, Solid State Phys. **14**, 1 (1963).

10. M. I. D'yakonov and V. I. Perel', Fiz. Tverd. Tela (Leningrad) **13**, 3581 (1971) [Sov. Phys. Solid State **13**, 3023 (1971)].

11. E. V. Orlenko and A. A. Rumyantsev, Zh. Éksp. Teor. Fiz. **97**, 439 (1990) [Sov. Phys. JETP **70**, 244 (1990)]; E. V. Orlenko and T. Yu. Latyshevskaya, Zh. Éksp. Teor. Fiz. **113**, 2129 (1998) [JETP **86**, 1167 (1998)].

12. A. A. Abrikosov, *Principles of the Theory of Metals* (Nauka, Moscow, 1987; North-Holland, Amsterdam, 1988).

13. R. Mair, SLAC Report 488, 1996.

Translated by P. Pozdeev

Technical Physics Letters, Vol. 26, No. 9, 2000, pp. 810–813. Translated from Pis'ma v Zhurnal Tekhnicheskoĭ Fiziki, Vol. 26, No. 18, 2000, pp. 9–16.
Original Russian Text Copyright © 2000 by Titov, Shilkina, Reznichenko, Dudkina, Razumovskaya, Shevtsova, Kuznetsova.

Structure Clusterization Preceding Concentration Phase Transitions

S. V. Titov, L. A. Shilkina, L. A. Reznichenko, S. I. Dudkina, O. N. Razumovskaya, S. I. Shevtsova, and E. M. Kuznetsova

Institute of Physics, Rostov State University, Rostov-on-Don, Russia

e-mail: klevtsov@iphys.rnd.runnet.ru

Received April 6, 2000

Abstract—The formation and development of bulk crystallochemical defects—mesoscopic clusters representing the nuclei of new phases—was studied in systems exhibiting concentration phase transitions. When a solid solution approaches a morphotropic region, the clusters exhibit a stepwise evolution involving several stages manifested by corresponding changes in macroscopic properties. The role of clusters in the development of the extreme electrophysical properties of the objects studied is discussed. © *2000 MAIK "Nauka/Interperiodica".*

Recent investigations into the problem of inhomogeneity development in condensed media pay special attention to the formation of bulk crystallochemical defects on a mesoscopic scale, representing clusters appearing upon the assimilation and ordering of vacancies and interstitial atoms. The phenomenon of structure clusterization was observed in many oxide systems, including simple monoxides, ferrites, and disordered ferroelectrics, where its role during polymorphous transformations, and its influence upon the macroscopic properties, were established [1, 2].

The purpose of this work was to study the development of cluster structures representing the nuclei of new phases in the vicinity of concentration phase transitions. The objects for investigation represent a series of solid solutions with the compositions $(1 - x)NaNbO_3$–$xPbTiO_3$ (1) and $xPbTiO_3$–$(1 - x - y)PbZrO_3$–$y\sum_n (PbB'_{1-\beta}B''_\beta O_3)_n$ (where B' = Nb, W; B'' = Li, Zn, Mg, Ni; n = 4) (2). The samples were obtained by solid-state synthesis followed by sintering without pressure (for compounds 1) or by hot pressing (for compounds 2). In system 1, the solid solutions corresponded to regions of the phase diagram with x = 0.2195–0.305 (orthorhombic PI region) and x = 0.40–0.70 (tetragonal T_1 region) situated between the morphotropic regions. In system 2, we studied the solid solutions with x = 0.30–0.37 belonging to the rhombohedral (Rh), tetragonal (T), and morphotropic (MT) regions.

The experiments showed the nonmonotonic behavior of the concentration dependence of an average parameter ($\bar{a}_2$) of the reduced perovskite unit cell, the X-ray density (ρ_1), and measured density (ρ_2) of the sintered ceramic samples, as well as of the characteristics describing smearing of the concentration phase transitions (Δ) and scattering of the electrophysical parameters ($\overline{\Delta\alpha}$, $\overline{\delta\alpha}$[1]) (Fig. 1).[1] Also observed was some decrease in the relative density, suggesting loosening of the solid solution structure. The observed pattern could not be explained within the framework of the model of neither ideal nor real (containing statistically distributed defects) solid solutions. Taking into account that all the compounds studied contained no impurity inclusions, the observed pattern of changes can be related to the formation and development of bulk crystallochemical defects on a mesoscopic scale—clusters, the appearance of which must be accompanied by local fluctuations in the composition. This was confirmed by the results of electron-microscopic investigations (performed in a Camebax-Micro scanning electron microscope–analyzer system). In the samples of system 1, the microanalysis revealed regions enriched with Pb and Ti, alternating with regions depleted of these elements. The elemental scans showed that variations in the content of these elements were minimum for the compositions far from (x = 0.40, 0.45) and close to (x = 0.70) the MT regions. The variations increased for x = 0.5 and reached maximum for x = 0.6.

In order to establish the nature of these deviations, we have studied in much detail the pattern of X-ray diffraction from the solid solutions studied, with analysis of the profiles of both Bragg's and diffusion components of the X-ray scattering. According to the data obtained, there was a redistribution of intensity between the interference maxima and background. In

[1] The value of Δ was determined by the empirical formula $\Delta = \Delta T/1.633$ [K] [3], where ΔT is the width of the temperature interval corresponding to $\varepsilon = 0.75\varepsilon_{max}$ in the temperature dependence of the dielectric permittivity ε; the absolute ($\overline{\Delta\alpha}$) and relative ($\delta\alpha$) deviations of the parameter α (in our case, $\alpha = \varepsilon_{33}^T/\varepsilon_0$ is the relative dielectric permittivity of a polarized sample) from the average were calculated by convectional formulas [4].

1063-7850/00/2609-0810$20.00 © 2000 MAIK "Nauka/Interperiodica"

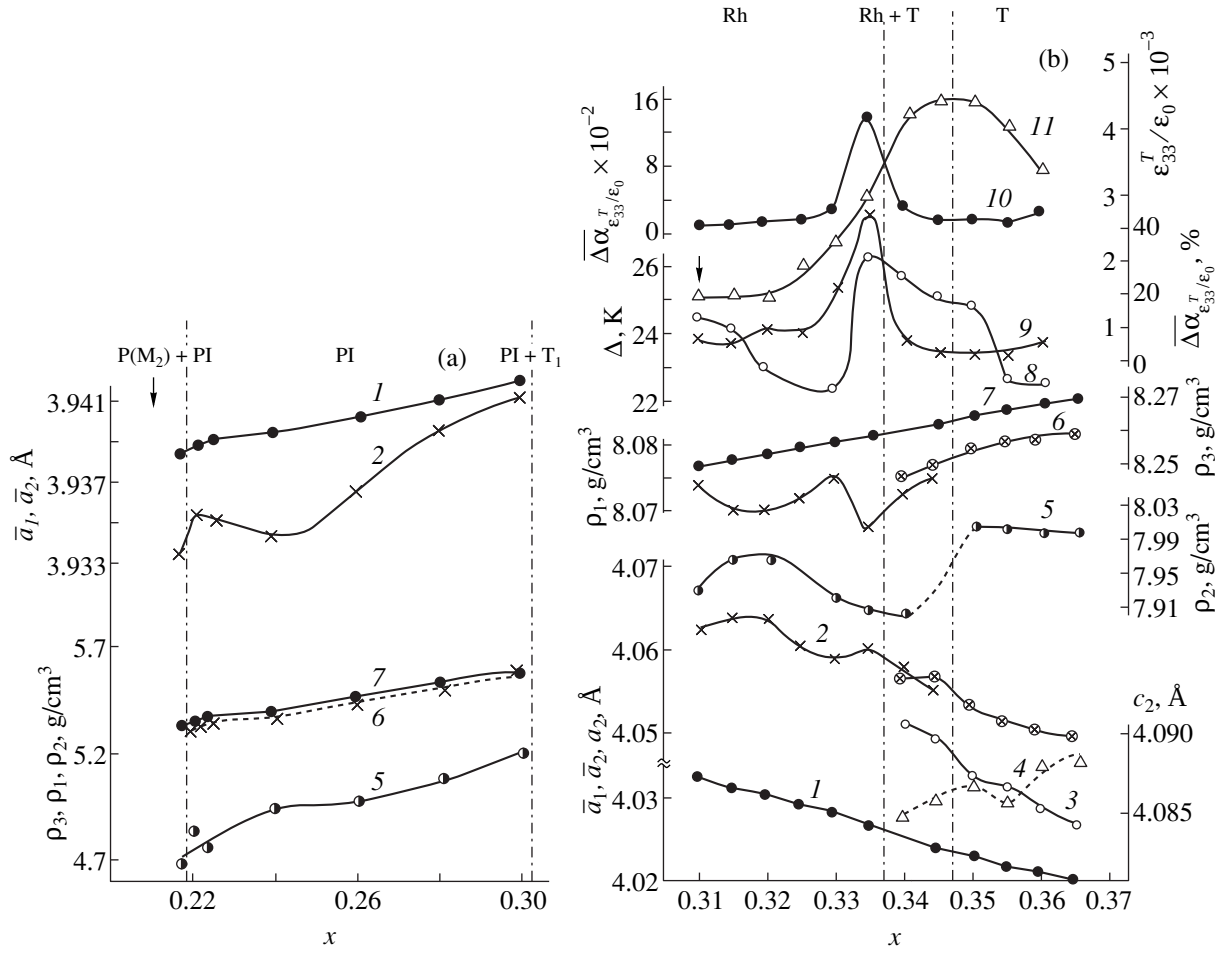

Fig. 1. The plots of (*1*) $\bar{a}_1$, (*2*) $\bar{a}_2$, (*3*) a_{T_2}, (*4*) c_{T_2}, (*5*) ρ_2, (*6*) ρ_1, (*7*) ρ_3, (*8*) Δ, (*9*) $\overline{\delta\alpha}_{\varepsilon_{33}^T/\varepsilon_0}$, (*10*) $\overline{\Delta\alpha}_{\varepsilon_{33}^T/\varepsilon_0}$, and (*11*) $\varepsilon_{33}^T/\varepsilon_0$ versus *x* in solid solutions of (a) system 1 and (b) system 2.

the region of system 1 on the left of the concentration phase transition (observed in the interval $0.75 < x < 0.85$), the fine structure of the background intensity in the region of $2\theta = 56°–57°$ (Fe_{K_α} radiation) varies depending on *x* (while retaining a general character of the X-ray diffraction pattern typical of the T_1 solid solution structure). Initially, the background exhibits small oscillations ($x = 0.40$) and begins to increase in intensity ($x = 0.45$); then several very weak diffuse maxima of equal intensity appear ($x = 0.50$) and merge together ($x = 0.60$) to form a strongly smeared halo. Simultaneously, the intensity of the 002 reflection corresponding to the main T_1 phase gradually increases as well.

The diffuse halo apparently results from a coherent X-ray scattering from mesoscopic objects—clusters. By determining a difference between the unit cell parameters of clusters and matrix, we may follow the development of clusters and estimate their dimensions from the halfwidth of the diffuse maximum: 80 Å ($x = 0.50$) and 90 Å ($x = 0.60$). In the samples with $x \geq 0.75$, the diffuse maximum is replaced by a diffraction line whose intensity gradually increases and whose width decreases with the growth of *x*. It was established that the interplanar distance ($\bar{d}_{002}$) in the cluster increases with *x* faster than the d_{002} value of the matrix T_1 phase. This is indicative of a nonuniform distribution of $PbTiO_3$ between the matrix and the new phase, the latter phase being enriched with this component. Taking into account that a concentration phase transition takes place at $x \geq 0.75$, it is naturally assumed that clusters represent the nuclei of a new T_2 phase formed in the T_1 matrix.

From the comparison of results of the electron-microscopic and X-ray diffraction investigations, we may conclude that system 1 features the formation of a region of heterogeneity, beginning at a distance of ~20 mol % from the MT region, characterized by the domains of coherent diffraction representing a new mesoscopic phase. Coincidence of the 100 lines of the "old" and "new" phases is evidence of the matrix and the cluster possessing a common (100) plane, suggesting that the cluster is coherently matched to the initial T_1 structure. When direct observation of cluster formation was impossible (because of close values of the unit

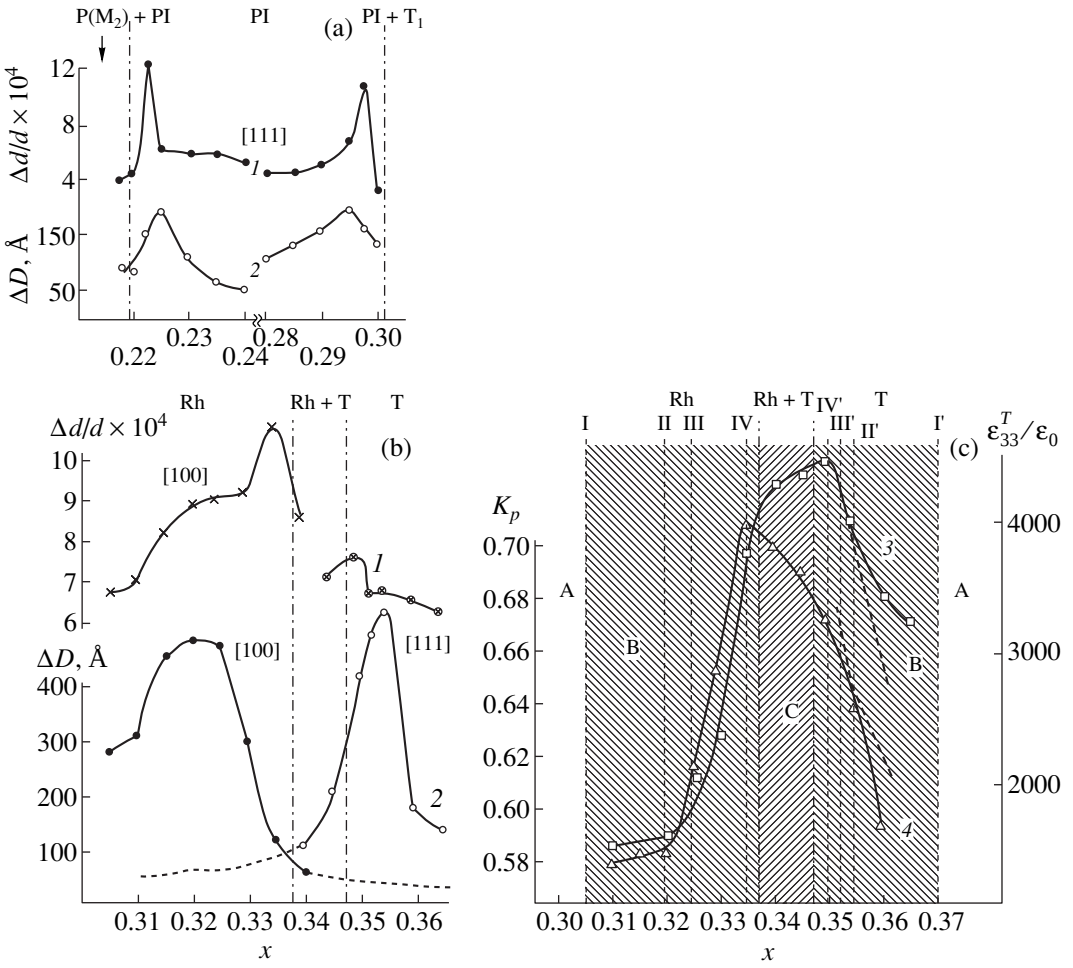

Fig. 2. The plots of (*1*) $\Delta d/d$, (*2*) ΔD, (*3*) $\varepsilon_{33}^{T}/\varepsilon_0$, and (*4*) K_p in solid solutions of (a) system 1 and (b, c) system 2. (a, b) Values in square brackets indicate the directions in which the $\Delta d/d$ and ΔD values were determined. (c) Cluster structure development stages: (I, I') the onset of cluster formation in the T and Rh phases, respectively; (II, II') the cluster size reaches a critical level; (III, III') the onset of cluster breakage from matrix; (IV, IV') clusters completely separate from matrix; (A) single-phase region; (B) heterogeneous region; (C) heterophase region.

cell parameters of the main and nucleating phases, leading to superposition of the corresponding X-ray reflections), the dynamics of cluster formation could be followed by monitoring a change in the difference ΔD of the coherent scattering domain size calculated using the halfwidths and the total widths of the diffraction lines. An increase in this difference at concentrations far from the MT region is indicative of the increasing number and size of the clusters (reaching a critical size at maximum ΔD); a decrease in the ΔD value on approaching the MT region reflects the separation of clusters from the matrix followed by the independent development of the new phase (Fig. 2a and 2b).

Since coherence between cluster and matrix is retained in the course of cluster growth, considerable elastic deformations arise in the plane of cluster matching to the matrix and increase with the size and number of clusters. At a certain instant, the process acquires an avalanche character leading to a sharp increase in the level of microdeformations ($\Delta d/d$) near the MT region. On reaching the elastic deformation threshold, the system enters the stage of plastic deformation resulting in the breakage of coherence between the old and new phases and in the separation of the new phase into an independent structural component. Because of the anisotropy of the medium, the breakage proceeds (rather than takes place simultaneously) involving an increasing number of clusters. This development is accompanied by a sharp drop in microdeformations and the relaxation of stress (Figs. 2a and 2b).

The stepwise evolution of clusters in the course of the variation of the solid solution composition not only determines the anomalous behavior of parameters of the fine crystalline structure but explains the variation of the electrophysical properties of the material both far from and close to the MT region as well. As seen from Fig. 2c, the "special" points (bends and extrema) on the curves of $\Delta d/d$, ΔD, $\varepsilon_{33}^{T}/\varepsilon_0$, and K_p (electromechanical

coupling coefficient) versus x correspond to definite stages in the cluster structure development. In connection to this, we believe that, in addition to the laws of extremal variation of the properties of solid solutions in the vicinity of the concentration phase transitions [5], an important contribution is due the mesoscopic inhomogeneities formed far from the MT region because of the loss of stability in one of the phases [6] leading to partial disordering on the initial structure.

The work was supported by the Russian Foundation for Basic Research, project no. 99-02-17575.

REFERENCES

1. V. I. Arkharov, in *Problems of Modern Physics* (Nauka, Leningrad, 1980), pp. 357–382.
2. O. A. Bunina, I. N. Zakharchenko, P. N. Timonin, and V. P. Sakhnenko, Kristallografiya **40** (4), 708 (1975) [Crystallogr. Rep. **40**, 655 (1995)].
3. A. A. Bokov, Zh. Éksp. Teor. Fiz. **111** (5), 1817 (1997) [JETP **84**, 994 (1997)].
4. O. N. Kasandrova and V. V. Lebedev, *Processing of the Results of Observations* (Nauka, Moscow, 1970).
5. E. G. Fesenko, A. Ya. Dantsiger, and O. N. Razumovskaya, *Novel Piezoelectric Ceramic Materials* (Rostov. Gos. Univ., Rostov-on-Don, 1983).
6. Yu. M. Gufan, *Structural Phase Transformations* (Nauka, Moscow, 1982).

Translated by P. Pozdeev

Technical Physics Letters, Vol. 26, No. 9, 2000, pp. 814–816. Translated from Pis'ma v Zhurnal Tekhnicheskoĭ Fiziki, Vol. 26, No. 18, 2000, pp. 17–23.
Original Russian Text Copyright © 2000 by Popov, Teperik.

The Effect of Interference in the Substrate on the Electromagnetic Wave Polarization Transformation under Cyclotron Resonance Conditions in a Two-Dimensional Electron System

V. V. Popov and T. V. Teperik

Saratov Division, Institute of Radio Engineering and Electronics, Russian Academy of Sciences, Saratov, Russia

e-mail: popov@ire.san.ru

Received March 15, 2000

Abstract—The effect of interference in the substrate on the polarization transformation of an electromagnetic wave in the presence of cyclotron resonance in a two-dimensional (2D) electron system is studied theoretically. It is predicted that the interference can dramatically enhance the transformation if the 2D electron system is situated on the rear face of a quarter-wave substrate plate. As a result, the reflected wave exhibits a virtually complete polarization transformation. © *2000 MAIK "Nauka/Interperiodica".*

The effect of interference in the substrate on the cyclotron-resonance line shape of a two-dimensional (2D) electron gas was studied theoretically and experimentally [1–4]. The relative variation in the total transmission coefficient (for both of the orthogonal polarizations) under the resonance conditions was measured and it was demonstrated that the position and the width of the cyclotron absorption line are oscillating functions of substrate thickness.

Interference in the substrate is often regarded as a nuisance, being suppressed by certain tricks to make the substrate deviate from a plane-parallel shape [5]. At the same time, some authors suggest using the interference as a means of enhancing relevant effects. In a 2D electron system, for example, plasma oscillations are excited far more efficiently if the substrate thickness is chosen appropriately [6]. This paper addresses the effect of interference in the substrate on the transformation of the electromagnetic-wave polarization under the cyclotron resonance conditions in a 2D electron system.

In [7], the effect was studied theoretically in the case where the electron system is situated at the interface of two dielectrics. It was shown that the polarization transformation is maximum for the reflected wave if the incident wave emerges from a medium with a higher optical density. However, this requirement cannot be met with ease in experiment a because it is difficult to inject an electromagnetic wave into such a medium. To solve the problem naturally, we consider a structure with a plane-parallel substrate. It is demonstrated below that interference in the substrate may dramatically enhance the polarization transformation in this structure.

Let a linearly polarized electromagnetic wave be normally incident on a plane-parallel dielectric substrate of thickness d, let a 2D electron layer be situated on one of the substrate faces, and let an external magnetic field $\mathbf{B}_0$ be perpendicular to the plane of the electron system.

The power transformation ratios for the incident wave are defined as in [7]:

$$R_{pp} = \frac{P_{rp}}{P_{ip}}, \quad R_{sp} = \frac{P_{rs}}{P_{ip}},$$
$$T_{pp} = \frac{P_{tp}}{P_{ip}}, \quad T_{sp} = \frac{P_{ts}}{P_{ip}}, \tag{1}$$

where P_{ip} is the power flux density of the incident wave, P_{rp} and P_{tp} are the respective power flux densities of the reflected and the transmitted wave that are polarized parallel to the incident wave, and P_{rs} and P_{ts} are the respective power flux densities of the reflected and the transmitted wave that are polarized normally to the incident wave. The ratios R_{sp} and T_{sp} are coefficients of the wave polarization transformation.

The power fluxes of the transmitted and the reflected wave are computed by solving Maxwell's equations in the substrate and the surrounding media. The response of the 2D magnetoactive electron plasma is allowed for by the corresponding boundary conditions on the interfaces. The dielectric constants of the surrounding media are taken equal to unity. The components of the

1063-7850/00/2609-0814$20.00 © 2000 MAIK "Nauka/Interperiodica"

electric conductivity tensor of the electron plasma in the magnetic field are expressed as

$$\sigma_\perp = \sigma_0 \frac{1 - i\omega\tau}{(\omega_c\tau)^2 + (1 - i\omega\tau)^2},$$
$$\sigma_\times = -\sigma_0 \frac{\omega_c\tau}{(\omega_c\tau)^2 + (1 - i\omega\tau)^2}, \quad (2)$$

where ω is the angular frequency of the wave, $\omega_c = |e|B_0/m^*$ is the cyclotron frequency, $\sigma_0 = e^2N_s\tau/m^*$ is the dc conductivity of the electron system in the absence of an external magnetic field, e is the electron charge, m^* is the effective electron mass, and N_s and τ are the surface concentration and the phenomenological momentum relaxation time of the electron system, respectively. In calculations the parameter values of the electron system were taken for gallium arsenide.

The computation testified that the polarization transformation is most efficient in the reflected wave, which is analogous to the result obtained in [7]. We therefore focus on R_{sp} and R_{pp} in what follows.

First, let us consider the case where the 2D electron system is on the front face of the substrate. Consequently, the incident wave emerges from the medium with lower optical density. Figure 1 shows computed dependences of R_{sp} and R_{pp} on the magnetic flux density, the electron scattering in the 2D system being neglected ($1/\tau = 0$). The curves are obtained for different values of the reduced substrate thickness

$$y = 2\sqrt{\varepsilon_s}d/\lambda - N, \quad (3)$$

where ε_s is the dielectric constant of the substrate material, λ is the wavelength of the electromagnetic wave *in vacuo*, and N is a natural number selected in such a way that the value of y falls within the interval $0 \le y < 1$. Figure 1 indicates that interference in the substrate strongly affects the height, width, and position of the resonance curves representing the transformation ratios. The polarization transformation is maximum at $y = 0$, that is for a half-wave substrate: $d = N\lambda/2\sqrt{\varepsilon_s}$. In this case the substrate has no effect on the wave so that the resonance curves behave as if the electron system were situated in homogeneous space with $\varepsilon = 1$.

A quarter-wave substrate with $d = (2N + 1)\lambda/4\sqrt{\varepsilon_s}$ corresponding to $y = 0.5$ offers maximum reflection and very small polarization transformation. This agrees with the results of [7] for the incident wave emerging from the medium of lower optical density. If $y = 0$ or 0.5, the polarization transformation is maximum at $\omega_c \simeq \omega$ and a slight increase in the resonance value of the magnetic field occurs at large electron concentrations in the 2D system. In [7], a similar effect was discussed for a structure without substrate. If $0 < y < 0.5$ ($0.5 < y < 1$), the resonance point shifts toward lower (higher) magnetic flux densities (Fig. 1). Thus, the positions, heights, and widths of the transformation ratio curves are oscillating functions of the substrate thickness. If y is other than 0 or 0.5, the curves are asymmetric, as was found for the cyclotron absorption in plane-parallel samples [1–4, 8, 9].

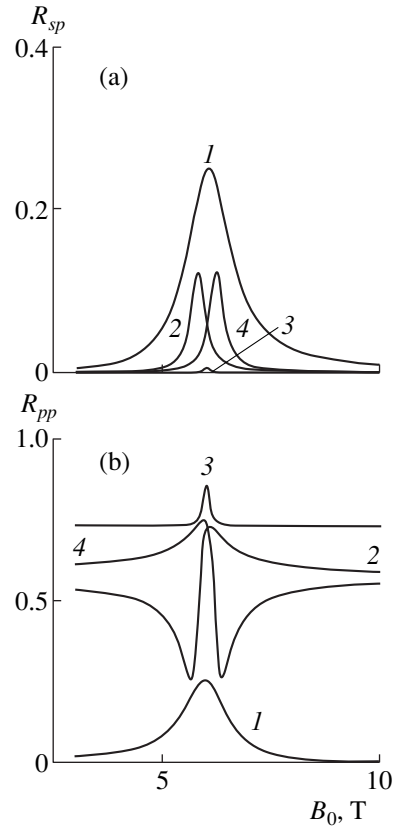

Fig. 1. Transformation ratios vs. magnetic flux density for a 2D electron system situated on the front face of the substrate with y = (*1*) 0, (*2*) 0.25, (*3*) 0.5, or (*4*) 0.75. The wavenumber is 80 cm^{-1}. The structure parameters are $\varepsilon_s = 12.8$, $1/\tau = 0$, $N_s = 2 \times 10^{12}$ cm^{-2}, and $m^* = 0.07m_0$, where m_0 is the mass of a free electron.

Figure 1 shows that the transformation ratio cannot exceed 30% if the electron system is on the front face. In this case, interference in the substrate decreases the polarization transformation coefficient.

Things become quite different if the electron system is moved to the rear face, after which R_{sp} for a quarter-wave substrate ($y = 0.5$) becomes much higher (Fig. 2a) and even exceeds the values reported in [7] for a structure without a substrate (cf. curve *6*). Another difference from the system without a substrate [7] is that R_{pp} (Fig. 2b) vanishes exactly at a point where R_{sp} peaks. Thus, the polarization transformation for the reflected wave is complete. Again, the parameters of the trans-

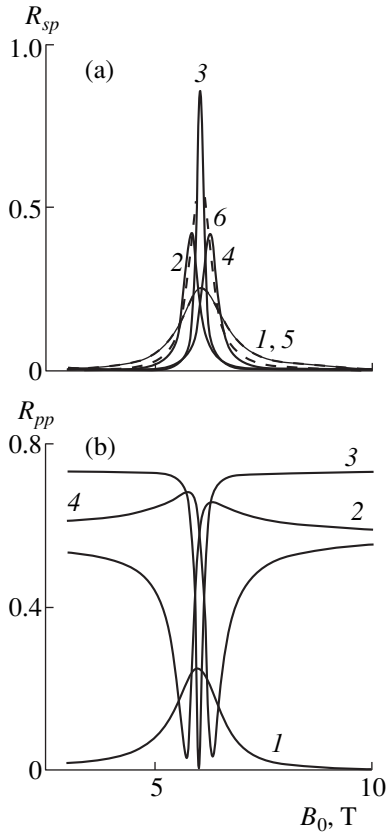

Fig. 2. Transformation ratios vs. magnetic flux density for a 2D electron system situated on the rear face of the substrate with y = (*1*) 0, (*2*) 0.25, (*3*) 0.5, or (*4*) 0.75. The wavenumber and the structure parameters are the same as in Fig. 1. The broken curves refer to the system without substrate. The wave is incident from a medium with dielectric constant $\varepsilon_1/\varepsilon_2$ = (*5*) 1 or (*6*) 12.8 and onto a medium with dielectric constant $\varepsilon_2 = 1$ [7].

formation ratio curves are oscillating functions of the substrate thickness. At $y = 0$, the curves are obviously the same for both configurations.

In conclusion, note that the polarization transformation in gallium arsenide is also pronounced in the presence of the electron scattering ($R_{sp} > 0.4$). This makes it possible to observe and use the effect in technological applications.

This study was funded under the terms of the Federal Special Program “State Support of the Integration of Higher Education and Basic Research for 1997–2000 ” (project no. 696.3) and the Russian Foundation for Basic Research (project no. 00-02-16440).

REFERENCES

1. M. von Ortenberg, Solid State Commun. **17** (11), 1335 (1975).
2. T. A. Kennedy, R. J. Wagner, B. D. McCombe, and J. J. Quinn, Solid State Commun. **14** (3), 275 (1976).
3. G. Abstreiter, J. P. Kotthaus, J. F. Koch, and G. Dorda, Phys. Rev. B **14** (6), 2480 (1976).
4. L. D. Suchalkin, Yu. B. Vasil’ev, and Yu. L. Ivanov, Fiz. Tekh. Poluprovodn. (St. Petersburg) **27** (11), 2075 (1993) [Semiconductors **27**, 1141 (1993)].
5. U. Merkt, M. Horst, T. Evelbauer, and J. P. Kotthaus, Phys. Rev. B **34** (10), 7234 (1986).
6. V. V. Popov and G. M. Tsymbalov, Pis’ma Zh. Tekh. Fiz. **24** (9), 70 (1998) [Tech. Phys. Lett. **24**, 361 (1998)].
7. V. V. Popov and T. V. Teperik, Pis’ma Zh. Tekh. Fiz. **25** (21), 21 (1999) [Tech. Phys. Lett. **25**, 855 (1999)].
8. H. Bluyssen, J. C. Maan, P. Wyder, *et al.*, Solid State Commun. **31** (1), 35 (1979).
9. L. S. Kim, N. D. Drew, H. Munekata, *et al.*, Solid State Commun. **66** (8), 873 (1988).

Translated by A. Sharshakov

Technical Physics Letters, Vol. 26, No. 9, 2000, pp. 817–818. Translated from Pis'ma v Zhurnal Tekhnicheskoĭ Fiziki, Vol. 26, No. 18, 2000, pp. 24–27.
Original Russian Text Copyright © 2000 by Krasikov, Shuvaeva.

Anomalous Relaxation in Polar and Nonpolar Liquids under Contactless Electric Field Action

N. N. Krasikov and O. V. Shuvaeva

Kovrov State Technological Academy, Kovrov, Russia

Received May 12, 2000

Abstract—An electric field action leads to polarization of both polar and nonpolar liquids not in contact with electrodes. Switch-off of the electric field leads to depolarization of the medium by an anomalous relaxation mechanism. © *2000 MAIK "Nauka/Interperiodica".*

Electric field action on liquids normally implies their contact with the potential electrodes. This gives rise to an electric current related to electrolysis (in solutions) and electrophoresis (in colloid–dispersed systems) and leads to polarization processes, the two phenomena being generally nonadditive.

We studied electric field action in a system where the field electrodes connected to a high-voltage source have no contacts with the liquid. Since the upper and lower electrodes are isolated from the liquid by an air gap and the dielectric bottom of the cell, respectively, we may neglect the electric current regardless of the electric conductivity of the liquid. We consider a three-layer capacitor model (upper electrode, air gap, liquid, insulator, and lower electrode) with an anomalous relaxation variation [1, 2] of the electric field strength in the bulk of the liquid.

The purpose of this work was to study the optical polarization processes in polar (butanol, C_4H_9O; $\varepsilon = 17.2$) and nonpolar (dodecane, $C_{12}H_{26}$; $\varepsilon = 2.08$) chemically pure liquids at $t° = 20.0 \pm 0.5°C$. A photoelectrocolorimetric setup used a polarized beam to illuminate the liquid in a transparent dielectric cell. The polarization plane made an angle of 45° with the applied electric field strength E. The experiments were performed by sequentially applying a voltage of 15, 10, and 8 kV to the electrodes. The thickness of the air gap was $l_1 = 17$ mm; the thickness of the liquid layer was $l_2 = 25$ mm; and the thickness of the dielectric bottom was $l_3 = 3$ mm [3]. Transmitted polarized light intensity was measured prior to the electric field application (to yield a reference value taken as 100%), in the course of a 5-min electric field action, and after its termination. See [3] for the details of the experimental technique.

The experimental results are shown in the figure.

The application of the electric field leads to a slow decrease in the transmittance of the polar liquid (C_4H_9O) down to a saturation level. Termination of the electric field action causes a gradual transmittance recovery to the initial level. These variations were clearly reproduced in successive measurements.

Dodecane ($C_{12}H_{26}$) exhibits a sharp increase in absorption immediately upon application of the electric field, followed by a gradual decrease in absorption. Termination of the electric field action leads to a sharp increase in transmittance, which can even exceed the

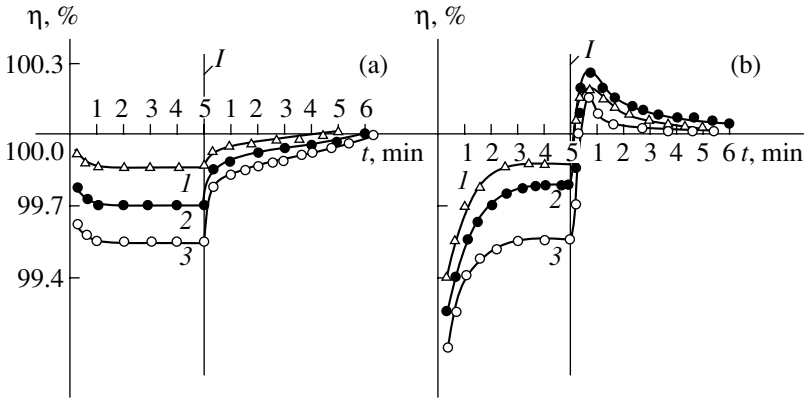

Fig. 1. Plots of the transmitted light intensity normalized to the initial value versus time in (a) butanol (C_4H_9O) and (b) dodecane at U = (*1*) 8, (*2*) 10, and (*3*) 15 kV. *I* denotes the field switch-on time.

1063-7850/00/2609-0817$20.00 © 2000 MAIK "Nauka/Interperiodica"

initial 100% level. Eventually, the transmittance gradually decreases to the initial level. The behavior of saturated hydrocarbons with the lower molecular weights exhibits jumps, and crosses the 100% level in both directions; reproducibility of the experimental results is lower than the experimental accuracy (10%). Note that the effect of polarization is weak in both cases and does not exceed 1% of the initial transmission value.

The polar and nonpolar liquids exhibit different behavior although polarization of light in both cases is related to structural changes in the bulk of the liquid. Apparently, a space charge polarization in the alcohol [4] leads to molecular ordering by means of the displacement of ions in the liquid boundary layers close to the potential electrodes. A limited number of ions leads to the formation of ion–molecular associates or clusters regularly arranged in the bulk of the liquid under the action of hydrogen bonds. The characteristic times of the formation of such structures under the electric field action and their disintegration upon its termination are longer than the characteristic time $\tau = \varepsilon\varepsilon_0\rho$ depending on the dielectric constant (ε) and the specific resistance (ρ) of the liquid.

The electric conductivity of the nonpolar liquid ($C_{12}H_{26}$) is 8–9 orders of magnitude lower than that of alcohol. Thus, it is hardly possible to characterize its polarization in the same way. The interpretation of the results is under discussion and needs a special approach. The switch-on of the electric field evidently leads to a fast process, possibly resulting in a partial orientation of the elongated molecules with CH_3 groups at the ends. Note that the saturated hydrocarbon with shorter molecules (hexane, C_6H_{14}, $\varepsilon = 1.98$) does not exhibit such changes in transmittance. A short-time increase in transmittance immediately following the switch-off of the electric field gives evidence of a fast decay of the orientation built up in the field. Slow processes in nonpolar liquids are apparently related to disordering effects typical of liquid systems on the whole.

We state, finally, that the weak polarization-optical phenomena reported in this paper are reproducible and can be classified as anomalous relaxation effects.

REFERENCES

1. N. N. Krasikov, Élektrotekhnika **4**, 57 (1996).
2. G. E. Skvortsov, Pis'ma Zh. Tekh. Fiz. **25** (7), 57 (1999) [Tech. Phys. Lett. **25**, 274 (1999)].
3. N. N. Krasikov and O. V. Shuvaeva, Zh. Tekh. Fiz. **70** (10) (2000) (in press) [Tech. Phys. **45** (2000) (in press)].
4. K. M. Polivanov, *The Electromagnetic Field Theory* (Énergiya, Moscow, 1969).

Translated by A. Chikishev

Technical Physics Letters, Vol. 26, No. 9, 2000, pp. 819–821. Translated from Pis'ma v Zhurnal Tekhnicheskoĭ Fiziki, Vol. 26, No. 18, 2000, pp. 28–35.
Original Russian Text Copyright © 2000 by Aleksenskiĭ, Osipov, Dideĭkin, Vul', Adriaenssens, Afanas'ev.

Ultradisperse Diamond Cluster Aggregation Studied by Atomic Force Microscopy

A. E. Aleksenskiĭ*, V. Yu. Osipov*, A. T. Dideĭkin*, A. Ya. Vul'*, G. J. Adriaenssens, V. V. Afanas'ev***

** Ioffe Physicotechnical Institute, Russian Academy of Sciences, St. Petersburg, 194021 Russia*

*** Catholic University of Leuven, B-3001, Heverlee-Leuven, Belgium*

Received April 27, 2000

Abstract—The structure of ultradisperse diamond (UDD) conglomerates was studied by scanning atomic-force microscopy (AFM). The UDD layers were prepared from a detonation carbon obtained by synthesis in an aqueous medium. The finest details in the AFM images of UDD layers are of the order of 10 nm, which does not allow individual 4.5-nm diamond clusters to be distinguished. The UDD conglomerates deposited and dried on a silicon substrate surface, exhibit certain deformation and differ from the initial (apparently, spherical) shape. This may imply that cohesion between the UDD nanoparticles is comparable with their adhesion to the silicon substrate. © *2000 MAIK "Nauka/Interperiodica".*

As is known, one of the main technological tasks encountered in growing diamond films by chemical vapor deposition (CVD) methods is to decrease the surface roughness of deposits. This is necessary for the films to be used as masks in X-ray lithography, optical coatings, or materials for microelectronics. The task can be solved by providing a very high (in the order of 10^{10} cm^{-2}) concentration of nucleation centers on the substrate surface [1].

Among the methods capable of providing the required concentration of nucleation centers, especially promising results were obtained by means of ultrasonic processing of the substrate surface with a suspension of diamond powders [2]. Using an ultradisperse diamond (UDD) powder with an average diamond cluster size of 50 Å synthesized by an explosion method, a surface concentration of the nucleation centers as high as 2×10^{11} cm^{-2} was reached [3, 4].

In order to further develop this method of substrate surface treatment, it is necessary to study the initial stages of UDD cluster deposition and aggregation on a substrate in aqueous suspensions of diamond powders. The purpose of this work was to study these processes by method of atomic force microscopy.

As is known, materials in the ultradisperse state possess very high surface energy. As a result, such powders (including UDD) occur in the form of conglomerates with dimensions of the order of a micron, rather than consist of individual clusters with a characteristic size of several nanometers.

Previous investigations of the behavior of UDD particles in hydrosols showed that these powders form conglomerates with dimensions ranging from several hundreds to a few thousand nanometers, depending on the pH of the aqueous dispersion medium. According to the optical microscopy data, UDD powders dried in air also form particles with dimensions of the order of several hundreds of nanometers. Analogous results were obtained by methods of electron microscopy [5, 6].

However, the above methods possess rather limited spatial resolution and sometimes only allowed the conglomerate size to be roughly estimated. Neither structure of these associates nor their packing mode nor the presence or absence of regular package have been established so far. To study these aspects of the UDD powder structure, we have used the method of scanning atomic force microscopy (AFM). Previous attempts at studying UDD samples by this method failed because of the high mobility of the sample particles relative to the substrate. Use of an organic binder to fix the particles could not solve the problem because the particle–binder interaction strongly changed the character of agglomeration in the UDD powder.

In this work, the UDD samples were prepared using a commercial detonation carbon synthesized from a trinitrotoluene–hexogen mixture in an aqueous medium by a procedure analogous to that described in [7]. The UDD powder was extracted from the detonation carbon by oxidation with 50% nitric acid at 220°C in an autoclave. The size of the coherent scattering domains evaluated from the X-ray diffraction line width was 4.5 nm. The size of the UDD particles suspended in an aqueous medium at pH 4, estimated from the sedimentation rate in the Stokes approximation assuming spherical shape, was about 200 nm—in agreement with the data reported previously [8].

The UDD samples for the AFM investigation were prepared by deposition from an aqueous suspension onto a silicon substrate followed by the evaporation of water [9]. The silicon substrates had the surface orien-

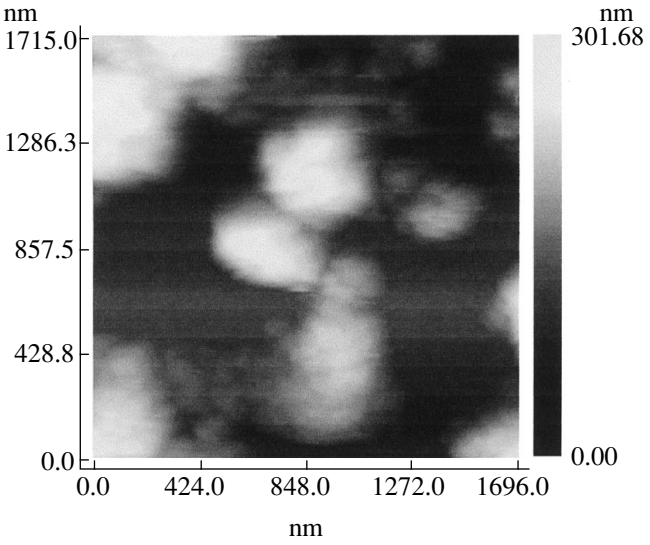

Fig. 1. A typical AFM image of UDD conglomerates on a silicon substrate. The scanned area size, 1700 × 1700 nm.

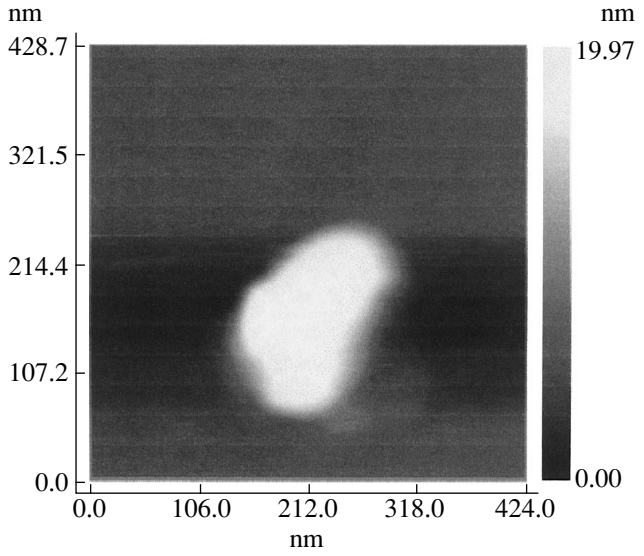

Fig. 2. An AFM image of UDD conglomerates on a silicon substrate. The scanned area size, 425 × 425 nm.

tation (100) and a surface roughness size not exceeding 1 nm. A thin continuous layer of the suspension with an UDD concentration of about 0.05% wt % was applied onto the surface of a horizontal silicon wafer and dried in a thermostat at 120°C for 1 h. The weight-average UDD layer thicknesses determined by ellipsometric measurements at a wavelength of $\lambda = 632.8$ nm ranged from 120 to 350 nm.

In order to obtain more contrast and clear AFM images, the samples were additionally treated for several hours by exposure to UV radiation in air. Apparently, the UV radiation produces etching of the residual amorphous carbon and C–H groups (not removed by the first extraction stage) [10] occurring on the surface of UDD aggregates. The etching is provided by interaction with ozone (formed from air under the UV irradiation), which is a stronger oxidizer than nitric acid used to extract UDD from detonation carbon. The UV radiation was emitted by a krypton-filled lamp (123.6 nm resonance line) with a MgF_2 output window (Cathodeon Ltd., Cambridge, UK). The specific UV light flux was about 10^{14} photon/(cm^2 s).

The sample surface images were obtained in an ARIS 3500 atomic force microscope (Burleigh Instruments Inc., USA) equipped with an ARIS 3005 scanning unit. Operating in the constant force mode (with a point loaded at ~5 nN), the instrument provided a spatial resolution of about 0.1 and 1 nm in vertical and lateral directions, respectively.

Figure 1 shows an AFM image of UDD conglomerates on a silicon substrate. The UDD layer was composed of islands with a height of about 20 nm and a longitudinal (lateral) size reaching hundreds of nanometers. The shape of the UDD conglomerates on the substrate surface showed neither signs of symmetry nor ordered package or preferred directions.

Figures 2 and 3 present AFM images obtained at a higher resolution, showing that the UDD conglomerates are composed of smaller particles with a wide range of shapes and dimensions. Elements sized from several hundreds to a few nanometers could be distinguished in the images. This structure confirmed the assumption concerning the fractal nature of the UDD powders [11] characterized by a self-similar shape of the particles in a range of dimensions from several hundreds to a few nanometers. None of the AFM images obtained, showed evidence of mutual orientation, tex-

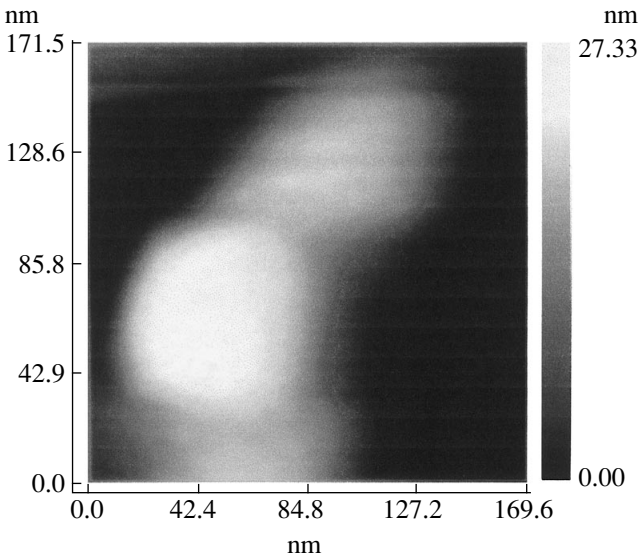

Fig. 3. An AFM image of UDD conglomerates on a silicon substrate. The scanned area size, 170 × 170 nm.

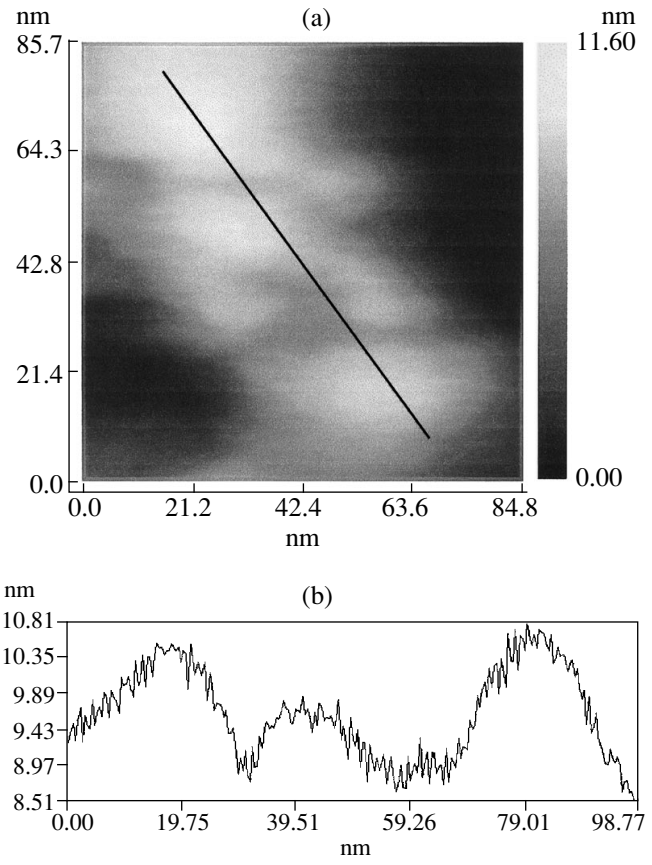

Fig. 4. (a) An AFM image of UDD conglomerates on a silicon substrate. The scanned area size, 85 × 85 nm. (b) An AFM profilogram of UDD conglomerates in the direction indicated by the straight line in the above image.

turing, packing, or faceting of the UDD particles. The finest elements of the AFM images corresponding to the maximum spatial resolution level attained (Fig. 4a) had dimensions in the order of 10 nm, which did allow individual clusters to be reliably distinguished. Although the transmission electron microscopy (TEM) allowed a higher resolution level to be reached, the AFM images have the advantage of providing information about the substance distribution in all three coordinates of a sample [5].

A profilogram presented in Fig. 4b shows that the characteristic height of the UDD conglomerates is about 2.5 nm, which is considerably smaller than the particle dimensions in the surface plane. This implies that deposition and drying of the UDD conglomerates on the substrate surface is accompanied by certain deformation, leading to the loss of the initial (apparently, spherical) shape. This may indicate that cohesive forces between the UDD nanoparticles are comparable with the adhesive forces holding the particles on the silicon substrate.

Thus, we have obtained for the first time the AFM images of ultradisperse diamond particles deposited from an aqueous suspension onto silicon substrates and determined characteristic dimensions of the aggregates.

The authors are grateful to V.I. Siklitskiĭ and M.V. Baĭdakov for fruitful discussions. V. Yu. Osipov is grateful to K. Yakubovskiĭ for his support in visiting the Laboratory of Semiconductor Physics at the Catholic University of Leuven (Belgium). The work was supported by the "Plenka-2" (Film-2) Project of the "Fullerenes and Atomic Clusters" Research Program and by the NATO Linkage Grant HTECHLG No. 973290.

REFERENCES

1. A. A. Smolin, V. G. Ralchenko, S. M. Pimenov, *et al.*, Appl. Phys. Lett. **62** (26), 3449 (1993).
2. C. Tang and D. C. Ingram, J. Appl. Phys. **78** (9), 5745 (1995).
3. T. Yara, H. Makita, A. Hatta, *et al.*, Jpn. J. Appl. Phys., Part 2 **34** (3A), L312 (1995).
4. H. Makita, K. Nishimura, N. Jiang, *et al.*, Thin Solid Films **282**, 279 (1996).
5. M. N. Aleksandrov, V. A. Brylyakov, A. L. Chuvilin, *et al.*, Carbon **29**, 665 (1991).
6. A. E. Aleksenskiĭ, M. V. Baĭdakov, A. Ya. Vul', *et al.*, Fiz. Tverd. Tela (St. Petersburg) **42** (8), 188 (2000) [Phys. Solid State **42**, 1575 (2000)].
7. A. E. Aleksenskiĭ, M. V. Baĭdakova, A. Ya. Vul', and V. I. Siklitskiĭ, Fiz. Tverd. Tela (St. Petersburg) **41** (4), 180 (1999) [Phys. Solid State **41**, 668 (1999)].
8. F. Z. Badaev, O. A. Besedina, P. M. Brylyakov, *et al.*, Dokl. Akad. Nauk SSSR **310** (2), 402 (1989).
9. A. E. Aleksenskiĭ, V. Yu. Osipov, N. A. Kryukov, *et al.*, Pis'ma Zh. Tekh. Fiz. **23** (22), 35 (1997) [Tech. Phys. Lett. **23**, 874 (1997)].
10. V. V. Afanas'ev, A. Stesmans, and M. O. Andersson, Phys. Rev. B **54** (15), 10820 (1996).
11. M. V. Baĭdakova, A. Ya. Vul', V. I. Siklitsikĭ, and N. N. Faleev, Fiz. Tverd. Tela (St. Petersburg) **40** (4), 776 (1998) [Phys. Solid State **40**, 715 (1998)].

Translated by P. Pozdeev

Technical Physics Letters, Vol. 26, No. 9, 2000, pp. 822–823. Translated from Pis'ma v Zhurnal Tekhnicheskoĭ Fiziki, Vol. 26, No. 18, 2000, pp. 36–40.
Original Russian Text Copyright © 2000 by Kleshchinov, Batyaev.

Luminescence of Holmium(III) Ions Activated by Titanium(III) Ions in Potassium-Aluminum-Silicon Phosphate Glass

E. B. Kleshchinov and I. M. Batyaev

State Pedagogical University, St. Petersburg, 191186 Russia

Received April 7, 2000

Abstract—A potassium-aluminum-silicon phosphate glass based phosphor activated by holmium(III) and titanium(III) was synthesized. It is demonstrated that holmium luminescence in the glass under study is sensitized by titanium ions by the dipole–dipole mechanism. No visible reverse energy transfer in the $Ho^{3+} \longrightarrow Ti^{3+}$ pair was observed. © *2000 MAIK "Nauka/Interperiodica".*

Laser phosphors use the phenomenon of luminescence activation to increase the efficiency of lamp pumping when the lasing ions exhibit narrow intrinsic absorption bands. The search for activates is especially important for the laser ions of rare-earth metals (Nd^{3+}, Yb^{3+}, Eb^{3+}, Eu^{3+}, Ho^{3+}, etc.), since the oscillator strengths of their absorption bands are below 10^{-6}. It was demonstrated [1–6] that an effective activation of the Nd^{3+}, Yb^{3+}, and Er^{3+} luminescence in phosphate and silicon phosphate glasses is provided by trivalent titanium ions exhibiting a wide absorption band in the visible part of the spectrum [7–9]. The purpose of this work was to study the possibility of activating the IR luminescence of trivalent holmium in potassium-aluminum-silicon phosphate glass (PASPG) by titanium(III).

Synthesis of the glassy matrix used the method of coprecipitation from solution which ensures a high uniformity of the glass. Concentrations of the activator ions were 0.5 (holmium) and 1 wt % (titanium). An SF-56 spectrophotometer and a high-transmission SDL-1 spectrometer measured the electronic absorption and luminescence spectra of the glasses, respectively. FEU-79 and FEU-62 photomultiplier tubes and a PbS photoresistor detected the luminescence signals. A TRSh (2850–3000 K) tungsten lamp of the known color temperature was used to calibrate the spectrometer. The accuracy of the spectral measurements was 5 cm^{-1}. A DRSh mercury lamp with a set of light filters and a helium–neon laser (λ = 630 nm, P = 55 mW) excited the luminescence. Intensities of the luminescence and luminescence excitation bands were corrected for the spectral sensitivities of detectors.

Based on the experimental results, we conclude that the luminescence of holmium is activated by titanium.

Figure 1 shows the absorption spectrum of a holmium-activated glass. The absorption bands are assigned to electronic transitions from the $^5I_8$ ground state to the ^5F_j, $^2S_2$, and $^3K_8$ components. The $^5I_8 \longrightarrow {}^2S_2$; ^5F_j electronic transition in holmium produces the most intense band peak at ca. 520 nm. The UV excitation of holmium in the glass leads to a weak green luminescence at about 548 nm via by the $^2S_2 \longrightarrow {}^5I_8$ channel and an IR luminescence by the $^5I_7 \longrightarrow {}^5I_8$ transition (Fig. 2).

The $^5I_5$ holmium(III) absorption level (λ = 915 nm) overlaps with the titanium(III) luminescence band (curve *B* in Fig. 1), which suggests a nonradiative energy transfer in this pair by a resonance mechanism. The studies of the PASPG–Ti^{3+}–Ho^{3+} luminescence spectra revealed a 1.25-fold decrease in the titanium luminescence intensity. The holmium luminescence band at 2010 nm did not exhibit any detectable

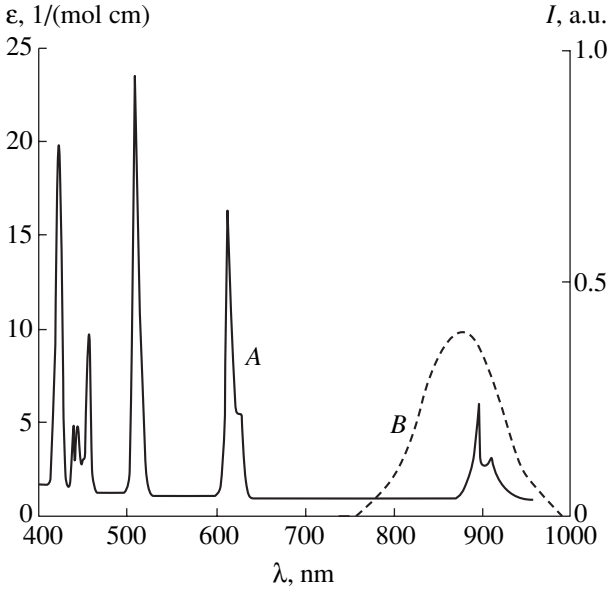

Fig. 1. (*A*) PASPG–Ho^{3+} absorption and (*B*) PASPG–Ti^{3+} luminescence spectra.

1063-7850/00/2609-0822$20.00 © 2000 MAIK "Nauka/Interperiodica"

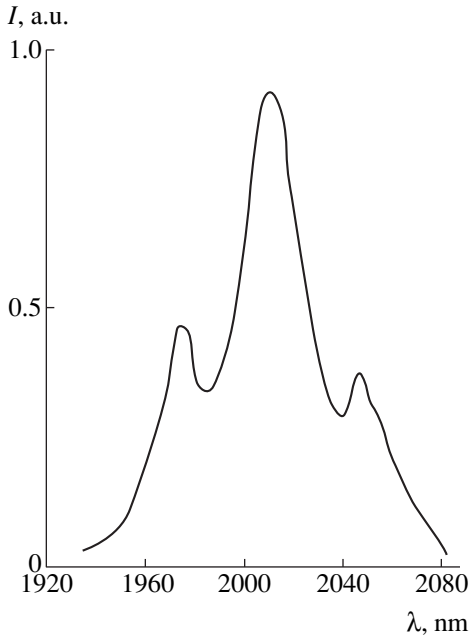

Fig. 2. Holmium luminescence spectrum in PASPG ($^5I_7 \longrightarrow {}^5I_8$ transition).

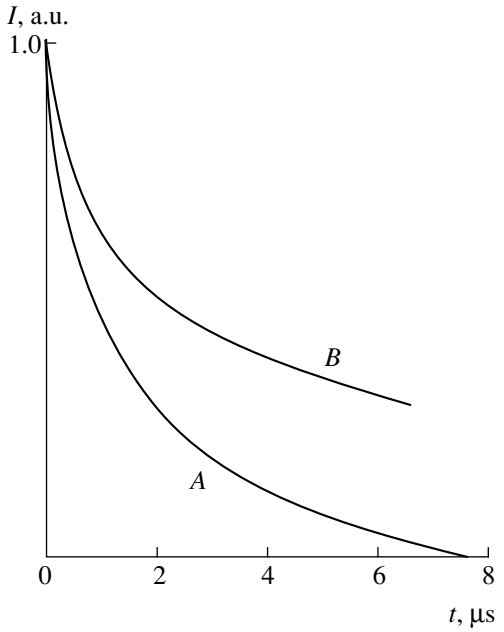

Fig. 3. Titanium(III) luminescence decay curves in (*A*) PASPG–Ti^{3+}–Ho^{3+} and (*B*) PASPG–Ti^{3+}.

changes. Figure 3 shows the luminescence decay curves of titanium(III) in PASPG–Ti^{3+}–Ho^{3+} and PASPG–Ti^{3+}. An analysis of these curves revealed a decrease from 6 to 4.6 μs in the mean lifetime of the excited state of titanium(III) in the presence of holmium.

Experimental data on a decrease in the titanium luminescence intensity and lifetime in Ti^{3+}–Ho^{3+} system give evidence of the nonradiative energy transfer. Excitation energy transfer is likely to proceed by the $Ti^{3+}({}^6B_{1g} - {}^2E_g) \longrightarrow Ho^{3+}({}^5I_8 - {}^5I_5)$ channel. The subsequent relaxation to a metastable $^5I_8$ level is accompanied by activated luminescence.

Modeling of the experimental kinetic curve using the known functions describing the donor luminescence decay in the presence of an acceptor [9] suggests a dipole–dipole energy transfer mechanism for the Ti^{3+}–Ho^{3+} pair. The calculation of the quantum efficiency of the transfer by the formula

$$n = \frac{\tau_{od} - \tau_d}{\tau_{od}},$$

where τ_d and τ_{od} are the donor luminescence lifetimes in the presence and absence of the acceptor, respectively, yields a rather low value of 0.24. The Ho^{3+} coactivation by titanium ions at such a low transfer efficiency can hardly lead to increasing efficiency of the holmium luminescence in glass. However, the variation in the matrix components will possibly allow an increase in the transfer efficiency. The $^5I_7 \longrightarrow {}^5I_8$ holmium laser channel in PASPG–Ti^{3+}–Ho^{3+} exhibits the luminescence lifetime close to that of the noncoactivated Ho^{3+} ions. This similarity indicates the absence of the holmium 2-μm luminescence quenching by titanium to encourage the further studies of the Ti^{3+}–Ho^{3+} pair in glasses.

Thus, we have demonstrated, for the first time a possibility of the holmium luminescence activation in glasses by titanium(III) ions.

REFERENCES

1. I. M. Batyaev and E. B. Kleshchinov, Opt. Spektrosk. **81** (5), 823 (1996) [Opt. Spectrosc. **81**, 753 (1996)].
2. I. M. Batyaev and E. B. Kleshchinov, Pis'ma Zh. Tekh. Fiz. **22** (12), 34 (1996) [Tech. Phys. Lett. **22**, 494 (1996)].
3. I. M. Batyaev and S. B. Sukhanov, Opt. Spektrosk. **72** (6), 1367 (1992) [Opt. Spectrosc. **72**, 765 (1992)].
4. I. M. Batyaev and I. V. Golodova, Opt. Spektrosk. **77** (1), 81 (1994) [Opt. Spectrosc. **77**, 45 (1994)].
5. I. M. Batyaev and E. B. Kleshchinov, Pis'ma Zh. Tekh. Fiz. **23** (21), 7 (1997) [Tech. Phys. Lett. **23**, 820 (1997)].
6. I. M. Batyaev and E. B. Kleshchinov, Zh. Obshch. Khim. **67** (7), 1207 (1997).
7. E. B. Kleshchinov, Author's Abstract of Candidate's Dissertation (Gertsen State Pedagogical Univ., St. Petersburg, 1997).
8. I. M. Batyaev and S. B. Sukhanov, Pis'ma Zh. Tekh. Fiz. **20** (10), 38 (1994) [Tech. Phys. Lett. **20**, 403 (1994)].
9. I. M. Batyaev and I. V. Golodova, Opt. Spektrosk. **78** (3), 468 (1995) [Opt. Spectrosc. **78**, 421 (1995)].

Translated by A. Chikishev

Technical Physics Letters, Vol. 26, No. 9, 2000, pp. 824–826. Translated from Pis'ma v Zhurnal Tekhnicheskoĭ Fiziki, Vol. 26, No. 18, 2000, pp. 41–46.
Original Russian Text Copyright © 2000 by Rukin, Tsyranov.

Subnanosecond Breakage of Current in High-Power Semiconductor Switches

S. N. Rukin and S. N. Tsyranov

Institute of Electrophysics, Ural Division, Russian Academy of Sciences, Ekaterinburg, Russia

Received February 25, 2000; in final form, May 15, 2000

Abstract—The process of high-density current breakage in an SOS diode structure was studied using a corresponding theoretical model. For a *p–n* junction depth of ~200 μm, a forward pumping time shorter than 60 ns, and a reverse pumping time of ~10–15 ns, the structure studied exhibits a subnanosecond breakage of a current with a density of up to 10^3–10^4 A/cm^2. The mechanism of current breakage involves the formation of two spatially separated domains featuring strong electric field build-up on the *p* side of the diode structure, which expand during the current breakage at a velocity close to the carrier velocity saturation level. © *2000 MAIK "Nauka/Interperiodica".*

1. In recent years, developments in the high-power nanosecond pulse technology have led to the creation of semiconductor switches of a new type, called SOS diodes, which are capable of switching pulses on a gigawatt level at a voltage of up to 10^6 V [1]. The SOS effect, representing a nanosecond breakage of a superhigh-density current in the semiconductor structure, can be observed in silicon-based p^+–p–n–n^+ structures at a pumping time in the order of 10^{-7} –10^{-6} s and a reverse current density of 1–60 kA/cm^2 [2, 3]. Under these conditions, the time of current breakage falls within 5–10 ns.

Since the process of current breakage in an SOS diode is related to the dynamics of excess electron-hole plasma generated in the diode structure, the commutation characteristic of the SOS diode must depend on the excess carrier plasma density profile. This was confirmed in [4] where the regime of subnanosecond current was observed upon decreasing the pumping time. The purpose of this work was to consider the physical processes in an SOS diode structure operating in a subnanosecond switching regime.

2. The electron-hole plasma dynamics was analyzed within the framework of a theoretical model described in [2]. Figure 1a shows a typical SOS diode structure with a deep aluminum diffusion profile. The depth of the *p–n* junction was 220 μm at a total silicon plate thickness of 320 μm. The calculations were performed for an SOS diode structure comprising a series of 80 units of this type with an area of 0.24 cm^2. The electric circuit parameters corresponded to the experiment described in [4]. After the forward pumping capacitor was switched on, a current with a density of up to 1 kA/cm^2 built up in the system within a time of less than 60 ns. The subsequent switching on of the reverse pumping capacitor gave rise to a reverse current build-up in the system within 10–15 ns, with the current density increasing up to 4 kA/cm^2 at the moment of current breakage.

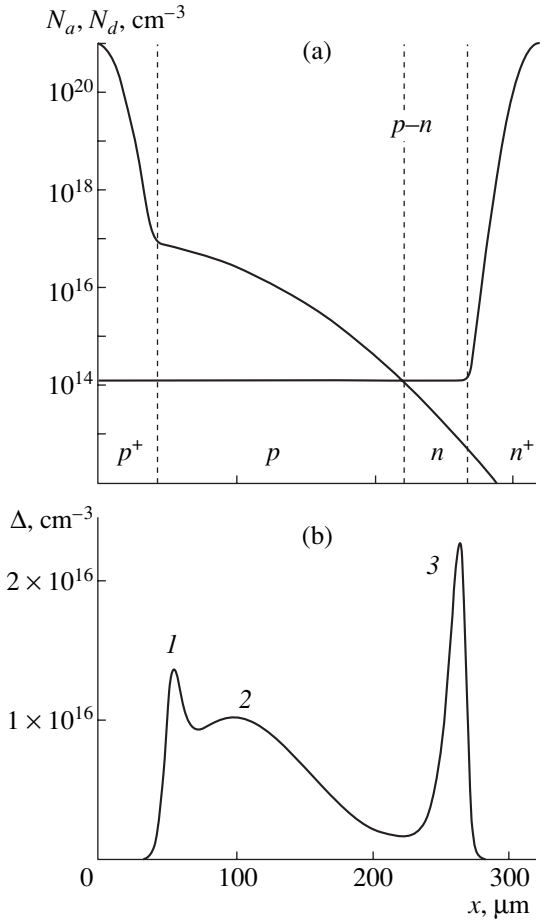

Fig. 1. SOS diode characteristics showing profiles of (a) the dopant (aluminum) diffusion and (b) the excess charge carrier concentration accumulated in the forward pumping stage.

1063-7850/00/2609-0824$20.00 © 2000 MAIK "Nauka/Interperiodica"

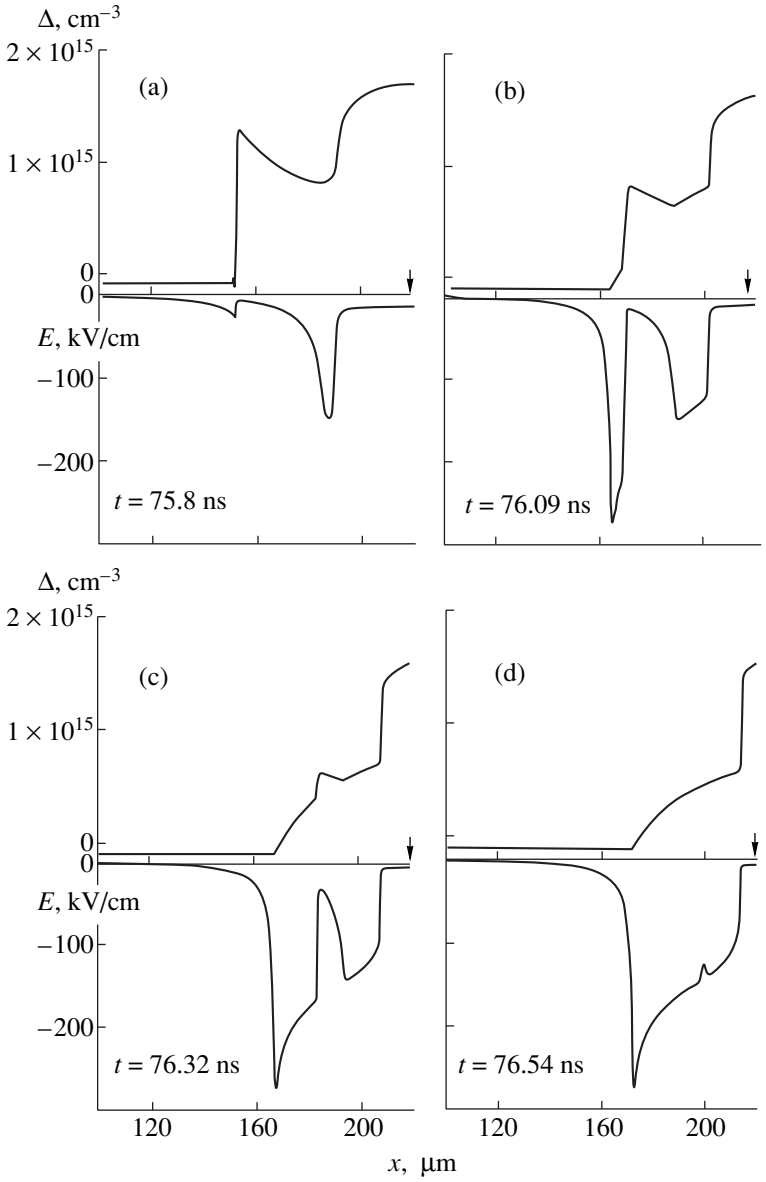

Fig. 2. Profiles of the excess charge carrier concentration and the electric field strength in the *p* region of a SOS diode structure at four sequential time instants of the process of subnanosecond current breakage (current density, 3.8 kA/cm^2). The arrow indicates the *p*–*n* junction position in the structure.

3. It was established that, for a forward pumping time $t^+ \leq 60$ ns and a forward current density of ~1 kA/cm^2, the charge carrier concentration accumulated in the left part of the SOS diode structure exhibited two characteristic maxima near the p^+–p junction (Fig. 1b, peaks *1* and *2*). A different pattern is observed for long periods (300–600 ns) of forward pumping, whereby a single carrier concentration maximum is observed in the same region [2]. In both cases, another carrier concentration maximum (Fig. 1b, peak *3*) is observed in the right part of the SOS diode structure near the n–n^+ junction. The excess carrier concentration Δ in the model under consideration (Figs. 1b and 2) is determined by the expression $\Delta = p - N_a = n - N_d$, where p, n are the total concentrations of holes and electrons, and N_a, N_d are the total concentrations of acceptors and donors, respectively.

The results of mathematical modeling showed that the appearance of two maxima (peaks *1* and *2*) instead of one is due to a field build-up near the p^+–p junction. The formation of peaks *1* and *2* is determined by the amount of charge Q^+ passed in the stage of forward pumping: for $t^+ \leq 60$ ns, this condition is fulfilled for $Q^+ = (2\text{–}6) \times 10^{-5}$ C/cm^2. The concentration of accumulated charge carriers corresponding to peaks *1* and *2* is ~10^{16} cm^{-3}. In the case of long forward pumping times, the Q^+ value accordingly increases and the p^+–p junc-

tion is filled with a dense plasma, which corresponds to a single carrier concentration maximum of ~10^{17} cm^{-3}.

Distribution of the concentration of carriers accumulated in the *p* region also exhibits two maxima. The first of these is situated between p^+ region and peak *1*, while the second takes place between peaks *1* and *2* (Fig. 1b). In the stage of reverse pumping, the excess carrier plasma moves toward the *p*–*n* junction. The concentration of charge carriers continuously decreases (to reach a level of (1–4) × 10^{15} cm^{-3} before the current breakage) and the carrier distribution profile retains the initial inhomogeneity manifested by two concentration maxima (peaks *1* and *2*). The process of current breakage begins when the velocity of carriers exhibits saturation in the SOS diode sections with minimum carrier plasma densities. Here, two domains of maximum electric field strength appear that facilitate the generation of additional charge carriers and the current passage.

Figure 2 illustrates the dynamics of the excess carrier plasma density and electric field strength variation in the SOS diode structure with a current density of 3.8 kA/cm^2. Here, the profiles show only a part of the *p* region of the structure in front of the *p*–*n* junction, that is, in the region where the strong field build-up and the current breakage processes take place. The first excess carrier concentration profile (Fig. 2a) corresponds to the breakage onset, where the current density decreases by 5%. The last profile (Fig. 2d) refers to the final stage of current breakage, when a maximum voltage across the structure is developed. A time interval between the first and last patterns just corresponds to the switching process duration and amounts to 740 ps in agreement with the experimental data reported in [4]. Note that another strong field domain appears at the instant of current breakage in the *n* region (on the left of peak *3*). However, having a width not exceeding 2.5 μm, this domain does not significantly contribute to the voltage drop and cannot significantly influence the process of current breakage.

4. An analysis of the mathematical modeling results indicated that a subnanosecond breakage of current is realized due to three principal factors. The first is the existence of two spatially separated domains of the electric field build-up which exhibit simultaneous expansion to overlap one another by the end of the commutation process, thus forming a region with a width of about 50 μm in which the field strength reaches up to 200 kV/cm. The second factor is a low excess carrier plasma density determining high velocity of motion of both plasma and field boundaries. Under these conditions, the average rate of formation of a common field domain responsible for the current breakage reaches 70% of the carrier velocity saturation level in silicon (which is 6–7 times the velocity of the field build-up in the case of long pumping times [1]). The third factor necessary for realization of the subnanosecond current breakage consists in using SOS diode structures with maximum possible width of the *p* region, where the *p*–*n* junction depth is in the order of 200–220 μm. This is necessary, on the one hand, in order to decrease the concentration of excess charge carriers accumulated in the stage of forward pumping and, accordingly, to increase the velocity of the plasma and field domain boundaries in the following stages of reverse pumping and current breakage. On the other hand, a higher velocity of the plasma boundary requires *p* region of a greater width, since the formation of a strong field domain must be finished by the time the excess plasma reaches the *p*–*n* junction.

REFERENCES

1. S. N. Rukin, Prib. Tekh. Éksp., No. 4, 5 (1999).
2. S. A. Darznek, G. A. Mesyats, and S. N. Rukin, Zh. Tekh. Fiz. **67** (10), 64 (1997) [Tech. Phys. **42**, 1170 (1997)].
3. S. A. Darznek, S. N. Rukin, and S. N. Tsiranov, Zh. Tekh. Fiz. **70** (4), 56 (2000) [Tech. Phys. **45**, 436 (2000)].
4. S. K. Lyubutin, G. A. Mesyats, S. N. Rukin, *et al.*, Dokl. Akad. Nauk **360** (4), 477 (1998) [Dokl. Phys. **43**, 349 (1998)].

Translated by P. Pozdeev

Technical Physics Letters, Vol. 26, No. 9, 2000, pp. 827–828. Translated from Pis'ma v Zhurnal Tekhnicheskoĭ Fiziki, Vol. 26, No. 18, 2000, pp. 47–49.
Original Russian Text Copyright © 2000 by Usanov, Gorbatov, Orlov, Wenig.

Resonances in a Semiinfinite Waveguide with Iris in Relation to the Excitation of Higher-Order Modes

D. A. Usanov, S. S. Gorbatov, V. E. Orlov, and S. B. Wenig

Saratov State University, Saratov, 410601 Russia

e-mail: WenigSB@info.sgu.ru

Received March 29, 2000

Abstract—New types of resonances were discovered in a structure comprising a short-circuited waveguide and a capacitive iris in the case when the distance between the iris and the short is in the order of several hundredths of the waveguide wavelength. The existence of these resonances is explained by the excitation of high-order modes in the iris aperture. It was found that a more complicated shape of the iris aperture results in the frequency characteristic of the electromagnetic structure considered becoming similar to that of a band-pass filter. This fact is explained by the enrichment of the spectrum of high-order modes. *© 2000 MAIK "Nauka/Interperiodica".*

In constructing various waveguide systems, designers commonly assume that the wave propagation conditions are only ensured for the fundamental mode. This assumption is also used in the design of devices with resonance features (an inductive post with a capacitive gap, resonant iris, etc.). Such elements are widely used in various microwave semiconductor devices operating at high microwave power levels. Analyzing the operation of these devices, researchers usually note that the field of the fundamental mode may be substantially distorted near the discontinuity (a post or an iris). This fact is associated with the excitation of rapidly decaying (evanescent) high-order modes.

We suggested that the resonance features may be observed if a discontinuity is placed near the waveguide wall, at a distance insufficient for the high-order modes to decay. This assumption was confirmed by placing a capacitive iris in a short-circuited waveguide at a dis-

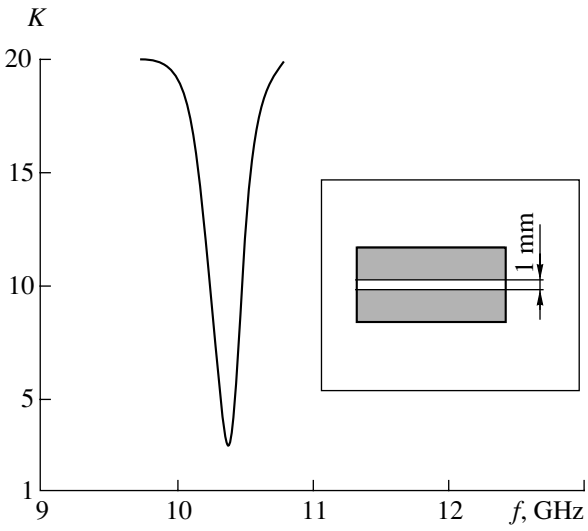

Fig. 1. The voltage standing-wave ratio K vs. frequency for a capacitive iris. The distance to the waveguide wall is 520 μm.

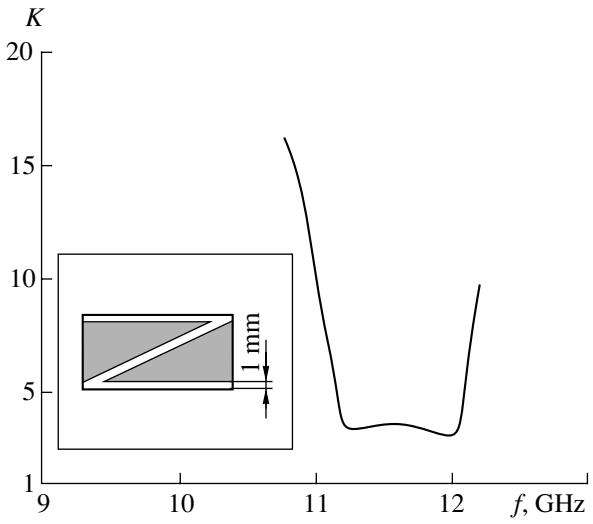

Fig. 2. The voltage standing-wave ratio K vs. frequency for an iris of complex shape. The distance to the waveguide wall is 400 μm.

1063-7850/00/2609-0827$20.00 © 2000 MAIK "Nauka/Interperiodica"

tance of ~$\lambda_w/100$ (where λ_w is the waveguide wavelength) from the short (Fig. 1). Evidently, if the iris configuration is more complex (Fig. 2), the spectrum of arising high-order modes may be substantially enriched. In this case, we may obtain frequency characteristics that are typical of a band-pass filter. Such characteristics are formed as a result of an overlap of the resonance curves related to individual high-order modes with close frequencies. A good illustration to validate the latter inference is the measured amplitude-frequency characteristic of a system comprising a short-circuited waveguide and an iris placed at a distance of $\lambda_w/100$ from the short (Fig. 2).

The above results show a possibility for designing new types of microwave devices, including semiconductor devices, with reduced overall dimensions.

Translated by A. Kondrat'ev

Technical Physics Letters, Vol. 26, No. 9, 2000, pp. 829–831. Translated from Pis'ma v Zhurnal Tekhnicheskoĭ Fiziki, Vol. 26, No. 18, 2000, pp. 50–56.
Original Russian Text Copyright © 2000 by Persiantseva, Popovicheva, Starik, Trukhin, Shoniya.

Hydrophilicity of Soot Particles Formed in the Combustion Chamber of a Jet Engine

N. M. Persiantseva, O.B. Popovicheva, A. M. Starik, M. E. Trukhin, and N. K. Shoniya

Moscow State University, Moscow, 119899 Russia
Central Institute of Aircraft Engine Building, Moscow, Russia

Received April 26, 2000

Abstract—The particles of soot, formed in the combustion chamber of a jet engine under conditions typical of a cruising power mode, are capable of adsorbing a considerable amount of water vapor owing to their microcrystalline structure, microporosity, and chemically heterogeneous surface. *© 2000 MAIK "Nauka/Interperiodica".*

Soot particles are an important component of the products formed upon combustion of aviation fuels. These particles play a significant role in the formation of the condensation trail of an aircraft and the tropospheric soot aerosol layer [1, 2]. The presence of sulfur-containing compounds in the aviation fuels and the possible appearance of these compounds in the soot aerosols may lead to the formation of additional cloud condensation centers [3]. It was commonly believed until recently that the soot particles formed in the combustion chamber of a jet engine are intrinsically hydrophobic and it is the interaction of these particles with gases in the exhaust stream that results in the modification of the surface properties of soot, after which the particles become capable of adsorbing water [4].

Now there are certain doubts as to whether the soot particles are inherently hydrophobic. Indeed, the experimental investigations of the hygroscopic properties of soot particles were usually performed either with the products obtained upon the combustion of hydrocarbons and natural fuels in a diffusion torch [5, 6], with a commercial soot [7], or with a soot formed from graphite electrodes under discharge conditions [6, 8]. However, significantly different conditions of soot formation are encountered in the combustion chamber of a jet engine. The hygroscopicity of soot particles is determined to a considerable extent by the nature of their surface, the physicochemical characteristics of which significantly depend on the conditions of the soot formation. Therefore, various samples of soot may considerably differ in both structure and reactivity. The purpose of this work was to study the hydration characteristics of soot particles collected in the in the combustion chamber of a jet engine.

The samples of soot were obtained using a setup based on the combustion chamber of an aircraft turbine engine, which provided the fuel combustion conditions typical of the cruising power mode (pressure P = 0.4 MPa; excess air coefficient, 3–4; combustion temperature, 1800–1500 K). Instead of the liquid aviation kerosene (usually comprising a mixture of C_8H_{18}, $C_{10}H_{20}$, and $C_{12}H_{24}$ with a small amount of impurities), we have used a gaseous fuel with the composition $0.9C_3H_8 + 0.1C_4H_{10}$ supplied to the engine via a nozzle to be mixed with hot (600 K) air. Numerical analysis showed that the conditions of combustion and the dynamics of changes in concentrations of the N-, H-, and C-containing components during the combustion of the gaseous mixture used were much like those for aviation fuel. Therefore, the process of soot formation from fuels of the two types must be essentially the same. The soot was collected on an air-cooled sampler situated at a distance of 12 cm from the combustion chamber output edge, in a stream of hot exhaust gases with a temperature of ~800–1000 K. We believe that the soot particles obtained under these conditions and used for the measurement of adsorption properties did not virtually interact with the gaseous combustion products because of very short time (≅1 ms) of exposure in the jet stream.

In order to study the mechanisms of water vapor adsorption on soot particles, it is necessary to gain information concerning the structure and physicochemical properties of the particle surface. The porosity and specific surface of the soot particles were determined from the results of gravimetric measurements of the isotherms of benzene adsorption on the sample surface. The measurements were performed in a high-vacuum temperature-controlled setup equipped with the McBain quartz balance. Features of the surface microstructure of soot particles were studied by Raman scattering spectroscopy.

Figure 1 shows the C_6H_6 adsorption–desorption isotherms for the soot sample studied. A considerable increase in the amount of adsorbed benzene in the ini-

1063-7850/00/2609-0829$20.00 © 2000 MAIK "Nauka/Interperiodica"

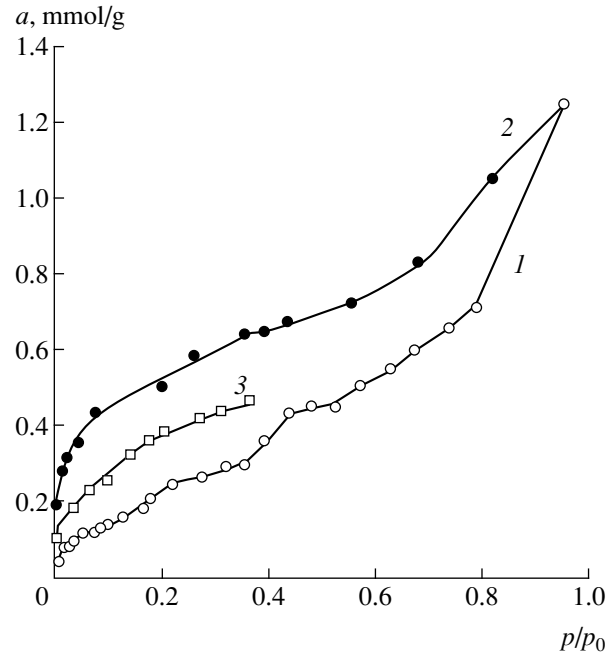

Fig. 1. Isotherms of room-temperature benzene (*1*, *3*) adsorption on and (*2*) desorption from soot. Curve *3* was measured during repeated adsorption upon termination of the first cycle.

tial region of the isotherm ($\bar{p} = p/p_0$, where p_0 is the saturated vapor pressure) is indicative of a sufficiently well developed surface of the soot particles. The nearly horizontal shape of the hysteresis loop suggests that the particles may contain narrow (slotlike) pores. The appearance of these pores is related to certain features in the microstructure of the particles determined from the Raman scattering data presented in Fig. 2. The presence of two peaks (1598 and 1347 cm^{-1}) with comparable intensities is characteristic of a graphitized material composed of disordered microcrystallites with a size of ~2–4 nm [9]. The space between graphite planes in the microcrystallites and the intercrystallite voids form micropores into which the adsorbed gas molecules may penetrate.

Using the benzene adsorption isotherm measured for the soot sample studied, we may estimate the specific surface S_s of soot particles by the BET method [10]. It was found that this value varies with the relative pressure $\bar{p}$: $S_s \cong 32$ m^2/g for the pressure interval $0.01 \le \bar{p} \le 0.1$ and $S_s \cong 48$ m^2/g for $0.2 \le \bar{p} \le 0.4$. Estimates obtained during another cycle of benzene adsorption give $S_s \cong 96$ m^2/g. The increase in specific surface with the pressure $\bar{p}$ is related to features of the porous structure of the soot, whereby the surface of the particles may transform under the action of adsorbed molecules. According to this phenomenon, known as the "swelling" of soot [10], once a definite amount of adsorbate is accumulated on the surface of soot particles, benzene molecules begin to penetrate into previously unaccessible micropores of dimensions comparable with the size of molecules. This leads to the deformation of the porous structure and is accompanied by the increasing adsorption capacity of the soot particles. As a result, a greater amount of C_6H_6 molecules adsorb on the same sample during repeated adsorption cycles (Fig. 1, curve *3*).

In the case of polar molecules such as H_2O, the adsorption is significantly affected, not only by the structural features of soot, but by the presence of active (especially, oxygen-containing) groups and chemisorbed oxygen as well. To analyze the adsorption of

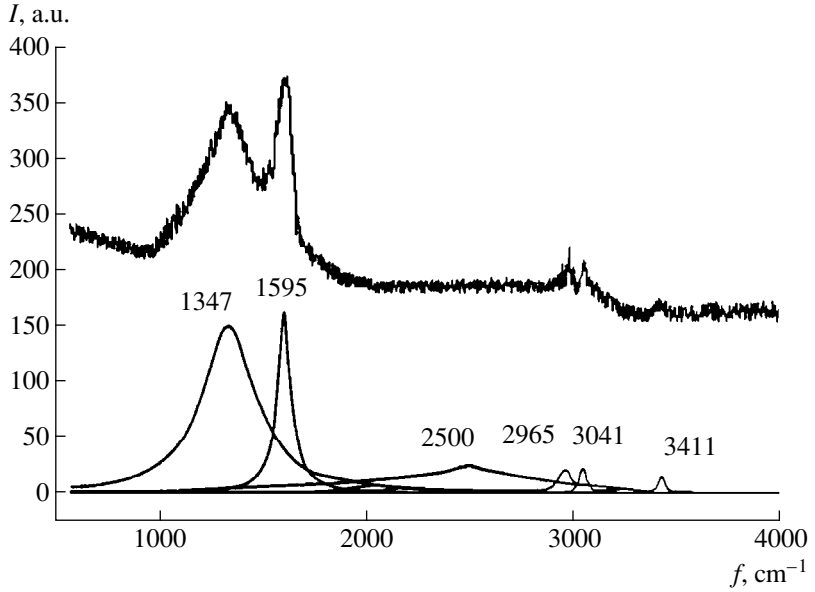

Fig. 2. Raman scattering spectra of soot (peak wavenumbers indicated in cm^{-1}).

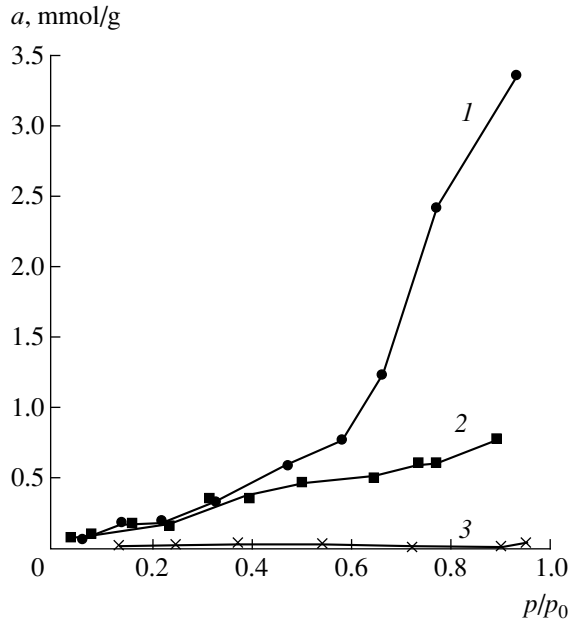

Fig. 3. Isotherms of water vapor adsorption: (*1*) on soot, (*2*) on the same soot preliminarily exposed to benzene, and (*3*) on a reference graphite sample.

water vapor on soot particles, we used a volumetric method consisting in the measurement of changes in the gas pressure caused by the loss of molecules from the gas phase as a result of adsorption on the surface of soot particles. Figure 3 shows the adsorption isotherms of water vapor on the soot particles studied and on a graphite sample ($S_s \cong 20$ m^2/g), the latter being used as a reference hydrophobic carbon-containing material. As seen, graphite features a very low water adsorption up to a pressure of $\bar{p} \cong 0.95$. The amount of water adsorbed on the soot is 10 times that on graphite even at $\bar{p} \cong 0.1$. This behavior can be explained by assuming that the adsorption of water at low relative pressures takes place on active surface centers. These centers can be represented by acid and base surface groups, the presence of which is indicated by relatively weak bands observed in the Raman spectra of soot at 2965 and 3041 cm^{-1} assigned to the antisymmetric vibrations of methyl (CH) and hydroxyl (OH) groups, respectively (Fig. 2).

As the relative pressure $\bar{p}$ increases, water molecules adsorb above the previously adsorbed species, which explains the continuous growth observed on the adsorption isotherm. A sharp increase in the amount of adsorbed molecules at $\bar{p} > 0.6$ is probably due to the formation of complexes between H_2O molecules in micropores, linked by intermolecular hydrogen bonds [10]. This mechanism is confirmed by the absence of enhanced water adsorption on soot at $\bar{p} > 0.6$ in the case of samples preliminarily exposed to benzene vapors (Fig. 3).

The results of our investigations showed that the particles of soot formed in the combustion chamber of a jet engine possess a nonrigid structure and a chemically heterogeneous surface. Owing to these properties, the soot particles are capable of adsorbing a considerable amount of water. Interaction of the sulfur-containing products, formed during the combustion of aviation kerosene, with the surface of soot particles will additionally increase their hydrophilic character. Therefore, the particles of soot ejected into atmosphere may be effective cloud condensation centers participating in the formation of a condensation trail of an aircraft and in the induced cloudiness production.

The authors are grateful to E.B. Rulev for measurement of the Raman spectra. The work was supported by the Russian Foundation for Basic Research (project no. 00-159-6554) and the EC Grant no. ENV4-CT97-0620.

REFERENCES

1. O. B. Popovicheva, A. M. Starik, and O. N. Favorskiĭ, Preprint No. 8-427, IVTAN (1998).
2. G. P. Brasseur, R. A. Cox, D. Hauglustaine, *et al.*, Atmos. Environ. **32** (13), 2329 (1998).
3. D. E. Hagen, M. E. Trueblood, and D. E. White, Aerosol. Sci. Technol. **10**, 63 (1989).
4. B. Karcher, Th. Peter, U. M. Biermann, and U. Schumann, J. Atmos. Sci. **53**, 3066 (1996).
5. A. R. Chughtai, N. J. Miller, D. M. Smith, and J. R. Pitts, J. Atmos. Sci. **34**, 259 (1999).
6. E. F. Mikhaĭlov, S. S. Vlasenko, A. A. Kiselev, and T. I. Ryshkevich, Izv. Akad. Nauk, Fiz. Atmos. Okeana **34**, 345 (1998).
7. C. A. Rogalsky, D. M. Golden, and L. R. Williams, Geophys. Res. Lett. **24**, 381 (1997).
8. R. Niessner, B. Daeumer, and D. Klockow, Aerosol. Sci. Technol. **12**, 953 (1990).
9. D. S. Knight and W. B. White, J. Mater. Res. **4**, 385 (1989).
10. S. J. Gregg and K. S. Sing, *Adsorption, Surface Area, and Porosity* (Academic, New York, 1982; Mir, Moscow, 1984).

Translated by P. Pozdeev

Technical Physics Letters, Vol. 26, No. 9, 2000, pp. 832–834. Translated from Pis'ma v Zhurnal Tekhnicheskoĭ Fiziki, Vol. 26, No. 18, 2000, pp. 57–62.
Original Russian Text Copyright © 2000 by Shuaibov, Dashchenko, Shevera.

Optical Diagnostics of Laser-Generated Indium Plasma

A. K. Shuaibov, A. I. Dashchenko, and I. V. Shevera

Uzhgorod State University, Uzhgorod, Ukraine

Received April 21, 2000

Abstract—The optical emission from a plasma torch formed at the surface of an indium target under the action of laser radiation with a wavelength of $\lambda = 1.06$ μm and a power of $(3–5) \times 10^8$ W/cm^2 was studied. Wide-scan (200–600 nm) emission spectra, relative intensity distributions of the emission In(I) and In(II) lines, and the dynamics of the emission from the plasma of the nucleus of the erosion torch were measured. The total emission spectrum of the plasma represents In(I) and In(II) lines on a continuous emission background. The most intense lines at 451.1, 410.2, 325.8 (6), and 271.1 (4) nm correspond to the upper excited states with energies in the range from 3.02 to 4.84 eV. The principal mechanism of occupation of the excited states of indium atoms and ions in the laser-generated plasma is the two-electron recombination. The emission duration for the In(II) transitions in plasma of the laser torch nucleus does not exceed 80–100 ns, while that for the In(I) transitions amounts to 400–700 ns. The corresponding upper limits of the recombination times for In(III) and In(II) ions are 50 and 500 ns, respectively. © *2000 MAIK "Nauka/Interperiodica".*

Indium is an important component in layered crystals such as $CuInS_2$ and $CuInSe_2$ widely used in the laser deposition of thin films. Since the mechanisms of formation and the parameters of laser-generated plasmas are frequently studied by optical methods, it is important to analyze the individual atomic components of the emission spectra for moderate powers of a laser (e.g., neodymium). In the third group of the Periodic Table, the optical characteristics of laser-generated plasma were most thoroughly studied for aluminum [1–3]. At the same time, the optical characteristics of the laser erosion plasma of indium (typically formed by short pulses of a Nd laser with a pulse energy of ≤10–20 mJ) were not studied using modern photoelectric registration systems.

Below we report on the spectroscopic diagnostics of a laser-generated indium plasma obtained using a moderate-power YAG:Nd^{3+} laser.

The experiments were performed with a periodic-pulse laser with a wavelength of $\lambda = 1.06$ μm capable of producing a power of $(1–5) \times 10^8$ W/cm^2 in a beam focused to a spot size of 0.3–0.5 mm on a target surface. The target represented a plate of special-purity indium mounted in a vacuum chamber with a residual pressure of 3–12 Pa. The optical emission from the laser-generated torch plasma was studied using a system comprising an MDR-2 monochromator, FEY-106 photoelectron multiplier tube, and a KSP-4 recorder with an amplifier calibrated for the 200–600 nm spectral range. The laser radiation pulses were registered using an ELU-14FS linear electron multiplier and a high-frequency 6LOR-04 oscillograph. The experimental system is described in more detail elsewhere [5]. The emission was taken with the aid of a lens in the direction of the plasma torch axis, from a point in the plasma of the laser torch nucleus at a distance of about d = 1 mm from the indium surface. The spectral lines were identified by reference to the data in [6, 7].

Figure 1 shows a wide-scan spectrum of emission from the plasma of a laser-generated torch at the indium target surface. Relative emission intensities I/k_λ (k_λ is the relative spatial sensitivity of the registration system) of the main spectral lines observed in the spectrum of emission from indium atoms are listed in the table. The emission lines corresponding to electron transitions in In(I) and In(II) were observed on a background of the continuous emission spectrum exhibiting a maximum intensity at the target surface. In the spectrum of line emission from the laser-generated plasma,

The most intense spectral lines of In(I) in the emission spectrum of laser-generated indium plasma

λ, nm	Transition	E_{up}, eV	I/k_λ, arb. units	Q_{max}, 10^{-18} cm^2 [7]
451.1	$5^3P_{3/2}$–$6^2S_{1/2}$	3.02	1.00	172
410.2	$5^2P_{1/2}$–$6^2S_{1/2}$	3.02	0.75	69
325.8	$5^2P_{3/2}$–$5^2D_{5/2}$	4.08	0.85	55
303.9	$5^2P_{1/2}$–$5^2D_{3/2}$	4.08	0.50	83
271.1	$5^2P_{3/2}$–$6^2D_{5/2}$	4.84	0.25	9

1063-7850/00/2609-0832$20.00 © 2000 MAIK "Nauka/Interperiodica"

the maximum intensity was observed for the In(I) emission lines at 451.1, 410.2, 325.8 (6), and 271.1 (4) nm. A comparison of the relative emission intensity distribution in the spectrum of the plasma of the laser torch nucleus to the values of the effective cross sections Q_{max} for the electron excitation of In(I) and In(II) [7] showed no evidence of a general correlation. Therefore, a more probable mechanism for the occupation of the excited states in In(I) and In(II), as well as in aluminum [4], is offered by the process of two-electron recombination in In(II) and In(III), respectively. The uppermost level of In(I) for which the emission was observed (with an energy of 5.37 eV) can be considered as a limiting point in the recombination flux.

For more detailed characterization of a mechanism responsible for excitation of the In(I) and In(II) levels in the laser-generated plasma, we have studied the kinetics of emission from the plasma of the erosion torch nucleus (Fig. 2). The beginning of the sweep in the oscillograms corresponds to the leading front of a pulse of the YAG:Nd^{3+} laser. A minimum duration of the continuous emission (20 ns) corresponded to the pulse width of the neodymium laser. The duration of emissions corresponding to transitions in the excited indium ions In(II) did not exceed 80–100 ns, while that for the transitions in indium atoms In(I) reached 500–700 ns. This scale of emission times for the transitions in In(I) and In(II), as well as that observed for the Al(II) and Al(I) emission lines [4], confirms the proposed recombination mechanism of the occupation of excited levels in In(I) and In(II).

As the energy of the uppermost level decreased (from E_{up} = 5.73 to 3.02 eV), the duration of the emission of the spectral lines of In(I) increased from 400 to 700 ns. This can be related both to the cascade occupation of the $6^2S_{1/2}$ state in In(I) and to the character of the recombination occupation process. The oscillograms of the emission intensity of In(II) and In(I) display two maxima that can be related to two stages in the target surface evaporation. In the first stage, the evaporation proceeds under the action of the laser pulse and in the second stage, indium is evaporated by radiation emitted from the plasma of the laser torch nucleus [4]. A maximum duration of the recombination of In(III) ions with electrons (estimated from an oscillogram of the 383.5 nm emission line in Fig. 2) does not exceed 50 ns, while the corresponding recombination time for In(II) (estimated from the trailing front of an oscillogram for the λ = 451.1 nm emission line of indium atoms) is ≤500 ns.

Thus, we have demonstrated that interaction of the pulsed radiation of a moderate-power YAG:Nd^{3+} laser with an indium target surface in vacuum generates a plasma torch with the most intense In(I) emission lines at 451.1, 410.2, 325.8 (6), and 271.1 (4) nm. The principal mechanism of occupation of the excited states of In(II) and In(I) particles in the laser-generated plasma is the two-electron recombination of In(III) and (In(II), respectively. A limiting point of the recombination flux populating the excited levels of In(I) occurs at E_{up} = 5.37 eV. The upper limits of the recombination times for In(III) and In(II) ions in the plasma torch does not exceed 50 and 500 ns, respectively. Most intense lines

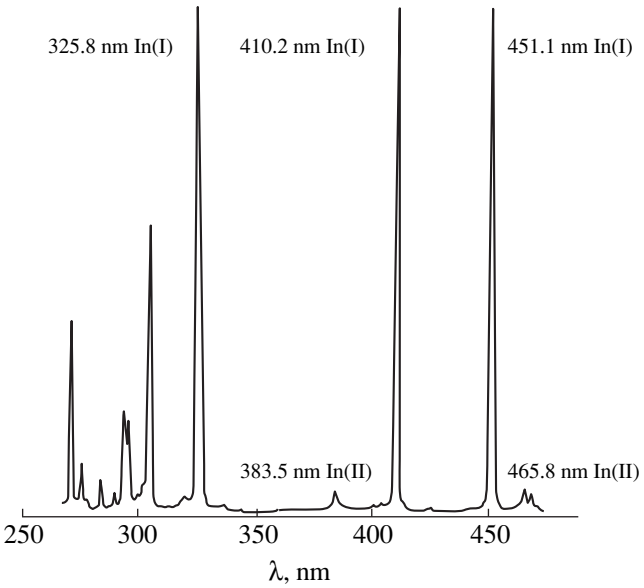

Fig. 1. A typical wide-scan spectrum of emission from the plasma of a laser-generated torch at the indium target surface (laser spot size d = 7 mm).

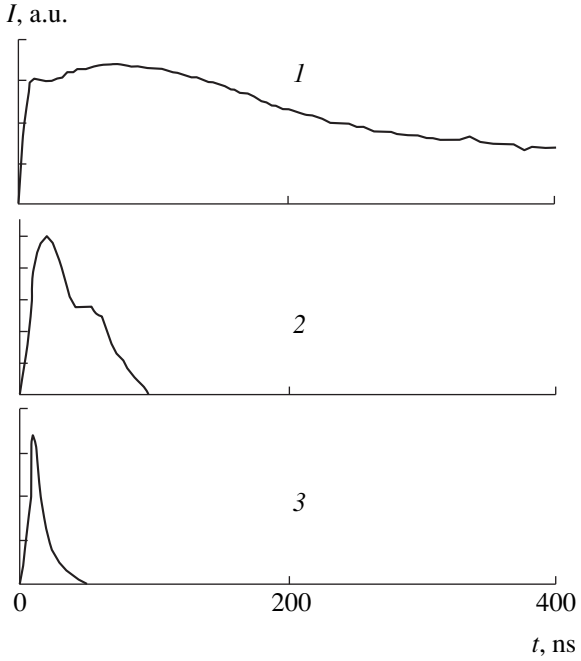

Fig. 2. Oscillograms showing the kinetics of optical emission from the plasma of the erosion torch nucleus: (*1*) 451.1 nm In(I) line; (*2*) 383.5 nm In(II) line; (*3*) 360 nm continuum.

in the emission from In(II) and In(I) can be used for the optical diagnostics of laser-generated plasma in the technology of thin film deposition by laser-beam sputtering of indium-containing compounds.

REFERENCES

1. O. B. Anan'in, Yu. A. Bykovskiĭ, V. V. Mlynskiĭ, and E. L. Stupitskiĭ, Kvantovaya Élektron. (Moscow) **16** (11), 2267 (1989).
2. L. Ya. Min'ko, A. N. Chumakov, V. V. Efremov, *et al.*, Zh. Prikl. Spektrosk. **51** (5), 746 (1989).
3. D. V. Gaĭdarenko, A. G. Leonov, and D. I. Chekhov, Fiz. Plazmy **17** (8), 918 (1991) [Sov. J. Plasma Phys. **17**, 534 (1991)].
4. L. T. Sukhov, *Laser Spectral Analysis (Physical Principles)* (Nauka, Novosibirsk, 1991).
5. A. K. Suaibov, L. L. Shimon, I. V. Shevera, and A. J. Minja, J. Phys. Stud. **3** (2), 157 (1999).
6. A. N. Zaĭdel', V. K. Prokof'ev, S. M. Raĭskiĭ, *et al.*, in *Tables of Spectral Lines* (Nauka, Moscow, 1969).
7. L. L. Shimon and É. I. Nepiĭpov, Ukr. Fiz. Zh. **19** (4), 626 (1974).

Translated by P. Pozdeev

Technical Physics Letters, Vol. 26, No. 9, 2000, pp. 835–836. Translated from Pis'ma v Zhurnal Tekhnicheskoĭ Fiziki, Vol. 26, No. 18, 2000, pp. 63–67.
Original Russian Text Copyright © 2000 by Milenin, Timofeev, Vul', Kidalov, Khodorkovskiĭ.

The Effect of Water Complexes on the Parameters of Glow Discharge in Argon–Hydroxyl Mixtures

V. M. Milenin, N. A. Timofeev, A. Ya. Vul', S. V. Kidalov, and M. A. Khodorkovskiĭ

Ioffe Physicotechnical Institute, Russian Academy of Sciences, St. Petersburg, 194021 Russia

Received May 18, 2000

Abstract—Experimental data are presented that demonstrate the dependence of the glow discharge parameters in argon–hydroxyl mixtures, including the UV emission efficiency, stability, and duration of the discharge, on the working mixture preparation conditions. Principles allowing the preparation of optimum inert gas–hydroxyl mixtures are established. The main point is to suppress the possible formation of water and/or hydroxyl complexes capable of hindering the realization of optimum conditions for the 306.4 nm OH resonance band excitation in the discharge stage. © *2000 MAIK "Nauka/Interperiodica".*

Previously [1–3], we have reported on the results of an experimental investigation into the glow discharge in mixtures of hydroxyl groups with inert gases. It was demonstrated that, under certain discharge conditions, a dominating role in the emission from discharge plasma in the visible and UV ranges belongs to the resonance band of OH molecules observed at 306.4 nm (I_{OH}). At the same time, the total relative intensity of lines representing the emission from inert gas atoms and the atomic decomposition products of water and hydroxyl (i.e., hydrogen and oxygen species) did not exceed 3–5% of the integral intensity of emission from discharge plasma in the visible and UV ranges.

An interesting feature of the discharge studied was the dependence of I_{OH} on the method of preparation of the initial working gas mixture composed of the molecules of argon and water. From this fact we inferred that the discharge parameters can be significantly affected by the presence of complexes involving water and hydroxyl molecules and/or mixed clusters of argon with water molecules. The purpose of this work was to elucidate the possible effect of such complexes on the glow discharge parameters.

As is known, the OH molecule responsible for the 306.4 nm emission band is a radical particle readily binding to other compounds occurring in a gaseous state or forming surfaces of any kind. For this reason, uncontrolled admission of OH or water molecules into the discharge device may lead to the formation of $(H_2O)_n$, $(OH)_m$, or $(H_2O)_n(OH)_m$ in the volume or on the surface of the discharge tube. These species, being sufficiently stable under the gas discharge conditions, rather poorly decompose with the formation of OH radicals. Therefore, the presence of these complexes decreases the efficiency of emission in the OH band at 306.4 nm and reduces the stability of the discharge.

In order to suppress the formation of the aforementioned complexes, we have used the following method of preparation of an initial working gas mixture filling the discharge device. A source of hydroxyl in our experiments was represented by $Ca(OH)_2$ heated to 400–600 K in a preliminarily evacuated volume V_0. A working mixture of an inert gas and water vapor formed in this volume was used for controlled admission into the discharge tube via a calibrated valve. Using an inductor coil of an RF generator situated near the V_0 volume, it was possible to create a discharge in this volume in order to form hydroxyl molecules.

For preparing a working gas mixture, the inert gas was admitted to V_0 and then $Ca(OH)_2$ was heated up to a temperature at which the saturated water vapor pressure was lower that the inert gas pressure by at least one order of magnitude. The heating temperature T was selected using a relationship obtained from the condition of chemical equilibrium [4]:

$$T \le B\{\ln(C/P_M)\}^{-1}, \quad \text{K},$$

where P_M is the pressure of inert gas atoms (molecules) [Pa]; the coefficients B [K] and C [Pa] are determined from the law of mass action. For $Ca(OH)_2$, $B = 1.2 \times 10^4$ K and $C = 3.6 \times 10^{13}$ Pa.

The working mixture can be prepared using other substances which decompose on heating with the liberation of water, such as $Mg(OH)_2$, $CuSO_4 \cdot H_2O$, $CuSO_4 \cdot 3H_2O$, $CuSO_4 \cdot 5H_2O$, $ZnSO_4 \cdot 7H_2O$, $BaCl_2 \cdot H_2O$, and $BaCl_2 \cdot 2H_2O$. Ice or supercooled water may serve a source of water molecules as well.

Semiempirical plots of the heating temperature T for the above substances versus inert gas pressure in the V_0 volume are presented in the figure. These plots were obtained using tabulated data [5], as well as the chemical equilibrium conditions (the law of mass action) relating the concentrations (pressures) of reagents and their molecular (atomic) characteristics to the temperature [4].

1063-7850/00/2609-0835$20.00 © 2000 MAIK "Nauka/Interperiodica"

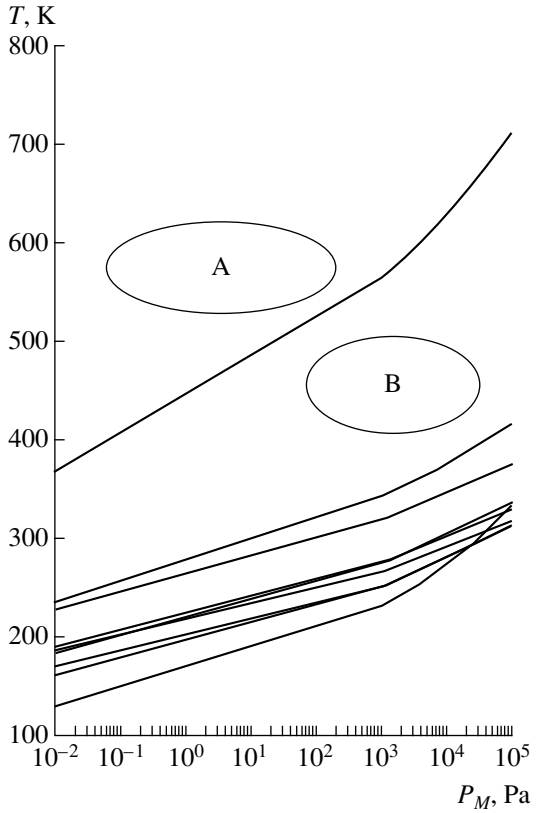

Semiempirical plots of the temperature of a source of water and hydroxyl molecules (T) versus the inert gas pressure P_M showing boundaries of the domains of the optimum gas mixture composition for various sources including $Mg(OH)_2$, supercooled water, ice, $ZnSO_4 \cdot 7H_2O$, $CuSO_4 \cdot 5H_2O$, $CuSO_4 \cdot 3H_2O$, $BaCl_2 \cdot 2H_2O$, and $BaCl_2 \cdot H_2O$, $CuSO_4 \cdot H_2O$, and $Ca(ON)_2$ (in the order of increasing temperature T).

To suppress the formation of complexes of the $(H_2O)_n$, $(OH)_m$, or $(H_2O)_n(OH)_m$ types, it is necessary to select the argon pressure and the evaporated (hydroxyl source) temperature so as to ensure that these parameters fall within the domain below the semiempirical curve corresponding to the substance chosen (see the figure).

Validity of the method proposed for selecting the parameters of the initial mixture components was confirmed by experiments. For example, conditions favoring generation of the OH resonance band at 306.4 nm with an intensity exceeding that of the main emission peaks of argon could not be achieved when water molecules were admitted into V_0 at an argon pressure below 500 Pa and a temperature of the $Ca(OH)_2$ source above 500 K (region A above the semiempirical curve corresponding to this compound in the figure). At the same time, the working mixture obtained at an argon pressure above 500 Pa and a temperature of the $Ca(OH)_2$ source below 500 K (region B under the semiempirical curve corresponding to this compound in the figure). The intensity of the OH resonance band at 306.4 nm dominated the UV and visible spectral ranges, and exceeded by more than one order of magnitude the intensity of the main emission peaks of argon.

A possible explanation for the observed effect consists in that undesired complexes of the $(H_2O)_n$, $(OH)_m$, or $(H_2O)_n(OH)_m$ types predominantly form in the volume V_0 at high partial pressures of the water and hydroxyl molecules. This process can be prevented by decreasing the partial pressure of water down to a level at which the frequency of collisions between water molecules is markedly lower that the frequency of their collisions with other particles (inert gas atoms). Moreover, mixed clusters of the $Ar_n(H_2O)_m$ type can form provided that the partial pressure of water is low and the inert gas pressure is sufficiently high, the presence of such complexes probably has a positive effect upon the discharge characteristics.

For example, it was demonstrated [6] that effective formation of the mixed argon–water clusters took place under molecular beam conditions in a supersonic nozzle channel at a 100:1 ratio of the argon to water vapor pressures. The mixed clusters of the $Ar_n(H_2O)_m$ type accounted for a considerable proportion of particles in the molecular beam, while water clusters were virtually absent. The same work showed that interaction of the mixed clusters with medium-energy electrons (15–70 eV) leads to the dissociative ionization, with positive hydroxyl ions being among the major products. Probably, low partial pressure of water and a sufficiently high argon pressure may also favor the formation of mixed clusters. The subsequent dissociation of these clusters may provide an additional channel for the formation of hydroxyl molecules.

This work was initiated and supported by the "Intellect" Scientific-Technological Association.

REFERENCES

1. A. Ya. Vul', S. V. Kidalov, V. M. Milenin, *et al.*, Pis'ma Zh. Tekh. Fiz. **25** (1), 10 (1999) [Tech. Phys. Lett. **25**, 4 (1999)].
2. A. Ya. Vul', S. V. Kidalov, V. M. Milenin, *et al.*, Pis'ma Zh. Tekh. Fiz. **25** (8), 62 (1999) [Tech. Phys. Lett. **25**, 321 (1999)].
3. V. Milenin, N. Timofeev, S. Kidalov, *et al.*, in *Proceedings of the XXIII ICPIG "The Effective Low-Pressure Gas Discharge Source of Optical Radiation Based on Hydroxyl OH," Toulouse, France, 1997*, Vol. 3, p. 56.
4. L. D. Landau and E. M. Lifshitz, in *Statistical Physics* (Nauka, Moscow, 1976; Pergamon, Oxford, 1980), Part 1.
5. *Concise Handbook of Physicochemical Quantities* (Khimiya, Moscow, 1976), p. 182.
6. A. N. Zavilopulo, A. I. Dolgin, and M. A. Khodorkovskiĭ, Phys. Scr. **50**, 696 (1994).

Translated by P. Pozdeev

Technical Physics Letters, Vol. 26, No. 9, 2000, pp. 837–838. Translated from Pis'ma v Zhurnal Tekhnicheskoĭ Fiziki, Vol. 26, No. 18, 2000, pp. 68–72.
Original Russian Text Copyright © 2000 by Ataev, Kamilov, Bagamadova, Mamedov, Makhmudov, Omaev, Shakhshaev.

Controlled Growth of Quasibicrystal Zinc Oxide Structures

B. M. Ataev, I. K. Kamilov, A. M. Bagamadova, V. V. Mamedov, S. Sh. Makhmudov, A. K. Omaev, and Sh. O. Shakhshaev

Institute of Physics, Dagestan Scientific Center, Russian Academy of Sciences, Makhachkala, Dagestan, Russia

Received April 25, 2000

Abstract—The first results on the controlled growth of quasibicrystal structures containing interblock boundaries in epitaxial zinc oxide layers on sapphire (α-Al_2O_3) are reported. The structures with boundaries oriented in a preset direction can be used as a base for submicron microelectronic devices. Using the method of buffer layers, it is possible to obtain highly oriented layers of $(11\bar{2}0)$ZnO and (0001)ZnO with clear boundaries between blocks on the same $(10\bar{1}2)Al_2O_3$ substrate surface. Data on the features of structure and morphology of these layers are presented. © *2000 MAIK "Nauka/Interperiodica".*

Bicrystal substrates are widely used for the obtaining of epitaxial layers with oriented grain boundaries for the elements and devices of submicron microelectronics such as single Josephson's junctions and their chains in Y–Ba–Cu–O high-temperature superconductors [1, 2] or giant-magnetoresistance devices based on substituted rare-earth manganites [3], etc. Devices involving epitaxial layers with oriented grain boundaries are frequently characterized by a higher (from a few times to several orders of magnitude) operation efficiency as compared to that of analogous devices manufactured by the conventional planar technology. However, operation of the improved systems is only possible provided that a clearly pronounced structural transition is formed in a certain direction, which implies the search for special bicrystals and substrates.

We suggest a method for the growth of quasibicrystal structures by preliminarily forming grain boundaries oriented in a preset direction of the substrate. A single grain boundary or a series of boundaries of this type can be formed in any part of the substrate as required by a particular technological task. In this work, we have selected α-Al_2O_3 (sapphire) as a substrate material and zinc oxide as an epitaxial material for the grain boundary formation, both substances being widely used in microelectronic technology. Note that the choice of both substrate and epitaxial layer material is rather arbitrary—any stable high-temperature oxide can be used as a medium for the grain boundary formation. At the same time, we believe that zinc oxide presents an additional interest because a nonlinear conductivity typical of the grain boundaries of some special ZnO-based ceramics is successfully used for the fabrication of varistors (see, e.g., [4]). We believe that the proposed method can be used, in particular, as a variant for the planar varistor technology.

The experiments were performed with 2×2 cm^2 $(10\bar{1}2)Al_2O_3$ substrates. During preparation, a part of the substrate surface was masked by a screen and the remaining part was coated with a 20–100 nm thick zinc oxide film. The film was deposited by DC magnetron sputtering (DCMS)—a method known to form (at least, at a substrate temperature below 600 K) deposits with the basal orientation irrespective of the substrate material and orientation (see [4, 5]). Then the substrate was placed in a low-pressure flow-type reactor and subsequent ZnO layers were grown over the entire sample surface to a total thickness of 3–5 μm by chemical vapor deposition (CVD) technique in a hydrogen atmosphere (for details, see [6]).

Study of the morphology and crystal structure of the CVD layers showed that the part of the $(10\bar{1}2)Al_2O_3$ substrate surface with a preliminarily deposited DCMS film favors the growth of a (0001)-oriented ZnO layer, while the epitaxial layer grown on the clean sapphire surface exhibits the $(11\bar{2}0)$ orientation (see, e.g, [5, 6]). Figure 1 presents a micrograph of the surface morphology in both parts of a ZnO layer grown by the CVD method on the substrate prepared as described above. Obtained with the aid of an MII-4 interference microscope at a magnification of ×350, the micrograph shows the surface of the ZnO layer grown (a) on the clean sapphire surface and (b) above the intermediate DCMS film. The image reveals the growth patterns characteristic of the indicated orientations, which are more sharp for $(11\bar{2}0)$ and less clearly pronounced for the (0001) layer (Figs. 1a and 1b, respectively). Note that a shadow observed at the boundary of two orientations is due to a difference between the ZnO layer

1063-7850/00/2609-0837$20.00 © 2000 MAIK "Nauka/Interperiodica"

Fig. 1. The surface morphology of an epitaxial ZnO layer with a grain boundary grown on a $(10\bar{1}2)Al_2O_3$ substrate: (a) $(11\bar{2}0)$ZnO; (b) (0001)ZnO (magnification, ×350).

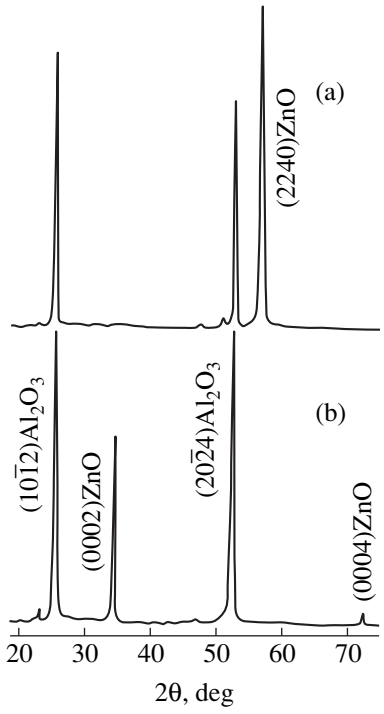

Fig. 2. Typical diffractograms from an epitaxial CVD ZnO layers grown by the CVD technique on (a) a clean sapphire surface and (b) over a preliminarily deposited DCMS underlayer.

thickness on the two sides of the boundary. This is caused by the crystal growth rate being markedly higher for the basal layer than for the $(11\bar{2}0)$ layer.

The structure of the ZnO layer was studied by X-ray diffraction on a DRON-2 diffractometer using Cu_{K_α} radiation monochromatized with the aid of a pyrographite crystal. Figure 2 shows typical diffractograms from the ZnO layers grown on the same $(10\bar{1}2)Al_2O_3$ substrate (a) without underlayer (on a clean surface) and (b) over a preliminarily deposited DCMS film. The former pattern is typical of the epitaxial $(11\bar{2}0)$ZnO layers and the latter corresponds to a highly oriented layer of the basal orientation. The ZnO layers on both parts of the substrate were additionally characterized by electron diffraction on an EMR-100 electronograph. The combined diffraction data confirmed perfect crystalline structure of the epitaxial ZnO layers grown on both parts of the substrate.

Thus, the proposed two-stage technique allows epitaxial ZnO layers to be obtained with clearly distinct crystal orientations, $(11\bar{2}0)$ and (0001), on the same $(10\bar{1}2)Al_2O_3$ substrate. The width of the boundary between two orientations depends to certain extent on the accuracy of the surface masking in the first stage of the process, whereby no DCMS material must be allowed to deposit on the masked substrate region. Apparently, a sequence of such junctions can be obtained provided that appropriate masks are employed during the DCMS deposition stage. The results of experiments with the junction chain formation by this method will be reported shortly after.

The work was supported by the Russian Foundation for Basic Research, project no. 98-02-16141.

REFERENCES

1. A. A. Verevkin, V. A. Il'in, A. P. Lipatov, *et al.*, Pis'ma Zh. Tekh. Fiz. **24** (24), 83 (1999) [Tech. Phys. Lett. **24**, 983 (1998)].
2. A. D. Mashtakov, K. I. Konstantinyan, G. A. Ovsyannikov, *et al.*, Pis'ma Zh. Tekh. Fiz. **25** (7), 1 (1999) [Tech. Phys. Lett. **25**, 249 (1999)].
3. N. D. Mathur, G. Burnell, S. P. Isaac, *et al.*, Nature **387**, 266 (1997).
4. T. Shiosaki, S. Ohnishi, and A. J. Kawabata, Appl. Phys. **50** (5), 3113 (1979).
5. B. M. Ataev, I. K. Kamilov, A. M. Bagamadova, *et al.*, Zh. Tekh. Fiz. **69** (11), 138 (1999) [Tech. Phys. **44**, 1391 (1999)].
6. A. Kh. Abduev, B. M. Ataev, and A. M. Bagamadova, Izv. Akad. Nauk SSSR, Neorg. Mater., No. 11, 1928 (1987).

Translated by P. Pozdeev

Technical Physics Letters, Vol. 26, No. 9, 2000, pp. 839–840. Translated from Pis'ma v Zhurnal Tekhnicheskoĭ Fiziki, Vol. 26, No. 18, 2000, pp. 73–77.
Original Russian Text Copyright © 2000 by Dolgopolov, Kirichenko.

Electromagnetic Wave Generation by an Electron Layer Rotating in Free Space

V. V. Dolgopolov and Yu. V. Kirichenko

Kharkov Physicotechnical Institute, National Research Center, Kharkov, Ukraine

Received April 25, 2000

Abstract—The generation of axially nonuniform electromagnetic waves by electrons rotating in crossed external fields in free space is studied theoretically. It is demonstrated that the wave increment increases with frequency under the Cherenkov resonance conditions, provided the radial electrostatic field is sufficiently strong. It is inferred that the generated frequency can be significantly increased by applying a strong radial electrostatic field. © *2000 MAIK "Nauka/Interperiodica".*

Previously, we have theoretically studied the generation of axially *uniform* electromagnetic waves by a layer of electrons revolving around a charged filament in free space (without a resonator) in the presence of a radial electrostatic or crossed electrostatic (radial) and magnetic (axial) fields [1, 2]. It was found that the generated frequencies satisfy the condition $\mathrm{Re}(\omega) \simeq mV/r$, where r is the radius of the layer, V is the azimuthal electron velocity, and m is the azimuthal wavenumber. We have also determined the conditions under which the increment of an unstable wave grows with $|m|$. However, the results of [1, 2] are valid under very stringent constraints on $|m|$. This paper demonstrates that the constraints are eliminated in the case of axially nonuniform waves, which provides possibilities for producing high-frequencies (submillimeter) waves by means of such systems.

Consider an infinitely long cylindrical layer of electrons rotating around a charged metal filament with a linear charge density Q. We use cylindrical coordinates r, φ, and z such that the z-axis coincides with the axis of the filament. For the filament, assume that its radius a is small and its conductivity is so large that the energy losses in the filament can be ignored as negligible. The electrons are confined to equilibrium circular orbits by the radial electrostatic field $E_0(r) = 2Q/r$ and the external axial magnetic field B_0. Note that $E_0(r)$ may have any sign. Let all of the perturbations depend on the coordinates and time via the factor $\exp[i(m\varphi + k_z z - \omega t)]$, with $m \neq 0$, where k_z denotes the axial wavenumber. The constant electrostatic and magnetostatic fields of the electron layer are neglected. The problem is treated in the hydrodynamic approximation. An unperturbed electron density $n(r)$ is assumed to be nonzero in the region between the surfaces $r = r_-$ and $r = r_+$ such that

$$\delta = \frac{r_+ - r_-}{r_-} \ll 1. \qquad (1)$$

In contrast to the case of $k_z = 0$ studied in [1, 2], we now deal with the case $k_z \neq 0$ so that all six components of the perturbation fields **E** and **H** are interrelated. This hinders the derivation of an equation for the E_φ component of the perturbation field **E**. We will assume that the rotating electrons are in the Cherenkov resonance with the perturbation wave:

$$\omega_m(r_-) \equiv \omega - \frac{mV}{r_-} \simeq 0, \qquad (2)$$

where V is the equilibrium electron velocity. Owing to condition (2), the equation $\mathrm{curl}\,\mathbf{E} = i\frac{\omega}{c}\mathbf{H}$ yields the following relationships between the components of **E** and **H** in the nonrelativistic approximation:

$$E_z = \frac{V}{c}H_r \simeq \frac{k_z r}{m}E_\varphi, \quad E_r + \frac{V}{c}H_z \simeq -i\frac{1}{m}\frac{d}{dr}(rE_\varphi). \qquad (3)$$

These formulas in turn allow us to express perturbations of the charge density ρ and the current density **j** in terms of E_φ and $\frac{d}{dr}(rE_\varphi)$. Then, starting from the equation $\mathrm{curl}\,\mathbf{H} = \frac{4\pi}{c}\mathbf{J} - i\frac{\omega}{c}\mathbf{E}$, we arrive at a differential equation for E_φ:

$$\frac{d}{dr}\left\{\left(1 - \frac{\Omega^2}{W}\right)r\frac{d}{dr}(rE_\varphi) + \frac{\Omega^2 mr\omega_d}{W\omega_m}E_\varphi\right\}$$

$$= \frac{\Omega^2 m\omega_d}{W\omega_m}\frac{d}{dr}(rE_\varphi) + \left\{k_z^2 r^2 + m^2 - \frac{\Omega^2 r^2 k_z^2}{\omega_m^2}\right. \qquad (4)$$

$$\left. - \frac{\Omega^2 m^2}{W}\left(1 - \frac{\omega_d}{\omega_m^2}\left(\frac{dV}{dr} - \frac{V}{r}\right)\right)\right\},$$

where $\Omega^2 = 4\pi e^2 n(r)/m_e$, $W = \omega_m^2 - \omega_d\left(\frac{V}{r} + \frac{dV}{dr} - \omega_c\right)$, $\omega_m = \omega - mV/r$, $\omega_d = 2V/r - \omega_c$, and $\omega_c = eB_0/m_e c$ (e and m_e denoting the electron charge and mass, respectively ($-e < 0$). The perturbation field components H_z and E_z obey the equations

$$r\frac{d}{dr}\left(r\frac{d}{dr}E_z\right) + (\mathcal{H}^2 r^2 - m^2)E_z = -i\frac{4\pi\omega}{c^2}r^2 J_z + i4\pi k_z r^2 \rho, \quad (5)$$

$$r\frac{d}{dr}\left(r - \frac{d}{dr}H_z\right) + (\mathcal{H}^2 r^2 - m^2)H_z = i\frac{4\pi m}{c}rJ_r - \frac{4\pi}{c}r\frac{d}{dr}(rj_\varphi), \quad (6)$$

where $\mathcal{H}^2 = \omega^2/c^2 - k_z^2$. It can be shown that condition (2) implies

$$\left|-\frac{4\pi\omega}{c^2}r^2 J_z + 4\pi k_z r^2 \rho\right| \ll \left|i\frac{4\pi m}{c}rJ_r - \frac{4\pi}{c}r\frac{d}{dr}(rj_\varphi)\right|. \quad (7)$$

Due to assumptions (1) and (2), inequality (7) is equivalent to the condition

$$|m|\delta \ll 1. \quad (8)$$

Inequality (7) means $|H_z| \gg |E_z|$: under the Cherenkov resonance conditions, the electron layer generates predominantly an H-wave.

Since the layer is thin [see assumption (1)], Eq. (4) in the region $r_- \le r \le r_+$ can be solved as in [1, 2] by the method of successive approximations. We thus obtain boundary conditions that connect the fields in the region $a < r < r_-$ to those in the region $r > r_+$. To within a term of the first order in the small parameter δ, the boundary conditions are

$$\left.\frac{dH_z}{dr}\right|_{r_+} = \left.\frac{dH_z}{dr}\right|_{r_-}, \quad H_z|_{r_+} - H_z|_{r_-} = \frac{1}{\omega_m(r_-)^2}G\left.\frac{dH_z}{dr}\right|_{r_-}, \quad (9)$$

where

$$G = \int_{r_-}^{r_+} dr\Omega^2 \frac{2E_0(r)/m_e r - \Omega^2 - \mu^2\omega_c^2}{2E_0(r)/m_e r + \Omega^2 + \omega_c^2}, \quad (10)$$

with $\mu = k_z r_-/m$. Expression (10) takes into account that $|\mu| \ll 1$. Let us solve Eq. (6) for the vacuum region under the assumption

$$\left|\frac{\omega^2}{c^2} - k_z^2\right| r^2 \ll 4|m|. \quad (11)$$

First, consider the case $\mathcal{H}^2 > 0$. Assumption (11) allows us to expand the Bessel and Neumann functions for $a < r < r_-$ and the Hankel functions for $r_+ < r$ in terms of a small independent variable. Using boundary conditions (9), we match the fields thus obtained and arrive at the dispersion equation

$$\omega_m(r_-)^2 = -\frac{|m|}{2r_-}\frac{\eta - 1}{\eta}G\{1 - 2i\Delta\}, \quad (12)$$

where $\Delta = \frac{\eta - 1}{2\eta}\frac{\pi(r_- \mathrm{Re}\, K)^{2|m|}}{(|m|-1)!|m|!2^{2|m|}} \ll 1$ and $\eta = (r_-/a)^{2|m|} > 1$. The parameter Δ refers to radiative losses to the free space ($\Delta = 0$ for $\mathcal{H}^2 \le 0$). Equation (12) implies

$$\mathrm{Re}(\omega) \simeq \frac{mV}{r_-}. \quad (13)$$

If the electric field $E_0(r)$ is so large that $G > 0$, then Eq. (12) yields an expression for the increment of a growing wave:

$$\mathrm{Im}(\omega) = |m|^{1/2}\left(\frac{\eta^{-1}}{2r_-\eta}\right)^{1/2} G^{1/2}. \quad (14)$$

It follows from formulas (13) and (14) that the increment and the frequency increase with $|m|$. The complex frequency ω satisfying Eq. (12) depends on k_z via terms of the order of $\delta^{1/2}$. In other words, the dependence of ω on k_z is very weak. Consequently, inequality (11) can be satisfied at any $|m|$ by setting k_z close to ω/c. This means that the system is free of the azimuth-velocity constraints on $|m|$, in contrast to that studied in [1, 2]. On the other hand, $|m|$ is limited by condition (8) as a result of the finiteness of the δ value. Thus, a radial electrostatic field such that

$$E_0(r_-) > 0, \quad \frac{2eE_0(r_-)}{m_e r_-} > \bar{\Omega}^2 + \mu^2\omega_c^2, \quad (15)$$

where $\bar{\Omega}$ is the average plasma frequency, can significantly increase the generated frequency irrespective of the magnetic field strength, including the case $B_0 = 0$. If $G < 0$, the waves grow due to the dissipative effects. The increments of these waves are small, going down as $|m|$ goes up. If $\mathcal{H}^2 \le 0$, the wave generated in the infinite annular beam does not loose energy through radiation into the free space. A semi-infinite annular beam would emit the radiation from its end.

REFERENCES

1. V. V. Dolgopolov and Yu. V. Kirichenko, Pis'ma Zh. Tekh. Fiz. **25** (21), 1 (1999) [Tech. Phys. Lett. **25**, 845 (1999)].
2. V. V. Dolgopolov and Yu. V. Kirichenko, Izv. Vyssh. Uchebn. Zaved., Radioélektron. **43**, 29 (2000).

Translated by A. Sharshakov

Technical Physics Letters, Vol. 26, No. 9, 2000, pp. 841–843. Translated from Pis'ma v Zhurnal Tekhnicheskoĭ Fiziki, Vol. 26, No. 18, 2000, pp. 78–84.
Original Russian Text Copyright © 2000 by Karasev, Suzdal'tsev, Yafarov.

The Formation of a Nondiamond Carbon Phase in a Microwave Gas Discharge Plasma under Electron Cyclotron Resonance Conditions

S. A. Karasev, S. Yu. Suzdal'tsev, and R. K. Yafarov

Saratov Department, Institute of Radio Engineering and Electronics, Russian Academy of Sciences, Saratov, Russia

Received March 21, 2000

Abstract—Special features in the nucleation and growth of a nondiamond carbon phase were studied in a microwave plasma of various acetylene-containing gas mixtures. *© 2000 MAIK "Nauka/Interperiodica".*

The synthesis of carbon films in a low-pressure gas discharge plasma is a promising method for the obtaining of carbon-containing materials for electronics, necessary for the creation of devices and instruments capable of operating under extremal conditions. An important circumstance is that carbon, by virtue of its chemical nature, may form materials with different types of chemical bonds and with a broad spectrum of physical properties. The limiting cases are offered by allotropic modifications of carbon such as graphite, diamond, fullerenes, carbin, etc. The synthesis of any allotropic carbon phase, for example nanocrystalline diamond—a material possessing unique emission properties, is usually accompanied by the growth of a graphitelike phase that is frequently a limiting stage of the process [1, 2]. For this reason, all syntheses must be performed taking into account optimum kinetic conditions facilitating the formation of a desired allotropic carbon phase and preventing the formation of a graphitelike modification. In connection with this, investigation of the growth of graphite (as one of the most stable carbon modifications) at low pressures and temperatures is an important task in development of the synthesis of carbon-based materials with preset physical properties. The purpose of this work was to study the nucleation and growth of nondiamond carbon films in various acetylene-containing gas mixtures activated by microwave electric discharge.

The films were deposited onto a glass substrate in a microwave gas discharge plasma under electron cyclotron resonance conditions using an experimental setup described in [3]. The substrate temperature (250°C) and the deposition time (20 min) remained the same. The deposited film thicknesses were determined using laser-ellipsometric and interference microscopes. Detailed investigation of the sample surface microtopography was performed in a scanning atomic-force microscope (AFM) and the structure of deposits was studied by X-ray diffraction using a DRON-3.0 diffractometer.

Figures 1 and 2 show the plots of film thickness h and average microcrystallite size d (height above the substrate surface) versus partial acetylene pressure for various gas mixtures. Clear differences are observed in the character of the variation of the h and d values for the media containing components that are inert (Ar, N_2) and active (O_2, H_2O) with respect to carbon. The carbon film deposition from acetylene mixtures with inert gases began at very small acetylene concentrations, while the process in mixtures with the active components was initiated only when the partial pressure of acetylene exceeded certain minimum (critical) levels. At a total gas pressure of 1 Pa, these critical values were not less that 0.25 Pa (25%) in the acetylene mixtures with water vapor and above 0.4 Pa (40%) in mixtures with oxygen. The nature and amount of additives to acetylene also markedly influenced the surface morphology of the graphitelike phase (Fig. 3), while not affecting the character of variation of the film thickness

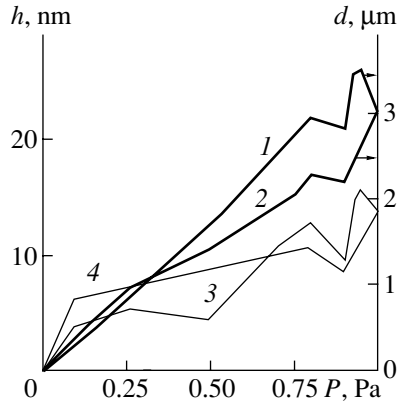

Fig. 1. The plots of (*1*, *2*) thickness h and (*3*, *4*) average microcrystallite size d versus the partial pressure of acetylene P for the nondiamond carbon films deposited from the microwave discharge plasma in acetylene mixtures with (*1*, *3*) argon and (*2*, *4*) nitrogen.

1063-7850/00/2609-0841$20.00 © 2000 MAIK "Nauka/Interperiodica"

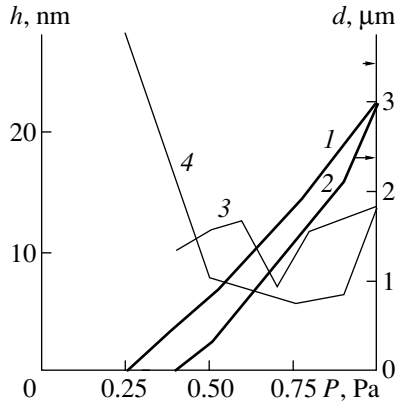

Fig. 2. The plots of (*1*, *2*) thickness *h* and (*3*, *4*) average microcrystallite size *d* versus the partial pressure of acetylene *P* for the nondiamond carbon films deposited from the microwave discharge plasma in acetylene mixtures with (*1*, *4*) water vapor and (*2*, *3*) oxygen.

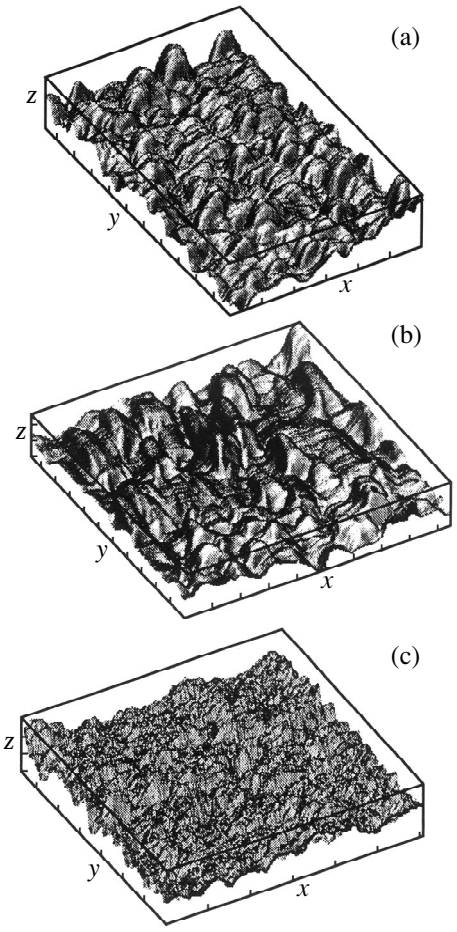

Fig. 3. Scanning AFM images of the surface of carbon films deposited under the electron cyclotron resonance conditions from the microwave discharge plasma in (a) pure acetylene (scale: *x*, 1 μm; *y*, 1 μm; *z*, 10 nm) and its mixtures (b) 25% C_2H_2 + 75% H_2O (scale: *x*, 1 μm; *y*, 1 μm; *z*, 10 nm) and (c) 10% C_2H_2 + 90% Ar (scale: *x*, 1 μm; *y*, 1 μm; *z*, 1 nm).

(crystallization rate). In the gas mixtures of both types, an increase in the partial pressure of C_2H_2 was accompanied by virtually linear growth in the carbon film thickness with the slope depending on the particular additives: 5, 4, 3.7, and 2.9 for oxygen, water vapor, argon, and nitrogen. The only exception was observed for the deposition process in acetylene mixtures with small amounts of argon, where the film thickness and microcrystallite size increased at a markedly higher rate than in pure acetylene.

Another feature in common for the plots depicted in Figs. 1 and 2 is a jump in the average microcrystallite size observed in the deposition curves in the region of minimum acetylene concentrations in mixtures with various additives. The maximum size of microcrystallites (up to 30–40 nm) was observed for the deposition from acetylene mixtures with water vapor (Fig. 3b); note that the microcrystallites were observed in the stage where the film thickness was not yet measured. Therefore, under the conditions of a small flux of carbon particles from the gas phase (and, accordingly, low nucleation rates), a nondiamond carbon phase precipitated predominantly in the form of separate microscopic islands (protrusions). The height of these islands sharply decreased (to 5–6 nm) with increasing film thickness (for a mixture containing more than 25% acetylene with water vapor). In the mixtures of acetylene with another carbon-active additive—oxygen—the size of microcrystallites observed in the absence of a detectable film thickness was about 10–12 nm. A similar (albeit much less pronounced) character of the initial stage of the graphite film growth on glass substrates was also observed for the mixtures of acetylene with inert gases.

The subsequent variation of the microcrystallite size with increasing partial pressure of acetylene also depended on the nature of the additives. For the carbon-active ones, the plots of microcrystallite size versus acetylene pressure exhibit minima in the region between the initial growth stage (for the threshold C_2H_2 concentrations) and the case of graphite deposition from pure acetylene. The most inhomogeneous growth (manifested by a maximum average size of the nondiamond microcrystallites on the film surface) was observed in pure acetylene (Fig. 3a) and acetylene–oxygen mixtures. In the latter case, the size of microcrystallites varied from 12–14 to 40 nm depending on the partial pressure of oxygen. The most smooth films were deposited from acetylene mixtures with water vapor: here, the microcrystallite size varied from 3 to 7 nm.

The average size of inhomogeneities monotonically decreased with decreasing film thickness and increasing content of inert gases in mixtures with acetylene. Slowly growing films exhibited a smoother appearance. The minimum average size of nanocrystallites was observed on the surface of carbon films deposited from a 90% Ar + 10% C_2H_2 mixture (Fig. 3c). Here, the aver-

age crystallite size approached 3 nm and was about half as small as the value for the film deposited from a 90% N_2 + 10% C_2H_2 mixture. This is probably related to the so-called "polishing" effect of argon ions possessing a greater mass and a higher sputtering efficiency as compared to the same properties of nitrogen ions. This assumption is confirmed by comparison of the average size of nanocrystallites observed on the surface of carbon films deposited at other partial pressures of the same inert gases added to acetylene. Indeed, Fig. 1 shows that the curve of the average size of microcrystallites for the acetylene–argon mixtures lies below the curve for the acetylene mixtures with nitrogen (having a molecular mass below that of argon). From these data we may conclude that the growth of nanocrystallites in a nondiamond carbon phase deposited from acetylene mixtures containing more than 30–40% of inert gases is limited by the physical sputtering of carbon by ions of these gases.

An analysis of the X-ray diffraction patterns obtained for carbon films deposited from acetylene mixtures with the additives studied showed that the deposits contain virtually no diamondlike phases except for the C(2OH) phase. The films are composed primarily of a fine-crystalline graphite (002) with a normal and defect layer package [4].

Conclusions:

(1) The rate of nondiamond carbon deposition from a microwave discharge plasma in acetylene mixtures with various chemically active and inert additives is proportional to the partial pressure of acetylene. The proportionality factor depends on the particular additive; for the additives inert with respect to carbon, this coefficient increases with the ion mass.

(2) The synthesis of carbon films from acetylene mixtures with carbon-active gases is possible only provided that the partial pressure of acetylene exceeds a certain critical level, which is not less than 0.25 Pa (25% in a C_2H_2 + H_2O mixture at 1 Pa) and more than 0.4 Pa (40% at a total pressure of 1 Pa).

(3) Small additives of argon (5–20%) to acetylene activate heterogeneous processes on the substrate surface and markedly intensify the growth of graphite and its microscopic aggregates on the growth surface. The layer thickness and the height of microaggregates for these mixtures are greater compared to those for the graphite films deposited from pure acetylene.

(4) The growth of nanocrystallites in a nondiamond carbon phase deposited from acetylene plasma containing more than 30–40% of inert gases is limited by the physical sputtering of carbon by ions of these gases.

(5) The plots of film thickness and average microcrystallite size for the nondiamond carbon deposited from acetylene plasma with inert gas additives are correlated with each other. No such correlation is observed for the carbon films deposited from mixtures containing additives that are active with respect to carbon.

(6) Because of unfavorable nucleation conditions, the growth of the nondiamond carbon phase from acetylene mixtures with carbon-active additives proceeds in the form of microscopic islands. The maximum dimensions of these islands are observed for the acetylene concentrations equal to the critical values for the corresponding additives.

REFERENCES

1. A. P. Rudenko and I. I. Kulakova, Vestn. Mosk. Univ., Ser. 2: Khim. **34** (6), 523 (1993).
2. S. Yu. Suzdal'tsev, S. V. Sysuev, and R. K. Yafarov, Pis'ma Zh. Tekh. Fiz. **24** (4), 25 (1998) [Tech. Phys. Lett. **24**, 135 (1998)].
3. N. N. Bylinkina, S. P. Mushtakova, V. A. Oleĭnik, *et al.*, Pis'ma Zh. Tekh. Fiz. **22** (6), 43 (1996) [Tech. Phys. Lett. **22**, 245 (1996)].
4. A. Ubbelohde and F. Lewis, *Graphite and Its Crystal Compounds* (Clarendon Press, Oxford, 1960; Mir, Moscow, 1965).

Translated by P. Pozdeev

Technical Physics Letters, Vol. 26, No. 9, 2000, pp. 844–848. Translated from Pis'ma v Zhurnal Tekhnicheskoĭ Fiziki, Vol. 26, No. 18, 2000, pp. 85–94.
Original Russian Text Copyright © 2000 by Kotov, Kosareva, Liokumovich, Markov, Medvedev, Nikolaev.

Multichannel Signal Detection in a Multimode Optical-Fiber Interferometer: Ways to Reduce the Effect of Amplitude Fading

O. I. Kotov, L. I. Kosareva, L. B. Liokumovich, S. I. Markov, A. V. Medvedev, and V. M. Nikolaev

St. Petersburg State Technical University, ul. Politekhnicheskaya 29, St. Petersburg, 195251 Russia

Received March 28, 2000; in final form, May 23, 2000

Abstract—For a multimode optical-fiber interferometer with a multichannel detector system, two alternative methods of signal processing in the presence of amplitude fading are studied theoretically and experimentally: (a) the summation of the signal magnitudes over various channels; (b) the selection of the channel whose signal modulus has the largest amplitude. It is shown that both methods can significantly reduce the signal amplitude fading at the interferometer output. A statistical model of the multimode interferometer is suggested assuming independent signal variations in different channels. For a ten-channel system with photodiode detectors, the computation and the measurements demonstrate that both variants of the data processing yield more than three-fold decrease in the ratio of the rms deviation under the fading conditions to the mean output signal. *© 2000 MAIK "Nauka/Interperiodica".*

The multimode optical-fiber interferometer (MFI) is among the most simple fiber interferometers in terms of design. The system comprises a multimode fiber illuminated by a coherent source with a coherence time exceeding differences between the group delays of the modes [1, 2]. The interference of modes produces a speckled pattern at the output end of the fiber. External factors acting upon the fiber cause the so-called differential phase modulation of the propagating radiation, whereby the phase differences between the modes vary in time. The differential phase modulation is manifested by intensity variations in different parts of the interference pattern, this effect being registered by a photodetector.

MFIs are employed in various fiber sensors of physical quantities [3, 4], continuous data-acquisition lines [5], phase-stable optical transmission lines [6], and optical signaling devices [7].

At the same time, MFIs suffer from a serious drawback, namely the amplitude fading of the useful signal [1, 2] caused by variations in the intermodal phase relationships.

The fading is usually reduced by multichannel detection and subsequent signal processing. For example, a four-channel detector with nonlinear elements was suggested for MFIs implementing second-harmonic modulated signal extraction [8]. To the best of our knowledge, no detailed analyses of MFIs with multichannel detectors have been published to embrace systems with different signal processing techniques and various channel numbers.

This paper presents a statistical model of an MFI with a multichannel photodetector and describes an experiment performed to evaluate the performance of the ten-channel system.

Consider a multimode isotropic optical fiber illuminated by a coherent source at a working frequency ω. The light flux intensity at an individual photodetector is [9, 10]

$$I(S) = \frac{1}{2}\sum_{i=1}^{N} A_i^2 \int_S E_i^2 ds + \sum_{\substack{i,k \\ i>k}}^{N} \left[A_i A_k^* \int_s E_i E_k^* ds \right] \cos(\Psi_{ik}), \quad (1)$$

where L is the fiber length, S is the interference pattern area covered by the photodetector, N is the total number of propagating modes, and $A_{i(k)}$ and $E_{i(k)}$ are the amplitude and the modal function of the ith (or kth) mode, respectively. The intermodal phase difference Ψ_{ik} is expressed as

$$\Psi_{ik} = (\beta_i - \beta_k)L + (\phi_i - \phi_k), \quad (2)$$

where $\beta_{i(k)}$ is the propagation constant of the ith (or kth) mode. The phase shifts $\phi_{i(k)}$ arise from the mode interaction and birefringence, and depend on the external factors acting on the fiber.

1063-7850/00/2609-0844$20.00 © 2000 MAIK "Nauka/Interperiodica"

Since MFIs typically operate as distributed sensors, it is convenient to represent Ψ_{ik} as

$$\Psi_{ik} = \Psi_{ik}^0 + \delta\Psi_{ik}, \quad (3)$$

where Ψ_{ik}^0 describes large but slow phase shifts caused by changes in the ambient conditions (temperature, pressure, etc.) and $\delta\Psi_{ik}$ represents small but rapid phase shifts caused by informative external agents (useful signal). The first term in Eq. (3) refers to phase shifts that are much larger than ($\gg\pi$) and exhibit a quasistatic character with frequencies in the 0–0.1 Hz range. The second term describes phase shifts that are much smaller than ($\ll\pi$), their characteristic frequencies being above 10 Hz. Using trigonometric formulas, we may rewrite the expression (1) as

$$I(S) = I_0(1 + \rho_0 + \rho_1). \quad (4)$$

Here, I_0 is a constant independent of the intermodal phase differences, and ρ_0 is a slowly varying quantity controlled by external conditions. The terms I_0 and ρ_0 are expanded as

$$I_0 = \frac{1}{2}\sum_{i=1}^{N} A_i^2 \int_S E_i^2 ds,$$

$$\rho_0 = \frac{1}{I_0}\sum_{i=1}^{N}\sum_{k=1}^{N}\left[A_i A_k^* \int_S E_i E_k^* ds\right]\cos(\Psi_{ik}^0).$$

The term ρ_1 is a rapidly varying quantity representing the MFI response:

$$\rho_1 = -\frac{1}{I_0}\sum_{i=1}^{N}\sum_{k=1}^{N}\left[A_i A_k^* \int_S E_i E_k^* ds\right]\sin(\Psi_{ik}^0)\delta\Psi_{ik}. \quad (5)$$

The quantity ρ_0 represents a quasistatic additive interfering signal that can be rejected by frequency filtering. In what follows, we ignore this term and concentrate on the value of ρ_1, which contains useful information.

Let δs represent a physical action upon the fiber. In the general case, the resultant phase shifts can be expressed as

$$\delta\Psi_{ik} = V_{ik}\delta s, \quad (6)$$

where the coefficients V_{ik} depend on the fiber parameters and the length of the exposed fiber segment. The response of the MFI to the signal δs is

$$\rho_1 = \left\{-\frac{1}{I_0}\sum_{i=1}^{N}\sum_{k=1}^{N}\left[A_i A_k^* \int_S E_i E_k^* ds\right]\sin(\Psi_{ik}^0)V_{ik}\right\}\delta s = \rho_2\delta s, \quad (7)$$

where

$$\rho_2 = \left\{-\frac{1}{I_0}\sum_{i=1}^{N}\sum_{k=1}^{N}[A_i A_k^* \int_S E_i E_k^* ds]\sin(\Psi_{ik}^0)V_{ik}\right\}$$

is the MFI transmission coefficient. The factor ρ_2 varies depending on the ambient conditions and produces a multiplicative interference with the useful signal, which is a manifestation of the fading effect.

It is seen from (7) that ρ_2 depends in a complicated manner on the fiber parameters and the ambient conditions. We therefore suggest a statistical approach to the analysis of the fading effects, whereby the value of ρ_2 at the instant of measurement is considered as a random variable.

Let us take a closer look at formula (7). The coefficient ρ_2 is the sum of sine terms. Their amplitudes, $A_i A_k^* (\int_S E_i E_k^* ds)V_{ik}$, are determined by the mode parameters, detection conditions, and the length of the exposed segment; they may have different signs and may considerably differ in magnitude from each other. The phases Ψ_{ik}^0 are determined by the fiber parameters and the ambient factors (such as the temperature or pressure), in particular, by the birefringence and the mode coupling due to inhomogeneities.

Let us therefore regard the phases Ψ_{ik}^0 corresponding to an arbitrary moment of detection as independent random variables. According to the central limit theorem, the random variable ρ_2 has a Gaussian distribution if the total number of the summands is large, the variance of ρ_2 is denoted by σ_2. On the whole, the response $\rho_1 = \rho_2\delta s$ to a given δs is a random variable with the variance $\sigma_1 = \sigma_2\delta s$. The probability density function (pdf) of ρ_1 is

$$W(\rho_1) = \frac{1}{\sqrt{2\pi\sigma_1}} e^{-\frac{\rho_1^2}{2\sigma_1^2}}. \quad (8)$$

Thus, for a fixed external action, fading makes the output MFI signal a zero-mean random variable. Note that pdf (8) is maximum near $\rho_1 = 0$. Consequently, the output signal may well be weak so that relevant data are basically lost.

The fading effect can be reduced by using an appropriate signal processing after detection. It seems most reasonable to take the absolute value of the signal. According to [11, 12], the pdf of $\eta = |\rho_1|$ is

$$w_1(\eta) = 2w(\eta), \quad \eta \geq 0. \quad (9)$$

The signal thus processed has a nonzero mean η with $k = \sqrt{D_\eta}/\bar{\eta} = 0.75$, where $\sqrt{D_\eta}$ is the rms deviation. The ratio is well suited to evaluation of the fading effects. On the other hand, the pdf is still maximum at

a zero signal level, which implies a high probability of losing useful data.

To reduce k, two alternative methods are suggested by analogy with the detection techniques used in multichannel wireless digital communications systems operating in the HF band [13, 14]:

(1) A sufficiently large number of photodetectors are taken, and the magnitudes of their output signals are added up.

(2) With a fixed number of photodetectors, the output signal with the largest magnitude is selected by means of a comparator.

Since the photodetectors have different sets of the mode amplitudes $A_i A_k^* (\int_S E_i E_k^* ds) V_{ik}$ entering into Eq. (7), we assume that the corresponding fading components in the output signals of various photodetectors are uncorrelated and the random variables ρ_2 are independent.

Consider the first method with M photodetectors. According to [12], the pdf of the sum signal $\xi = \sum_{k=1}^{M} \eta_k$, where η_k are independent random variables, can be found from the following recurrence relation:

$$w_M^{(1)}(\xi) = \int_0^\xi w_{M-1}(x) w_1(\xi - x) dx, \quad \xi \geq 0. \qquad (10)$$

Using the second method for M photodetectors, we deal with M independent identically distributed random variables, the pdf being $w_1(\eta)$. According to [11, 12], the selected maximum variable has the pdf

$$w_M^{(2)}(\xi) = MF^{M-1}(\xi) w_1(x), \qquad (11)$$

where $F(\xi)$ is the probability distribution function

$$F(\xi) = \int_0^\xi w_1(x) dx. \qquad (12)$$

The above formulas enable one to evaluate the mean, the variance, and the ratio k as functions of the number of photodetectors for each of the two methods.

The experiment was carried out with a gas laser operating at $\lambda = 0.63$ μm and $P = 2$ mW, a multimode graded-index fiber, and a ten-channel photodiode detector system connected to a computer via a multichannel ADC. (The fiber had a core diameter of 50 μm, a numerical aperture of 0.12, and a length of 480 m.) A 5-m segment of the fiber was placed into an adjust-

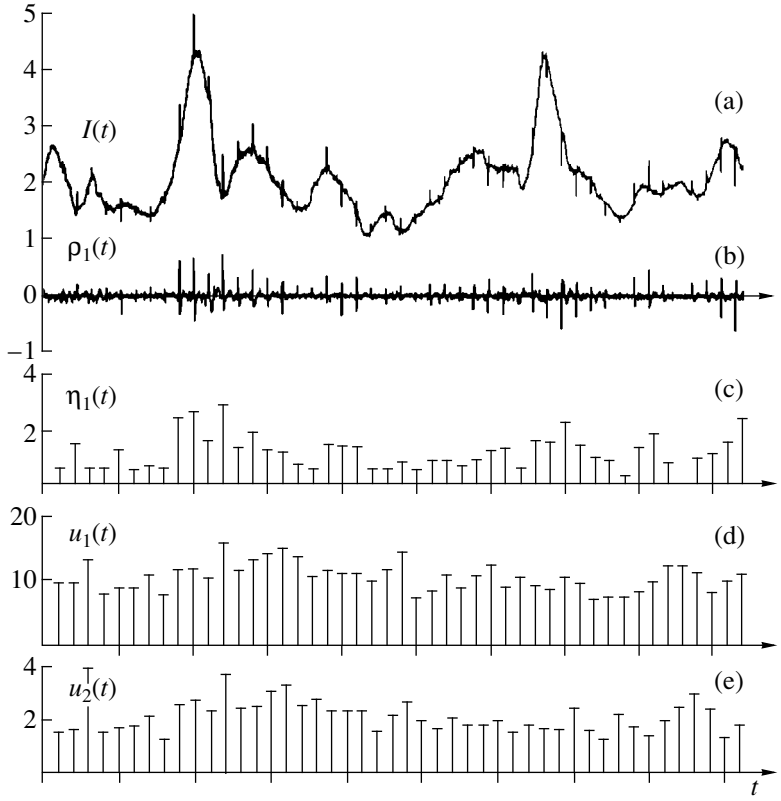

Fig. 1. Interferometer signals vs. time: (a) a fragment of the output signal of a photodetector; (b) the output signal of a photodetector after the rejection of quasi-static components; (c) signal pulse amplitudes extracted from the output of a photodetector; (d) signal pulse amplitudes processed by the "sum-of-magnitudes" method ($M = 10$); (e) signal pulse amplitudes processed by the "maximum magnitude" method ($M = 10$).

able thermostat, and a 10-cm segment was subjected to a weak mechanical disturbance simulating the useful signal δs.

The "total" signal from the photodetector is described by expression (4). The subsequent filtering and processing are performed by the computer.

During the measurements, which lasted for about 1000 s, the fiber experienced mechanical disturbance and slow heating by about 20°C to produce fading. Figure 1a shows a waveform fragment of the $I(t)$ signal from one of the detector channels. It is seen that one can easily discriminate between the quantities involved in (4): I_0, ρ_0, and $\rho_1 = \rho_2 \delta s$. Note that the respective temperature-induced variations in ρ_0 and ρ_2 are uncorrelated, although both refer to the same channel. After digital filtering (by a second-order high-pass filter), the signal contains only the component $\rho_1(t)$ representing the signal δs with a multiplicative interference ρ_2 (see Fig. 1b). From these signals, the amplitudes of the signal pulses were determined (Fig. 1c) and subjected to subsequent processing and analysis. Note that changes in the magnitude and the sign of ρ_1 are caused by those of ρ_2 rather than by changes in the sign of δs (the amplitude and sign of the last quantity being constant). Use of any of the two methods for processing the signals from ten photodetectors (for the sum of moduli u_1 or the maximum modulus u_2) increases the mean value of the signal (Figs. 1d, 1e).

In the computation and the experiment, the ratio of the areas of the photodetector aperture and the output spot of the fiber were maintained at a constant level, while the number of channels was increased. Ten photodetectors, each having a diameter of 4 mm, were arranged in three rows (3 + 4 + 3). The diameter of the array was somewhat smaller than that of the output spot in the far-field zone.

The computation and the experiment showed that the first method perfectly corresponds to the classical case of adding M independent random variables: the mean of the sum grows in proportion to M, while the rms deviation is proportional to $\sqrt{M}$ (see curves *1* in Fig. 2), so that the ratio k_1 goes down. The spread in the values obtained by the processing of measured data results from taking into account all of the possible combinations of M photodetectors for $M \neq 10$.

With the second method, an increase in the number of channels causes no growth in the variance of the output signal but raises the mean somewhat, thus decreasing k_2 again (see curves *2* in Fig. 2).

The high correspondence between the computed and the measured dependences supports the above assumption that fading processes corresponding to different channels are uncorrelated and that the statistical model can be applied to MFIs.

Each of the proposed multichannel signal processing methods sharply reduces the probability that the useful signal will be suppressed by fading. For example, with $M = 10$, the probability that the level of ρ_1 will be below $0.1\sigma_1$ is $P(\rho_1 < 0.1\sigma_1) = P(\rho_2 < 0.1\sigma_2) < 10^{-6}$ in both cases.

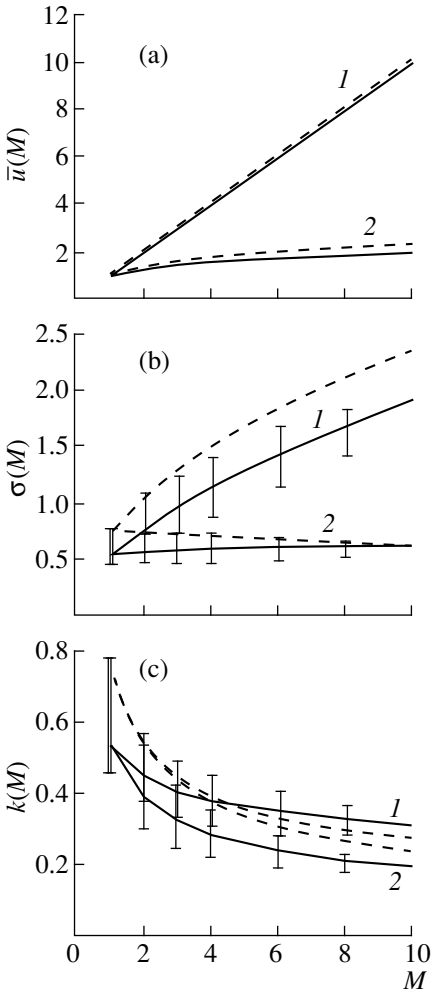

Fig. 2. The plots of (a) mean signal value u, (b) rms deviation σ, and (c) their ratio k on the number of photodetectors. The solid and broken curves refer to the experiment and the computation, respectively. (The spread in the measured values results from taking into account all of the possible combinations of M photodetectors for $M \neq 10$.) Curves *1* and *2* refer to the "sum-of-magnitudes" and the "maximum-magnitude" methods of signal processing, respectively.

REFERENCES

1. S. A. Kingsley and D. E. N. Davies, Electron. Lett. **14** (11), 322 (1978).
2. S. A. Kingsley, Electron. Lett. **14** (11), 335 (1978).
3. M. Spajer, B. Carquille, and H. Maillotte, Opt. Commun. **60** (5), 261 (1986).
4. M. R. Layton and J. A. Bucaro, Appl. Opt. **18** (5), 666 (1979).
5. B. Calshaw, P. R. Ball, J. C. Pond, and A. A. Sadler, Electron. Power **11** (2), 148 (1981).

6. V. I. Gasyuk, O. I. Kotov, L. B. Liokumovich, and V. M. Nikolaev, Pis'ma Zh. Tekh. Fiz. **20** (8), 1 (1994) [Tech. Phys. Lett. **20**, 644 (1994)].
7. A. V. Medvedev, L. I. Kosareva, O. I. Kotov, *et al.*, in *Proceedings of the International Workshop NDTCS-99*, Proc. SPIE **4064**, 2000 (1999).
8. P. R. Ball, B. Culshaw, and S. A. Kingsley, Proc. SPIE **232**, 216 (1980).
9. K. Petermann, IEEE J. Quantum Electron. **QE-16** (7), 761 (1980).
10. L. I. Kosareva, O. I. Kotov, L. B. Liokumovich, *et al.*, Pis'ma Zh. Tekh. Fiz. **26** (2), 53 (2000) [Tech. Phys. Lett. **26**, 70 (2000)].
11. B. R. Levin, *Theoretical Principles of Statistical Radio Engineering* (Sov. Radio, Moscow, 1989).
12. E. S. Venttsel' and L. A. Ovcharov, *Applied Problems of the Probability Theory* (Moscow, 1983).
13. A. M. Fink, *Theory of the Transmission of Discrete Communication* (Sov. Radio, Moscow, 1963).
14. I. S. Andronov and L. M. Fink, *Transmission of Discrete Communication via Parallel Channels* (Sov. Radio, Moscow, 1971).

Translated by A. Sharshakov